BIOGEOCHEMICAL (BGC) ARGO IMPROVES UNDERSTANDING AND QUANTIFICATION OF THE OCEAN'S BIOLOGICAL CARBON PUMP

by

Bin Wang

Submitted in partial fulfilment of the requirements
for the degree of Doctor of Philosophy

at

Dalhousie University
Halifax, Nova Scotia
October 2022

Table of Contents

LIST OF TABLES

LIST OF FIGURES

ABSTRACT

The ocean's biological carbon pump (BCP) contributes to the sequestration of organic carbon in the deep ocean and influences atmospheric CO_2 levels. Despite its significance, the BCP remains poorly characterized due to insufficient observations. Recent advances of Biogeochemical-Argo (BGC-Argo) program have greatly increased the availability of biogeochemical observations including those which contain a wealth of information about the BCP. Therefore, the application and interpretation of these new observations warrants further investigation. This thesis presents applications of BGC-Argo data to improve estimates and mechanistic understanding of the BCP by exploring their synergies with biogeochemical models, and by performing comprehensive analyses of high-frequency BGC-Argo observations. Specifically, I carried out model optimizations using different combinations of satellite chlorophyll and BGC-Argo observations. Results show that the inclusion of BGC-Argo profiles of multiple biogeochemical properties in the parameter optimization greatly improved the model's representation of subsurface biological distributions and vertical carbon flux. Since the availability of BGC-Argo profiles is so far insufficient for sequential data assimilation in most regions, multivariate data assimilation of satellite observations was applied to a coupled physical-biogeochemical model. Repeating data assimilation experiments by using an alternative light parameterization that had been *a priori* calibrated with BGC-Argo profiles showed that a well-calibrated model with accurate parameterizations is fundamental to data assimilation. This motivated me to investigate to what extent BGC-Argo data can help in distinguishing different parameterizations of vertical carbon flux. I set up a 1D model framework and calibrated it using BGC-Argo data to compare common parameterizations of vertical carbon flux in the same model environment. Results show great potential for BGC-Argo to inform vertical flux parameterizations and in determining the associated parameter values. Finally, I applied a new method, based on the mass balance of particulate organic carbon and oxygen, to BGC-Argo data to estimate vertical carbon flux due to different mechanisms. Results show that, in addition to the gravitational sinking flux of large particles, small particles make a significant contribution to the vertical flux at 100 m due to multiple mechanisms and at 600 m due to fragmentation of large particles.

LIST OF ABBREVIATIONS AND SYMBOLS USED

Abbreviations:

1D	One-dimensional
3D	Three-dimensional
AOU	Apparent Oxygen Utilization
AVHRR	Advanced Very High-Resolution Radiometer
AVISO	Archiving Validation and Interpretation of Satellite Oceanographic Data
bbp470	Backscatter at 470 nm
bbp670	Backscatter at 670 nm
bbp700	Backscatter at 700 nm
BCP	Biological Carbon Pump
BGC-Argo	Biogeochemical-Argo
BLINGv2	Biogeochemistry with Light, Iron, Nutrients and Gas Version 2
BOEM	Bureau of Ocean Energy Management
CbPM	Carbon-based Productivity Model
CMIP6	The sixth phase of the Coupled Model Intercomparison Project
COBALTv2	Version 2 of the Carbon, Ocean Biogeochemistry and Lower Trophics
Corr	Correlation Coefficient
CTD	Conductivity-Temperature-Depth
DCM	Deep Chlorophyll Maximum
DEnKF	Deterministic Ensemble Kalman Filter
DIC	Dissolved Inorganic Carbon
doy	day of year
ECMWF	European Centre for Medium-Range Weather Forecast
EKE	Eddy Kinetic Energy

EnKF	Ensemble Kalman Filter
EOFs	Empirical Orthogonal Functions
ERA-interim	ECMWF Reanalysis-Interim
ERA5	ECMWF Reanalysis v5
ESA	European Space Agency
ESMs	Earth System Models
FABM	Framework for Aquatic Biogeochemical Models
GFDL	Geophysical Fluid Dynamics Laboratory
GLORYS	Global Ocean Reanalysis and Simulation
GOM	Gulf of Mexico
GOTM	General Ocean Turbulence Model
HAMOCC6	Hamburg Oceanic Carbon Cycle model
HYCOM	HYbrid Coordinate Ocean Model
IPSL	Institut Pierre Simon Laplace
MARBL	Marine Biogeochemistry Library
MDT	Mean Dynamic Topography
MERIS	Medium Resolution Imaging Spectrometer
MODIS	Moderate Resolution Imaging Spectroradiometer
MPDATA	Multidimensional Positive Definitive Advection Transport Algorithm
MPI-M	Max Planck Institute for Meteorology
NCAR	National Center for Atmospheric Research
NCODA	Navy Coupled Ocean Data Assimilation
NPP	Net Primary Production
OC-CCI	Ocean Colour Climate Change Initiative
PAR	Photosynthetically Active Radiation
PISCESv2	Pelagic Interactions Scheme for Carbon and Ecosystem Studies volume 2
POC	Particulate Organic Carbon
PON	Particulate Organic Nitrogen
PP	Primary Production

RMSD	Root Mean Square Difference
RMSE	Root Mean Square Error
ROMS	Regional Ocean Modeling System
SeaWiFS	Sea-viewing Wide Field-of-view Sensor
SLA	Sea Level Anomaly
SSH	Sea Surface Height
SST	Sea Surface Temperature
T-S	Temperature-Salinity
TA	Total Alkalinity
TE	Transfer Efficiency
US	United States
VGPM	Vertically Generalized Production Model
VIIRS	Visible Infrared Imaging Radiometer Suite
WMO	World Meteorological Organization
WOA	World Ocean Atlas
WOD13	World Ocean Database 2013

Symbols:

Att	Light attenuation coefficient (m^{-1})
A^a	Analysis ensemble anomaly
A^f	Forecast ensemble anomaly
Agg_{PL}	Aggregation of large phytoplankton (mmol N m^{-3} day^{-1})
Chl	Chlorophyll (mg m^{-3})
CO_2	Carbon Dioxide
d	Observations
D_L	Large detritus (mmol N m^{-3})
D_S	Small detritus (mmol N m^{-3})
$F(\vec{p})$	Misfit between the model and observations (unitless)
$F_A(\vec{p})$	Misfit in optimization experiments group A (unitless)
$F_B(\vec{p})$	Misfit in optimization experiments group B (unitless)
$F_C(\vec{p})$	Misfit in optimization experiments group C (unitless)
$F_v(\vec{p})$	Misfit for observation type v (unitless)
$f_{Ca:N}$	Rain ratio of $CaCO_3$ production to organic nitrogen (mmol $CaCO_3$ (mmol N)$^{-1}$)
f_{O_2}	Oxygen-dependence on remineralization (unitless)
f_T	Temperature-dependence on remineralization (unitless)
$Graz_{PL}$	Grazing of large phytoplankton (mmol N m^{-3} day^{-1})
H	Measurement operator mapping the model state onto the observations
H_{MLD}	Mixed layer depth (m)
K	Kalman gain matrix (unitless)
K_{Z1}	Diffusion coefficient in the turbulent surface layer of 1D model (m^2 day^{-1})
K_{Z2}	Diffusion coefficient in the quiescent bottom layer of 1D model (m^2 day^{-1})
LDeN	Large fast-sinking detritus (mmol N m^{-3})
$Mortal_{PL}$	Mortality of large phytoplankton (mmol N m^{-3} day^{-1})

NH$_4$	Ammonium (mmol N m^{-3})
NO$_3$	Nitrate (mmol N m^{-3})
$NS(k,t)$	Net source of small POC within the k-th vertical layer (mg C m^{-2} day^{-1})
N_v	Number of observations for each variable (unitless)
O_2	Dissolved oxygen concentration (mmol O$_2$ m^{-3})
P^f	Model error matrix
P_L	Large micro-phytoplankton (mmol N m^{-3})
P_S	Small pico-phytoplankton/nano-phytoplankton (mmol N m^{-3})
$\vec{p}$	Parameter vector
Phy	Phytoplankton (mmol N m^{-3})
$Prod_{DL}$	Production of large detritus (mmol N m^{-3} day^{-1})
Q	Model sensitivity to parameters (unitless)
R	Observation error matrix
$Resp$	Respiration (mmol C m^{-2} day^{-1})
$Remin_{DL}$	Remineralization of large detritus (mmol N m^{-3} day^{-1})
R^2	Coefficient of determination (unitless)
SChl	Surface chlorophyll (mg m^{-3})
SDeN	Small suspended detritus (mmol N m^{-3})
$\vec{u}$	Velocity vector (m s^{-1})
V	Number of different observation types (unitless)
$\bar{x}$	Ensemble mean
x^a	Analysis ensemble
x^f	Forecast ensemble
y_{Base}	Model results in the base case
y_{Test}	Model results in test cases
Zoo	Zooplankton (mmol N m^{-3})
Z_L	Large, meso-zooplankton (mmol N m^{-3})
Z_S	Small, micro-zooplankton (mmol N m^{-3})
$\beta(140°,700nm)$	Volume scattering function at a centroid angle of 140° and a wavelength of 700 nm (m^{-1} sr^{-1})

σ_v	Standard deviation of each variable type
κ	Diffusivity coefficient (m s^{-2})
Δz	Thickness of the vertical layer (m)
∇	Gradient operator

ACKNOWLEDGEMENTS

First and foremost, I would like to express my deepest and sincerest gratitude to my supervisor, Dr. Katja Fennel, for her consistent guidance, support, help, encouragement, and patience throughout my PhD program. It is her insightful comments and suggestions that steer me in the right direction and play vital roles in completing this thesis. In addition, her confidence in my research and encouragement always inspires me when I feel depressed. I am so honoured to have her as my supervisor and working as a PhD student in her group has been the most precious and memorable experience for me. Many thanks also go to my thesis committee members, Drs. Stephanie Kienast, Christopher Algar, and Michael Dowd, for their constructive suggestions, helpful discussions, and important contributions to improve this thesis work.

I would like to thank the great colleagues that I have met in Marine Environmental Modelling group, Arnaud Laurent, Fabian Grosse, Timothee Bourgeois, Fehmi Dilmahamod, Robert Izett, Liuqian Yu, Krysten Rutherford, Chris Gordon, Lina Garcia, Melina Mehlmann, Edmundo Garcia Larez, and Adam Stoer, for their helps and encouragements. Special thanks should go to Liuqian Yu for her development of data assimilation algorithms, to Arnaud Laurent for his help with running the ROMS model, and to Chris Gordon for processing the BGC-Argo float data.

Last but not least, I would like to thank my parents for their endless love and support throughout my PhD journey. I am also extremely grateful to my wife, Jingdi Wu, who gives me unlimited support, encouragement, accompany, and love.

CHAPTER 1

INTRODUCTION

1.1 Background

The ocean's biological carbon pump (BCP) is an important component of the global carbon cycle. It transports organic carbon that is produced at the surface to the deep ocean through different mechanisms and sequesters carbon out of contact with the atmosphere over time scales of hundreds to thousands of years thus controlling the partitioning of CO_2 between ocean and atmosphere. A long-standing paradigm is that the BCP is mainly fueled by the gravitational sinking flux of large organic particles, e.g., aggregates and fecal pellets. However, this was challenged by the realization that the metabolic carbon demand in the mesopelagic ocean (200 to 1000 m) is in excess of the organic matter supplied by gravitational sinking (Burd et al. 2010) suggesting that some alternative mechanisms might exist. Additional carbon fluxes into the deep ocean can be due to the "biological migrant pump" and the "physical injection pump" (Boyd et al. 2019). The former refers to the transport of organic carbon by vertically migrating zooplankton and larger carnivorous organisms. The latter includes physical subduction driven by different mechanisms including a deepening of the mixed layer (also termed the "mixed-layer pump"; Dall'Olmo and Mork 2014; Bol et al. 2018; Lacour et al. 2019), the large scale circulation ("Ekman pump"; Resplandy et al., 2019), and mesoscale eddies or frontal structures ("eddy subduction pump"; Llort et al., 2018; Omand et al., 2015). Unlike gravitational settling, these alternative mechanisms act on suspended and dissolved organic carbon which is not subject to gravitational settling out of the euphotic zone.

Despite its significance, the BCP remains poorly characterized in terms of its magnitude and underlying mechanisms, primarily due to insufficient observations. This limits the validation of biogeochemical models and hence their predictive capabilities with regard to biological carbon export. The uncertainty in global estimates of carbon export

out of the euphotic zone is large, varying from 4 to over 10 Pg C yr^{-1} (Henson et al. 2011, 2012, 2015; Siegel et al. 2014; DeVries and Weber 2017; Bisson et al. 2020). Conventionally, the magnitude of the BCP is measured directly by sediment traps (Francois et al. 2002; Honjo et al. 2008; Giering et al. 2018) and quantified from radioactive tracers, e.g. ^{234}Th-^{238}U and ^{210}Pb-^{210}Po (Buesseler et al. 2006; Le Moigne et al. 2013). These observations can then be upscaled to the global ocean using empirical relationships with satellite observations, e.g., sea surface temperature and net primary production (Dunne et al. 2005; Henson et al. 2011) but with large uncertainties given the limited spatial and temporal coverage of observations and a measurement bias towards productive regions. The magnitude of the BCP can be also derived from budgets of dissolved biogeochemical tracers such as nutrients (Wilson et al. 2015; Weber et al. 2016) and dissolved oxygen (Hennon et al. 2016; DeVries and Weber 2017; Quay et al. 2020). However, these approaches are subject to several sources of uncertainty including from ocean circulation. The currently available observations of carbon flux and dissolved biogeochemical tracers may not be sufficient to constrain the BCP highlighting the importance of additional independent observations. For instance, analyses of existing observations have yielded two contrasting global patterns of the transfer efficiency, the fraction of the exported organic matters out of the euphotic zone that can reach the deep ocean (Henson et al. 2012; Lima et al. 2014; Weber et al. 2016; DeVries and Weber 2017). Specifically, some studies put forward the idea that the transfer efficiency is high in low latitudes and decreases to high latitudes (Henson et al. 2012; Lima et al. 2014; Guidi et al. 2015), while other studies suggest an opposite pattern with low transfer efficiency in low latitudes (Marsay et al. 2015; Weber et al. 2016; DeVries and Weber 2017). Recent studies also suggested that available observations cannot distinguish between alternative parameterization schemes of carbon flux. Although different parameterizations fit the observations equivalently well they produced markedly different distributions of vertical carbon flux and atmospheric CO_2 levels (Cael and Bisson 2018; Lauderdale and Cael 2021).

Proxies of the particulate organic carbon (POC) concentration, which is dynamically related to the POC flux, may be an important complement to the currently available observations for studying the BCP. Due to recent advances in autonomous platforms and bio-optical sensors, proxies measurements of the POC concentration can be made in high

spatial and temporal resolution over a broad spatial scale and for an extended period. This includes the Biogeochemical (BGC)-Argo floats which are providing a large number of profile observations in the ocean interior at an unprecedented scale (Roemmich et al. 2019; Chai et al. 2020). These observations contain a wealth of information regarding particle abundance (e.g., POC concentration), particle size (e.g., small versus large particles; Briggs et al. 2011; Lacour et al. 2019), and particle transformations (e.g., fragmentation; Briggs et al. 2020) and have been used to infer contributions to the BCP from different mechanisms, e.g., the gravitational settling (Briggs et al. 2011), the mixed layer pump (Dall'Olmo and Mork 2014; Kheireddine et al. 2020), and the eddy subduction pump (Llort et al. 2018). Therefore, application of this new type of observations for improving our understanding and quantification of the BCP is promising and warrants further investigation.

In addition, BGC-Argo observations are useful for informing numerical biogeochemical models. Such models are increasingly used for providing three dimensional estimates of the BCP (Lima et al. 2014; Henson et al. 2015), improving understanding of the controlling processes (Weber and Bianchi 2020; Nowicki et al. 2022), and predicting the future response to climate changes (Laufkötter et al. 2016, 2017; Palevsky and Doney 2021). However, model estimates are subject to potentially inappropriate parameterizations of natural processes, errors from numerical approximation, inaccuracies in model input forcing, and require specification of many poorly known parameters. Data assimilation, which, in a broad sense, refers to any technique for constraining a numerical model using observations (Edwards et al. 2015), is a standard method to compensate for some of these deficiencies. There are two broad applications of data assimilation in biological oceanography that depend on the intended purpose: parameter optimization, which aims to correct systematic biases due to model deficiencies such as inappropriate model structures and inaccurate parameter values, and state estimation, which is used to reduce random errors typically due to stochastic processes (Fennel et al. 2022). For instance, parameter optimization perturbs poorly known parameters systematically to seek their optimum values by minimizing misfits between model and observations (Fennel et al. 2001; Xiao and Friedrichs 2014a; Kuhn et al. 2018). In addition, it can be used to objectively compare model structures with different levels of

complexity and to remove processes that cannot be well constrained by observations (Ward et al. 2013; Xiao and Friedrichs 2014b; Kuhn and Fennel 2019). In contrast, state estimation adjusts the model state variables to reduce their discrepancies with observations and then re-initializes the model from this updated field sequentially (Kerry et al. 2016; Mattern et al. 2017; Yu et al. 2018; Pradhan et al. 2019). Nevertheless, both these applications critically depend on appropriate observations.

1.2 Objectives

This thesis explores the application of BGC-Argo data for improving estimates and our mechanistic understanding of the BCP. Since the North Atlantic Ocean is highly productive and plays critical roles in the ocean's BCP and climate regulation, I focus on two contrasting ecosystems in the North Atlantic: the low-latitude, oligotrophic Gulf of Mexico and the productive subpolar North Atlantic including the Labrador Sea, which is one of only a few regions where deep convection occurs. I address four specific research questions in the following four chapters:

(1) What is the value of BGC-Argo profiles for parameter optimization (Chapter 2)?

Biogeochemical models are powerful tools, but their performance is largely determined by the appropriate choice of model parameter values. Parameter optimization is a standard method for addressing this issue but typically cannot constrain all parameters with confidence, even for the simplest biogeochemical models, because of insufficient information provided by available observations (Matear 1995; Fennel et al. 2001; Ward et al. 2010). For instance, the satellite estimates of surface chlorophyll, a major source of observations used for parameter optimization (e.g. Prunet et al., 1996; Xiao and Friedrichs, 2014a, 2014b), do not provide information below the surface and are not direct measures of carbon-based phytoplankton, which is a base of marine ecosystems. In the context of recent advances in BGC-Argo floats that allow for the simultaneous profiling measurement of multiple biogeochemical variables (i.e., oxygen, chlorophyll, nitrate, particulate backscattering, pH, and downwelling irradiance) over broad spatial scales and for sustained periods (Johnson and Claustre, 2016; Roemmich et al., 2019), the objective of this chapter

is to assess the value of the BGC-Argo profiles versus ocean color observations for optimizing a biogeochemical model.

(2) Can data assimilation of satellite observations in combination with *a priori* model calibration by BGC-Argo profiles improve 3D distributions of biological properties (Chapter 3)?

Apart from poorly known parameters, biogeochemical models are also subject to uncertainties from stochastic processes. State estimation is therefore required to address these uncertainties, but current data streams of biogeochemical observations are generally considered insufficient. Although the recent advances in BGC-Argo implementation has provided us abundant profile measurements of key biogeochemical variables (Biogeochemical-Argo Planning Group 2016; Roemmich et al. 2019; Chai et al. 2020), these observations are insufficient so far for state estimation either in global or regional applications except in a few specific regions with high float densities, e.g., the Mediterranean Sea (Cossarini et al. 2019) and the Southern Ocean (Verdy and Mazloff 2017). Elsewhere, assimilation of BGC-Argo float data has been limited to parameter optimization (Wang et al. 2020) and twin experiments (Yu et al. 2018; Ford 2020). In this chapter, a multivariate data assimilation scheme was applied to the coupled physical-biogeochemical model which had been optimized in Chapter 2 to evaluate whether the assimilation of satellite observations in combination with a prior model calibration by BGC-Argo profiles can improve the 3D distributions of biogeochemical properties.

(3) Do BGC-Argo float data add information when assessing the predictive skill of alternative vertical carbon flux parameterizations (Chapter 4)?

The remineralization length scale, defined as the distance over which the vertical carbon flux attenuates by a factor of $1/e$ (~ 63%), is known to increase with depth. This indicates that either the remineralization rate is getting slower, or the sinking velocity is getting faster. Both of these are used in vertical carbon flux parameterizations within biogeochemical models to achieve the increase in remineralization length scale. Previous studies that compared different parameterization schemes have placed emphasis on the schemes' ability to reproduce the sparse in-situ observations of POC flux and

climatological datasets of nutrients (Cael and Bisson 2018; Lauderdale and Cael 2021) and found that different schemes can match observations equally well within the observational uncertainties but result in very different predictions of atmospheric CO_2 levels. This suggests that the currently available observations of POC flux and nutrients are insufficient to determine which parameterization scheme is more mechanistically appropriate and that additional observations are needed. POC concentration, which is dynamically related to the POC flux, has received little attention for calibration of biogeochemical models. This chapter addresses the question of what value proxy observations of POC concentration can add to the currently available observations when calibrating biogeochemical models.

(4) What are the relative contributions from small and large particles to deep carbon sequestration (Chapter 5)?

The BCP includes a range of processes that transport organic matter from the surface to the deep ocean, where it is remineralized and sequestered as inorganic carbon for decades to millennia. However, the magnitude of this vertical carbon transport remains poorly constrained by observations and the detailed processes involved are insufficiently understood. In particular, attention to the contribution of small particles has increased in recent years but previous estimates of the associated vertical carbon flux are likely biased because they have ignored remineralization and particle fragmentation. In this chapter, I present a new method for estimating i) vertical carbon flux of small and large organic particles and ii) the effect of remineralization and particle fragmentation on mesopelagic (100-1000 m) flux attenuation using BGC-Argo profiles of backscattering and dissolved oxygen.

1.3 Outline

This thesis is organized as follows:

In Chapter 2, a suite of optimization experiments is carried out in the Gulf of Mexico using different combinations of satellite chlorophyll and profile measurements of chlorophyll, phytoplankton, and POC from BGC-Argo floats to assess the value of BGC-Argo profiles for parameter optimization. As parameter optimization in 3D models is

computationally expensive, I optimize the parameters in a 1D model version and then perform 3D simulations using these parameters.

In Chapter 3, to evaluate whether data assimilation of satellite observations with a prior model calibration by BGC-Argo profiles can improve 3D distributions of biological properties, the multivariate deterministic ensemble Kalman filter (DEnKF) is implemented to assimilate physical and biological observations into a three-dimensional coupled physical-biogeochemical model which has been calibrated in the Chapter 2 for the Gulf of Mexico. The impact, especially on the subsurface distributions of biological properties, is assessed by comparing forecast results from the data-assimilative models to independent observations from five BGC-Argo floats that were not assimilated. In addition, an alternative light parameterization that is tuned *a priori* using BGC-Argo observations is applied to test the sensitivity of the data assimilation impact on subsurface biological properties.

In Chapter 4, to evaluate the information that BGC-Argo float data can add when assessing the alternative vertical carbon flux parameterizations, I first classify the vertical carbon flux parameterizations from 12 Earth System Models (ESMs) from the sixth phase of the Coupled Model Intercomparison Project (CMIP6). To isolate the model-to-model differences in vertical carbon flux across ESMs that are due to the choice of parameterization schemes from other sources of model discrepancies, e.g., model resolution, differences in biogeochemical model complexity, etc. the two most common schemes are implemented in a common 1D model framework. The 1D model is calibrated using BGC-Argo float data thus enabling an objective comparison between the ballast scheme, where a fraction of sinking POC is protected from remineralization by minerals, and the Wlin scheme, where the sinking velocity is assumed to increase with depth. In addition, sensitivity experiments are conducted to evaluate whether profiles of POC concentration can provide a unique estimate of POC flux.

In Chapter 5, I introduce a new method for estimating vertical carbon flux based on a mass balance of POC and dissolved oxygen to quantify the relative contributions from small and large particles to deep carbon sequestration. I then apply this method to BGC-Argo floats in the subpolar North Atlantic and estimate the vertical carbon flux due to

different mechanisms by explicitly accounting for the remineralization and fragmentation of organic particles.

An overarching summary of my main conclusions and the outlook for future work are given in Chapter 6.

Chapters 2-5 are based on four individual papers. Specifically, Chapter 2 was published in Biogeosciences under the title of "Assessing the value of biogeochemical Argo profiles versus ocean color observations for biogeochemical model optimization in the Gulf of Mexico" (Wang et al. 2020). Chapter 3 was published in Ocean Science under the title of "Can assimilation of satellite observations improve subsurface biological properties in a numerical model? A case study for the Gulf of Mexico" (Wang et al. 2021). Chapter 4 is in preparation for journal submission. Chapter 5 was published in Limnology and Oceanography under the title of "Biogeochemical-Argo data suggest significant contributions of small particles to the vertical carbon flux in the subpolar North Atlantic" (Wang and Fennel 2022).

CHAPTER 2

ASSESSING THE VALUE OF BGC ARGO PROFILES VERSUS OCEAN COLOUR OBSERVATIONS FOR BIOGEOCHEMICAL MODEL OPTIMIZATION IN THE GULF OF MEXICO[1]

2.1 Introduction

Oceanic primary production forms the basis of the marine food web and fuels the biological pump, which contributes to the sequestration of atmospheric CO_2 in the ocean's interior, thus mitigating global warming. An accurate quantification of primary production and biological carbon export is therefore important for our understanding of the marine carbon cycle and for predicting how carbon cycling and marine ecosystems will interact with climate change.

Direct observations of primary production and export flux are relatively sparse because of the cost and effort involved in measuring these fluxes. Numerical models can complement sparse observations. Well validated and calibrated models are useful tools for hindcasting and nowcasting past and present biogeochemical fluxes and are the most common tool for projecting future changes.

In recent years, many biogeochemical models with different complexities have been developed to study ocean biogeochemical processes. Regardless of their complexities, the performance of these models is highly dependent on the appropriate choice of model parameter values (e.g., maximum growth, grazing and mortality rates), most of which are poorly known. A standard method for choosing these parameters is optimization, a process by which the misfit between model results and available observations is minimized by iteratively varying parameters (Matear, 1995; Prunet et al., 1996a, 1996b; Fennel et al.,

---

2001; Friedrichs et al., 2007; Kuhn et al., 2015, 2018). However, even formal optimization typically cannot constrain all biogeochemical parameters (i.e., provide optimal parameter estimates with relatively small uncertainties) because of insufficient information in the available observations (Matear 1995; Fennel et al. 2001; Ward et al. 2010; Bagniewski et al. 2011). For example, Matear (1995) used a so-called simulated annealing algorithm to optimize three different ecosystem models and found that, even for the simplest nutrient-phytoplankton-zooplankton model, not all independent parameters could be constrained well, leaving the others with large uncertainty ranges. A more recent study reported that the lack of zooplankton observations led to poor accuracy of the optimized zooplankton-related parameters when using a suite of Lagrangian-based observations during the North Atlantic spring bloom (Bagniewski et al. 2011). A broader suite of observation types should be favourable to parameter optimization although complications can arise. For example, when optimizing a suite of 1D models for the Mid-Atlantic Bight, the use of satellite particulate organic carbon (POC) observations in addition to satellite chlorophyll did not yield further improvements in model-data fit but degraded the representation of chlorophyll (Xiao and Friedrichs 2014a).

Typically surface ocean chlorophyll from satellite is the main source of observations for model validation (e.g. Doney et al., 2009; Gomez et al., 2018; Lehmann et al., 2009) and parameter optimization (Prunet et al. 1996b; Xiao and Friedrichs 2014a; b), supplemented by other observation types as available. However, satellites only see the ocean surface and do not resolve the vertical distribution of chlorophyll. This is especially problematic in oligotrophic regions where the deep chlorophyll maximum (DCM) is relatively deep and hardly observed by the satellite (Fennel and Boss 2003; Cullen 2015). In addition, although chlorophyll has long been used as a proxy of phytoplankton biomass and to estimate primary production based on some assumptions (Behrenfeld and Falkowski 1997), it is not a direct measure of carbon-based phytoplankton biomass. The ratio of chlorophyll-to-phytoplankton carbon varies by at least an order of magnitude due to physiological responses of phytoplankton to their ambient environment (e.g. nutrients, light, and temperature) (Geider 1987; Fennel and Boss 2003; Cullen 2015). Changes in chlorophyll may result from physiologically induced modifications of the chlorophyll-to-phytoplankton ratio rather than actual changes of phytoplankton biomass (Mignot et al.

2014; Pasqueron de Fommervault et al. 2017). Satellite surface chlorophyll alone is therefore likely insufficient for model validation and for constraining biogeochemical models via parameter optimization.

Recent advances in autonomous platforms and sensors have opened opportunities for simultaneous measurement of several biological and chemical properties throughout the upper ocean with high resolution, over broad spatial scales and for sustained periods (Roemmich et al. 2019). In particular, the biogeochemical (BGC) Argo program (Johnson and Claustre, 2016; Roemmich et al., 2019) will provide temporally evolving 3D information on biogeochemical variability at previously unobserved scales. Here I assess to what degree observations of chlorophyll fluorescence and particle backscatter from Argo profiles improve the prospects of optimizing a biogeochemical model for the Gulf of Mexico.

Since the high computational cost and storage demands of 3D models make direct application of most parameter optimization techniques difficult (but see Mattern et al., 2012; Mattern and Edwards, 2017; Tjiputra et al., 2007 for exceptions), they are typically applied in computationally efficient 1D models before using the resulting parameters in 3D version (e.g. Hoshiba et al., 2018; Kane et al., 2011; Kuhn and Fennel, 2019; Schartau and Oschlies, 2003). I follow the latter approach here.

The main objective of this chapter is to assess the added value of bio-optical profile information from Argo floats for biogeochemical model optimization in the Gulf of Mexico. I first examine the feasibility of improving the 3D model by applying the optimal parameters from 1D model optimizations with some minor manual modifications. I find that the gains from the 1D optimizations transfer to the 3D version. Then, by using different combinations of satellite and float observations, I show that parameters optimized with respect to satellite data cannot reproduce subsurface distributions unless the float observations (i.e. chlorophyll, phytoplankton, and POC) are also used.

2.2 Study region

The Gulf of Mexico (GOM) is a semi-enclosed marginal sea (Fig. 2.1) which is characterized by eutrophic coastal waters on the northern shelf and an oligotrophic deep

ocean. The high productivity in the northern coastal region is fueled by large nutrient and freshwater inputs from the Mississippi and Atchafalaya Rivers. The large nutrient load and strong stratification driven by Mississippi and Atchafalaya River inputs lead to summer hypoxia and ocean acidification in bottom waters on the northern shelf (Yu et al. 2015; Laurent et al. 2017), but nutrient export across the shelf break into the open Gulf is minor (Xue et al. 2013).
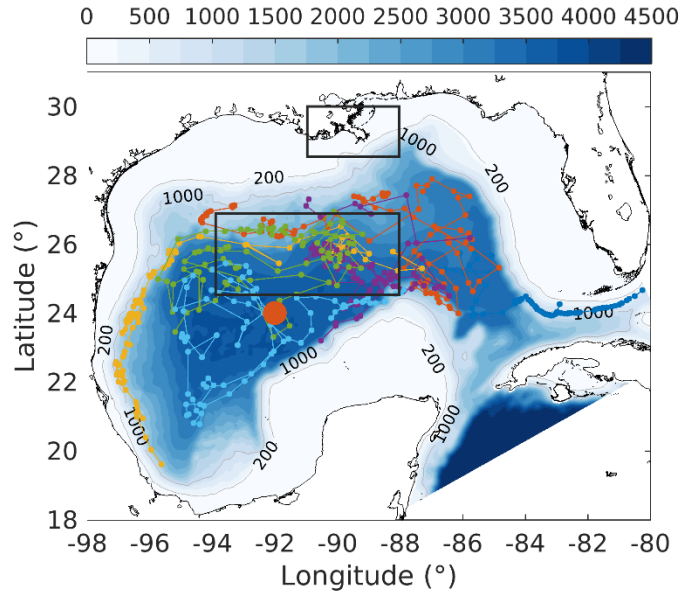
Figure 2.1. Model bathymetry (unit: m) with trajectories of six bio-optical floats (small colored dots and lines) which were operated in the Gulf of Mexico from 2011 to 2015. The location of the 1D model is denoted by the large orange dot. The north and south black boxes represent the Mississippi Delta and the central gulf, respectively, to show comparisons of surface chlorophyll in Fig. B.5.

The deep ocean of the GOM is oligotrophic. Previous satellite-based studies have revealed a clear seasonal cycle in surface chlorophyll, with highest concentrations in winter and lowest in summer (Muller-Karger et al. 1991, 2015; Martínez-López and Zavala-Hidalgo 2009). Thanks to advances in autonomous profiling technology, recent studies based on simultaneous measurements of subsurface chlorophyll and backscatter have demonstrated that the seasonal variability of surface chlorophyll might be a result of the vertical redistribution of subsurface chlorophyll and/or physiological response to solar radiation of phytoplankton (Green et al. 2014; Pasqueron de Fommervault et al. 2017).

2.3 Methods

2.3.1. Biological observations

Monthly averaged satellite chlorophyll from the Ocean Colour Climate Change Initiative project (OC-CCI, https://www.oceancolour.org) with a spatial resolution of 4 km from 2010 to 2015 was used for model validation and parameter optimization. These data were provided by the European Space Agency (ESA), which produced a set of validated and error-characterized global ocean color products by merging SeaWiFS (Sea-viewing Wide Field-of-view Sensor), MODIS (Moderate Resolution Imaging Spectroradiometer), MERIS (Medium Resolution Imaging Spectrometer), and VIIRS (Visible Infrared Imaging Radiometer Suite) products.

In addition to the satellite-based measurements, bio-optical measurements from six autonomous profiling floats were used (Fig. 2.1), which were deployed by the Bureau of Ocean Energy Management (BOEM) and operated in the deep GOM from 2011 to 2015. These floats were equipped with a CTD and bio-optical sensors to collect biweekly profiles of temperature, salinity, chlorophyll, and backscatter at 700 nm (bbp700 (m^{-1})) from the surface to 1000 m depth (see Pasqueron de Fommervault et al., 2017; Green et al., 2014, for more details). Chlorophyll was derived from fluorescence based on the sensor manufacturer's calibrations and compared with the satellite estimates of surface chlorophyll. While the surface chlorophyll measurements from the floats and the satellite estimates both showed a typical seasonal cycle and were highly correlated (R^2=0.74; see Figs. B.1 and B.2a in the Supplement), the satellite underestimated the float-measured chlorophyll concentrations in winter (Fig. B.1c). Satellite estimates were therefore corrected following the regression equation shown in Fig. B.2a.

The backscatter sensor carried by the floats provided the volume scattering function at a centroid angle of 140° and a wavelength of 700 nm ($\beta(140^o, 700nm)$ m^{-1} sr^{-1}). The profiles were filtered (Briggs et al., 2011) to remove spikes and then converted into bbp700 following Green et al. (2014). After that, profiles of bbp700 were converted into bbp470 based on a power law (Boss and Haëntjens 2016) to obtain the phytoplankton (mmol N m^{-3}) and POC (mg C m^{-3}) estimates:

$$bbp(\lambda1) = \left(\frac{\lambda1}{\lambda2}\right)^{-\gamma} bbp(\lambda2), \qquad\qquad\qquad (2.1)$$

$$Phy = 30100 \times \frac{bbp470 - 76 \times 10^{-5}}{12 \times 6.625}, \qquad\qquad\qquad (2.2)$$

$$log10(POC) = 1.22 \times log10(bbp470) + 5.15, \qquad\qquad\qquad (2.3)$$

where $\lambda1$ and $\lambda2$ represented the measured wavelength, and γ was estimated as 0.78 based on the global measurements. The relationships for phytoplankton (Martinez-Vicente et al., 2013; Eq. 2.2) and POC (Rasse et al., 2017; Eq. 2.3) were obtained from a data set for the Atlantic Ocean that covered a wide range of oceanographic regimes from eutrophic to oligotrophic ecosystems. The scale factors of 12 and 6.625 in Eq. 2.2 represented the molecular weight of carbon and the Redfield ratio to convert phytoplankton concentrations from mg C m^{-3} to mmol N m^{-3}. The intercept 76×10^{-5} in Eq. 2.2 represented the background backscatter of nonalgal detritus, which based on Behrenfeld et al. (2005) was the backscatter value when chlorophyll was zero. However, in this chapter, the majority (87%) of bbp470 in the upper 200 m was below the intercept and the resulting phytoplankton concentrations were therefore close to zero, which is unrealistic in the Gulf of Mexico. Therefore, the satellite estimate of bbp670 from OC-CCI was converted into bbp700 and compared with the float measurements. Compared to surface chlorophyll, surface bbp700 has a less distinct seasonal cycle (Fig. B.3). For example, the coefficient of variation, defined as the ratio between standard deviation and mean to show the extend of variability, is much lower for bbp700 (0.09 and 0.07 for floats and satellite, respectively) than for chlorophyll (0.31 and 0.26 for floats and satellite, respectively). The float bbp700 is weakly correlated with the satellite estimates (R^2=0.11) and generally lower by a factor of 0.45 than the satellite estimates (Fig. B.2b). The bbp700 profiles were therefore multiplied by 2.2 before being converted to bbp470. As a result, the mean value of the bbp470 ($88 \times 10^{-5}\ m^{-1}$) is close to the intercept in Eq. 2.2 when chlorophyll went to zero. Furthermore, the resulting concentrations of phytoplankton biomass and POC as well as the ratio of chlorophyll to phytoplankton biomass are reasonable (please see Figs. 2.4 and 2.10). This gave me confidence in my conversion process for float backscatter and my choice of empirical equations relating backscatter to phytoplankton and POC.

2.3.2. Three-dimensional model description

The physical model was configured based on Regional Ocean Modeling System (Haidvogel et al., 2008, ROMS, https://www.myroms.org) for the Gulf of Mexico (Fig. 2.1). The model has a horizontal resolution of ~5 km and 36 terrain-following sigma layers with refined resolution near the surface and bottom as in Yu et al. (2019). The model solved the horizontal and vertical advection of tracers using the multidimensional positive definitive advection transport algorithm (MPDATA, Smolarkiewicz and Margolin, 1998). Horizontal viscosity and diffusivity were parameterized by a Smagorinsky-type formula (Smagorinsky 1963), and vertical turbulent mixing was calculated by the Mellor-Yamada 2.5-level closure scheme (Mellor and Yamada 1982). Bottom friction was specified by a logarithmic drag formulation with a bottom roughness of 0.02 m. The model was forced by 3-hourly surface heat and freshwater fluxes; 6-hourly air temperature, sea level pressure, and relative humidity; and 10 m winds from the European Centre for Medium-Range Weather Forecast ERA-Interim product with a horizontal resolution of 0.125° (ECMWF reanalysis, https://www.ecmwf.int/en/forecasts/datasets/reanalysis-datasets/era-interim). A bulk parameterization was applied to calculate the surface net heat fluxes and wind stress. The model was one-way nested inside the $1/12^{\circ}$ data-assimilative global HYCOM/NCODA (https://www.hycom.org). Tidal constituents were neglected in the model.

The biogeochemical model used a seven-component model (Fennel et al. 2006) to simulate the nitrogen cycle in the water column. The model described the dynamics of two species of dissolved inorganic nitrogen (nitrate, NO_3, and ammonium, NH_4), one function of phytoplankton (Phy), chlorophyll (Chl) as a separate state variable which allowed photoacclimation based on the model of Geider et al. (1997), one function of zooplankton (Zoo), and two pools of detritus (i.e., small suspended detritus, SDeN, and large fast-sinking detritus, LDeN). Water-sediment interactions were simplified by an instantaneous remineralization parameterization, where detritus sinking out of the water column immediately resulted in a corresponding influx of ammonium into the bottom layer. Detailed descriptions of the model equations can be found in Fennel et al. (2006) and Laurent et al. (2017). The biological model parameters are listed in Table 2.1.

Table 2.1. Initial values and ranges of primary parameters used in the biogeochemical model

Descriptions (unit)	Symbol	Value	Range
Radiation threshold for nitrification (W m^{-2})	I_0	0.0095[a]	0.005[b]-0.01[b]
Half-saturation radiation for nitrification (W m^{-2})	k_I	0.1[a]	0.01[b]-0.5[b]
Maximum nitrification rate (day^{-1})	n_{max}	0.2[c]	0.01[b]-0.35[b]
Phytoplankton growth at 0 °C (Dimensionless)	μ_0	0.69[a]	0.1[b]-3.0[b]
Initial slope of P-I curve (mg C (mg Chl W m^{-2} day)$^{-1}$)	α	0.125[a]	0.007[a]-0.13[a]
Half-saturation for NO$_3$ uptake (mmol N m^{-3})	k_{NO3}	0.5[a]	0.007[a]-1.5[a]
Half-saturation for NH$_4$ uptake (mmol N m^{-3})	k_{NH4}	0.5[a]	0.007[a]-1.5[a]
Phytoplankton mortality (day^{-1})	m_P	0.075	0.01[b]-0.2[b]
Aggregation parameter (day^{-1})	τ	0.1	0.01[b]-25[b]
Maximum chlorophyll to carbon ratio (mg Chl mg C^{-1})	θ_{max}	0.0535[c]	0.005[a]-0.15[b]
Phytoplankton sinking velocity (m day^{-1})	w_{Phy}	0.1[a]	0.009[a]-25[a]
Maximum grazing rate (day^{-1})	g_{max}	0.6[a]	0.1[b]-4[b]
Half-saturation for phytoplankton ingestion ((mmol N m^{-3})^2)	k_P	0.5	0.01[b]-3.5[a]
Zooplankton assimilation efficiency (Dimensionless)	β	0.75[a]	0.25[b]-0.75[b]
Zooplankton basal metabolism (day^{-1})	l_{BM}	0.01	0.01[b]-0.15[b]
Zooplankton specific excretion (day^{-1})	l_E	0.1[a]	0.05[b]-0.35[b]
Zooplankton mortality (day^{-1})	m_Z	0.2	0.02[b]-0.35[b]
Small detritus remineralization (day^{-1})	r_{SD}	0.3[c]	0.005[b]-0.25[a]
Large detritus remineralization (day^{-1})	r_{LD}	0.1	0.005[b]-0.25[a]
Small detritus sinking velocity (m day^{-1})	w_{SDet}	0.1[a]	0.009[a]-25[a]
Large detritus sinking velocity (m day^{-1})	w_{LDet}	1[a]	0.009[a]-25[a]

[a]Fennel et al. (2006); [b]Kuhn et al. (2018); [c]Yu et al. (2015)

The model received freshwater, nutrients (NO$_3$ and NH$_4$) and organic matter inputs from major rivers along the Gulf coast. Freshwater and nutrients from the Mississippi and Atchafalaya rivers were prescribed based on the daily measurements by the US Geological Survey river gauges. River particulate organic nitrogen (PON) was assigned to the small detritus pool and determined as the difference between total Kjeldahl nitrogen and

ammonium (Fennel et al. 2011). Other rivers utilized the climatological estimates of freshwater, nutrients, and PON as in Xue et al. (2013).

Initial and open boundary conditions for NO$_3$ were specified by applying an empirical relationship between NO$_3$ and temperature, derived from the World Ocean Atlas (WOA; Fig. B.4a), that was applied to the temperature fields from HYCOM/NCODA. Analogously, empirical relationships between chlorophyll and density (Fig. B.4b), phytoplankton and density (Fig. B.4c), and POC and density (Fig. B.4d) were obtained from the median profiles of the bio-optical floats and used to derive initial and boundary conditions for these variables. Zooplankton and small detritus were assumed to amount to 10% of phytoplankton biomass and the remaining fractions of POC attributed to large detritus. Sensitivity tests showed that changing these allocations had little impact on model results.

A 6-year (5 January 2010 – 31 December 2015) hindcast was performed that included the period of operation of the bio-optical floats. The first year was considered model spin-up and the next five years are discussed.

2.3.3. One-dimensional model description

As optimizing a 3D biogeochemical model is computationally expensive, it was more practical to perform the optimization using a reduced-order model surrogate. A surrogate can be a coarser resolution model, a simplified model, or a reduced-dimension model. In this chapter, a 1D model was used to optimize the biological parameters of the 3D model. This approach has been successfully used previously (Oschlies and Schartau 2005; Kane et al. 2011; Hoshiba et al. 2018).

The 1D model, which is similar to that used by Lagman et al. (2014) and Kuhn et al. (2015), covered the upper 200 m of the ocean with a vertical resolution of 5 m and was configured at one location in the open Gulf (see Fig. 2.1). This relatively fine vertical resolution was used because it was close to that of the BGC-Argo floats (4~6 m in upper 200 m) and was much higher than the 3D model whose vertical resolution varies from a few meters near the surface to about 50 m near at 200 m depth around the 1D station. In the vertical direction, the water column was divided into two layers: the turbulent surface

layer and a quiescent layer below. A higher diffusion coefficient ($K_{Z1} = \max(H_{MLD}^2/$ 400,10)$, in unit of m^2 day^{-1}) was applied in the turbulent surface layer and a lower diffusion coefficient ($K_{Z2} = K_{Z1}/2$) was assigned to the quiescent bottom layer. The interface between these two layers was determined by the mixed layer depth (H_{MLD}, in unit of m), defined as the depth where the temperature was 5°C lower than at the surface, and was obtained from daily outputs of the 3D model. The model was integrated in time using the Crank-Nicolson scheme for vertical turbulent mixing and an implicit time-stepping scheme for the biogeochemical tracers, which were treated identically to the 3D model. Some of the biogeochemical parameterizations required input of temperature and solar radiation, which were also taken from the 3D model. As the 1D model did not consider horizontal and vertical advection, NO$_3$ below 100 m was nudged to that from the 3D base simulation with a nudging time scale of 20 days. The 1D model was run for the year 2010 repeatedly for three cycles, with the first two being model spin-up and the last annual cycle used to calculate the misfit between model and observations.

2.3.4. Parameter optimization method

The evolutionary algorithm described by Kuhn et al. (2015, 2018) was used to search for optimal model parameters by minimizing the misfit between the model and observations. The misfit was measured by the following cost function:

$$F(\vec{p}) = \sum_{v=1}^{V} F_v(\vec{p}), \tag{2.4}$$

$$F_v(\vec{p}) = \frac{1}{N_v \sigma_v^2} \sum_{i=1}^{N_v} \left(\hat{y}_{i,v} - y_{i,v}(\vec{p}) \right)^2, \tag{2.5}$$

where $\vec{p}$ represented the parameters vector, V was the number of different observation types, N_v was the number of observations for each variable, $F_v(\vec{p})$ was the misfit for observation type v measured as the mean-square difference between observations ($\hat{y}$) and corresponding model estimates ($y(\vec{p})$). The cost function $F_v(\vec{p})$ was normalized by the standard deviation of each variable type (σ_v) in order to remove the effect of different units.

The algorithm is inspired by the rules of natural selection. Following Kuhn et al. (2015), an initial parameter population of 30 parameter vectors was randomly generated within a predefined range of parameters (see Table 2.1). The model was evaluated for each parameter vector and the resulting cost function was calculated. For this initial generation and each of the following generations, the half of the population with the lower misfit survived into the next generation. The other half was regenerated through a recombination of survivors in a process analogous to genetic crossover. In addition, each newly generated population was subject to random mutations by multiplying the parameter values by a random value between 0 and 2. Parameter values exceeding the predefined range were replaced by their corresponding minimum or maximum limits to avoid unrealistic values. The above procedure was performed iteratively for 300 generations to reach the minimum of the cost function, which corresponded to the optimal parameter set.

Previous parameter optimization studies have shown that it is difficult to constrain all model parameters even for very simple ecosystem models because the information content of available observations is typically insufficient (Matear, 1995; Fennel et al., 2001; Ward et al., 2010). Here I conducted sensitivity tests to identify the parameters that were most sensitive to the available observations and chose a subset of these to be optimized. In the *base case*, all parameters were at their initial guess values obtained from the previous literature and some initial tuning (Table 2.1). Then the *test cases* were run multiple times by incrementally changing one parameter at a time to be the minimum; the first, second and third quartile; and the maximum of its corresponding range while setting the other parameters to their initial guess value (Table 2.1). The sensitivity was measured as the sum of a normalized absolute difference between the base case (y_{Base}) and the test case (y_{Test})

$$Q(y, \vec{p}) = \frac{1}{m} \sum_{i=1}^{m} \frac{1}{n} \sum_{j=1}^{n} \frac{|y_{Base} - y_{Test}|}{y_{Base}}, \qquad (2.6)$$

where *m* is the number of parameter increments (here 5) and *n* is the number of base-test pairs consisting of all 1D model grid cells throughout the whole simulation period for all variables to be compared.

Results of the sensitivity analysis are shown in Fig. 2.2, where parameters are ranked by sensitivity with respect to chlorophyll (Fig. 2.2a) and the sum of chlorophyll, phytoplankton, and POC (Fig. 2.2b). POC is the sum of phytoplankton, zooplankton, and small and large detritus.
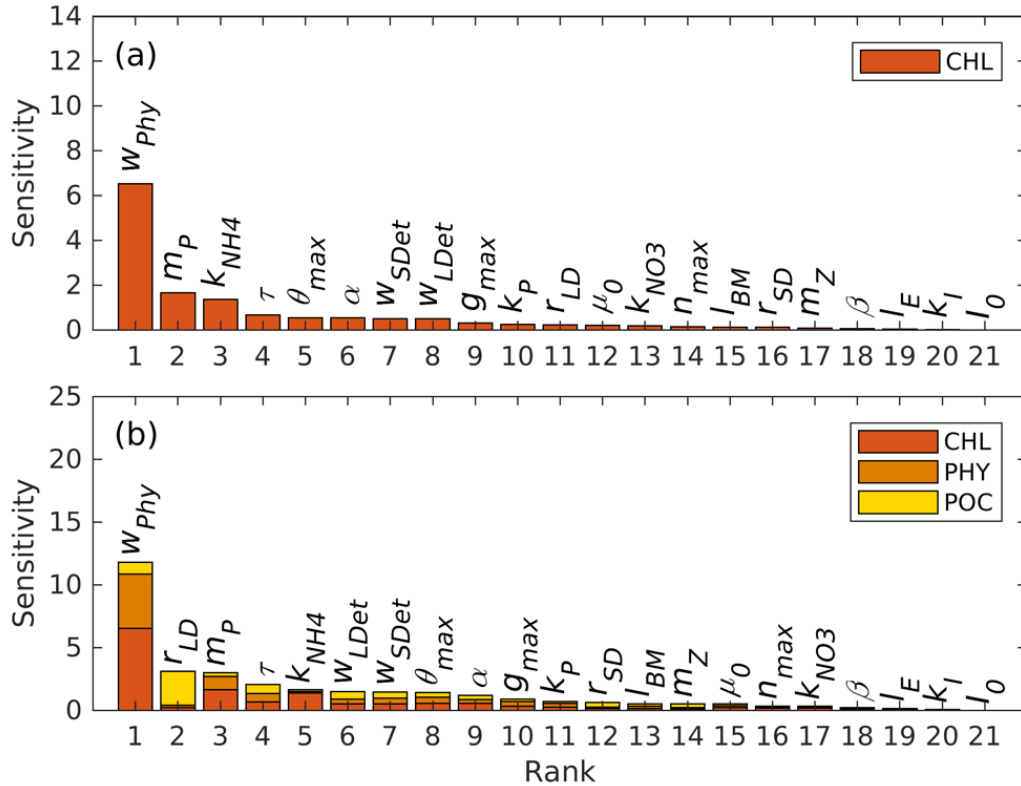
Figure 2.2. Parameter sensitivities (unit: dimensionless) with respect to (a) chlorophyll and (b) the sum of chlorophyll, phytoplankton, and POC.

2.3.5. Parameter optimization experiments

For the parameter optimization of the 1D model, satellite chlorophyll within a 3×3 pixel (12 km×12 km) area around the 1D station and monthly climatological profiles from the BGC-Argo floats were used. For the climatological profiles, all float profiles in the gulf were averaged because the deep Gulf of Mexico is homogenous horizontally and only few profiles were available in the immediate vicinity of the 1D station.

To assess the effects of the optimization with respect to the different observation types, I conducted three groups of experiments in which (A) surface satellite chlorophyll only, (B) surface satellite chlorophyll and float profiles of chlorophyll, and (C) surface satellite chlorophyll and float profiles of chlorophyll, phytoplankton, and POC were used. For each of these three groups, four to five optimizations were conducted, starting with the three most sensitive parameters and then adding one more parameter at a time (Table 2.2) guided by the sensitivity analysis with respect to the observed variables they used. Specifically, groups A and B were based on the sensitivity analysis with respect to chlorophyll, while group C was based on sensitivity analysis with respect to the sum of chlorophyll, phytoplankton, and POC. Each optimization was replicated four times. The optimization with smallest model-data misfit within each group was then used. Prior tests have shown that the available observations cannot simultaneously constrain the sinking rates of small and large detritus (w_{SDet} and w_{LDet}) because an increase in one parameter can be counteracted by a decrease in the other. Therefore, a constant ratio of 0.1 between these two parameters ($w_{SDet} = 0.1 \times w_{LDet}$) was imposed based on their prior values and only one of the two was optimized. In groups A and B, the aggregation parameter τ was fixed at 0.05 because prior tests generated unreasonably high values for this parameter.

I report two different metrics of misfits for these groups of experiments. The first metric, which I refer to as the case-specific cost function value, is based on the optimized observations in a given experiment and was minimized by the optimization algorithm, i.e.

$$F_A(\vec{p}) = F_{SurfCHL}(\vec{p}), \tag{2.7}$$

$$F_B(\vec{p}) = F_{SurfCHL}(\vec{p}) + F_{CHL}(\vec{p}), \tag{2.8}$$

$$F_C(\vec{p}) = F_{SurfCHL}(\vec{p}) + F_{CHL}(\vec{p}) + F_{Phy}(\vec{p}) + F_{POC}(\vec{p}). \tag{2.9}$$

However, the models with lower case-specific misfit do not necessarily have better predictive skill in reproducing the unoptimized observations because of the so-called overfitting problem (e.g. the model might be tuned to reproduce optimized observations through wrong mechanisms, Friedrichs et al. 2006). To account for this, a second metric referred to as the total misfit is given by Eq. 2.9. For group C, the second metric is the same

as the case-specific cost function. For groups A and B, the total misfit metric allows me to assess improvements in the model's predictive skill to represent unoptimized fields.

2.4 Optimization of 1D models

2.4.1   Observations and base case

To provide context for the evaluation of the optimization experiments, the observations and the base case will be described first. As shown in Fig. 2.3a, the observed surface chlorophyll shows a clear seasonality with the high concentrations in winter and low concentrations in summer. In the base case, the simulated surface chlorophyll fits observations well. Unlike the surface chlorophyll, the observed integrated chlorophyll as well as the phytoplankton and POC over the upper 200 m tend to be more constant with much less seasonality (Fig. 2.3b-d). This has been reported by Pasqueron de Fommervault et al. (2017), who attributed the seasonality of surface chlorophyll to the vertical redistributions of subsurface chlorophyll and/or photoacclimation rather than real changes in biomass.

The DCM is a ubiquitous phenomenon in the oligotrophic regions and can form independently of the biomass maximum (Fennel and Boss 2003; Cullen 2015). In this chapter, I define the DCM depth as where the maximum of subsurface chlorophyll is. Observations detect a predominant DCM at around 60-100 m depth throughout the whole year, with a sharp deepening in June and gradual shoaling after July (Fig. 2.3e), reflecting the seasonality of the solar radiation. Unlike the large variability in the depth of the DCM, its magnitude is relatively constant at around 0.62 mg m^{-3} (Fig. 2.3f). In the annually averaged profiles, the observed DCM is located at about 80 m depth with a concentration of 0.52 mg m^{-3} (Fig. 2.4a). The base case succeeds in reproducing the DCM at 65±7 m depth. However, it fails to reproduce the deepening of the DCM in June, and the simulated annually averaged depth of DCM is shallower by about 15 m than the observed. The simulated magnitude of the DCM is about 2-fold larger than the observed (Fig. 2.3f and Fig. 2.4a), and hence the base case generally overestimates vertically integrated chlorophyll (Fig. 2.3b).
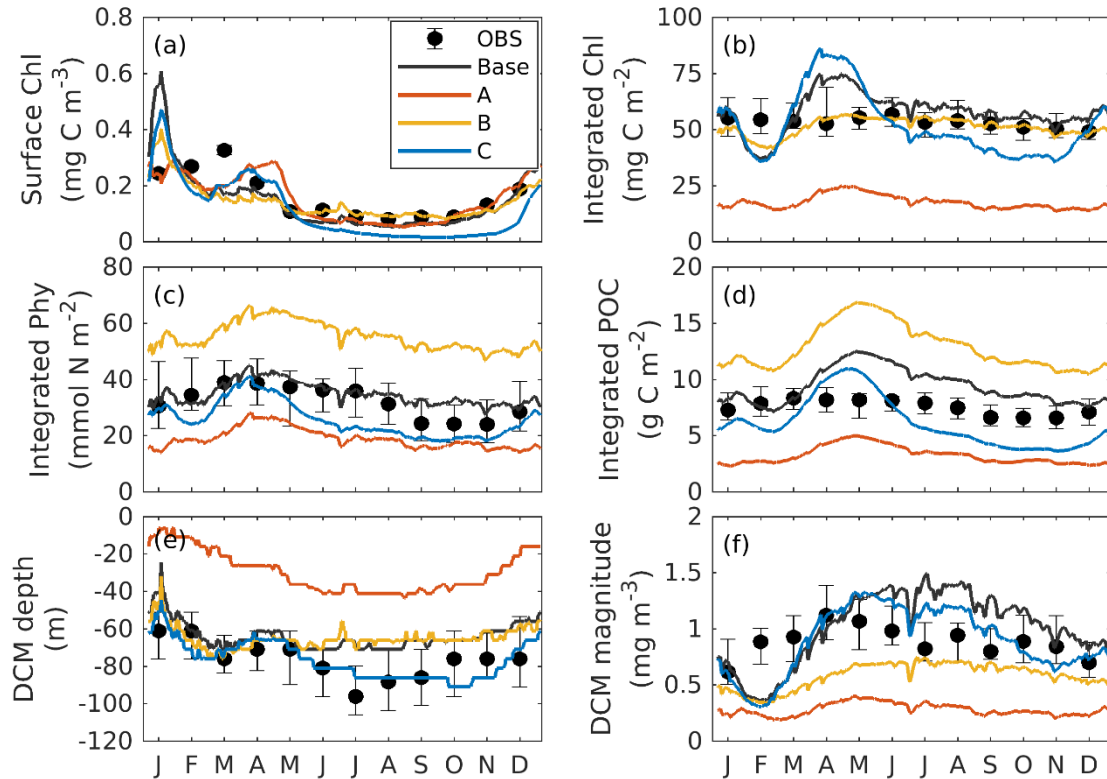
Figure 2.3. Annual cycle of surface chlorophyll (a), vertically integrated chlorophyll (b), vertically integrated phytoplankton (c), vertically integrated POC (d), and the depth (e) and magnitude (f) of the DCM from observations (black dots with error bars); the base case (black lines); the experiment A (orange lines; only satellite surface chlorophyll is used), B (yellow lines; satellite surface chlorophyll and float profiles of chlorophyll are used), and C (blue lines; all available observations are used). Chlorophyll, phytoplankton, and POC are integrated over the top 200 m. Black error bars represent the interquartile range of observations.

With respect to phytoplankton and POC, the observed maximum concentration occurs at about 60 m depth, which is 20 m above the DCM (Fig. 2.4b-c). The observed vertical distributions of phytoplankton and POC are not well captured by the base case. For example, phytoplankton and POC in the upper layer are overestimated with the model-data discrepancies exceeding the variability of the observations (Fig. 2.4b-c). As a result, the base case yields an overall overestimation of the vertically integrated phytoplankton and POC (Fig. 2.3c-d).
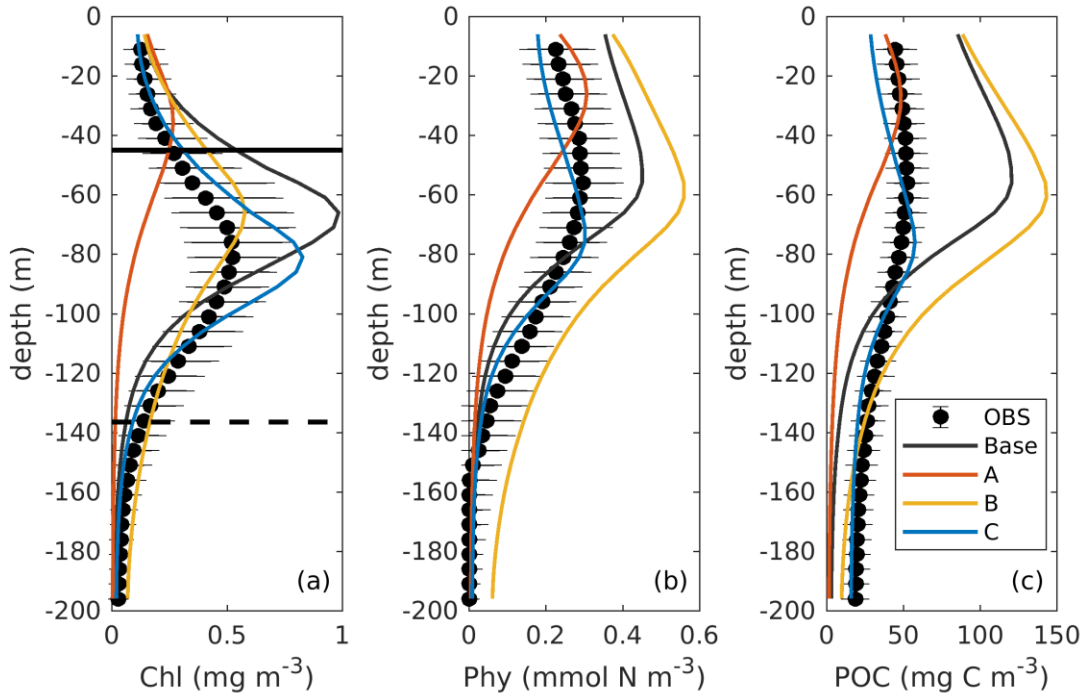
Figure 2.4. Observed (black dots with error bars) and simulated (colored lines) vertical profiles of chlorophyll, phytoplankton, and POC. Black errors represent the interquartile range of observations. The solid and dashed black lines in (a) represent the median values of mixed layer depth from July and December.

Figure 2.4b also shows that both observed and simulated phytoplankton approach zero at about 160 m depth. Unlike phytoplankton, the observations show that the POC concentrations are 19 mg C m^{-3} at about 200 m depth because of the existence of detritus, or zooplankton, or both (Fig. 2.4b, c). However, the base case fails to reproduce this non-zero POC concentrations, indicating that the model might be underestimating the carbon export fluxes at 200 m.

2.4.2   Results of the optimizations

2.4.2.1 Model-data misfits

The case-specific cost function values and total misfits for the different 1D optimizations are shown in Fig. 2.5. Not surprisingly, all optimizations result in a reduction of the case-specific cost function values. The extent of the reductions depends on the specific subset of parameters that were optimized. However, the total misfits are not reduced in all optimizations. Optimizations A1 and A2 lead to slightly larger total misfits

than the base case, and optimization B2 leads to a significantly larger total misfit. The smallest total cost function values are achieved in A4, B4, and C4, i.e., in the experiments where a larger subset of parameters was optimized (six parameters). The optimal parameter sets (A4, B2, and C4), which are selected based on case-specific misfit from these three groups, will be used in subsequent analyses and hereafter are denoted simply as experiment A, experiment B, and experiment C. Further comparisons are presented below to assess the impact of the different combinations of observations.
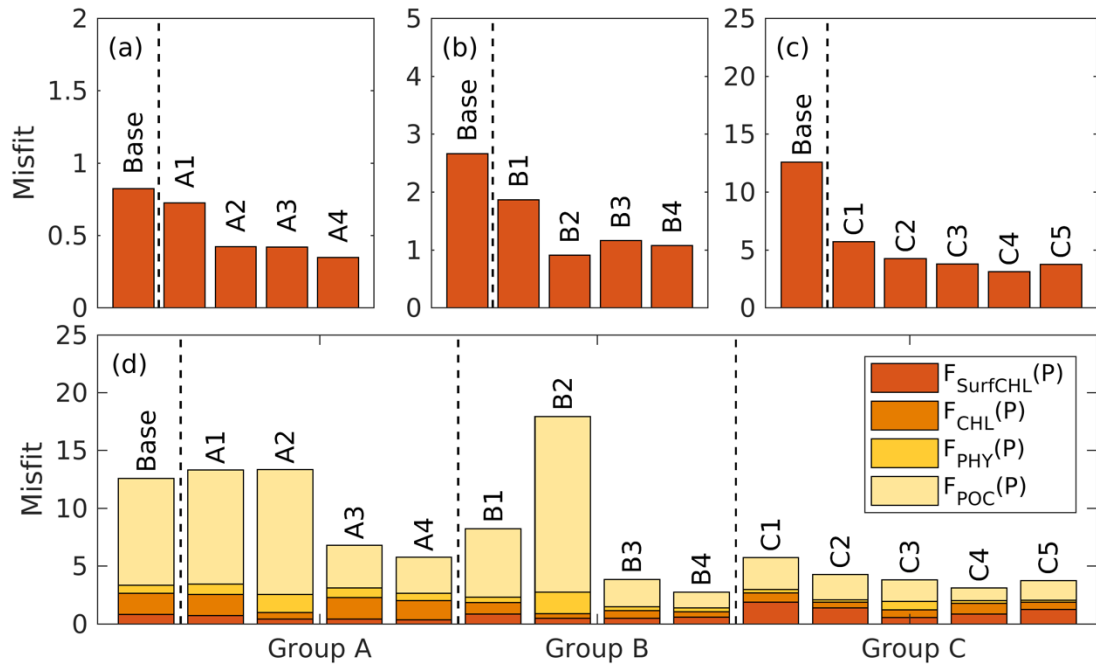
Figure 2.5. The case-specific cost function values (a-c) and total misfits (d) of the base case and the different optimizations.

2.4.2.2 Experiment A: satellite chlorophyll only

The optimal parameters (Table 2.2) from experiment A yield a 58% reduction in the misfit for surface chlorophyll (Fig. 2.5d). However, the vertical structure of chlorophyll deteriorates relative to the base case (Fig 2.4a) because of inappropriate estimates of the initial slope (α=0.0101; see Table 2.2) and the maximum ratio of chlorophyll to carbon (θmax=0.0191; see Table 2.2). The annually averaged depth of the DCM is lifted up to around 30±10 m and the magnitude of DCM strongly decreases (Figs. 2.3a and 2.4b). Similar to chlorophyll, these deteriorations also manifest in the vertical phytoplankton and

POC distributions (Fig. 2.4b-c). As a result, experiment A underestimates vertically integrated chlorophyll, phytoplankton, and POC (Fig. 2.3b-d).

Table 2.2. The best fit of parameter set for each optimization experiment. Dashed lines represent these parameters are not included in the parameter optimization and use their prior values. The optimal optimization A4, B2, and C4 which are further discussed and are denoted simply as experiment A, B, and C are highlighted as bold.

		w_{Phy}	m_P	k_{NH4}	τ	θ_{max}	α	w_{LDet}
	Base	0.1000	0.0750	0.5000	0.1000	0.0535	0.1250	1.000
	A1	0.0608	0.0100	1.5000	--	--	--	--
1D model	A2	0.6863	0.0100	0.0195	--	0.0169	--	--
	A3	1.6567	0.1978	0.1004	--	0.0250	0.0219	--
	A4	**0.9468**	**0.0737**	**0.2454**	**--**	**0.0191**	**0.0101**	**4.9694**
3D model	A	0.9468	0.0737	0.0100	--	0.0191	0.0101	4.9694
	B1	0.2863	0.0983	1.5000	--	--	--	--
1D model	**B2**	**0.4217**	**0.0130**	**0.0300**	**--**	**0.0158**	**--**	**--**
	B3	2.1016	0.0176	1.5000	--	0.0346	0.0079	--
	B4	0.0090	0.0100	1.5000	--	0.0361	0.0405	8.3514
3D model	B	0.4217	0.0130	0.0100	--	0.0158	--	--
		w_{Phy}	r_{LD}	m_P	τ	k_{NH4}	w_{LDet}	θ_{max}
	Base	0.1000	0.1000	0.0750	0.1000	0.5000	1.0000	0.0535
	C1	1.9231	0.2500	0.1805	--	--	--	--
	C2	0.9755	0.2500	0.0100	1.1402	--	--	--
1D model	C3	0.4071	0.0630	0.0100	1.8531	0.0070	--	--
	C4	**0.0090**	**0.0050**	**0.0634**	**0.0995**	**0.0431**	**5.6623**	**--**
	C5	0.0090	0.2245	0.0100	0.6451	1.5000	2.5202	0.0614
3D model	C	0.0090	0.0050	0.0634	0.0500	0.0100	5.6623	--

2.4.2.3 Experiment B: satellite chlorophyll and chlorophyll profiles

Due to the addition of observed chlorophyll profiles to the optimization in experiment B, the misfits for surface and subsurface chlorophyll decrease relative to the base case (Fig. 2.5d), but the reduction in the misfit for surface chlorophyll (38%) is smaller than that in

experiment A (58%). A straightforward interpretation is that the addition of subsurface observations reduces the model's degrees of freedom to fit one single observation type (surface chlorophyll). The vertical profile of chlorophyll is reproduced better in experiment B than in the base case and experiment A in that the magnitude of the DCM is closer to the observations, although the DCM depth is still too shallow, on average by about 20 m (Fig. 2.4a). The improvement in the vertical chlorophyll structure results in a better model-data fit of vertically integrated chlorophyll (Fig. 2.3b).

Despite the improvements in chlorophyll, the vertical profiles of phytoplankton and POC exhibit a marked deterioration relative to the base case and experiment A (Fig. 2.4b-c) because the parameter optimization underestimates the maximum chlorophyll-to-carbon ratio (θmax =0.0158; see Table 2.2). Experiment B leads to an overestimation of phytoplankton and POC relative to the base case with misfits roughly 2.7 and 1.6 times larger than those of the base case, respectively (Fig. 2.5d). Although experiment B reproduces the non-zero POC concentrations at about 200 m depth, the proportion of phytoplankton in the POC pool is incorrect. In contrast to the observations where the phytoplankton's contribution is neglectable (Fig. 2.4), the simulated POC at 200 m is dominated by phytoplankton (49%).

2.4.2.4 Experiment C: all available observations

Incorporating all observations (i.e., surface chlorophyll and profiles of chlorophyll, phytoplankton, and POC) in experiment C improves the model-data misfits for almost all aspects except for surface chlorophyll (Fig. 2.3). Although a slight increase in the misfit occurs for the surface chlorophyll (~ 5%), the total misfit is reduced by 75% compared to the base case. As shown in Fig. 2.4a, the annually averaged depth of DCM of 80 m coincides with the observed DCM, primarily because experiment C reproduces the deepening of the DCM in summer. The magnitude of the DCM is also decreased relative to the base case but remains higher than the observed. Phytoplankton and POC profiles exhibit only minor deviations from the observations (Fig. 2.4b-c). Importantly, experiment C reproduces the non-zero POC concentrations at 200 m. In contrast to experiment B, phytoplankton in experiment C drops to zero at about 160 m and POC is dominated by detritus (85%), which is more consistent with the observations.

2.4.3　Simulated carbon fluxes

　　Annually averaged carbon fluxes within the upper 200 m are shown for each experiment in Fig. 2.6. The primary production in the base case amounts to 0.78 g C m^{-2} day^{-1}, of which 37% is consumed by zooplankton, and the remaining 63% flows into detritus pools through sloppy feeding, mortality, and aggregation of phytoplankton. As for the production of detritus, contributions from the phytoplankton and zooplankton pools account for 70% and 30%, respectively. Most of the produced detritus is recycled into the nutrient pool fueling recycled primary production, and only a small fraction is removed from the upper layer through gravitational sinking. As a result, carbon export, which is estimated as the sum of sinking fluxes by phytoplankton and detritus, is only 0.00032 g C m^{-2} day^{-1} and accounts for 0.04% of primary production.
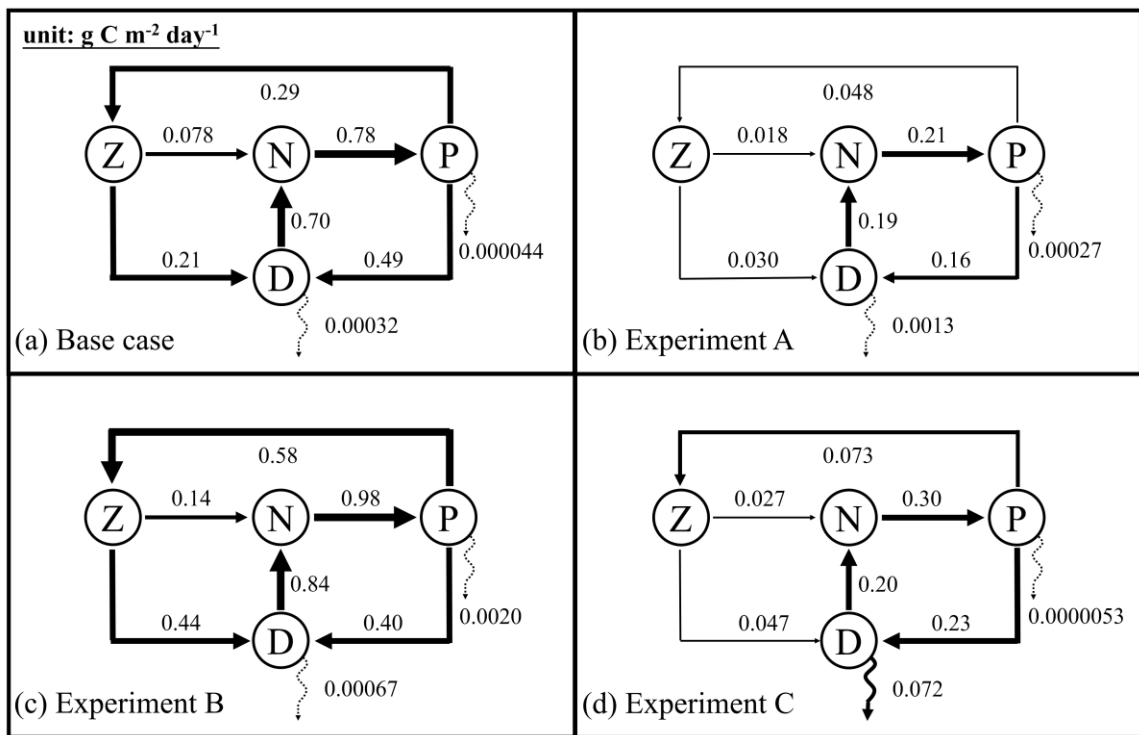
Figure 2.6. Annually averaged carbon fluxes integrated over the upper 200 m (unit: g C m^{-2} day^{-1}) for the base case (a) and optimized experiments A, B, and C. The N, P, Z, and D stand for the pools of nutrient, phytoplankton, zooplankton, and the sum of small and large detritus, respectively. The thickness of arrows scales with the magnitude of fluxes. Dashed arrows represent fluxes lower than 0.01 g C m^{-2} day^{-1}.

Due to the underestimation of phytoplankton in experiment A, primary production is reduced to 0.21 g C m^{-2} day^{-1} in that case. All other fluxes in the top 200 m decrease relative to the base case as well, except for the export flux which increases to about 0.8% of primary production. This relative increase in export is the result of larger sinking rates of phytoplankton and detritus (w_{Phy}=0.95, w_{LDet} =4.97; see Table 2.2) than those used in the base case.

In contrast to experiment A, experiment B yields an increase of primary production relative to the base case. The proportion of the grazing flux to primary production and the contribution of zooplankton to the production of detritus also increase to about 59% and 52%, respectively. Unlike in the other three experiments, carbon export in experiment B is dominated by the sinking of phytoplankton, reflecting its large contribution to POC at 200 m. Although the simulated POC concentration at 200 m is very close to the observations, the relative contributions of phytoplankton, zooplankton, and detritus are problematic and likely do not result in a better estimation of carbon export (in this case 0.3% of primary production).

In experiment C, primary production is 0.30 g C m^{-2} day^{-1}, with 24% flowing to zooplankton. The mortality of zooplankton causes a flux of 0.047 g C m^{-2} day^{-1} to detritus, which accounts for 17% of the production of detritus. Finally, about 24% of primary production is removed from the upper 200 m through gravitational sinking. The simulated export ratio of 24% is within the wide range of reported export ratios, from 6% to 43%, at 120 m depth in the Gulf of Mexico (see Table 3 of Hung et al., 2010). Despite the high degree of uncertainty that exists when estimating export ratios (e.g., the global mean export ratio varies from ~10% Henson et al., 2012; Lima et al., 2014; Siegel et al., 2014 to ~20% Henson et al., 2015; Laws et al., 2000), it is obvious that only experiment C reproduced an export ratio of a reasonable magnitude. A more detailed validation of primary production and export fluxes will be presented in the following sections.

2.5 Three-dimensional biogeochemical model

The optimal parameter sets from the 1D optimizations of A, B, and C were applied in the 3D model for the whole GOM for five years (2011-2015). The performance of the 3D

model can be regarded as a cross-validation of the parameters optimized in 1D at different times and locations. It is possible that the optimization algorithm has modified parameters to compensate for biases between 1D and 3D simulations, e.g., the absence of advection in 1D model as well as the differences in the model domain, model period, and model resolution, that degrades the 3D model performance (Kane et al., 2011). Indeed, directly applying the optimal parameter sets from the 1D version to the 3D model yields lower model-data agreement than the 1D counterpart but preserves the most important features well. For instance, when the resulting parameters are used in the experiment C, chlorophyll concentrations in the upper layer were lower in the 3D model and farther away from the observations. However, the DCM depth and the non-zero POC concentrations at 200 m with appropriate contributions from each component are well reproduced in the 3D model. I therefore performed a few manual tests and made the following modifications to the optimized parameters to bring the model-data agreement of 3D model in better alignment with that of 1D version (Table 2.2): the half-saturation for NH_4 uptake (k_{NH4}) was decreased to 0.01 in experiment B and C, and the aggregation parameter (τ) was decreased to 0.05 in the experiment C.

2.5.1   Spatial patterns of surface chlorophyll

First, the annual climatological surface chlorophyll from satellite and model are compared from 2011 to 2015. The satellite estimates show high chlorophyll in the coastal regions and low chlorophyll in the deep ocean (Fig. 2.7a). This spatial pattern of surface chlorophyll is well reproduced in all simulations except in experiment A, which even fails to reproduce the relatively high chlorophyll near the Mississippi-Atchafalaya River systems because of the high sinking rate of phytoplankton (w_{Phy}=0.95; see Table 2.2). The largest model-data differences occur in the coastal regions, where all simulations underestimate the observed surface chlorophyll. Since all BGC-Argo floats operated in the deep ocean (Fig. 2.1) and the parameter optimization is performed at one central station without any influence from coastal environments, only the model results in the deep ocean (depth > 1000 m) will be considered in the following discussion.
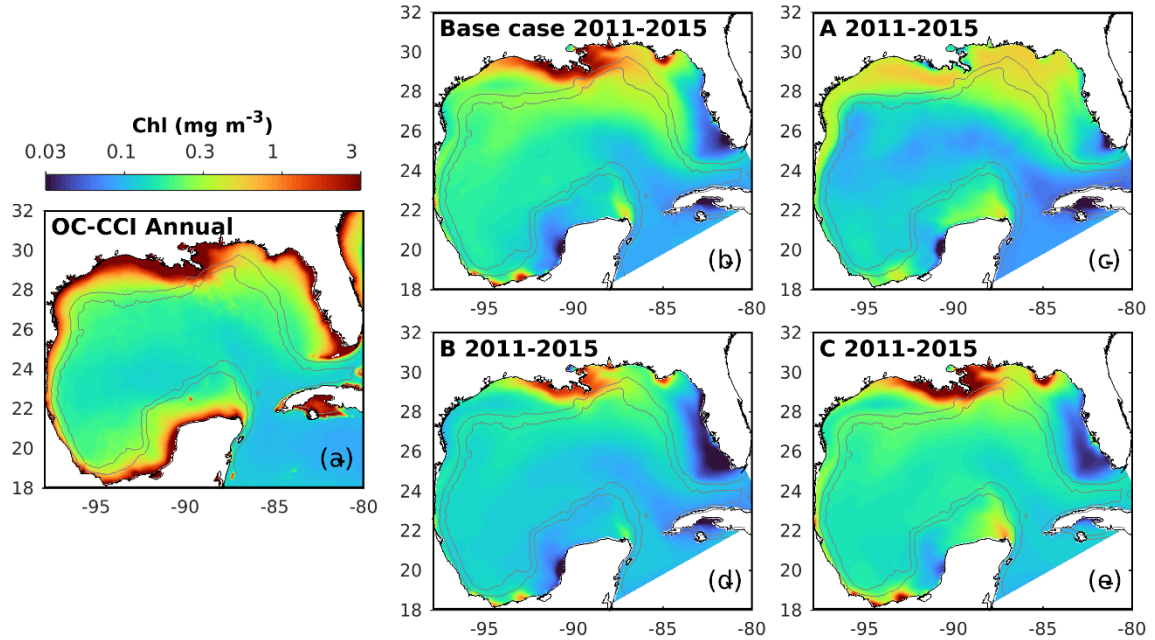
Figure 2.7. Spatial distributions of the annual mean chlorophyll in the surface layer from the satellite (OC-CCI) climatology (2011-2015) and the different model versions. The gray contours mark the bathymetric depths of 200 and 1000 m.

2.5.2 Subsurface distributions

Figure 2.8 shows the seasonal cycles of surface chlorophyll as well as the vertically integrated chlorophyll, phytoplankton, and POC within the deep ocean (depth > 1000 m). Analogous to the 1D models, chlorophyll, phytoplankton, and POC were integrated over the upper 200 m. Here again the whole deep ocean was averaged because it is homogenous horizontally. In addition, I compare surface chlorophyll with satellite estimates in two sub-regions from the Mississippi Delta and the central Gulf in Fig. B.5.

Comparisons of vertical profiles between observations and model results are given in Fig. 2.9. In general, the main features in the 3D models are very similar to those in 1D. Experiment A cannot constrain the vertical profiles of chlorophyll because of the inappropriate estimation of initial slope (α), experiment B overestimates phytoplankton and its contribution to POC since the maximum ratio of chlorophyll to carbon (θmax) is weakly constrained, and experiment C shows significant improvements in the model-data agreement.
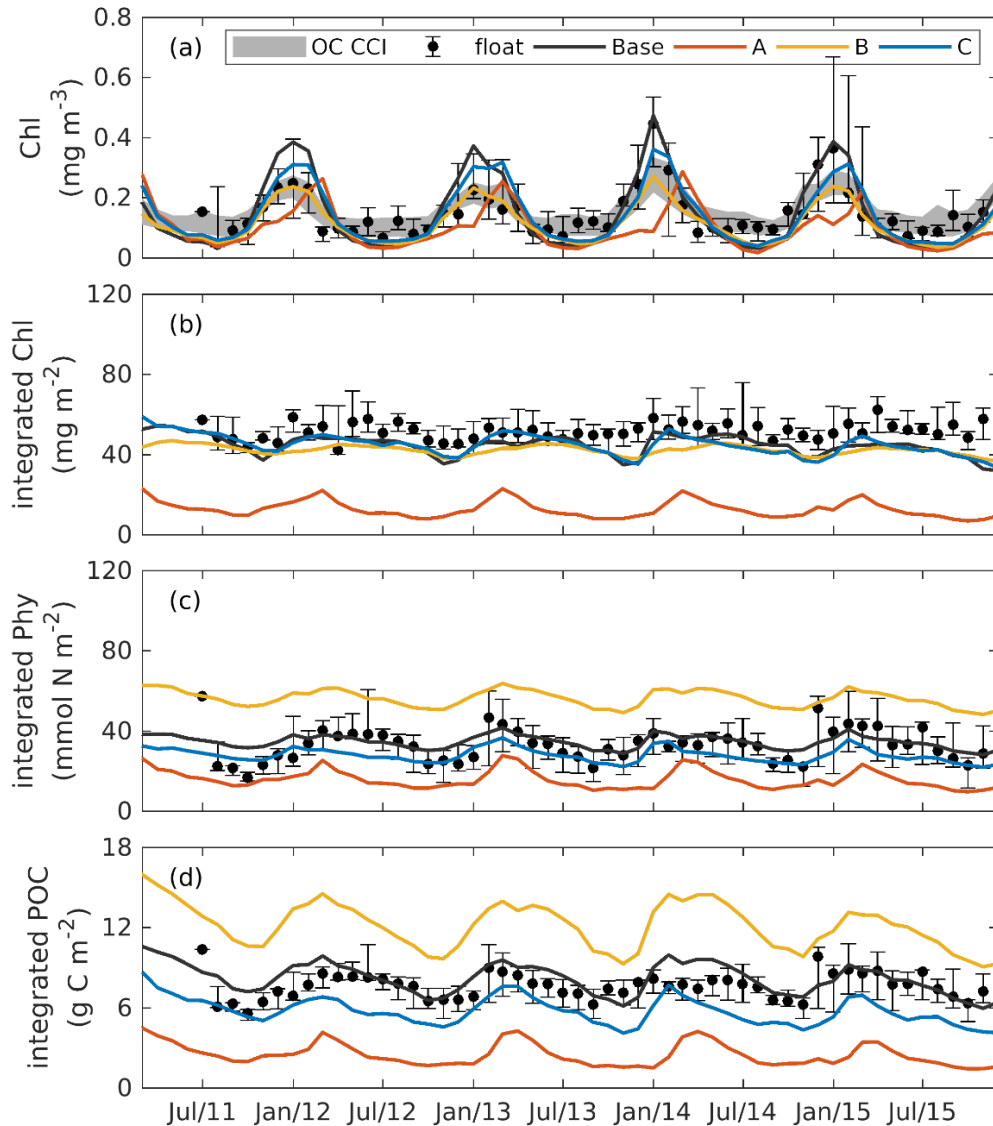
Figure 2.8. Observed and simulated seasonal cycles of surface chlorophyll (a), vertically integrated chlorophyll (b), vertically integrated phytoplankton (c), and vertically integrated POC (d) from each 3D model. Solid lines represent the median values over the deep ocean of GOM (depth > 1000 m). Error bars and shades show the 25% and 75% percentiles. Chlorophyll, phytoplankton, and POC are integrated over the top 200m.

Additional comparisons of the chlorophyll-to-carbon ratio, primary production, and carbon export fluxes from 1D and 3D models with observations are given in Fig. 2.10. The chlorophyll-to-carbon ratio is estimated as the vertically integrated chlorophyll divided by phytoplankton in the upper 200 m (Fig. 2.10a). As an important indicator of phytoplankton physiological status (Geider 1987), the observed chlorophyll-to-carbon ratio varies considerably in response to the ambient environment. In general, the ratios derived from

the 3D models are lower than their corresponding 1D values, but the differences are still within the range of variability. Without utilizing the observations of phytoplankton and POC, experiments A and B in both the 1D and the 3D versions underestimate the chlorophyll-to-carbon ratio. In experiment C, the simulated chlorophyll-to-carbon ratios from 1D and 3D are in good agreement with the observations although the observed variability is underestimated.
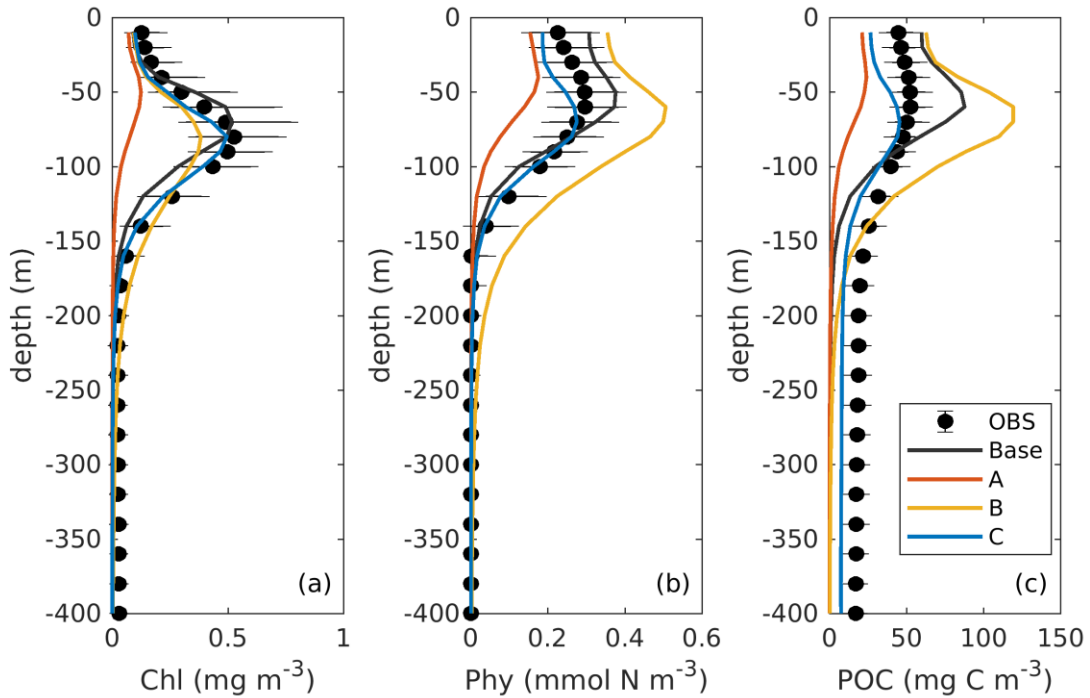
Figure 2.9. Observed and simulated vertical profiles of chlorophyll, phytoplankton, and POC from each 3D model.
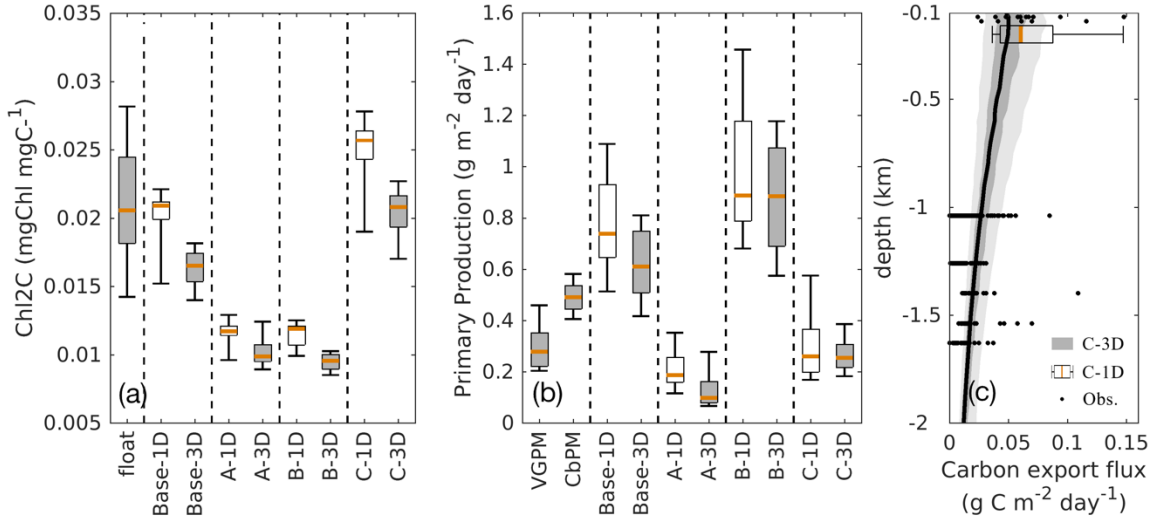
Figure 2.10. Comparisons of the chlorophyll-to-carbon ratio (a), primary production (b), and carbon export fluxes (c) between the 1D and 3D models.

For reference, satellite-based primary production (PP) is provided by two algorithms, the Vertically Generalized Production Model (VGPM, Behrenfeld and Falkowski, 1997) and the Carbon-based Productivity Model (CbPM, Westberry et al., 2008). As shown in Fig. 2.10b, satellite-based PP differs depending on the algorithm applied. PP results from all 3D simulations which were integrated down to 200 m are qualitatively similar to the 1D simulations. Experiment C provides the best estimates of PP when compared to satellite-based estimates from VGPM and CbPM, both in 1D and 3D.

The base case and experiments A and B yield carbon export fluxes smaller by 1 to 2 orders of magnitude than experiment C. Thus, only experiment C from the 1D and 3D models are shown in Fig. 2.10c in comparison to observations from sediment traps (see Appendix B). The carbon export fluxes at 200 m from the 1D and 3D are similar in magnitude although the 1D model yields higher fluxes and larger variability. Despite the scarcity of carbon export observations in the GOM, the model estimates are within the range of observations down to ~1600 m and capture the observed declining trend of carbon export with depth.

In summary, all the results above demonstrate the feasibilities of using the locally optimized parameters from the 1D model to improve the 3D simulation. In addition, by incorporating all available observations (i.e., surface chlorophyll from satellite estimates,

profiles of chlorophyll, phytoplankton, and POC from bio-optical floats), experiment C cannot only simulate the biogeochemical processes well in the upper 200 m, but also reproduce the carbon export flux and its associated attenuation in the deep ocean (200-1600m) of the GOM.

2.6 Discussion

2.6.1 Trade-offs between different observations for parameter optimization

The results of the optimization experiments vary dramatically depending on how many observation types are used. Using only satellite surface chlorophyll in experiment A succeeds in reducing the misfits of surface chlorophyll, but at the expense of the vertical structure since the predominant DCM disappears in experiment A. Satellite surface chlorophyll alone cannot constrain several vital parameters, including the initial slope of the productivity-irradiance curve (α) and the maximum ratio of chlorophyll to carbon (θmax), with confidence. This result highlights the importance of subsurface observations for parameter optimization and similarly for model validation.

The floats provide valuable subsurface observations, but chlorophyll profiles alone are not sufficient for parameter optimization. In experiment B, the addition of chlorophyll profiles leads to significant improvements in vertical chlorophyll distributions; however, the profiles of phytoplankton and POC deteriorate largely because the maximum ratio of chlorophyll to carbon (θmax) is poorly constrained. Using estimates of phytoplankton biomass and POC derived from backscatter measurements in experiment C yields the best estimation of plankton-related state variables and carbon fluxes (i.e., primary production and carbon export). Only in this experiment do the improvements obtained from observations in the upper 200 m extend to the deep ocean as reflected in the improved carbon export estimates below 1000 m.

It should be noted, however, that degradation of unoptimized variables did not occur in all optimizations within experiments A and B. In some cases, the unoptimized fields were improved. For example, the A2 optimization yields a 69% reduction in the misfit for subsurface chlorophyll (Fig. 2.5d) and large improvements of chlorophyll profiles (Fig. B.6a) even though no observations of subsurface chlorophyll are used. Another example is

that B1 optimization improves simulations of phytoplankton and POC (Fig. 2.5d and Fig. B.6b-c) through the correlations between the observed chlorophyll and phytoplankton (R^2 = 0.69) and POC (R^2 = 0.69). Similar findings have been reported in Prunet et al. (1996b), where the improvements of chlorophyll profiles within the mixed layer were obtained by using surface chlorophyll in a 1D model. In a more recent study by Xiao and Friedrichs (2014a), where satellite data was used, subsurface fields were improved in addition to surface fields.

In optimizations A2 and B1, the improvement in unoptimized fields occurred because the poorly constrained parameters were not optimized but well defined coincidently (α = 0.125 in the optimization A2 and θmax= 0.0535 in the optimization B1; see Table 2.2). Including the poorly constrained parameters into the parameter optimization can return a lower misfit with respect to the observations used in optimization but increases the risk of overfitting and reduces the model's predictive skill, i.e., the ability to simulate unoptimized observations and those collected at different locations and times. This is consistent with previous studies (Friedrichs et al. 2006, 2007; Ward et al. 2010). For example, Friedrichs et al. (2006) optimized three ecosystem models of different complexities against three seasons of observations, and the resulting parameters were used to quantify the predictive skill for the fourth season. Cross-validation showed that exclusion of the poorly constrained parameters from the optimization increased the predictive skill.

Although prior knowledge of the parameters allows one to exclude those poorly constrained ones from the optimization and thus can prevent degradation in unoptimized variables, most parameters are poorly known. Thus, the ultimate resolution of this issue should be to increase availability of observations so that more parameters can be constrained with confidence. In addition, even if the poorly constrained parameters are well-known, a lack of observations hampers our ability to recognize improvements in the model's predictive skill and hence may prevent us from identifying the optimal solutions. For example, without the observations of phytoplankton and POC, I could not have known that optimization B1 improved simulations of phytoplankton and POC, let alone that the optimization B1 was a better solution than the optimization B2 (the experiment B) in terms of the lower total misfit as shown in Fig. 2.5d.

It has been suggested that when performing a parameter optimization not only parameter values but also parameter uncertainties should be taken into account (Fennel et al., 2001; Ward et al., 2010; Bagniewski et al., 2011). The parameter uncertainties can be assessed by performing an uncertainty analysis (Prunet et al. 1996b; a; Fennel et al. 2001), replicating the parameter optimization (Ward et al. 2010), and cross-validating the resulting parameters (Xiao and Friedrichs 2014a). In this chapter, a cross-validation of the parameters was conducted by evaluating the model's predictive skill with respect to different variables, times, and locations. However, even when cross-validation at different times and locations produces large misfits, I cannot conclude that the models reproduce observations through wrong mechanisms. This is because the large misfit can be a result of intrinsic heterogeneity of biological parameters at different times (Mattern et al. 2012) and locations (Kidston et al. 2011). Therefore, it is important to evaluate the predictive skill of unoptimized variables.

Collectively, the discussion above highlights the values of BGC float data for parameter optimization and model validation, not only because of their high spatiotemporal coverage but also their ability to measure multiple properties simultaneously.

2.6.2 Feasibilities of applying the local optimized parameters to 3D models

As the high computational cost makes direct optimization for a 3D biogeochemical model impractical, I performed parameter optimizations first in a 1D surrogate model with the same biogeochemical component as the 3D model. However, there are some difficulties in porting the locally optimized parameters to the basin-scale model.

Firstly, the 1D model necessarily neglects advection and inevitably differs from the 3D model, e.g., in model domain and model resolution. The optimized parameters from the 1D model may have been adjusted to compensate for biases between 1D and 3D models, and, as a result, this may degrade the 3D simulations (Kane et al. 2011). Although counter examples also exist where the 3D simulations outperform the 1D models with respect to vertical profiles of phytoplankton and nitrate (Hoshiba et al. 2018), some manual modifications might be necessary before the optimal 1D parameters can be applied in the 3D model. In this chapter, despite some degradations in 3D simulations, the benefits of the

1D optimization were mostly preserved in the 3D simulations. This greatly simplified the following subjective tuning of the 3D model by limiting the number of parameters that needed to be adjusted and confirmed the feasibility of improving the 3D model by optimizing a 1D surrogate.

Secondly, the spatial heterogeneity of parameters (e.g., Kuhn and Fennel 2019) is another issue that influences the portability of parameters from 1D to 3D models. For example, the underestimation of surface chlorophyll in the coastal regions may result from the contrasting ecosystem functioning between coastal regions and deep ocean, whereby the highly productive continental shelf in the northern GOM is fueled by the large nutrient load from the Mississippi and Atchafalaya River systems with primary production being as high as 4 g C m^{-2} day^{-1} near the Mississippi River delta (Fennel et al. 2011), while the deep ocean is oligotrophic and nutrient limited with the primary production ranging from 0.2 to 0.5 g C m^{-2} day^{-1} (see Fig. 2.10). In some studies, the parameter optimization has been performed at several contrasting stations with a goal of using different parameter sets in different regions of the 3D model (Hoshiba et al. 2018). In other studies different stations were optimized simultaneously to obtain one single optimized parameter set (Schartau and Oschlies 2003; Oschlies and Schartau 2005; Kane et al. 2011). Such parameters compromise the misfit in each single station but take into account all stations and can often yield an overall better simulation of all these stations as shown by, e.g., Kuhn and Fennel (2019).

2.7 Conclusions

In this chapter, I have performed parameter optimization for a 1D biogeochemical model and then used the resulting parameters with a few modifications to generate simulations with a corresponding 3D model in the GOM. Three experiments have been conducted by using different combinations of observations (surface chlorophyll from satellite estimates, vertical profiles of chlorophyll, phytoplankton biomass and POC from BGC Argo floats) in order to examine the trade-offs between the different observations for parameter optimization. Two misfit metrics have been defined using the case-specific

misfit and the total misfit to measure the models' abilities to reproduce the optimized and unoptimized observations.

Model results show that satellite surface chlorophyll alone cannot reproduce well the vertical structures in a biogeochemical model unless profile observations are used in addition. BGC Argo floats are an excellent platform for obtaining such observations at high spatiotemporal coverage and for a relatively broad suite of parameters. Only adding chlorophyll profiles is not sufficient because they fail to constrain the ratio of chlorophyll to phytoplankton, but the addition of backscatter, which allows estimation of phytoplankton biomass and POC, enables us to constrain the subsurface carbon state variables and reproduce PP and carbon export fluxes to below 1000 m depth well. Finally, the 3D model was improved and reproduced similar results to the 1D version, which is promising for the application of parameter optimization.

CHAPTER 3

CAN ASSIMILATION OF SATELLITE OBSERVATIONS IMPROVE SUBSURFACE BIOLOGICAL PROPERTIES IN A NUMERICAL MODEL? A CASE STUDY FOR THE GULF OF MEXICO[2]

3.1 Introduction

Given the multiple and increasing pressures of ocean warming, acidification, deoxygenation, and changes in primary productivity on ocean ecosystem health, accurate model simulations are urgently needed to assess past and current states of marine ecosystems, forecast future trends, and predict the ocean's response to different scenarios of climate change and management policies. In practice, numerical models are imperfect representations of the natural system, and their accuracy is limited by many factors including insufficient model resolution, inaccuracies in discretization schemes and model formulations, parameterization of unresolved processes, and uncertainties in model inputs. Data assimilation is a practical approach used to compensate for these model deficiencies. It is a statistical method to interpolate and extrapolate sparse observations into the regular model space in a dynamically consistent way. Its success critically depends on well-resolved observations. While any practice to constrain a model by observations can be referred to as data assimilation, in this chapter I specifically refer to state estimation, i.e., sequential updates of the model state.

Data assimilation is well developed in physical oceanography (Edwards et al. 2015) but less mature in biogeochemical ocean modelling, largely due to insufficient observations (Fennel et al. 2019). Thus far, satellite data on ocean color (e.g. chlorophyll) have been the

---

major source of observations to be assimilated (e.g., Ford and Barciela, 2017; Gregg, 2008; Hu et al., 2012; Mattern et al., 2013; Pradhan et al., 2019; Teruzzi et al., 2018) because of their relatively high resolution and routine availability. More recent advances have focused on the incorporation of other satellite-derived products including size-fractionated chlorophyll (e.g., Ciavatta et al., 2018, 2019; Pradhan et al., 2020; Skákala et al., 2018) and optical properties (e.g., Ciavatta et al., 2014; Gregg and Rousseaux, 2017; Jones et al., 2016; Shulman et al., 2013; Skákala et al., 2020). However, these measurements are limited to the surface ocean and provide little information about the subsurface and ocean interior. In addition, it has been acknowledged that assimilating satellite data of ocean color often fails to improve and even degrades simulation of unobserved biological variables (Fontana et al. 2013; Ford and Barciela 2017; Ciavatta et al. 2018; Skákala et al. 2018; Teruzzi et al. 2018). Problems also remain in accounting for the co-dependencies or covariances between biological variables. For instance, Fontana et al. (2013) found subsurface nitrate was barely impacted by assimilating the satellite surface chlorophyll because of its weak correlations with surface chlorophyll. Although BGC-Argo floats may ultimately provide us with abundant subsurface measurements of multiple key biogeochemical properties (Biogeochemical-Argo Planning Group 2016; Roemmich et al. 2019; Chai et al. 2020), the profiling observations will likely remain insufficient for three-dimensional data assimilation for a number of years, making satellite data the main observation streams for sequential data assimilation in biogeochemical models (Ford 2021).

The insufficient availability of subsurface and interior ocean biogeochemical observations is reflected not only in the immaturity of biogeochemical data assimilation but also its skill assessment. When compared with the surface, the subsurface has received less attention in skill assessments of biogeochemical data assimilation systems. Although there have been studies that compared vertical structures with in situ observations and/or climatological datasets (e.g., Fontana et al., 2013; Ford and Barciela, 2017; Mattern et al., 2017; Ourmières et al., 2009; Teruzzi et al., 2014), these validations were often limited to low spatiotemporal resolution. The recent growth of autonomous observation systems, especially BGC-Argo floats and gliders, make it possible to evaluate biogeochemical data assimilation systems below the surface in high resolution (e.g., Cossarini et al., 2019; Salon et al., 2019; Skákala et al., 2021; Verdy and Mazloff, 2017).

Finally, since physical processes affect biological properties through advection and diffusion of biological tracers as well as some temperature-dependent biological activities (e.g., phytoplankton growth), deficiencies in biological models can arise from imperfect simulation of the physics (Doney 1999; Oschlies and Garçon 1999; Doney et al. 2004). Although there have been studies demonstrating a positive effect of physical data assimilation on biological properties (Ourmières et al. 2009; Fiechter et al. 2011), often this approach degrades biological distributions because of elevated vertical velocities and violation of consistency between physical and biological properties (Anderson et al. 2000; Raghukumar et al. 2015; Yu et al. 2018). To address these issues, joint assimilation of physical and biological observations (Song et al. 2016a; b) or multivariate updates based on the cross-covariances between physical and biological properties (Yu et al. 2018; Goodliff et al. 2019) have been suggested.

In this chapter, a multivariate physical-biological data assimilation scheme is applied to a coupled physical-biological model in the Gulf of Mexico. The rationale for choosing the Gulf of Mexico is that the dominant circulation, including the Loop Current and its associated mesoscale eddies, is stochastic and can influence the subsurface biological distributions, e.g., deep chlorophyll maximum (Pasqueron de Fommervault et al. 2017). In addition, I test how data assimilation impacts depend on model calibration when using two alternative light parameterizations. By comparing forecast results from the assimilative model with independent observations from five BGC-Argo floats which are not assimilated but used in *a priori* tuning of the biogeochemical model, I rigorously evaluate whether the main biological observation stream (satellite estimates of surface chlorophyll) in combination with physical observations (satellite estimates of sea surface height and sea surface temperature) can inform the 3D ocean distributions in high spatial and temporal resolution.

3.2 Tools and methods

3.2.1 Coupled physical and biological model

The coupled physical and biological model used in this chapter is based on the Regional Ocean Modeling System (ROMS; Haidvogel et al., 2008) configured in the Gulf of Mexico (red rectangle in Fig. 3.1 shows the model domain) with a horizontal resolution

of ~ 5 km and 36 vertical sigma levels (Yu et al. 2019; Wang et al. 2020). The model used a multidimensional positive definitive advection transport algorithm (MPDATA; Smolarkiewicz and Margolin, 1998) to solve the horizontal and vertical advection of tracers, a Smagorinsky-type formula (Smagorinsky 1963) to parameterize horizontal viscosity and diffusivity, and the Mellor-Yamada 2.5-level closure scheme (Mellor and Yamada 1982) to calculate the vertical turbulent mixing. Atmospheric forcing is provided by the European Centre for Medium-Range Weather Forecast ERA-Interim product (ECMWF reanalysis; Dee et al., 2011) with a horizontal resolution of 1/8º (approximately 12 km×14 km) to calculate the surface wind stress as well as the net heat fluxes and freshwater fluxes.

The biological model uses a nitrogen-based model (Fennel et al. 2006) to simulate transportation and transformation of seven pelagic variables, i.e., nitrate (NO_3), ammonium (NH_4), chlorophyll (Chl), phytoplankton (Phy), zooplankton (Zoo), small detritus (SDeN), and large detritus (LDeN). As a separate state variable, chlorophyll accounts for photoacclimation based on Geider et al. (1997). In the coupled model, the biological tracers are advected and diffused as part of the 3D circulation but provide no feedback to the physical model. Biological parameters are from the parameter optimization study of Wang et al. (2020) except that the half-saturation constant of nitrate was subjectively re-tuned based on the BGC-Argo floats data from 0.5 mmol N m^{-3} to about 1.4 mmol N m^{-3} because the previous model underestimated the nitrate in the euphotic zone.
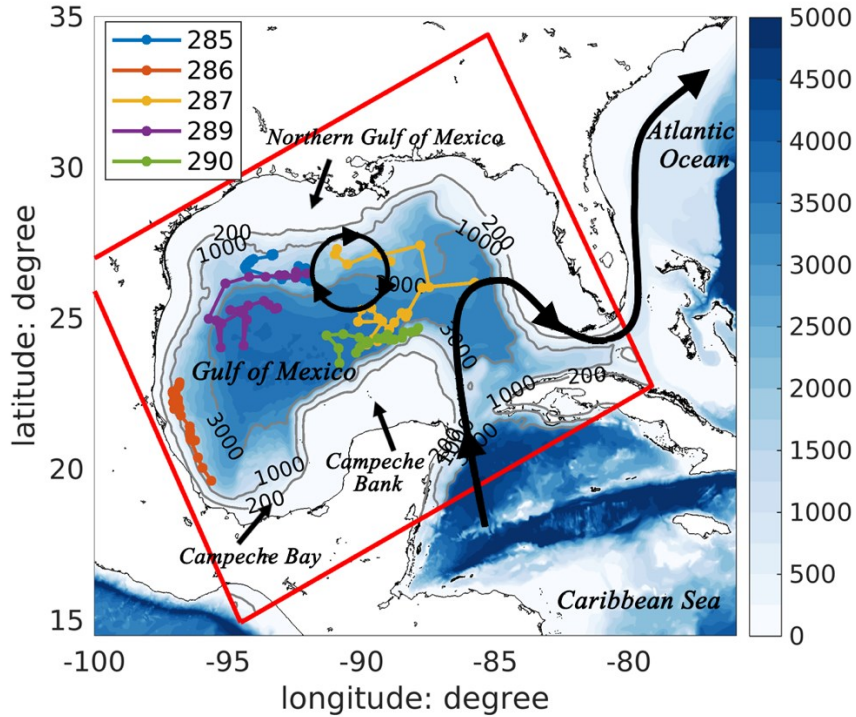
Figure 3.1. Bathymetric map of the Gulf of Mexico with a schematic pattern of the Loop Current (black curve with arrows) and Loop Current eddies (black circle with arrows). Trajectories of five BGC- Argo floats (colored lines) in 2015 are also shown in the figure. The model domain is represented by the red rectangle.

The coupled model receives freshwater and nutrients inputs from the Mississippi-Atchafalaya River systems, which are specified by the daily measurements from the US Geological Survey river gauges and those from other major rivers that utilize the climatological estimates (Xue et al. 2013). To ensure a dynamically consistent biological field, a 1-year spin-up is performed in 2014 wherein the physical model is initialized from the output of the 1/12º data-assimilative global HYCOM/NCODA (Chassignet et al. 2005) and the biological model starts from a regressed 3D field of nitrate based on its climatological relationship with temperature (see Fig. C.1). A semi-prognostic method is used during the spin-up period to reduce model drift by replacing model density with a linear combination of model and climatological density fields when calculating the horizontal pressure gradient (Sheng et al. 2001; Greatbatch et al. 2004). After the spin-up, experiments are performed for a year from January 2015 to December 2015.

3.2.2   Data assimilation technique

In this chapter, the data assimilation scheme uses the deterministic formulation of the Ensemble Kalman Filter (DEnKF), which was first introduced by Sakov and Oke (2008). The approach consists of two steps: (1) the forecast step in which an ensemble of state variables is integrated forward in time by the model, and (2) the analysis step in which observations are assimilated to update the forecasted ensemble following the Kalman Filter equations:

$$x^a = x^f + K(d - Hx^f), \tag{3.1}$$

$$K = P^f H^T (H P^f H^T + R)^{-1}, \tag{3.2}$$

where x represents the model state estimate, d represents the available observations, H represents the observation operator mapping the model state onto observations, and K represents the Kalman gain matrix, which is determined by the model error matrix P and observation error matrix R (Eq. 3.2). Superscripts "a" and "f" represent analysis (i.e., updated) and forecast (i.e., prior to the update) estimates, and T represents the matrix transpose. Unlike the original stochastic EnKF, which updates each ensemble member with perturbed observations, the DEnKF updates ensemble mean ($\bar{x}$) and anomalies ($A = x - \bar{x}$) separately without perturbating observations, i.e., the former is updated as in Eq. 3.1 while the latter is updated by

$$A^a = A^f - \frac{1}{2} KHA^f . \tag{3.3}$$

More details of the DEnKF can be referred in Sakov and Oke (2008) and Yu et al. (2018).

The data assimilation framework and configurations are the same as in Yu et al. (2019) wherein twin experiments were performed in the same model domain. In this chapter, I extend the work to jointly assimilate the physical and biological observations into a coupled model. For the sake of keeping the data assimilation experiments computationally affordable, I chose an ensemble size of 20 which has been successfully used in previous studies including an idealized channel (Yu et al. 2018), the Middle Atlantic Bight (Hu et al. 2012; Mattern et al. 2013), and the Gulf of Mexico (Yu et al. 2019). Spurious

correlations, which can arise with relatively small ensembles, are avoided here by applying a distance-based localization with a radius of 50 km (Evensen 2003). Vertical localization is not applied. Ensemble anomalies are inflated by 1.05 in each update step to account for unrepresented sources of model uncertainty (Anderson and Anderson 1999). Values of the localization radius and inflation factor were determined in Yu et al. (2019).

In order to account for uncertainties in the model's initial, boundary and atmospheric forcing conditions, and biological parameters, the ensemble is initialized from 20 different daily outputs, centered on the initial date of 1 January 2015, from a previous deterministic model simulation (as described above in Section 3.2.1) and is forced by open boundary conditions, which are lagged by up to ± 10 days for the different ensemble members. Furthermore, each ensemble member is forced by a perturbed version of the wind forcing. Specifically, the wind forcing from the deterministic run is decomposed into empirical orthogonal functions (EOFs) and then the first 4 EOFs are perturbed by multiplying random numbers with zero mean and variance of 1 as in Li et al. (2016) and Thacker et al. (2012). In addition, four sensitive biological parameters, namely the mortality rate of phytoplankton, the maximum ratio of chlorophyll to carbon, the grazing rate of zooplankton, and the growth rate of phytoplankton at 0 ºC, were identified in sensitivity experiments. Specifically, a 1D version of model, described in Wang et al. (2020) was run multiple times while incrementally perturbing one parameter at a time by factors ranging from 0.25 to 1.75 with an increment of 0.25. The four sensitive parameters were selected based on the normalized absolute differences between the perturbed and unperturbed run. In the data assimilation experiments, these parameters are subject to a Gaussian perturbation with a relative variance of 75%, but they are not updated. The parameters are resampled from their distributions before each forecast step to prevent some extreme parameter values being used throughout the whole data assimilation experiment.

3.2.3 Observations

In this chapter, physical and biological observations are jointly assimilated to constrain the coupled model. The observations assimilated include sea surface height (SSH), sea surface temperature (SST), Argo T-S profiles, and satellite estimates of surface chlorophyll.

The SSH observations for assimilation are obtained by adding the 1/4º mapped sea level anomaly (SLA) from Archiving Validation and Interpretation of Satellite Oceanographic Data (AVISO) to a mean dynamic topography (MDT) from Rio et al. (2013), and they are adjusted by removing the spatially averaged mismatches between assimilated and forecasted SSH to account for differences in reference time between the SLA data (1993-2012) and the coupled model (2015) (Haines et al. 2011; Xu et al. 2012; Song et al. 2016a). This is equivalent to assimilating the SSH gradient into the model, as it is the only dynamically meaningful quantity for driving the geostrophic component of ocean currents and adjusting subsurface thermohaline structures. The SST observations are the Advanced Very High Resolution Radiometer (AVHRR; Martin et al., 2012) product with a horizontal resolution of 0.01º. Observation errors are specified as 0.02 m for SSH and 0.3ºC for SST (Song et al. 2016a; Yu et al. 2018, 2019).

The surface chlorophyll is provided by the Ocean-Colour Climate Change Initiative project (OC-CCI; Sathyendranath et al., 2018) at a daily frequency with a spatial resolution of 1/24º. However, for the daily chlorophyll field, a large portion of data can be missing due to cloud cover and inter-orbit gaps. In 2015 for the Gulf of Mexico, the spatial coverage of surface chlorophyll varies from 0 to 63% with a mean coverage of 9.5±9.0%. Hence, to increase the availability of observations, an asynchronous data assimilation method (Sakov et al. 2010) is applied so that not only the daily records of surface chlorophyll at the date of update but also the daily records within the preceding 7 days are assimilated. Errors associated with the surface chlorophyll are set to be 35% of the measured concentrations, which has been commonly used in previous applications (e.g., Fontana et al., 2013; Ford, 2021; Ford and Barciela, 2017; Hu et al., 2012; Mattern et al., 2017; Santana-Falcón et al., 2020; Song et al., 2016b; Yu et al., 2018). In this chapter, the update is performed on actual chlorophyll concentrations because my prior tests showed that it outperforms assimilating log-chlorophyll in the open Gulf (with depth >1000 m). There are previous examples in which the actual chlorophyll values have been assimilated successfully (e.g., Hu et al., 2012; Yu et al., 2018) although I note that assimilating the actual chlorophyll values is theoretically suboptimal because of their non-Gaussian distribution.

Profiling observations are from the International Argo project (hereafter referred to as Argo floats) and five BGC-Argo floats, which were funded by the Bureau of Ocean Energy Management (hereafter referred to as BOEM floats). In 2015, the Argo floats provided nearly 800 T-S profiles extending from the surface to 2000 m depth in the Gulf of Mexico. These are treated either as independent observations for model skill assessment or, in the DAargo experiment (see Section 3.2.4), assimilated with uncertainties of $0.3^{o}C$ for temperature and 0.01 for salinity. The BOEM floats collected more than 500 profiles of temperature, salinity, chlorophyll, and backscatter at a biweekly frequency from 2011 to 2015, 114 of which were collected in 2015 (see Fig. 3.1 for their locations) and are used as independent observations. Backscatter is converted into phytoplankton and particulate organic carbon (POC) concentrations following Wang et al. (2020). In the absence of direct measurements for nitrate, I estimate it along the BOEM float trajectories based on their climatological relationship with temperature (Fig. C.1).

3.2.4 Simulation strategy

I performed five 1-year simulations in 2015. The first one is a deterministic model simulation without data assimilation (henceforth referred to as Free simulation). The second one is an ensemble run assimilating satellite data (SSH, SST, and satellite surface chlorophyll) only (henceforth DAsat), and the third one is an ensemble run assimilating Argo T-S profiles in addition to satellite data (henceforth DAargo). The calculations (Att $= 0.04+0.025\times$Chl) used in these three simulations are from literatures (e.g., Fennel et al., 2006, 2011); the light attenuation coefficient, Att, is strongly determined by water depth and not very sensitive to chlorophyll concentrations. The Free run and DAsat run are repeated by using an alternative light parametrization (henceforth referred to as Free-alt and DAsat-alt simulations, respectively) to evaluate its effect on the data-assimilation impact on subsurface biological properties. This alternative light parameterization (Att $= 0.027+0.075\times$Chl$^{1.2}$) is subjectively tuned based on the BGC-Argo observations and emphasizes the self-shading effect of chlorophyll on light attenuation.

A two-step update is used on a weekly data assimilation cycle in the assimilative experiments, in which the physical observations are first assimilated to update both physical and biological state variables through the multivariate covariance, and chlorophyll

observations are assimilated next to update only biological state variables. Although the DEnKF can update all state variables based on their cross-covariance, I limit updates to two physical variables (temperature and salinity) and four biological variables (nitrate, chlorophyll, phytoplankton, and zooplankton) that are key to the coupled physical-biogeochemical system. As the circulation features in the open Gulf (the Loop Current and its associated mesoscale eddies) are primarily in geostrophic balance, an update of temperature and salinity can improve three-dimensional circulation features in large scales effectively, as shown in the twin experiments in Yu et al. (2019). All these state variables are updated throughout the whole water column, while other variables are adjusted by internal model dynamics.

To evaluate the prediction skill, I calculate the root mean square error (RMSE), the bias, and the correlation coefficient (Corr) of the model forecast (M) with respect to assimilated and independent observations (O):

$$RMSE = \sqrt{\frac{1}{N}\sum(M-O)^2} \tag{3.4}$$

$$bias = \frac{1}{N}\sum(M-O) \tag{3.5}$$

where N represents the number of model-data pairs available. To account for the overestimation of nitrate in warm waters, which typically occurs in the euphotic zone (Fig. C.1), an unbiased root mean square error (unbiased RMSE) is used to quantify the model-data misfit of nitrate.

$$unbiased\ RMSE = \sqrt{\frac{1}{N}\sum(M-O-bias)^2} \tag{3.6}$$

3.3 Results

3.3.1 Assimilation impacts on physical properties

As the biological model provides no feedback to the physical model, the alternative light parameterization does not affect physical properties. The physical results from Free-alt and DAsat-alt runs are thus not displayed in this section.
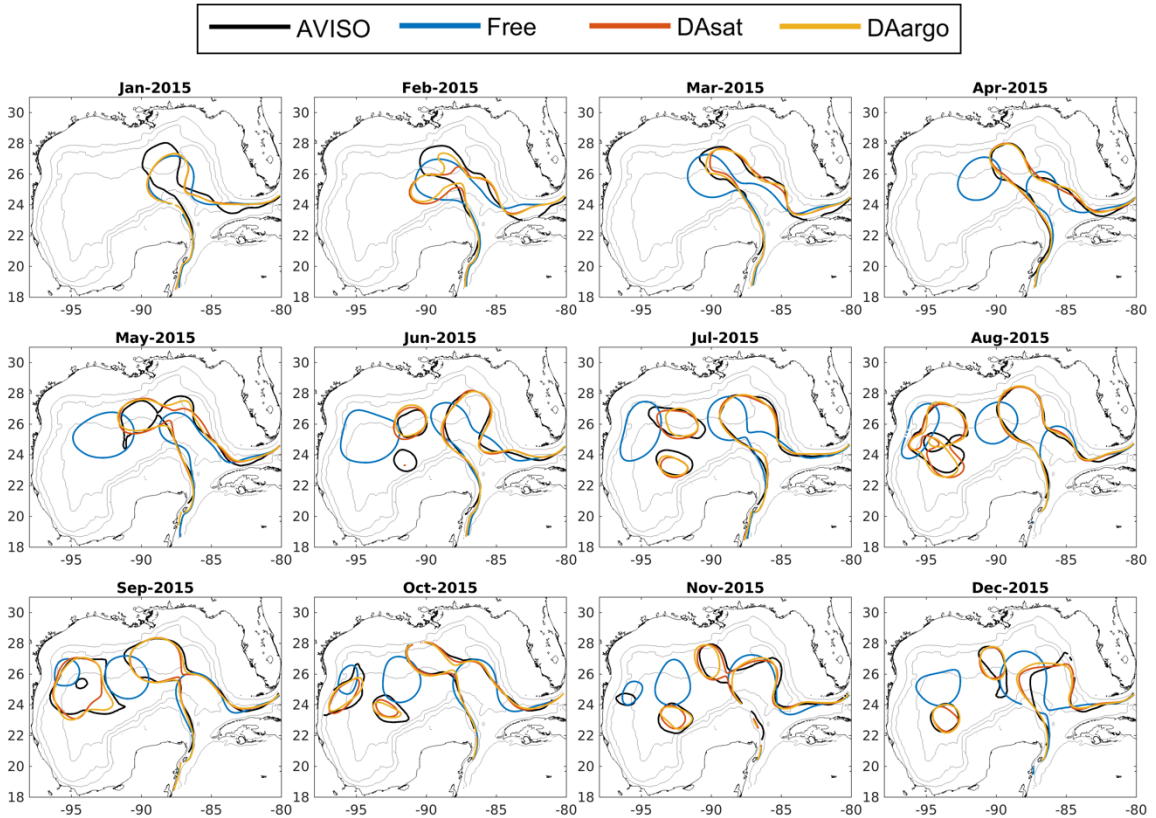
Figure 3.2. Monthly averaged Loop Current and Loop Current eddies based on the 10 cm SSH contour from satellite data (black), the Free run (blue), the DAsat run (orange), and the DAargo run (yellow). The gray contours represent the isobaths of 200, 1000, and 3000 m.

The dominant circulation features in the Gulf of Mexico, the Loop Current and Loop Current Eddies, are assessed by comparing their fronts, defined here as the 10-cm SSH contour, from satellite data, the Free run, and two data-assimilative runs (i.e., the DAsat and DAargo runs). In the first 2 months, all model estimates of the Loop Current are different from satellite observations due to the influence of initial conditions (Fig. 3.2).

After March, the SSH field shows a similar northward and westward extension of the Loop Current intrusion between two assimilative runs and satellite observations, but large deviations from observations remain in the Free run. In addition, all estimates except for the Free run reproduce the satellite-observed timing of eddy shedding well, as well as the size, shape, and position of Loop Current eddies.
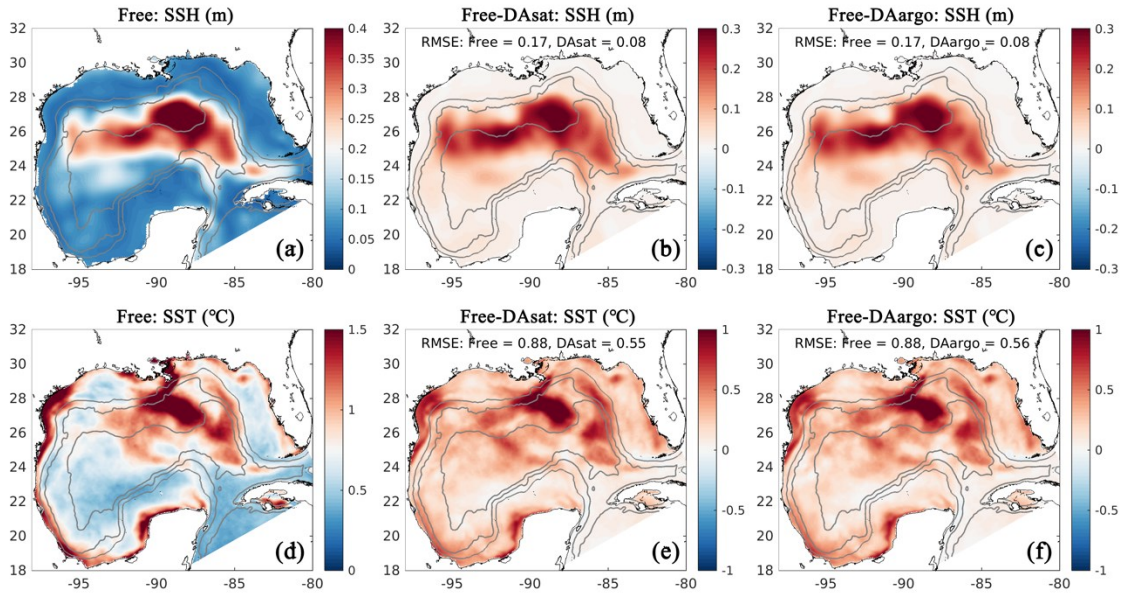
Figure 3.3. Spatial map of root mean square error (RMSE) in the Free run (a, d) and its differences between the Free run and the two data-assimilative runs for SSH and SST (b, c, e, f). Positive values represent improvements, while negative values represent deteriorations by data assimilation. Gray contours represent the 300, 1000, and 3000 m isobaths.

For a more quantitative assessment, the daily output of SSH and SST fields from the three runs is compared with the satellite estimates. The spatial distribution of RMSE from the Free run and the RMSE changes in two data-assimilative runs are shown in Fig. 3.3. In the regions influenced by the Loop Current and Loop Current eddies, this figure shows high RMSE for SSH in the Free run (Fig. 3.3a) and large RMSE reductions in two data-assimilative runs (Fig. 3.3b-c). In contrast, the reductions in SST RMSEs are more spatially homogeneous. A summary of the overall RMSE, the bias, and the correlation coefficient (Corr) for physical variables from the Free run and two data-assimilative runs are shown in Table 3.1. In general, the two data-assimilative runs both significantly improved SSH and SST with reduced RMSEs and increased correlation coefficients. Although the two

data-assimilative runs tend to underestimate the satellite observations of SST, the bias (-0.06 ℃) is relatively small.
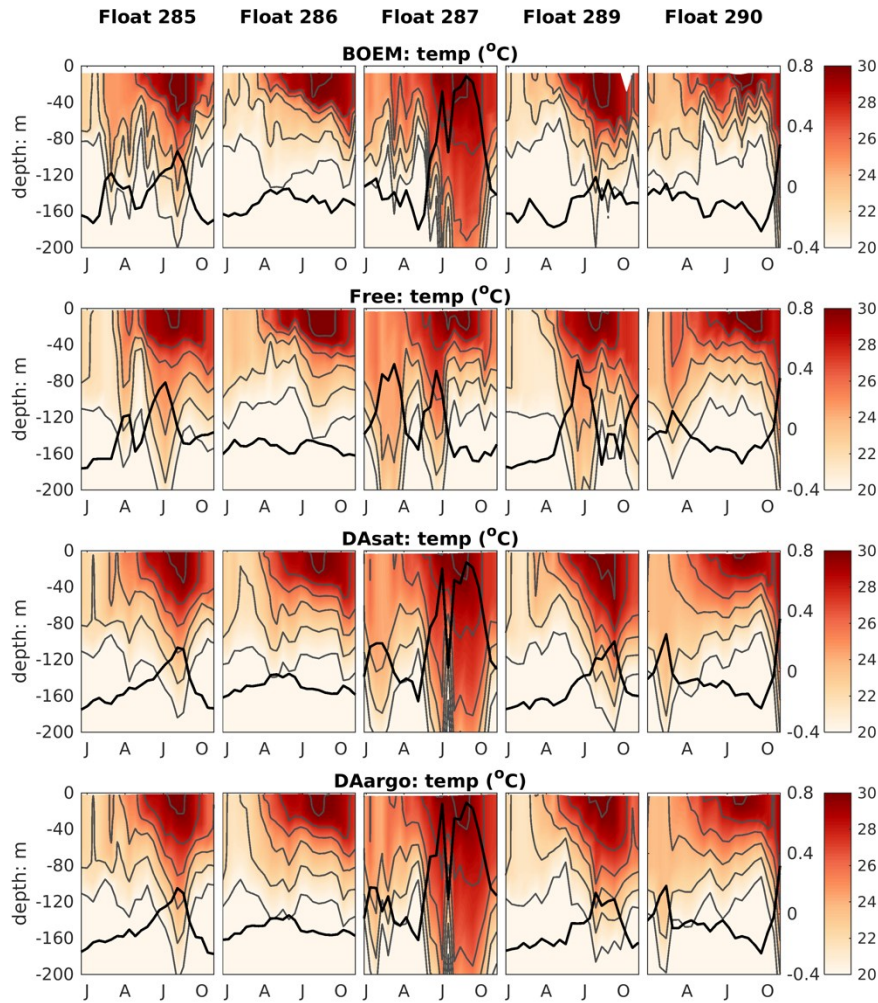
Figure 3.4. Vertical distributions of temperature from BOEM floats, the Free run, the DAsat run, and the DAargo run. Gray lines represent isothermal lines with an interval of 2 ℃. Thick black lines represent SSH. The observed SSH is obtained from the matching record of altimeter observations.

The correction of mesoscale features by data assimilation was not limited to the surface but extend to the subsurface and even deep waters. Specifically, the two assimilative runs corrected the position, the amplitude, and the polarity of mesoscale eddies and hence better represented the elevated and depressed thermoclines within these eddies (Fig. 3.4). The most noticeable improvement (by 60% - 61%) was witnessed by float 287, which captured a newly detached Loop Current eddy with features of high SSH and depressed thermoclines

during July and October. In addition, assimilation of Argo T-S profiles in the DAargo run led to slight further improvements in the subsurface temperature distributions when compared with the DAsat run. For instance, although the DAsat run greatly improved subsurface temperature distributions along the trajectory of float 285, an underestimation of temperature at a depth of about 200 m remains within the peak of the anticyclonic eddy. Corrections imposed by assimilating Argo profiles increased temperature here and decreased the bias from observations. These small but localized further improvements can also be observed by other floats, e.g., in July-October for float 289 and February for float 290.

Table 3.1. The root mean square error (RMSE), bias, and correlation coefficient (Corr) for SSH and SST, as well as vertical profiles of temperature and salinity from Argo and BOEM floats. Percentages in the parentheses represent the relative reductions in RMSE values. Since the spatial and temporal average of mismatch between the modelled and observed SSH is removed, the bias of SSH is not shown here.

	SSH (m)	SST (ºC)	Argo Temp (ºC)	salt	BOEM Temp (ºC)	salt
			RMSE			
Free	0.17	0.88	1.70	0.22	1.55	0.18
DAsat	0.08	0.55	0.89	0.14	0.83	0.11
	(54%)	(37%)	(48%)	(36%)	(46%)	(39%)
DAargo	0.08	0.56	0.86	0.13	0.79	0.10
	(54%)	(36%)	(49%)	(41%)	(49%)	(44%)
			Bias			
Free	--	0.00	0.07	0.02	0.26	0.03
DAsat	--	-0.06	0.12	0.02	0.24	0.02
DAargo	--	-0.06	0.06	0.02	0.21	0.02
			Corr			
Free	0.72	0.96	0.96	0.92	0.97	0.95
DAsat	0.94	0.98	0.99	0.97	0.99	0.98
DAargo	0.94	0.98	0.99	0.97	0.99	0.98

In general, assimilating the satellite data in the DAsat run resulted in large reductions in RMSEs of 3D temperature (by 46%-48%; Table 3.1) and salinity (by 36%-39%; Table 3.1) with respect to Argo floats and BOEM floats (Fig. 3.5). The reductions extend to over 1000 m and a depth of about 800 m for temperature and salinity, respectively. It should be noted again that data from both Argo and BOEM floats are independent in the DAsat run. Although assimilating the Argo profiles in the DAargo run only yields marginal further improvements in RMSEs of temperature (~ 3%) and salinity (~ 5%), it notably reduces the overestimation of temperature that occurs below the surface in the DAsat run (Table 3.1).
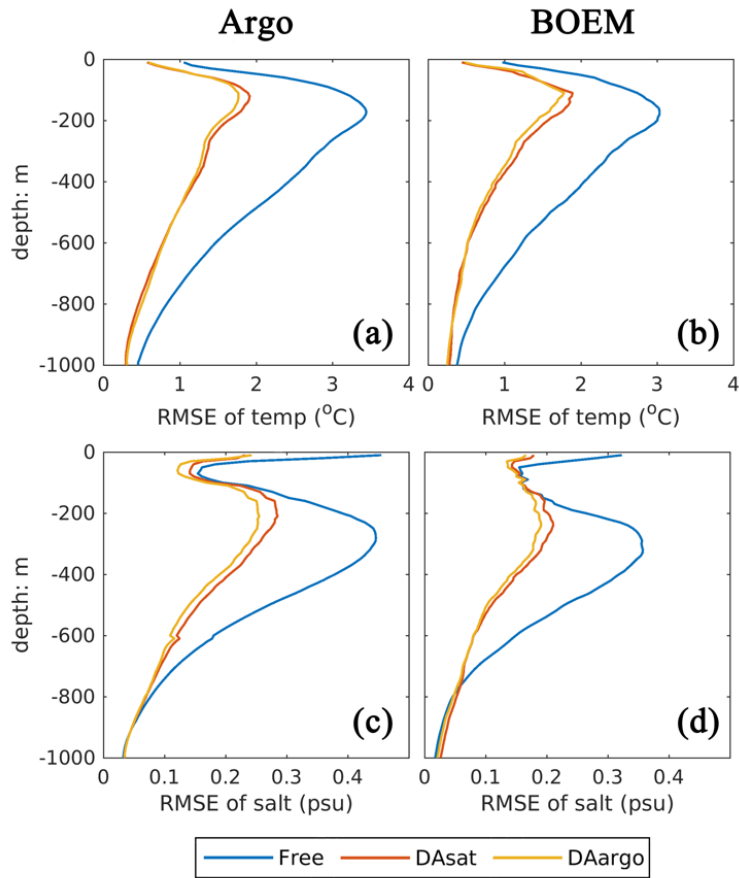
Figure 3.5. Vertical profiles of root mean square error (RMSE) for temperature and salinity with respect to Argo and BOEM floats.

3.3.2 Assimilation impacts on biological properties

Assimilating satellite observations in the DAsat run reduced RMSEs of surface chlorophyll almost everywhere, with only 3% of the model domain experiencing

degradation (Fig. 3.6b). Although large reductions in RMSE were achieved in the coastal regions, e.g., in the northern Gulf of Mexico, on Campeche Bank, and in Campeche Bay, the simulated chlorophyll concentrations remained much lower than the satellite estimates because of high observational uncertainties and a large background misfit in the Free run (Fig. 3.6a). This was expected because the biological model was optimized for the open Gulf (Wang et al. 2020). Table 3.2 shows the RMSE, the bias, and the correlation coefficient for biological variables from the Free run and the data assimilative runs. A relative reduction in RMSE equal to or exceeding 10% is considered as a significant improvement. In the open Gulf, encompassed by the 1000 m isobath, the overall RMSE of surface chlorophyll was reduced by 19% from 0.13 mg m^{-3} in the Free run to 0.11 mg m^{-3} in the DAsat run (Table 3.2). In addition, the correlation coefficient increased from 0.52 to 0.68. Assimilating Argo T-S profiles in the DAargo run led to lower reductions in the overall RMSEs of surface chlorophyll (Table 3.2) and even more deteriorations (Fig. 3.6c).
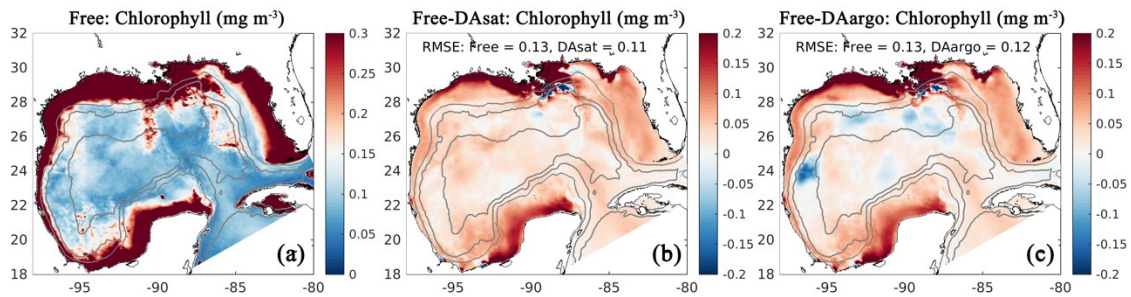
Figure 3.6. The same as Fig. 3.3 except for surface chlorophyll.

To evaluate the impacts of data assimilation on subsurface biological properties, the temporal evolution of nitrate in different model experiments is shown in Fig. 3.7 in comparison to nitrate estimated based on its climatological relationship with temperature. The temperature-based nitrate tends to be overestimated in the upper layers (Fig. C.1). Because of its high correlation with temperature, the nitrate distribution was modulated in the two assimilative runs along with the improvement in temperature fields. For instance, the two assimilative runs reproduce the Loop Current eddy observed by float 287 and hence capture the depressed thermoclines that are not present in the Free run (Fig. 3.4). At the same time, the nitraclines are also depressed and the nitrate concentrations become lower within this Loop Current eddy (Fig. 3.7). As a result, the unbiased RMSE of nitrate

following this float is reduced by 40% in the DAsat run and 38% in the DAargo run. These depressed (upwelled) nitraclines due to the increase (decrease) in SSH by data assimilation can also be observed elsewhere, e.g., in August for float 285, in April-July for float 286, January-April for float 287, and in August-October for float 290, although the amplitude of these mesoscale eddies is smaller. In general, data assimilation improved the overall agreement of subsurface nitrate with correlation coefficients and decreased RMSEs by 28% and 30% in the DAsat and DAargo runs relative to the Free run (Table 3.2).
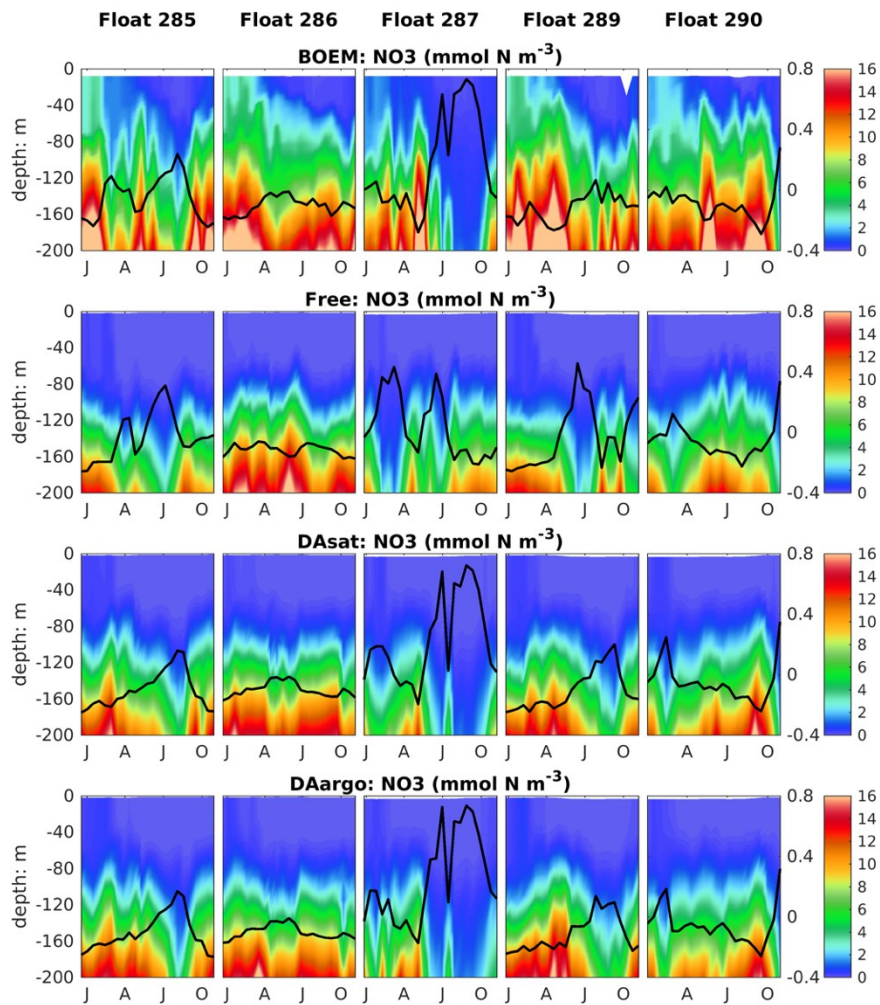
Figure 3.7. Vertical distributions of nitrate, which are estimated based on its climatological relationship with temperature and modeled by different experiments, superimposed with the SSH (thick black lines).

Table 3.2. The root mean square error (RMSE), bias, and correlation coefficient (Corr) for surface chlorophyll in the open gulf, along with vertical profiles of NO_3, chlorophyll, phytoplankton, and POC, as well as the depth of the deep chlorophyll maximum with respect to observations from BOEM floats. Percentages in the parentheses represent the relative reductions in RMSE values. Only a reduction in RMSE larger than or equal to 10% is considered a significant improvement. The NO_3 is estimated based on its climatological relationship with temperature. Since the estimated NO_3 tends to be overestimated in warm regions, the unbiased RMSE of NO_3 is reported and the bias is not shown here.

	SChl	NO_3	Chl	Phy	POC	DCM depth
	(mg m^{-3})	(mmol N m^{-3})	(mg m^{-3})	(mmol N m^{-3})	(mg C m^{-3})	(m)
RMSE						
Free	0.13	3.71	0.18	0.11	18.62	25.48
DAsat	0.11	2.66	0.17	0.10	16.46	21.08
	(19%)	(28%)	(6%)	(9%)	(12%)	(18%)
DAargo	0.12	2.58	0.17	0.10	16.77	22.39
	(9%)	(30%)	(6%)	(9%)	(10%)	(12%)
Free_alt	0.17	3.71	0.18	0.11	17.55	24.35
DAsat_alt	0.13	2.63	0.17	0.10	15.53	20.42
	(26%)	(29%)	(6%)	(9%)	(12%)	(16%)
Bias						
Free	-0.01	--	-0.04	-0.02	-8.01	-0.98
DAsat	0.02	--	-0.04	-0.01	-5.05	0.45
DAargo	0.03	--	-0.02	-0.01	-3.84	2.59
Free_alt	0.00	--	-0.04	-0.02	-6.57	-1.09
DAsat_alt	0.03	--	-0.03	-0.00	-3.15	1.83
Corr						
Free	0.52	0.94	0.73	0.72	0.63	0.25
DAsat	0.68	0.97	0.76	0.75	0.71	0.50
DAargo	0.65	0.97	0.74	0.75	0.70	0.45
Free_alt	0.58	0.94	0.73	0.72	0.64	0.43
DAsat_alt	0.70	0.97	0.76	0.75	0.72	0.58
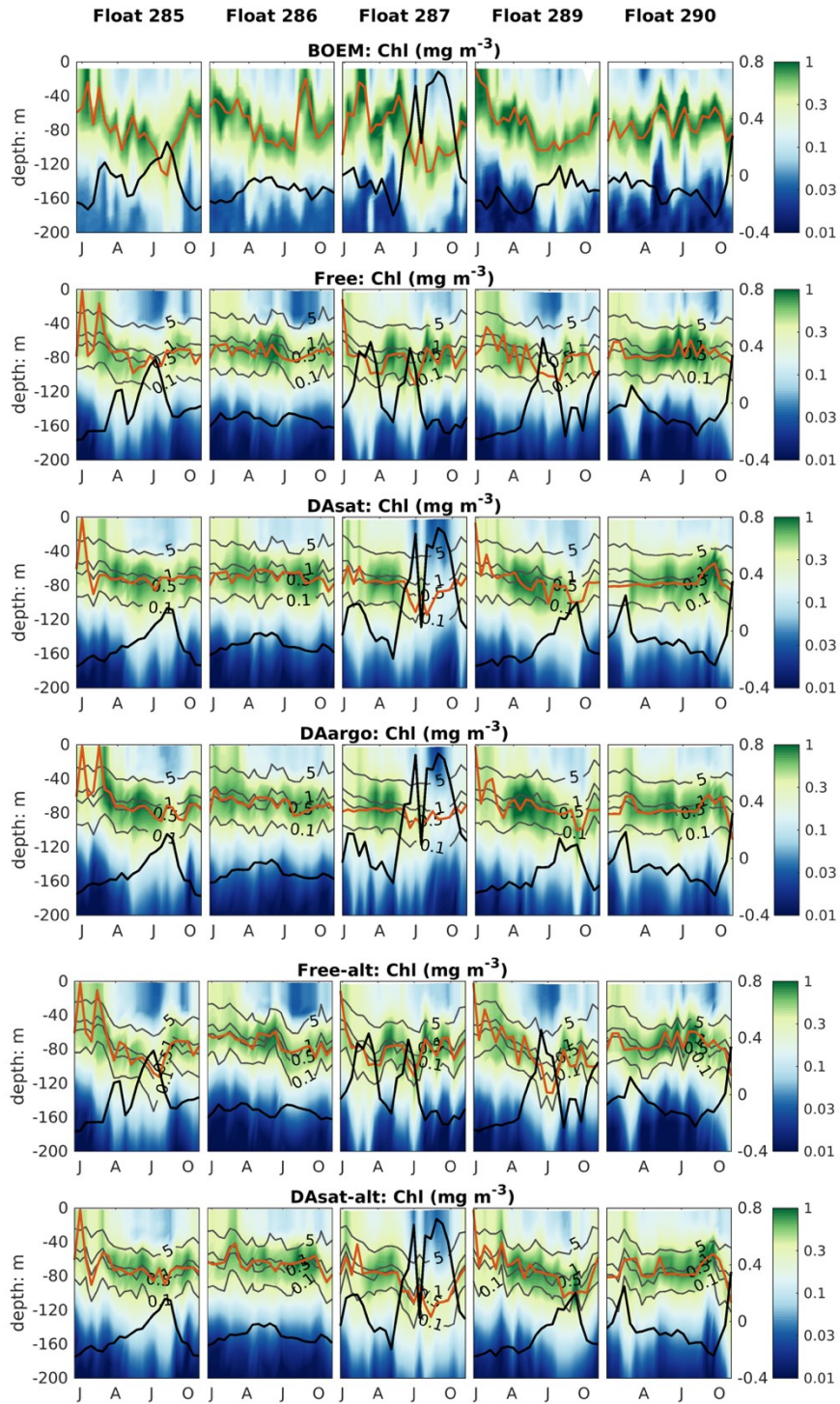
Figure 3.8. Same as Fig. 3.4 but for chlorophyll. Gray contours represent the simulated isolumes, and red lines represent the depth of the deep chlorophyll maximum. Thick black lines represent SSH.

The impacts of assimilation on subsurface chlorophyll are more complicated because of the high nonlinearity of the model with regard to chlorophyll. Although the mean vertical profiles of chlorophyll are well reproduced in all three experiments (Fig. C.2), all failed to resolve the high spatiotemporal variability in subsurface chlorophyll, which is at least partly due to the presence of mesoscale eddies (Fig. 3.8). As a result, assimilation improved subsurface chlorophyll RMSEs marginally, even in the Loop Current eddy for float 287 for which the most noticeable improvements of temperature (~ 60%) and nitrate (~ 40%) RMSEs were obtained. Results for phytoplankton and POC are similar to chlorophyll, although the reductions in their RMSEs are larger because assimilating the satellite data reduces their biases, especially in the upper layer (Fig. C.2, Table 3.2).

The model's inability to reproduce the spatiotemporal variability of subsurface chlorophyll is also reflected by the positions of the deep chlorophyll maximum (DCM, denoted by red lines in Fig. 3.8). As a ubiquitous phenomenon in the oligotrophic regions, a distinct DCM is observed throughout the whole year in the open Gulf of Mexico, and its depth is inversely correlated with SSH (correlation coefficient = -0.6). Although the mean position and magnitude of the DCM are well reproduced by the model with and without data assimilation (Fig. C.2), the simulated DCM depth is much more stable and less sensitive to SSH variations. As a result, the reduction in the RMSE of DCM depth is limited to 18% in DAsat run but is significant (Table 3.2).

3.3.3   Sensitivity of subsurface chlorophyll to the light parameterization

Both with and without data assimilation, the alternative parameterization led to higher correlations between simulated SSH and DCM depth with correlation coefficient of -0.60 in Free-alt run and -0.67 in DAsat-alt run. As a result, the alternative parameterization produces slightly lower RMSEs and a higher correlation coefficient for DCM depth (Table 3.2) and yields larger improvements in chlorophyll within the Loop Current eddy of float 287 (Fig. 3.8). To illustrate the underlying reasons, the mean vertical profiles of nitrate, the intensity of photosynthetically active radiation (PAR), the chlorophyll, and the phytoplankton within the center of this Loop Current eddy are shown in Fig. 3.9. When using the original parameterization, assimilating the satellite data depresses the DCM depth from 70 m in the Free run to 90 m in the DAsat run but with a considerable bias of 20 m

when compared to the observations. However, the chlorophyll is underestimated in the DAsat run, and as a result its RMSEs are barely improved. In contrast, in the DAsat-alt run the DCM depth is corrected to 120 m, in agreement with the observations, and represents the vertical chlorophyll distribution more accurately, although the nitrate profile is almost the same as in DAsat run. This was because the alternative parameterization accounted for the elevated PAR intensity as a response to reduced chlorophyll concentrations in the upper layer, which in turn facilitated the synthesis of chlorophyll and hence corrected their concentrations toward the observations
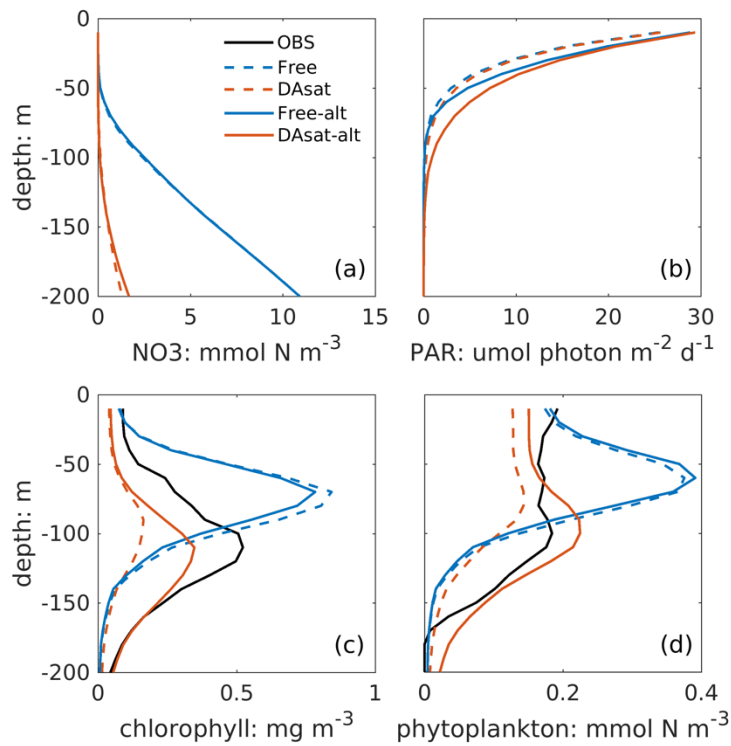
Figure 3.9. Mean vertical profiles of nitrate, light intensity (photosynthetically active radiation, PAR), chlorophyll, and phytoplankton within the center of the newly detached Loop Current eddy from the Free run, the DAsat run, the Free-alt run, and the DAsat-alt run.

3.4 Discussion

I implemented a coupled data assimilation scheme for jointly assimilating physical and biological observations in a biogeochemical model and evaluated to what degree satellite observations can inform subsurface distributions, especially of biological properties. The

degree to which the data assimilation impact can depend on model calibration was tested by using an alternative light parametrization. Although biological data assimilation has received much attention in recent years, observations that are assimilated and used in skill assessment are typically limited to the surface ocean. The increasing availability of BGC-Argo data now makes it possible to validate and improve model performance below the surface (Cossarini et al. 2019; Salon et al. 2019; Terzić et al. 2019; Wang et al. 2020) but so far these observations have been too sparse for sequential assimilation in three dimensions; hence, relevant applications are limited to idealized twin experiments (Yu et al. 2018; Ford 2021) and a few specific regions with high float densities, e.g., the Mediterranean Sea (Cossarini et al. 2019). In addition, since a biogeochemical model is coupled to a physical model, assimilating physical observations theoretically should confer improvements on the biological model by correcting the circulation (e.g., Fiechter et al., 2011; Raghukumar et al., 2015; Song et al., 2016b, 2016a) and potentially by providing additional constraints via multivariate updates to biological variables (e.g., Goodliff et al., 2019; Yu et al., 2018). This is particularly important when the physical model is biased (Yu et al. 2018).

This chapter shows that assimilating satellite data (DAsat run) can constrain the main circulation features in the Gulf of Mexico, i.e., the Loop Current and its associated mesoscale eddies. Temperature and salinity are also improved down to a depth of ~1000 m because of the correction of mesoscale eddies. When calculating the reductions in RMSE for SSH and each single profile of temperature and salinity, I find that the improvement in SSH is highly correlated with those in temperature (correlation coefficient = 0.96) and salinity (correlation coefficient = 0.92, Fig. C.3). Assimilating the satellite data also improves subsurface nitrate because it is tightly correlated with the density structure expressed by SSH and temperature profiles. However, improvements in temperature and nitrate do not necessarily yield better simulations of chlorophyll or phytoplankton because they tend to be light-limited below the surface. In this biogeochemical model, the light intensity is attenuated by water and chlorophyll and is not directly updated by the data assimilation scheme but only adjusted indirectly through changes in chlorophyll during forecast steps. This, in turn, impacts the synthesis of chlorophyll and growth of phytoplankton. However, in the original parameterization, light attenuation is mainly

controlled by water depth and much less sensitive to chlorophyll concentrations than it appears to be in reality. By applying an alternative light parameterization with more pronounced self-shading by chlorophyll, the subsurface chlorophyll and phytoplankton distributions are further improved after assimilating the satellite data. These results show that the biological variables can be improved through model dynamical response to data assimilation. However, the efficiency of this mechanism depends on the accuracy of the biological model. That is why data assimilation generally benefits from a well-calibrated model. For example, the usage of suboptimal biological parameters can yield a substantial degradation of data assimilation efficiency, especially with respect to unobserved variables (Song et al. 2016b). Although BGC-Argo profiles have so far been insufficient for sequential assimilation, they can provide substantial benefits for biogeochemical prediction by enabling a priori model tuning, e.g., of biological parameter values (Wang et al. 2020) and the key parameterization schemes (Terzić et al. 2019).

In addition to the model's dynamical response, the biological fields can be directly updated by physical and biological observations through multivariate covariances. To distinguish their influence, I show the increments obtained from assimilating each observation type in the DAsat run (Fig. 3.10). The increment of DCM depth is defined analogously to other state variables as changes due to the update. As shown in Fig. 3.10a, b, assimilating physical observations has a much stronger impact than biological observations on nitrate, and therefore I conclude that the improvement of nitrate in this chapter is mainly obtained from assimilating physical observations. This is consistent with previous studies (e.g., Ciavatta et al., 2018; Skákala et al., 2018; Teruzzi et al., 2018) wherein assimilating surface chlorophyll had little impact on nitrate and even degraded it in both variational and sequential data assimilation. In variational data assimilation, it is hard to define the background errors accurately (Mattern et al. 2017; Teruzzi et al. 2018) and the biological model can fit itself to observed chlorophyll through many different pathways, e.g., direct changes of biomass or an indirect way through nitrate. However, observations are often insufficient to provide this information (Mattern et al. 2017). In sequential data assimilation, the multivariate covariance between surface chlorophyll and subsurface nitrate can be considered, but typically this covariance is not linear or constant. For instance, Fontana et al. (2013) assimilated satellite surface chlorophyll into a biological

model in the North Atlantic and found that subsurface nitrate was barely influenced because it was weakly correlated with surface chlorophyll, leading the authors to suggest that it is impossible to fully constrain a 3D biogeochemical model by only assimilating the surface chlorophyll. This issue remains when assimilating the surface chlorophyll to update other biological variables (Yu et al. 2018), e.g. phytoplankton functional groups (Ciavatta et al. 2018).
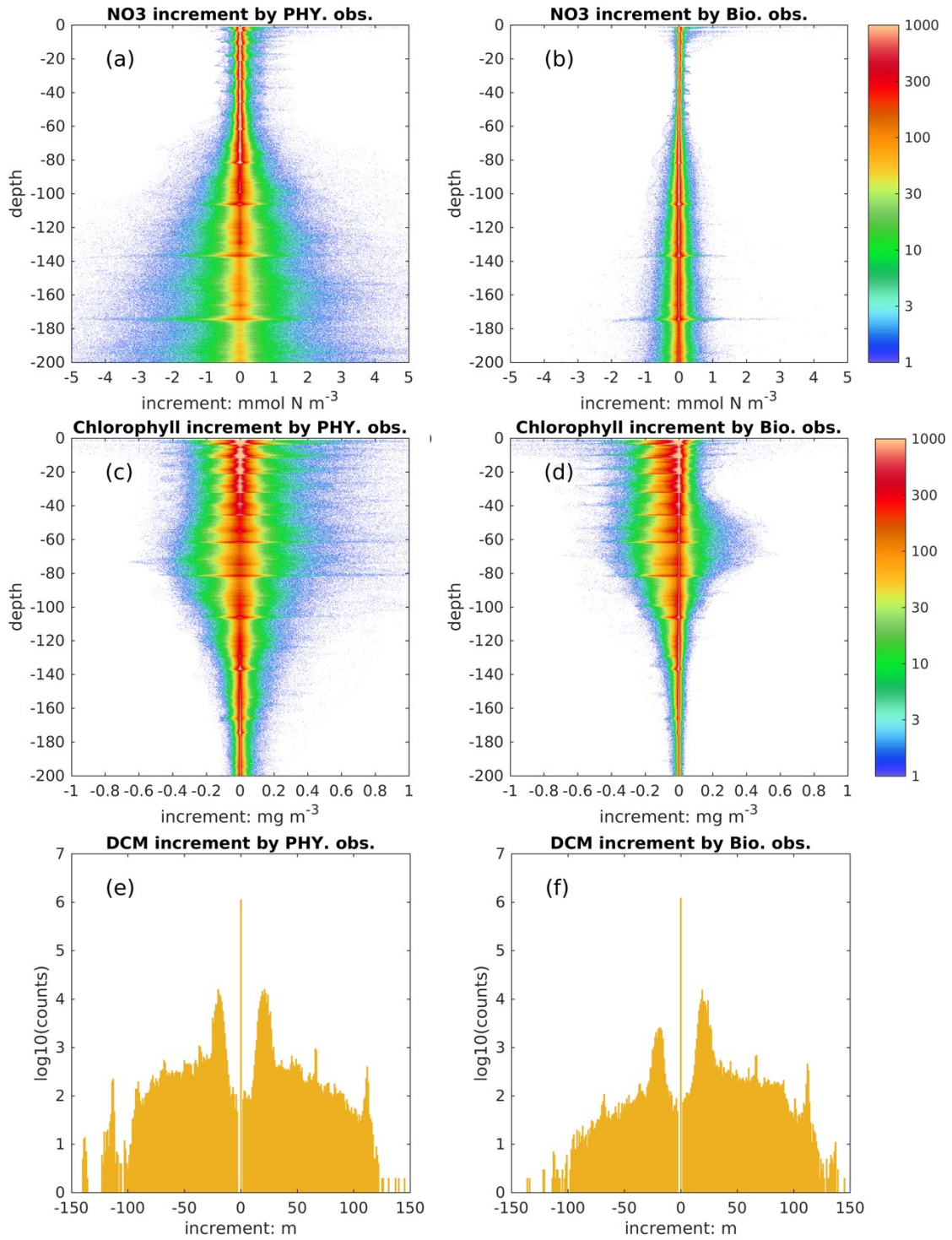
Figure 3.10. Histogram of increments in nitrate (mmol N m^{-3}), chlorophyll (mg m^{-3}), and DCM depth (m) obtained by assimilating physical and biological observations.

In contrast to nitrate, assimilating satellite data from physical and biological observations has a comparable influence on subsurface chlorophyll (Fig. 3.10c-f). Specifically, they can change subsurface chlorophyll concentrations even below a depth of 100 m and vertical structures of chlorophyll by adjusting the DCM depth; e.g., there are 10% and 5% of profiles with changes in DCM depth exceeding ±20 m due to the update of physical and biological observations, respectively. Because BGC-Argo profiles are currently sparse, i.e., only 14 profiles are available at all update steps, it is hard to draw definitive conclusions about these impacts on chlorophyll and DCM depth.

Assimilating Argo T-S profiles in the DAargo run yields slightly further improvements with respect to independent profiles of temperature and salinity, similar to the twin experiments in Yu et al. (2019). To diagnose it, I calculate the root mean square difference (RMSD) of temperature between two data-assimilative runs with respect to each profile from the BOEM floats. In general, the RMSD between two data-assimilative runs decreases with distance to the nearest Argo profiles that have been assimilated recently but shows no significant decreasing trends with the days after update (Fig. C.4). This means that the differences induced by assimilating Argo profiles are sustained locally by model dynamical adjustments. The overall similarities between two data-assimilative runs (i.e., DAsat and DAargo runs) in Fig. 3.4 can be explained to some extent by the large distances between BOEM and Argo profiles. However, it does not mean that increasing the localization radius can necessarily improve the data assimilation performance. I note that the current localization radius was determined in Yu et al. (2019). The additional benefits in physical properties obtained by assimilating Argo T-S profiles are also translated into the simulation of subsurface nitrate but not into other biological fields, i.e., chlorophyll, phytoplankton, and POC. Moreover, assimilating the Argo T-S profiles can even degrade surface chlorophyll because of spurious correlations. This issue has also been reported in a recent study (Goodliff et al. 2019) that assimilated sea surface temperature to update both physical and biological variables, and this issue was alleviated by muting the multivariate update of phytoplankton, zooplankton, and detritus.

In general, coupled data assimilation of both physical and biological satellite observations can improve subsurface biological properties because it benefits from the high

correlations of some biological distributions, especially nutrients, with the vertical density structure and because of the dynamical responses to improvements in circulation in the forecast step. However, this is preconditioned on the coupled model being well calibrated *a priori*. Therefore, this chapter provides an intermediate step toward 3D updates of biological properties before the BGC-Argo profiles ultimately become more abundant.

3.5 Conclusions

In this chapter, a coupled data assimilation scheme for both physical and biological satellite observations was implemented to investigate whether these observations can inform subsurface distributions. In addition, Argo T-S profiles were assimilated to assess their impact beyond satellite observations. The multivariate update was applied by using the covariance structure between physical and biological variables. The Gulf of Mexico was selected as the study region because the dominant physical features, the Loop Current and its associated mesoscale eddies, are stochastic and can substantially influence the biological properties in three dimensions. Results show that assimilating satellite data leads to significant improvements in the simulation of SSH and SST and also projects these improvements from the surface to a depth of about 1000 m for temperature and salinity, as shown by an assessment of the independent BGC-Argo profiles. With respect to biological fields, the subsurface nitrate distribution benefits greatly from the tight correlation with density and the improved fidelity of mesoscale features. However, initially there were only slight improvements in other biological variables below the surface, i.e., chlorophyll, phytoplankton, and POC, because a suboptimal light parameterization did not react to the changed chlorophyll concentrations appropriately and failed to provide accurate feedbacks on the synthesis of chlorophyll and growth of phytoplankton. I tested an alternative light parameterization with a larger relative contribution from chlorophyll to light attenuation. As a result, the subsurface chlorophyll and phytoplankton were further improved. This highlights the importance of a priori tuning to achieve better assimilation performance. Finally, assimilating the Argo T-S profiles on top of satellite observations yields slight further improvements with respect to independent vertical profiles of temperature and salinity, which also translated into improvements in subsurface nitrate.

CHAPTER 4

AN ASSESSMENT OF VERTICAL CARBON FLUX PARAMETERIZATIONS USING BACKSCATTER DATA FROM BGC ARGO

4.1 Introduction

The ocean's biological carbon pump (BCP) is a collection of processes that create organic carbon in the surface ocean and transport a fraction from the surface to the deep ocean thus sequestering carbon. Respiration of this organic matter during its vertical transport affects the distribution of biogeochemical properties such as nutrients, oxygen, and dissolved inorganic carbon (Howard et al. 2006; Kwon et al. 2009; Niemeyer et al. 2019). Although only a relatively small fraction of the organic carbon produced at the surface is sequestered deeper than 1000 m for centuries to millennia, variations in biological carbon sequestration can significantly influence atmospheric CO_2 levels and thus climate (Kwon et al. 2009; Gloege et al. 2017).

Despite its significance, the BCP remains poorly characterized in that current estimates of its magnitude vary greatly (Henson et al. 2011, 2012, 2015; Siegel et al. 2014; DeVries and Weber 2017; Bisson et al. 2020) and its future projections are highly uncertain (Laufkötter et al. 2016; Henson et al. 2022). While Earth System Models (ESMs) are considered as the best tools for predicting the future response of the BCP to climate change, their utility critically depends on their ability to make skillful predictions. To date, model parameterizations of vertical carbon flux remain poorly constrained by observations. For example, previous studies have shown that the sparse in-situ observations of particulate organic carbon (POC) flux and climatological datasets of nutrients and dissolved oxygen are insufficient for distinguishing between vertical flux models that yield vastly different

atmospheric CO_2 levels but fit the observations equally well within their range of uncertainty (Cael and Bisson 2018; Lauderdale and Cael 2021).

Respiration of organic carbon during its vertical transport is often described by the Martin curve, which is a power law equation fitted to in-situ measurements of POC flux from sediment traps (Martin et al. 1987). In this empirical parameterization, the remineralization length scale, defined as the distance over which the vertical carbon flux declines by a factor of $1/e$ (about 63%), is increasing with depth. This implies that either the remineralization rate is getting slower ($r \propto 1/z$) or the sinking velocity is getting faster with depth ($w \propto z$) or a combination of both. One mechanistic interpretation of this behavior is that organic carbon is a complex mixture of compounds with different liabilities and sinking velocities. Since labile and/or slow-sinking particles are more likely to be respired at a shallower depth, their relative contributions will decline with depth and the bulk remineralization rate (sinking velocity) will decrease (increase) with depth.

To reproduce the increase in remineralization length scale, different mechanisms and parameterizations have been proposed from these two perspectives and been incorporated into biogeochemical models. The ballast hypothesis, proposed by Armstrong et al. (2001) based on observed correlations between the deep flux of POC and minerals (e.g. $CaCO_3$, opal, and dust), assumes that these minerals facilitate the vertical transport of POC by protecting it from remineralization and/or increasing the sinking velocity because of their higher density. The ballast hypothesis has been widely implemented in biogeochemical models (e.g. Gehlen et al. 2006; Yool et al. 2011; Stock et al. 2020; Long et al. 2021). In contrast, the remineralization rate and sinking velocity are simulated prognostically in some biogeochemical models by incorporating a continuous spectrum of reactivity and particle size that reproduces the evolution of POC composition over depth (e.g., Aumont et al. 2015, 2017; Tjiputra et al. 2020). In a more simplified version, the sinking velocity is parameterized to increase linearly with depth to account for the preferential respiration of slow-sinking particles implicitly (e.g. Aumont et al. 2015; Tjiputra et al. 2020).

The choice between the different sinking schemes has a big influence on projected future changes in carbon sequestration. The BCP is expected to decrease in ESMs because they project a declining trend in globally integrated biological carbon export out of the

euphotic zone over the 21st century (Laufkötter et al. 2016; Henson et al. 2022). However, in addition to changes in carbon export out of the euphotic zone, respiration in the mesopelagic (200-1000 m) and bathypelagic zones (> 1000 m) exerts a strong influence on carbon sequestration. The lysocline is expected to become shallower because of rising atmospheric CO_2 levels. Then dissolution of $CaCO_3$ will occur at shallower depths reducing the protection of POC flux from minerals. In a model that parameterizes sinking according to the ballast hypothesis, the shallowing of the lysocline will amplify any productivity-related decreases in carbon sequestration while in models that do not consider ballast effects it will not (Henson et al. 2012).

BGC Argo measures backscatter, a proxy of POC concentration, in high spatial and temporal resolution from the sub-mesoscale to the global scale (Roemmich et al. 2019; Chai et al. 2020). POC concentration is dynamically related to POC flux and an important complement to currently available observations. Over the last decade, BGC-Argo floats have provided hundreds of thousands of backscatter profiles in top 2000 m of the global ocean. These observations have been used to derive POC fluxes (Briggs et al. 2011; Dall'Olmo and Mork 2014) and associated processes such as the fragmentation rate and sinking velocity (Briggs et al. 2020; Wang and Fennel 2022). However, backscatter as a proxy of POC concentration has received less attention as a means of calibrating biogeochemical models aside from a few examples (e.g., Bagniewski et al. 2011; Wang et al. 2020; Galí et al. 2022).

Here I evaluate to what extent BGC-Argo data can help in calibrating biogeochemical models that aim to study the BCP. For this purpose, I first provide a classification of different ESMs that are part of the sixth phase of the Coupled Model Intercomparison Project (CMIP6) with regard to the vertical flux parameterizations employed and compare their simulated POC flux. Depth-resolved POC flux is made available for the first time in CMIP6. To isolate the model-to-model differences in vertical carbon flux that are due to the choice of vertical flux parameterization from differences due to other sources for discrepancies, e.g., model resolution, surface ocean biogeochemical representation, degree of parameter tuning to the observations, and definitions of POC, I implement the two most widely accepted sinking schemes for vertical carbon flux in an otherwise identical model

environment. The two parameterizations are the ballast scheme and the scheme with a linear increase in sinking velocity, which is referred to as WLin hereafter. Both are implemented in a suite of float-following 1D models that represent the conditions encountered by individual BGC-Argo floats in the northern North Atlantic Ocean. Both schemes have been widely used in large-scale biogeochemical models and reproduce the increase of remineralization length scale, one by decreasing remineralization rate with depth and the other by increasing sinking velocity. Model results from the two sinking schemes are then compared to assess whether measurements of POC concentration can help in distinguishing between the different parameterizations. Sensitivity experiments are then conducted to investigate whether knowledge of POC concentration can constrain the remineralization rate and sinking velocity independently, provided that the appropriate model parameterization scheme is known. Results show that the observations of POC concentration hold great value in complementing existing sparse observations of POC flux as they can inform on the appropriate parameterization scheme and constrain the related parameters, i.e., the remineralization rate and sinking velocity.

4.2 Comparisons between Earth System Models

4.2.1   Description of sinking parameterizations in Earth System Models

In this chapter, 12 ESMs from CMIP6 are used (Table 4.1). Monthly outputs in the northern North Atlantic (Fig. 4.1) from the historical simulations were averaged over 15 years (2000-2014) to produce monthly and annual climatologies. Only one ensemble member (r1i1p1f1) is used for each model. To facilitate comparisons between models, the model outputs were remapped onto a common 1°×1° regular grid.

In-situ observations of POC flux were compiled by (Mouw et al. 2016). In the study domain (Fig. 4.1), most of the available in-situ observations (~90%) were collected by sediment traps deployed for less than 30 days while the remaining measurements were conducted over years. These short- and long-deployment measurements are compared to the monthly and annual climatologies of POC fluxes in the nearest model grid cell of each ESMs. The model performance is assessed by three statistical metrics including the correlation coefficient (Corr), the bias, and the root-mean-square-errors (RMSE).
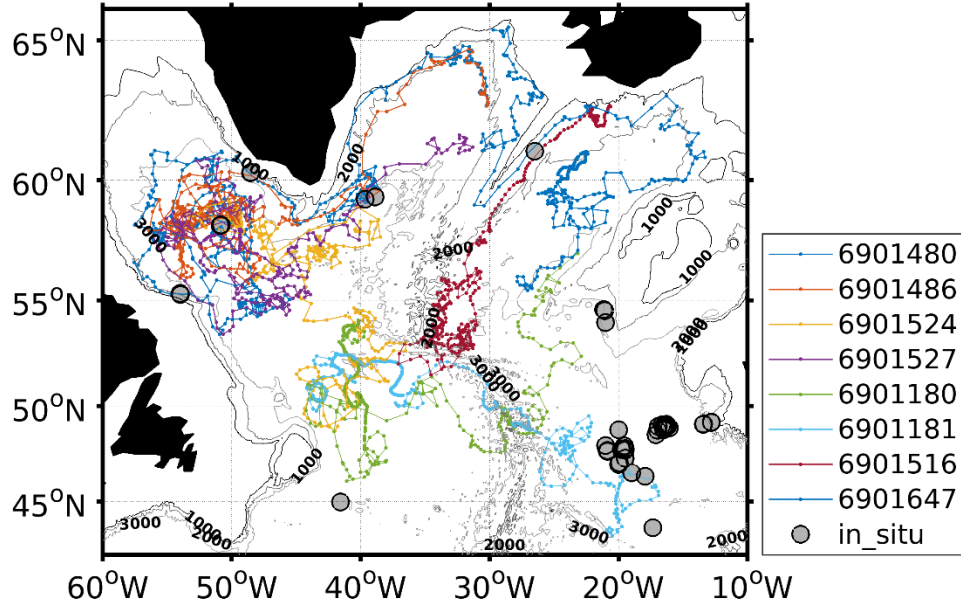
Figure 4.1. A bathymetric map of the northern North Atlantic superimposed with the in-situ observations of POC flux from sediment traps and ^{234}Th observations (denoted as gray circles) and trajectories of BGC-Argo floats (small colored dots).

Table 4.1. List of 12 ESMs used. Acronyms: National Center for Atmospheric Research, USA (NCAR), NOAA Geophysical Fluid Dynamics Laboratory, USA (GFDL), Institut Pierre Simon Laplace, France (IPSL), Max Planck Institute for Meteorology, Germany (MPI-M)

Institute	Model name	Ocean BGC model	Model Grid
NCAR	CESM2	MARBL	320×384×60
NCAR	CESM2-FV2	MARBL	320×384×60
NCAR	CESM2-WACCM	MARBL	320×384×60
NCAR	CESM2-WACCM-FV2	MARBL	320×384×60
GFDL	GFDL-CM4	BLINGv2	1440×1080×75
GFDL	GFDL-ESM4	COBALTv2	720×576×75
IPSL	IPSL-CM5A2-INCA	PISCESv2	182×149×31
IPSL	IPSL-CM6A-LR	PISCESv2	362×332×75
IPSL	IPSL-CM6A-LR-INCA	PISCESv2	362×332×75
HAMMOZ-Consortium	MPI-ESM-1-2-HAM	HAMOCC6	256×220×40
MPI-M	MPI-ESM1-2-HR	HAMOCC6	802×404×40
MPI-M	MPI-ESM1-2-LR	HAMOCC6	256×220×40
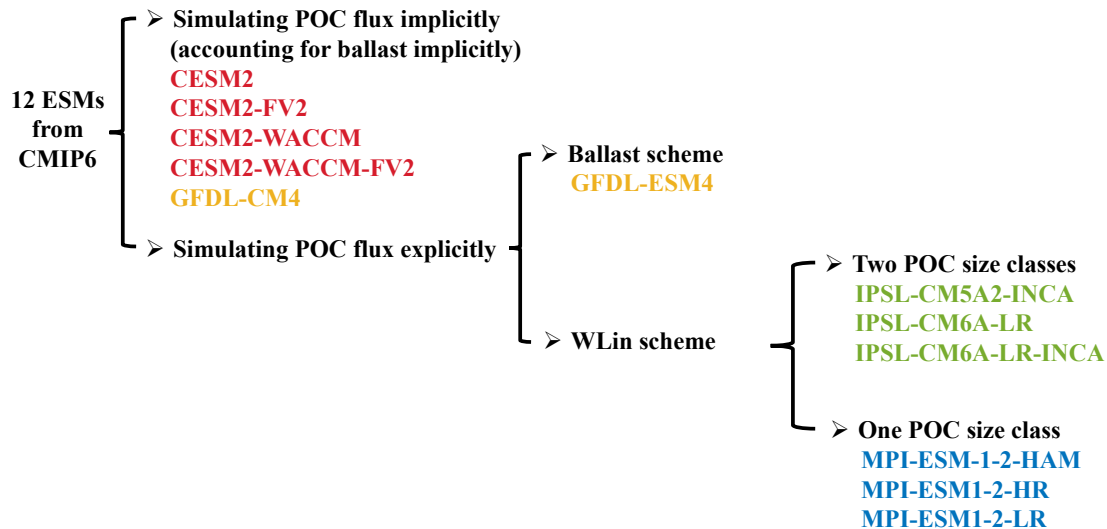
Figure 4.2. Classification of the vertical carbon flux schemes in the 12 CMIP6 ESMs considered in this chapter. Model acronyms are in the same color as used in Fig. 4.3.

The ocean biogeochemical components of these ESMs vary a lot with different degrees of complexity in representing processes in the euphotic zone as well as the subsequent remineralization and gravitational sinking of organic particles after escaping the euphotic zone (Fig. 4.2). Five out of the 12 ESMs (CESM2, CESM2-FV2, CESM2-WACCM, CESM2-WACCM-FV2, and GFDL-CM4) use the biogeochemical models MARBL (Long et al. 2021) or BLINGv2 (Dunne et al. 2020) and simulate the POC flux implicitly. This means there are no tracers that represent the POC concentration in these models. Instead, POC flux is represented by instantaneously redistributing new production in the water column using a prescribed remineralization length scale. Ballasting effects from minerals are considered in both biogeochemical models where the minerals are modelled implicitly as well and the POC flux associated with minerals attenuates with a prolonged remineralization length scale. MARBL includes protections by $CaCO_3$, opal, and dust while BLINGv2 ignores opal. The remineralization length scale of free POC is prescribed to increase with depth and in the presence of low-oxygen conditions. In BLINGv2, the remineralization length scale is also dependent on temperature.

POC concentration and flux are simulated explicitly in the other 7 ESMs. To reproduce the increased remineralization length scale with depth, the biogeochemical component of GFDL-ESM4 (COBALTv2; Stock et al. 2020) simulates the ballasting effects from

minerals, while in the other 6 ESMs (IPSL-CM5A2-INCA, IPSL-CM6A-LR, IPSL-CM6A-LR-INCA, MPI-ESM-1-2-HAM, MPI-ESM1-2-HR, MPI-ESM1-2-LR) the biogeochemical components (PISCESv2; Aumont et al. 2015 and HAMOCC6; Mauritsen et al. 2019) allow for the sinking velocity to increase with depth.

In COBALTv2, the ballasting minerals ($CaCO_3$, opal, and dust) are simulated explicitly and $CaCO_3$ is further divided into calcite and aragonite. A part of POC is protected by ballasting minerals and is free from remineralization. The amount of protected POC declines with depth due to dissolution of minerals. The dissolution rates of calcite and aragonite are controlled by their saturation states which are functions of the carbonate ion concentration. Opal dissolves at a rate that is dependent on temperature while the dissolution rate of dust is assumed to be constant. The fraction of POC that is free of ballasting minerals is remineralized at a temperature- and oxygen-dependent rate. The sinking velocity of free and protected POC is assumed to be constant at 100 m day^{-1}.

In HAMOCC6, the remineralization rate of POC is dependent on oxygen and the sinking velocity is assumed to increase linearly with depth. PISCESv2 uses an oxygen- and temperature-dependent remineralization rate and there are two POC classes based on particle size: small, slow-sinking POC that sinks at a constant rate and large, fast-sinking POC with a sinking velocity that increases with depth. In PISCESv2, large POC is remineralized into small POC first and then further into the dissolved organic carbon (DOC), while at the same time, the small POC and DOC can in turn aggregate into the large POC.

4.2.2   Results of Earth System Models

The vertical profiles of POC flux and transfer efficiency averaged over the northern North Atlantic from 12 ESMs are compared in Fig. 4.3. Since POC flux in the deep ocean is determined by carbon export out of the euphotic zone, defined here as the top 100 m, and POC remineralization occurring below 100 m, the transfer efficiency was calculated relative to the flux at 100 m. The POC flux at 100 m varies a lot with an extremely high value of 190 mg C m^{-2} day^{-1} in the GFDL-CM4 (Fig. 4.3a and Table D.1). Even without considering GFDL-CM4, there is a 3-fold range in the POC flux at 100 m. Of the remaining

ESMs, 4 CESM models simulate the highest POC flux ranging from 88 mg C m^{-2} day^{-1} in CESM2 to 93 mg C m^{-2} day^{-1} in CESM2-FV2. The next highest flux is simulated by GFDL-ESM4 with 79 mg C m^{-2} day^{-1} and the 3 IPSL ESMs ranging from 55 mg C m^{-2} day^{-1} in IPSL-CM6A-LR to 62 mg C m^{-2} day^{-1} in IPSL-CM5A2-INCA. The 3 MPI ESMs simulate the lowest POC flux at 100 m ranging from 32 mg C m^{-2} day^{-1} in MPI-ESM1-2-LR to 35 mg C m^{-2} day^{-1} in MPI-ESM1-2-HR.
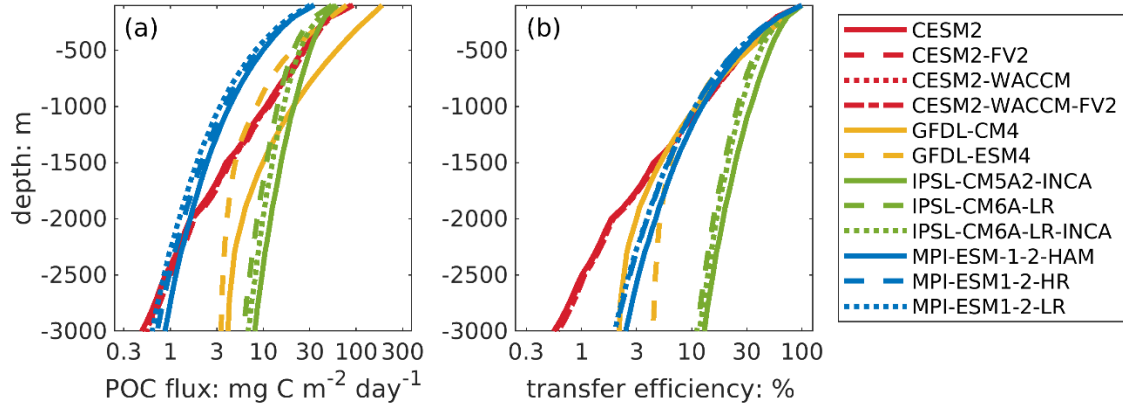
Figure 4.3. The mean vertical profiles of POC flux (a) and transfer efficiency (b) averaged over the northern North Atlantic (see Fig. 4.1 for the spatial scope) from 12 CMIP6 models.

Differences in POC flux increase with depth and the order of largest to smallest POC flux across 12 ESMs also changes. POC fluxes vary 6-fold at 1000 m compared to 3-fold at 100 m. At about 1000 m, IPSL-CM5A2-INCA has become the model with the highest POC flux. At 3000 m, the range of POC fluxes has further increased to about 17 folds, and the lowest POC fluxes are in the 4 CESM ESMs while the highest fluxes are simulated by the 3 IPSL ESMs. This means that the transfer efficiency varies across the 12 ESMs and shows patterns that are different from the POC flux (Fig. 4.3b). At 1000 m, the 3 IPSL ESMs simulate the highest transfer efficiency from 26% in IPSL-CM6A-LR to 34% in IPSL-CM5A2-INCA, indicating that the lowest fractions of the POC flux at 100 m are respired before reaching 1000 m. Although the POC flux at 1000 m varies a lot across the remaining 9 ESMs, their transfer efficiencies are clustered at $12 \pm 0.78\%$. Transfer efficiencies start to diverge into two clusters below 1000 m. At 3000 m, the transfer efficiency in the 4 CESM ESMs is the lowest around 0.60% and at least 4-fold higher in the other 5 ESMs (i.e., GFDL-CM4, GFDL-ESM4, MPI-ESM-1-2-HAM, MPI-ESM1-2-HR, and MPI-ESM1-2-LR).

To facilitate further comparison, I fit the simulated vertical profiles of transfer efficiency to a power law equation, the most widely used empirical equation (i.e., the Martin curve) with its exponent b used as an indicator to represent variability in transfer efficiency (Fig. D.7 and Table D.2). The resulting exponent b varies from 0.57 in IPSL-CM5A2-INCA to 0.97 in MPI-ESM1-2-HR and MPI-ESM1-2-LR. If this variation in the exponent b ($\Delta b = 0.40$) were applied to the global ocean, it would change the equilibrium atmospheric CO_2 levels by about 40 ppm based on the most realistic model in Kwon et al., (2009). The different degrees of misfit between the simulated transfer efficiency and their corresponding Martin curves would introduce additional variability (Lauderdale and Cael 2021).

When comparing the simulated POC fluxes from the 12 ESMs to in-situ observations, the 4 CESM ESMs agree well with the in-situ observations in the top 2000 m but underestimate the POC flux below (Fig. 4.4). This suggests an overestimation of respiration below 2000 m. In general, GFDL-CM4 and IPSL-CM5A2-INCA overestimate the in-situ observations throughout the water column, while the 3 MPI ESMs underestimate it. Among these 12 ESMs, the GFDL-ESM4 as well as the IPSL-6A-LR and IPSL-6A-LR-INCA have the best agreement with the in-situ observations with the highest correlation coefficient (>0.70) and lowest RMSE (~0.40) and bias (~0.10) even though there are large differences in their vertical profiles of POC flux and transfer efficiency (Fig. 4.3) despite the favorable statistical metrics.
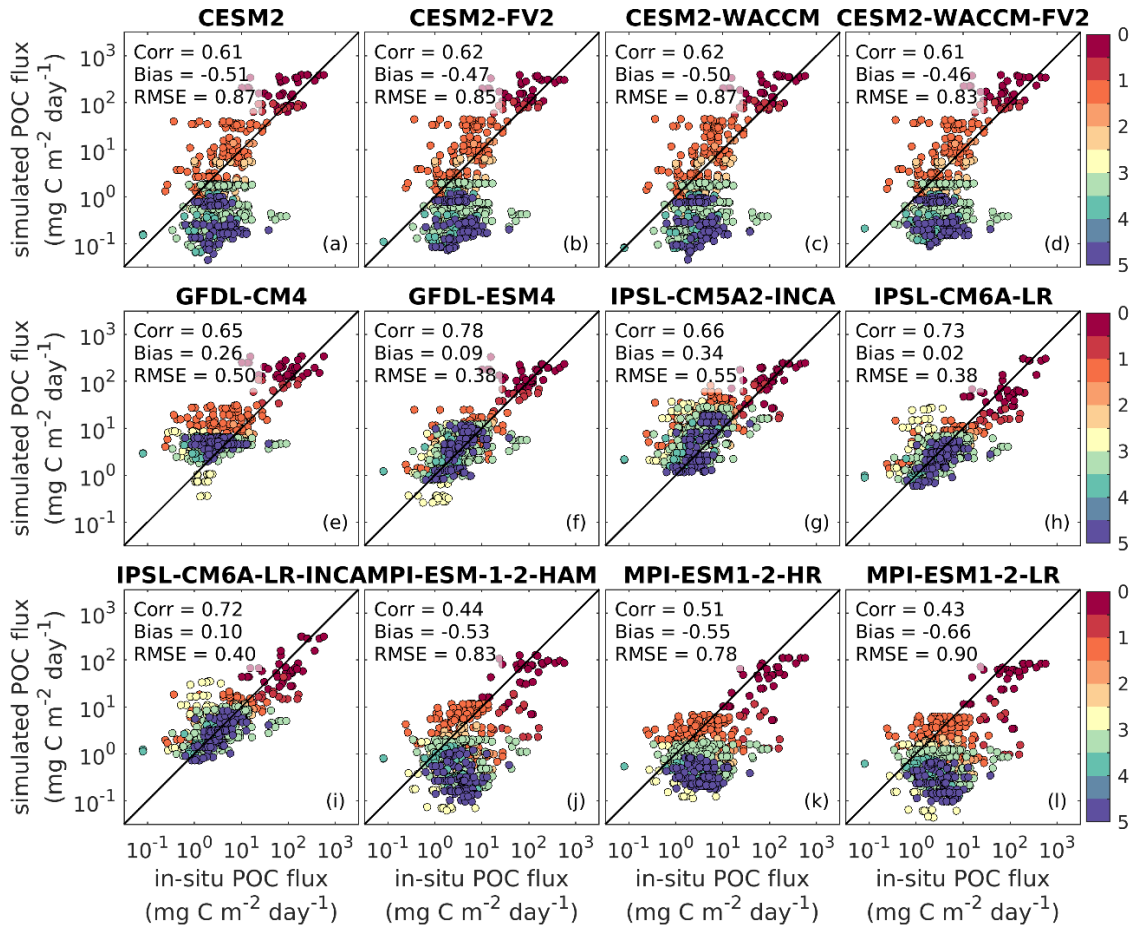
Figure 4.4. Comparison of POC flux simulated by CMIP6 models and in-situ observations in log space. Black lines indicate the 1:1 relationship. The colors represent depth (km) below the surface.

4.3 Comparison between 1D models

4.3.1 BGC-Argo float data

Data from eight BGC-Argo floats in the northern North Atlantic (Fig. 4.1) are used. These floats were equipped with a chlorophyll fluorometer and a sensor for particle backscatter at 700 nm (bbp700, m^{-1}) and deployed for at least one year. The data set includes over 3000 profiles spanning all seasons from 2013 to 2020, with the most of profiles sampling the top 1000 m and only a few profiles extending to 2000 m (Table 4.2). The chlorophyll and bbp700 profiles were smoothed following Briggs et al. (2011). Then the smoothed chlorophyll concentration was divided by a factor of 2 to account for the systematic calibration error in Web Labs fluorometers (Roesler et al. 2017). The baseline

of bbp700 was converted into bbp440 using a power law equation to estimate the phytoplankton concentration (Phy, mmol N m^{-3}):

$$bbp_{440} = \left(\frac{440}{700}\right)^{-\gamma} \times bbp_{700}, \tag{4.1}$$

$$Phy = 13000 \times (bbp_{440} - intercept) \times \frac{1}{12 \times 6.625}, \tag{4.2}$$

where γ is 0.78 based on the global measurements (Boss and Haëntjens 2016), the slope of 13,000 mg C m^{-2} is obtained from Behrenfeld et al. (2005), and the intercept was determined by the regression analysis between chlorophyll and bbp440.

Table 4.2. Number of profiles reaching 1000 and 2000 m for each BGC-Argo float used here.

Float WMO id	Number of profiles reaching 1000 m	Number of profiles reaching 2000 m
6901480	337	39
6901486	295	38
6901524	305	7
6901527	310	14
6901180	293	0
6901181	230	0
6901516	400	0
6901647	314	0

To obtain POC concentrations, the instrument noise was removed from the spike signals of bbp700 following Briggs et al. (2020) and a background baseline value, which is defined as the median between 950 m and 1000 m (Lacour et al. 2019), was subtracted. The resulting spike signals and baseline of bbp700 were used to estimate large, fast-sinking POC (Briggs et al., 2011) and small, slow-sinking POC (Dall'Olmo & Mork 2014) by multiplying a factor of 37,537 mg C m^{-2} in the mixed layer and a slightly lower factor of 31,519 mg C m^{-2} below (Cetinić et al. 2012; Lacour et al. 2019). The mixed layer depth is defined as the depth where density first increases to 0.01 kg m^{-3} above the reference density at 5 m depth.

4.3.2 Description of the 1D model

I set up a one-dimensional (1D) physical-biogeochemical model which follows the trajectories of the BGC-Argo floats shown in Fig. 4.1 simulating the top 1500 m for float 6901647, 2000 m for float 6901516, and 3000 m for the other floats based on the bathymetry. There are 600 evenly distributed vertical layers with the layer thickness ranging from 2.5 m to 5 m across different BGC-Argo floats. The physical model is the General Ocean Turbulence Model (GOTM; https://gotm.net/portfolio/), a 1D water column model that simulates the vertical turbulent fluxes of momentum, heat, and tracers. It is forced with hourly atmospheric data from the ERA5 reanalysis (https://www.ecmwf.int/en/forecasts/datasets/reanalysis-datasets/era5) including air temperature, air pressure, humidity, cloud coverage, shortwave radiation, net longwave radiation, precipitation, and wind speed at 10 m. To account for the absence of advection in the 1D model, temperature and salinity are nudged to the float observations in the top 1000 m and to the daily reanalysis data from GLORYS (https://doi.org/10.48670/moi-00021) below with a timescale of one day, because most of BGC-Argo profiles used are limited to the top 1000 m.

The biogeochemical model used here is an updated version of the biogeochemical model described in Laurent et al. (2021) and is coupled to GOTM through the Framework for Aquatic Biogeochemical Models (FABM; Bruggeman and Bolding 2014). Since the biogeochemical model has been comprehensively described in Laurent et al. (2021), I will restrict myself to a brief description with particular emphasis on the model's representation of the gravitational settling and remineralization of large detritus, which were updated. The model simulates two functional groups of phytoplankton (small pico-phytoplankton/nano-phytoplankton, P_S and large micro-phytoplankton, P_L) and zooplankton (micro-zooplankton, Z_S and meso-zooplankton, Z_L). The growth of phytoplankton is limited by light, temperature, and two nutrients (ammonium, NH_4 and nitrate, NO_3). The chlorophyll for each phytoplankton functional group is modelled as a separate prognostic variable which accounts for photoacclimation based on Geider et al. (1997).

Table 4.3. Parameters associated with large detritus

Descriptions (unit)	symbol	Values
Ballast scheme		
Large detritus sinking velocity (m day^{-1})	w_L	55
Remineralization rate at 0°C for large detritus (m day^{-1})	r_L^0	0.20
Protection capacity of $CaCO_3$ (mol N mol Ca^{-1})	p_{CaCO_3}	0.088
Polar $CaCO_3$:organic C production (mol $CaCO_3$ mol C^{-1})	f_{90^o}	0.02
Equatorial $CaCO_3$:organic C production (mol $CaCO_3$ mol C^{-1})	f_{0^o}	0.10
The Si:N ratio of large phytoplankton (mol Si mol N^{-1})	$f_{Si:N}$	1.0
Protection capacity of opal (mol N mol Si^{-1})	p_{opal}	0.02
Opal dissolution rate (day^{-1})	d_{opal}	0.0275
WLin scheme		
Large detritus sinking velocity in top 100m (m day^{-1})	$w_{L,min}$	58
Large detritus sinking velocity at 5,000m (m day^{-1})	$w_{L,max}$	200
Remineralization rate at 0°C for large detritus (m day^{-1})	r_L^0	0.15

The biogeochemical model also simulates two functional groups of detritus, i.e., small detritus (D_S) and large detritus (D_L), which have different remineralization rates and sinking velocities. Small detritus is produced by the mortality of two phytoplankton functional groups (P_S+P_L) and micro-zooplankton (Z_S), and sloppy grazing by two functional groups of zooplankton (Z_S+Z_L). It is assumed to sink at a slow and constant rate and is remineralized with a temperature-dependent rate. Large detritus is generated by the mortality of meso-zooplankton (Z_L) and the aggregation of small detritus (D_S) and micro-phytoplankton (P_L). In the previous version of this model, the large detritus was parameterized similarly to the small detritus except that its sinking velocity was faster. For this chapter, the model was updated to include two different sinking schemes, the ballast scheme and the WLin scheme, which aim to reproduce the increasing remineralization length scale with depth. Detailed descriptions of these two schemes follow in sections 4.3.2.1 and 4.3.2.2. Model parameters were first calibrated for the ballast scheme using BGC-Argo data of chlorophyll, phytoplankton, and small and large POC concentrations.

For the model with the WLin scheme, parameters associated with large detritus were re-calibrated (Table 4.3) and other parameters are unchanged (Table D.3).

The biogeochemical model is initialized using a parameterization of NO_3 derived from a machine-learning approach that relates in-situ data of NO_3 to six predictor variables (temperature, salinity, time, longitude, latitude, and depth) from the World Ocean Database 2013 (WOD13; Boyer et al., 2013). The resulting parameterization has been validated with independent data from BGC-Argo floats (see supplementary material). Since the 1D model does not account for advection, simulated NO_3 is relaxed to profiles derived from the machine-learning parameterization at a time scale of 100 days.

4.3.2.1 Ballast scheme

The ballasting effects from minerals including $CaCO_3$ and opal are simulated in a manner similar to that of Yool et al. (2011) and Stock et al. (2020). Specifically, large detritus is divided into two components: the mineral associated component that is assumed to be protected, and the remaining free component that is subject to temperature-dependent remineralization according to

$$Remin_{DL} = r_L^0 \cdot f(T) \cdot (D_L - p_{opal} \cdot opal - p_{CaCO_3} \cdot CaCO_3), \qquad (4.4)$$

where r_L^0 (day-1) is the nominal remineralization rate of free large detritus and the actual remineralization rate is temperature-dependent ($f(T)$) with a Q10 value of 1.9. The protection capacity of opal (p_{opal}) and $CaCO_3$ (p_{CaCO_3}) are specified as 0.02 mol N (mol Si)$^{-1}$ and 0.088 mol N (mol Ca)$^{-1}$ based on Yool et al. (2011) and Stock et al. (2020). The free and protected large detritus are assumed to have a constant sinking velocity (w_L, m day^{-1}).

Opal is synthesized by diatoms and produced through mortality ($Mortal_{PL}$) and aggregation (Agg_{PL}) of micro-phytoplankton. Since opal is not utilized by zooplankton, the loss of micro-phytoplankton due to grazing by the two zooplankton groups is all transferred into opal such that

$$\frac{\partial opal}{\partial t} = f_{Si:N} \cdot (Graz_{PL} + Mortal_{PL} + Agg_{PL}) - d_{opal} \cdot opal - w_L \cdot \frac{\partial opal}{\partial z}. \qquad (4.5)$$

The intracellular Si:N ratio of micro-phytoplankton ($f_{Si:N}$) is fixed as 1.0 in this chapter. As opal is subject to dissolution, the amount of large detritus protected by opal declines with depth but at a much slower rate than unprotected detritus. The dissolution rate of opal (d_{opal}) is specified so that its remineralization length scale is 2000 m (Yool et al. 2011).

There are different ways of simulating production of $CaCO_3$; it has been related to the activities of coccolithophores (e.g. Stock et al. 2020; Long et al. 2021), the production of detritus (e.g. Yool et al. 2011; Oke et al. 2013), and the export flux at the base of euphotic zone (e.g. Zahariev et al. 2008). Here, $CaCO_3$ production is parameterized as a function of large detritus production ($Prod_{DL}$), following Yool et al. (2011), as

$$\frac{\partial CaCO_3}{\partial t} = f_{Ca:N} \cdot Prod_{DL} - w_L \cdot \frac{\partial CaCO_3}{\partial z}, \tag{4.6}$$

where the rain ratio ($f_{Ca:N}$) between $CaCO_3$ and detritus production is a function of latitude as follows

$$f_{Ca:N} = 6.625 \times \left(f_{90^o} + (f_{0^o} - f_{90^o}) \cdot \frac{90 - |lat|}{90} \right). \tag{4.7}$$

For sake of simplicity, I assume no dissolution of $CaCO_3$ because the lysocline is relatively deep. Given that the dissolution of $CaCO_3$ is controlled by its saturation state, which is a function of the carbonate ion concentration, this simplification allows us to avoid simulating the carbonate system (i.e., DIC and TA) but may result in an overestimation of $CaCO_3$ concentration below the lysocline.

4.3.2.2 WLin scheme

In the WLin scheme, the sinking velocity of large detritus is assumed to increase linearly with depth as

$$w_L = w_{L,min} + \left(w_{L,max} - w_{L,min} \right) \cdot \frac{\max(0, z - 100)}{5000}, \tag{4.8}$$

where $w_{L,min}$ and $w_{L,max}$ are the minimum and maximum sinking velocity of large detritus. This WLin model has been applied in other biogeochemical models (e.g. Aumont

et al. 2015; Tjiputra et al. 2020) to account for the preferential remineralization of slow-sinking particles and the increasing proportion of fast-sinking particles implicitly.

4.3.3　1D model results

To facilitate model-data comparison, the BGC-Argo float data and the 1D model results are grouped by day of year into a daily climatology. The observed small POC is compared to the sum of simulated pico-/nano-phytoplankton (P_S), the micro-phytoplankton (P_L), the micro-zooplankton (Z_S), and the small detritus (D_S), while the observed large POC is compared to the sum of simulated meso-zooplankton (Z_L) and large detritus (D_L). In addition to the BGC-Argo float data, I also compare the simulated net primary production (NPP) to satellite estimates from three algorithms, the Vertically Generalized Production Model (VGPM; Behrenfeld and Falkowski 1997), the Eppley version of the VGPM model (Eppley; Morel 1991), and the Carbon-based Productivity Model (GbPM; Westberry et al. 2008).
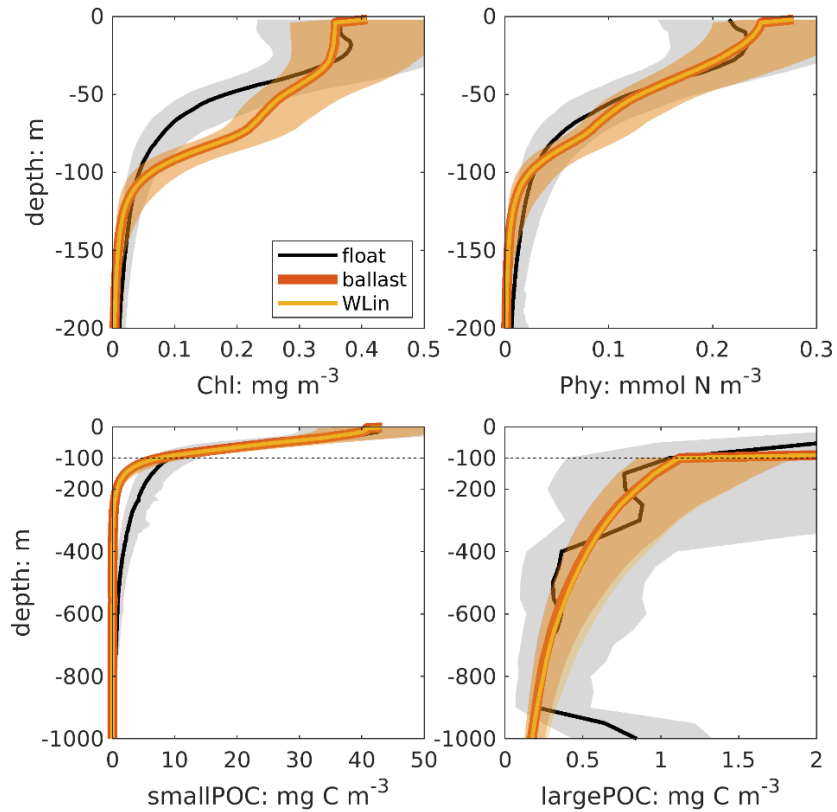
Figure 4.5. Vertical profiles of chlorophyll, phytoplankton, small and large POC from the 1D model results and BGC-Argo floats.

Despite the different underlying mechanisms, both model schemes reproduce well the large POC concentrations derived from BGC Argo data in terms of their vertical pattern and seasonal variability in the top 1000 m (Figs. 4.5-4.6). The simulated small POC concentration is lower than the observations before May and below 100 m. This is because the 1D models underestimate the growth of phytoplankton driven by intermittent re-stratification early in the year (Fig. 4.6), which manifests in an underestimation of net primary production when compared to the VGPM- and Eppley-algorithms before May (Fig. 4.7). In addition, the parameterization of small POC is relatively simple when compared to large POC and may overestimate its attenuation below 100 m. Despite the discrepancies in small POC concentrations in spring, the 1D model is useful for evaluating the differences between the two vertical sinking schemes.
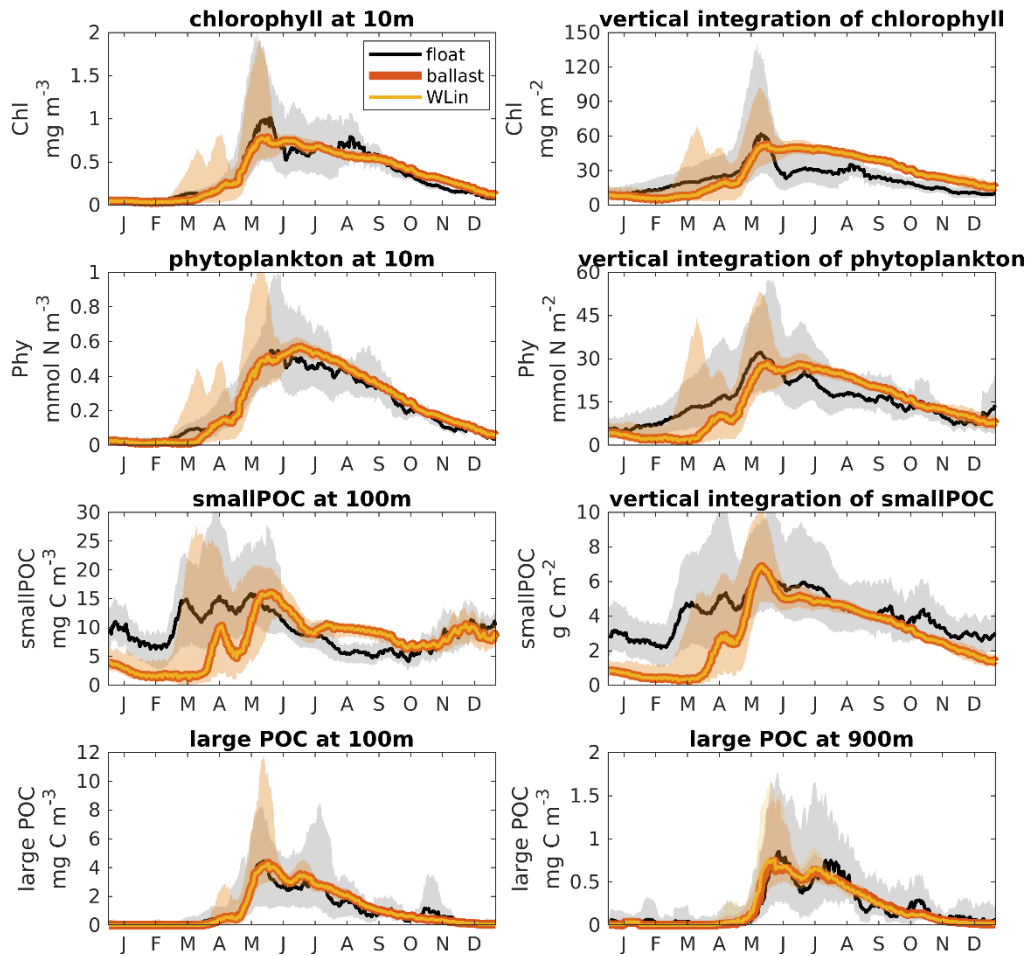
Figure 4.6. Seasonal cycles of chlorophyll, phytoplankton, small and large POC from the 1D model results and BGC-Argo floats.
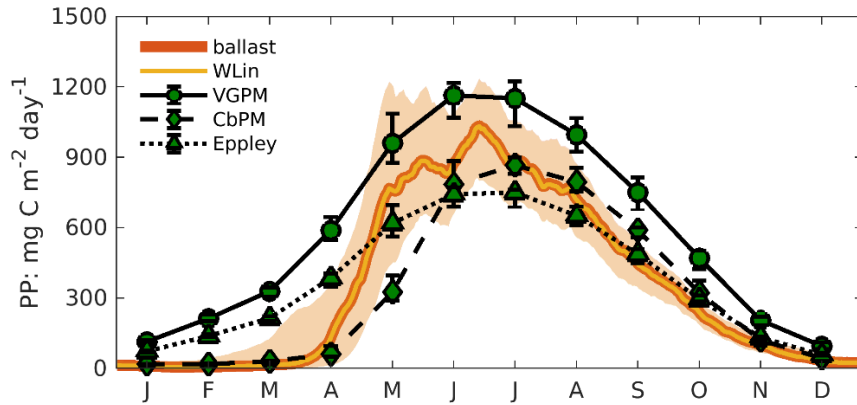
Figure 4.7. Comparisons of net primary production between 1D model results and satellite estimates.
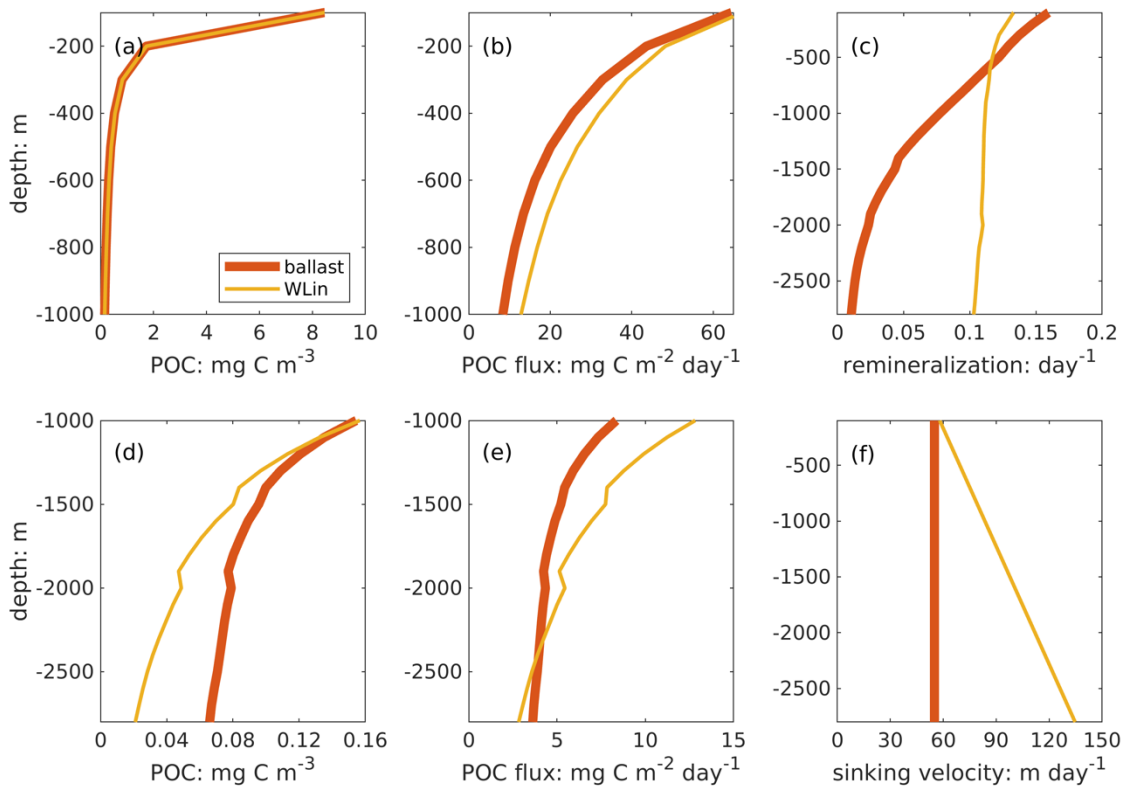
Figure 4.8. Vertical profiles of total POC concentration (a, d) and POC flux (b, e) above and below 1000 m, as well as the sinking velocity (c) and remineralization rate (f) of large POC from the ballast and WLin schemes.

The vertical profiles of POC concentration and POC flux from the two model schemes are compared in Fig. 4.8. Since large POC dominates the POC flux in the deep ocean, its remineralization rate and sinking velocity are also shown in Fig. 4.8 where the

remineralization rate in the ballast scheme is an average over the free and protected large POC. Although the distributions of POC concentration are almost identical between the two model schemes in the top 1000 m (Fig. 4.8a), they are very different below and their differences increase with depth (Fig. 4.8d). In general, the POC concentration below 1000 m is higher in the ballast scheme because a fraction of the large POC is protected by minerals, i.e., $CaCO_3$ and opal, which results in a much lower remineralization rate (Fig. 4.8c). In addition, the vertically increasing sinking velocity in the WLin model accelerates the settling of large POC and removes it from the water column more rapidly than in the ballast scheme (Fig. 4.8f). As a result, there is a 3-fold difference in POC concentration (0.07 and 0.02 mg C m^{-3} in the ballast and WLin schemes, respectively) between the two model schemes at 2800 m.

The two model schemes also have different patterns for POC flux (Fig. 4.8b, e). Specifically, the WLin scheme produces a higher POC flux in the top 2400 m because the sinking velocity of large POC is faster than in the ballast scheme. Differences in POC flux between the two model schemes first increase with depth with maximum differences at 1000 m and then decrease with depth. The POC flux is similar between the two model schemes at 100 m with 64 mg C m^{-2} day^{-1} in the ballast scheme and 67 mg C m^{-2} day^{-1} in WLin scheme. The flux decreases to about 8.4 mg C m^{-2} day^{-1} and 13 mg C m^{-2} day^{-1} at 1000 m in the ballast scheme and WLin scheme, respectively, which amounts to a 50% difference between the two model schemes. In general, the maximum differences in POC flux between the two model schemes are less distinct than in the POC concentration.

The implications of the two different model schemes for the distribution of respiration and nutrients are shown in Fig. 4.9. The respiration is defined as a reduction of the transfer efficiency (TE) within a unit of depth ($\partial TE / \partial z$, m^{-1}). As shown in Fig. 4.9a, b, the respiration in the ballast scheme is higher within the top 500 m and slows down below. This implies that the ballast scheme distributes the biologically regenerated nutrients shallower than the WLin scheme. In this chapter, the simulated NO_3 concentrations are similar between the two model schemes because they are relaxed to the same profile to account for the absence of advection in the 1D model. To diagnose the impact of respiration on nutrients, the nitrification rate, which produces NO_3 from NH_4, is shown in Fig. 4.9c.

Since in the 1D model, small and large POC are respired first into the NH_4, and then into the NO_3 through nitrification, this process serves as a useful diagnostic. The differences in nitrification between the two model schemes are similar to the differences in respiration (Fig. 4.9d).
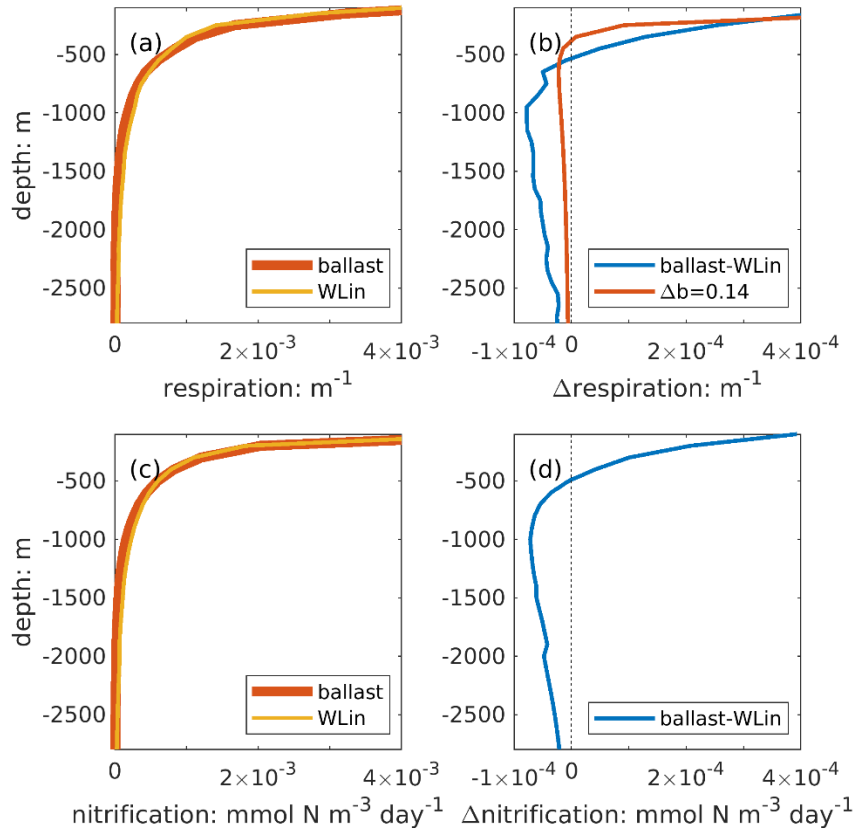
Figure 4.9. Vertical profiles of respiration and nitrification as well as their differences between the two model schemes.

4.3.4 Sensitivity experiments

One of research questions is whether observations of POC concentration can provide a unique estimate of POC flux provided the parameterization scheme is known. Since the structure of vertical profiles of POC concentration and POC flux is determined by the remineralization length scale, which is the ratio between the sinking velocity and remineralization rate, I conducted sensitivity experiments by perturbing these two related parameters simultaneously by $\pm 25\%$ (Table 4.4) which leaves the remineralization length

scale unchanged. In addition, in the model with ballast scheme, the dissolution rate of opal was changed to maintain its remineralization length scale as 2000 m.

Table 4.4. Overview of sensitivity experiments

Experiment	Description
ballast	Experiment with the ballast scheme
ballast (+25)	Same as the ballast experiment except that the remineralization rate (r_L^0) and sinking velocity (w_L) of large detritus as well as the dissolution rate of opal (d_{opal}) are increased by 25%
ballast (-25)	Same as the ballast experiment except that the remineralization rate (r_L^0) and sinking velocity (w_L) of large detritus as well as the dissolution rate of opal (d_{opal}) are decreased by 25%
WLin	Experiment with the WLin model scheme
WLin (+25)	Same as the WLin experiment except that the remineralization rate (r_L^0) and sinking velocity ($w_{L,min}$ and $w_{L,max}$) of large detritus are increased by 25%
WLin (-25)	Same as the WLin experiment except that the remineralization rate (r_L^0) and sinking velocity ($w_{L,min}$ and $w_{L,max}$) of large detritus are decreased by 25%

Relative changes in large POC concentration, large POC flux, and nitrification are shown in Fig. 4.10 for the sensitivity experiments with the ballast ($\pm$25%) and WLin ($\pm$ 25%) schemes in comparison to their corresponding base cases. The results show that the vertical profiles of POC concentration are highly sensitive to simultaneous changes in remineralization rate and sinking velocity. When the remineralization rate and sinking velocity are increased by 25%, the POC concentration decreases by about 20%. In contrast, a 25% decrease in the remineralization rate and sinking velocity increases the POC concentration by about 33%. However, the POC flux remains unchanged because the remineralization length scale is fixed. Furthermore, since nitrification and NO_3 are fueled by POC respiration, or the reduction of POC flux with depth, they do not change either.
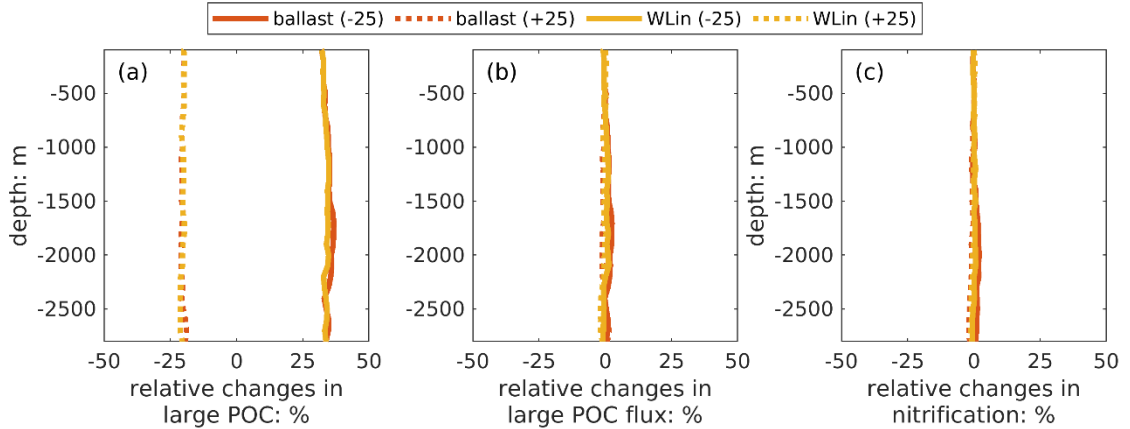
Figure 4.10. Relative changes of the large POC concentration (a), large POC flux (b), and nitrification (c) in ballast ($\pm 25\%$) and WLin ($\pm 25\%$) sensitivity experiments when compared to their corresponding base cases (i.e., the ballast and WLin case, respectively).

4.4 Discussion

Parameterizations of vertical carbon flux in biogeochemical models are critically important for simulating the BCP and its role in climate change. Currently, two schemes with different mechanistic underpinnings for reproducing the increase of remineralization length scale with depth are in use. Previous studies aimed at comparing and evaluating the different parameterization schemes placed emphasis on their ability to reproduce sparse in-situ observations of POC flux and climatological datasets of nutrients and dissolved oxygen. These studies found that the different parameterization schemes can match these observations equivalently well within the observational uncertainties while yielding different atmospheric CO_2 levels (Cael and Bisson 2018; Lauderdale and Cael 2021). This suggests that the currently available observations of POC flux, nutrients, and dissolved oxygen are insufficient for distinguishing between different parameterization schemes and for constraining the two main parameters, sinking speed and remineralization rate, with sufficient accuracy. This is a well-known issue in biogeochemical modeling, referred to as the underdetermination problem, and common when calibrating biogeochemical models (Fennel et al. 2022). The only solution to this problem is to provide additional constraints from independent observations or mechanistic insight. This chapter seeks to evaluate the value that abundant proxy observations of POC concentration from profiling floats may

add for assessing and calibrating the vertical carbon flux parameterization in biogeochemical models.

First, I described the parameterization schemes from 12 ESMs that are part of CMIP6 and classified them into three categories (Fig. 4.2): two categories where POC is simulated explicitly and the increase in remineralization length scale is addressed either by decreasing the remineralization rate or increasing the sinking velocity, and one category where POC flux and ballast effects are simulated implicitly. There are large model-to-model differences in the vertical profiles of POC flux and transfer efficiency between the 12 ESMs. Comparisons between the simulated POC flux and in-situ observations show that the GFDL-ESM4 as well as the IPSL-6A-LR and IPSL-6A-LR-INCA have the best agreement with observations. However, despite their similar agreement with the observations GFDL-ESM4, IPSL-6A-LR and IPSL-6A-LR-INCA simulate vastly different transfer efficiencies. This supports previous conclusions by other authors that the currently available observations of POC flux are not sufficient to distinguish between different alternative parameterization schemes (Cael and Bisson 2018; Lauderdale and Cael 2021).

To isolate the influence of parameterization scheme from other sources of discrepancies in the ESM models, I set up a suite of 1D models to compare the two most common parameterizations, the ballast scheme and the WLin scheme, in the same model environment. Both have been widely used in large-scale biogeochemical models and reproduce the increase of remineralization length scale either by decreasing the remineralization rate or by increasing sinking velocities. Unlike previous studies that used observations of POC flux, nutrients, and dissolved oxygen, here the 1D models are calibrated using BGC-Argo float observations of POC concentration in the top 1000 m, where the largest vertical gradient is present.

Comparison of the two schemes in the 1D model framework shows notable differences in their vertical profiles of POC flux, which also influences nutrient distributions through respiration. Specifically, the respiration in the deep ocean (below 500 m) is higher and therefore the nutrients are re-distributed deeper with the WLin scheme. This has global implications because deeper respiration enables the global meridional overturning

circulation to transport more nutrients from North Atlantic to the Southern Ocean and North Pacific, results in longer-term sequestration of CO_2, and decreases the equilibrium atmospheric CO_2 levels (Kwon et al. 2009; Lauderdale and Cael 2021). Lauderdale and Cael (2021) perturbed their exponent b by ± 0.14 from a reference value of 0.84 and reported changes of biologically regenerated carbon in the deep ocean by up to approximately 20 mmol C m^{-3} and 50 mmol C m^{-3} in the Atlantic and Pacific, respectively. In addition, this perturbation in the respiration changed the equilibrium atmospheric CO_2 levels by -22 ppm and +25 ppm in their model simulations. The changes in respiration between the two 1D model schemes are even higher than in Lauderdale and Cael (2021) (Fig. 4.9b) and would likely result in substantial differences in nutrient distributions and atmospheric CO_2 levels when applied to the global ocean.

The two model schemes produced almost identical profiles of POC concentration within the top 1000 m but yielded substantially different predictions below, especially below 2000 m, because of their different underpinning mechanisms. Specifically, the POC concentration in the WLin scheme is lower than that in the ballast scheme because the relatively faster remineralization rate and sinking velocity can remove organic particles more easily from the water column. The influence of remineralization rate on POC concentration has also been discussed in Aumont et al., (2017) who compared two different parameterizations of vertical carbon flux. They found that POC concentration was underestimated below 200 m by at least one order of magnitude in the model version where the remineralization rate is dependent on temperature. In contrast, using the model version with a continuous reactivity spectrum of POC resulted in a decrease in remineralization rate with depth and led to an improved agreement with the observed POC concentration without degrading the POC flux. Both model versions used a constant sinking velocity of POC. The ballast scheme, which divides large POC into the free and protected components, is similar to the reactivity spectrum but uses a finite number of POC pools with different reactivities and therefore can enhance preservation of POC concentration in the deep ocean when compared with the WLin scheme. However, the ballast scheme and the reactivity spectrum reproduce the decrease of remineralization rate due to different mechanisms and hence their future projections of carbon sequestration have different sensitivities to climate change. Given the rising atmospheric CO_2 levels, the dissolution of $CaCO_3$ will be

shallower, which decreases the protection of POC from remineralization. As a result, the projected decrease of carbon sequestration will be amplified in models with the ballast scheme while in other models, e.g., with the reactivity spectrum, it will not. Distinguishing between these two parameterizations requires further investigation and is beyond the scope of this chapter.

Both the ballast scheme and WLin scheme can reproduce the increase of remineralization length scale with depth, one by decreasing the remineralization rate and the other by increasing sinking velocity. The higher POC concentration in the ballast scheme implies that it is probably more accurate than the WLin scheme, or at least it is more important in explaining the increase of remineralization length scale. Since there are observational supports for both of the mechanistic assumptions (e.g., McDonnell et al., 2015; Villa-Alfageme et al., 2014, 2016), it could be a combination of both in reality and an ideal parameterization scheme likely should incorporate these two mechanisms. However, for a quantitative understanding of their relative importance more observations are needed. Results suggest that proxy observations of POC concentration below 2000 m would be very valuable. Presently BGC-Argo floats are limited to the top 2000 m; however, an integration of backscatter sensors into the Deep Argo program, a new component of Argo that will sample the ocean from surface to 4000 m and even 6000 m (Roemmich et al. 2019) could accomplish this. Such an extension of the BGC Argo to the full depth of the ocean would provide important information for distinguishing between different parameterization schemes and promoting process-based understanding of the BCP.

Although POC concentrations, unlike the POC flux, hold great potential for validating and constraining mesopelagic (200-1000 m) and deep-ocean carbon sequestration, much less attention has been paid so far to their usage for calibrating biogeochemical models. The linkage between POC concentration and POC flux requires additional assumptions or knowledge of sinking velocity. I conducted a suite of sensitivity experiments to evaluate whether observations of POC concentration can well constrain the POC flux if the model parameterization scheme has been determined. The sensitivity experiments show that the POC concentration is sensitive to simultaneous changes of remineralization rate and sinking velocity. This implies that observations of POC concentration can determine these

two related parameters independently and therefore can derive a unique estimate of POC flux, but the inverse is not true because the POC flux and the nutrients are almost unchanged. High-frequency observations of POC concentration contain information on remineralization rate and sinking velocity, which have been successfully derived from changes of POC concentration over time and depth (Briggs et al. 2011, 2020).

In general, this chapter suggests that observations of POC concentration are valuable in complementing the existing sparse observations of vertical flux because they can inform us on the most appropriate parameterization scheme and can provide unique estimates of POC flux. In addition, when compared with traditional POC flux measurements (e.g., sediment traps and radioactive tracers), autonomous platforms (e.g., BGC-Argo floats) and bio-optical sensors make it more cost-effective to measure the POC concentration in high resolution and over extended spatial and temporal scales. Therefore, I recommend the usage of observations of POC concentration in addition to other observation types for calibration of biogeochemical models.

4.5 Conclusion

This chapter shows large model-to-model differences in the simulated vertical profiles of POC flux and transfer efficiency across ESMs regardless of the vertical flux parameterization that is used. Comparison of the two most common parameterizations, the ballast scheme and the WLin scheme, within an otherwise identical 1D model framework suggest that the WLin scheme is likely underestimating POC concentrations in the deep ocean, especially below 2000 m, and that the ballast scheme is probably more accurate. Differences in predicted POC concentrations below 2000 m suggest that it would be possible to better distinguish between the skill of the two schemes and evaluate their accuracy if backscatter measurements from BGC-Argo floats were available below 2000 m. Sensitivity experiments suggest that observations of POC concentration can simultaneously constrain the remineralization rate and sinking velocity, if the parameterization scheme is known, and can therefore be used to derive a unique estimate of POC flux.

CHAPTER 5

BIOGEOCHEMICAL ARGO DATA SUGGEST SIGNIFICANT CONTRIBUTIONS OF SMALL PARTICLES TO THE VERTICAL CARBON FLUX IN THE SUBPOLAR NORTH ATLANTIC[3]

5.1 Introduction

The ocean's biological carbon pump, a key component of the global carbon cycle, includes a range of processes by which 10% to 20% of global net primary production (NPP) is exported downward from the euphotic zone (e.g., Henson et al. 2011; Siegel et al. 2014; Bisson et al. 2020). However, most of this downward organic carbon flux is recycled within the mesopelagic zone (100 to 1000 m depth) and recirculated back to the surface within years to decades. Only a small fraction, estimated to vary from 5% to 40% globally (DeVries and Weber 2017), is sequestered in the deep ocean (>1000 m) for centuries to millennia (Guidi et al. 2015; Boyd et al. 2019). The ratio between the vertical flux at 100 m and a given depth, e.g., 1000 m, is defined as the transfer efficiency of vertical carbon transport. Variations in the amount of organic carbon transported to and subsequently sequestered in the deep ocean exert a strong control on atmospheric CO_2 levels (Falkowski et al. 1998). Accurate estimates of the strength and transfer efficiency of the vertical carbon flux thus are of paramount interest to climate research.

A long-standing paradigm is that the vertical carbon flux is mainly fueled by the gravitational settling of large, fast-sinking particulate organic carbon (POC). This view has been challenged because estimates of carbon demand by heterotrophic organisms exceed those of organic carbon supplied by sinking, suggesting that other mechanisms may contribute to the vertical carbon flux (Burd et al. 2010). Recent studies have revealed

important contributions from small, slow-sinking POC to vertical carbon flux (Dall'Olmo and Mork 2014; Omand et al. 2015; Baker et al. 2017). In addition to its relatively slow gravitational settling, small POC can be injected into greater depths by different physical and biological processes (Boyd et al., 2019) that are episodic and localized and thus hard to measure (Llort et al. 2018; Resplandy et al. 2019). Recent advances with autonomous platforms and biogeochemical sensors now enable POC observations at high spatial and temporal resolution (Biogeochemical-Argo Planning Group 2016; Roemmich et al. 2019; Chai et al. 2020). The vertical flux of small POC at the base of euphotic zone has been estimated previously from BGC-Argo observations by assuming that it equals the seasonal accumulation of small POC within the mesopelagic zone during the transition period from winter to summer (e.g., Dall'Olmo and Mork 2014; Bol et al. 2018). However, the seasonal accumulation is a result of multiple processes. Besides the vertical flux from the upper layer, small POC can be supplied by the fragmentation of large POC within the mesopelagic zone (Giering et al. 2016; Baker et al. 2017; Briggs et al. 2020) and is partly remineralized. Overlooking these factors may introduce errors into estimates of the vertical carbon flux and the relative contributions of small POC.

The vertical transfer efficiency is even more poorly constrained. Some studies put forward the idea that it is higher in low latitude regions and decreases to high latitudes (Henson et al. 2012; Guidi et al. 2015), while others suggest the opposite latitudinal pattern (Marsay et al. 2015; Weber et al. 2016; DeVries and Weber 2017). The large uncertainty in estimates of the transfer efficiency is due to the scarcity of in-situ observations and a lack of mechanistic understanding of the controlling processes. The transfer efficiency is determined by a competition between local processes (i.e., remineralization and fragmentation) and vertical transfer (incl. sinking, subduction, and mixed layer deepening) of POC. Many studies have revealed that the remineralization rate is highly variable geographically and is modulated by local environmental factors, e.g., temperature and oxygen (Weber et al. 2016; Laufkötter et al. 2017; Kheireddine et al. 2020). Fragmentation has been suggested as the single most important process controlling the loss of large POC (Briggs et al., 2020; Giering et al., 2014). Hence, a better quantification of remineralization and fragmentation can improve our understanding of the transfer efficiency.

To address these issues, I present a method for estimating the vertical flux of large and small POC using observations of backscattering and dissolved oxygen from BGC-Argo floats. This method, an extension of the model of Dall'Olmo and Mork (2014), explicitly accounts for remineralization and fragmentation of organic particles. I apply this method to evaluate the vertical carbon flux due to different mechanisms and its transfer efficiency in the subpolar North Atlantic, while explicitly accounting for remineralization and fragmentation for the first time. Results show that the gravitational sinking flux of large POC is the most important mechanism and the most effective pathway for long-term sequestration. Small POC is transported out of the euphotic zone and can also contribute significantly to the vertical carbon flux at 600 m since it is produced by fragmentation of large POC in the mesopelagic zone.

5.2 Material and methods

5.2.1   BGC-Argo floats

This chapter uses measurements of oxygen and backscattering at 700 nm (bbp700; unit: m^{-1}) from BGC-Argo floats in the subpolar North Atlantic (Fig. 5.1). The baseline and spike signals were decoupled from the raw bbp700 profiles following Briggs et al. (2011). The instrument noise was removed from the spike signals and added to the baseline following Briggs et al. (2020). The resulting baseline and spike signals are used as a proxy of small, slow-sinking POC (Dall'Olmo and Mork 2014) and large, fast-sinking POC (Briggs et al. 2011), respectively. POC concentrations (Fig. 5.2) were obtained from these proxy measurements by using a factor of 37537 mg C m^{-2} in the mixed layer, defined here as the depth where density first exceeds 0.125 kg m^{-3} plus the reference density at 5 m depth (Hennon et al. 2016), and a slightly lower factor of 31519 mg C m^{-2} below (Cetinić et al. 2012; Lacour et al. 2019). A background value, defined as the median of the baseline between 950 and 1000 m (Lacour et al. 2019) was first subtracted before estimating the small POC.
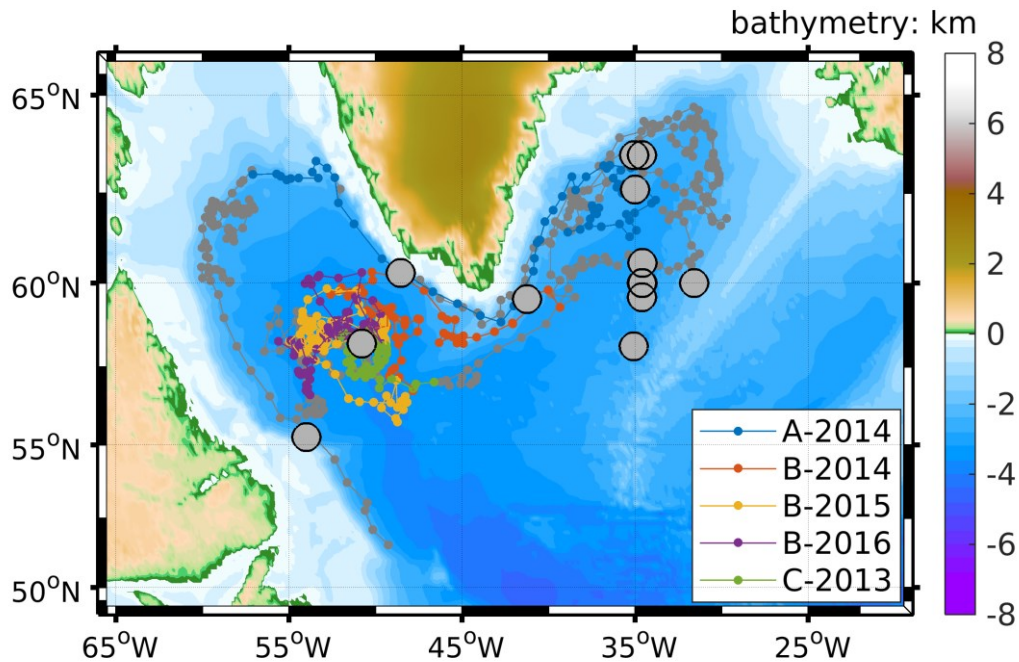
Figure 5.1. Trajectories of BGC-Argo floats that measured both oxygen and backscattering (gray and colored lines). The colors show one-year segments that were used in the analysis. The floats' WMO numbers are 6901485 (float A), 6901486 (float B), and 6901523 (float C). The large gray circles indicate where in-situ measurements of vertical carbon flux at 100 m are available.

As shown in Fig. 5.1, floats can move large horizontal distances over the course of their deployment and thus encounter different physical and biogeochemical regimes and different mesopelagic remineralization rates and export fluxes. To minimize this effect, I divided each float trajectory into several one-year segments (from January to December; Fig. 5.2) and estimated the vertical flux for each segment. As float C (WMO number 6901523) was influenced by a relatively low-oxygen water mass from July to December 2014, the corresponding segment was defined from May 2013 to May 2014 but is referred to as C-2013 (Fig. 5.2).
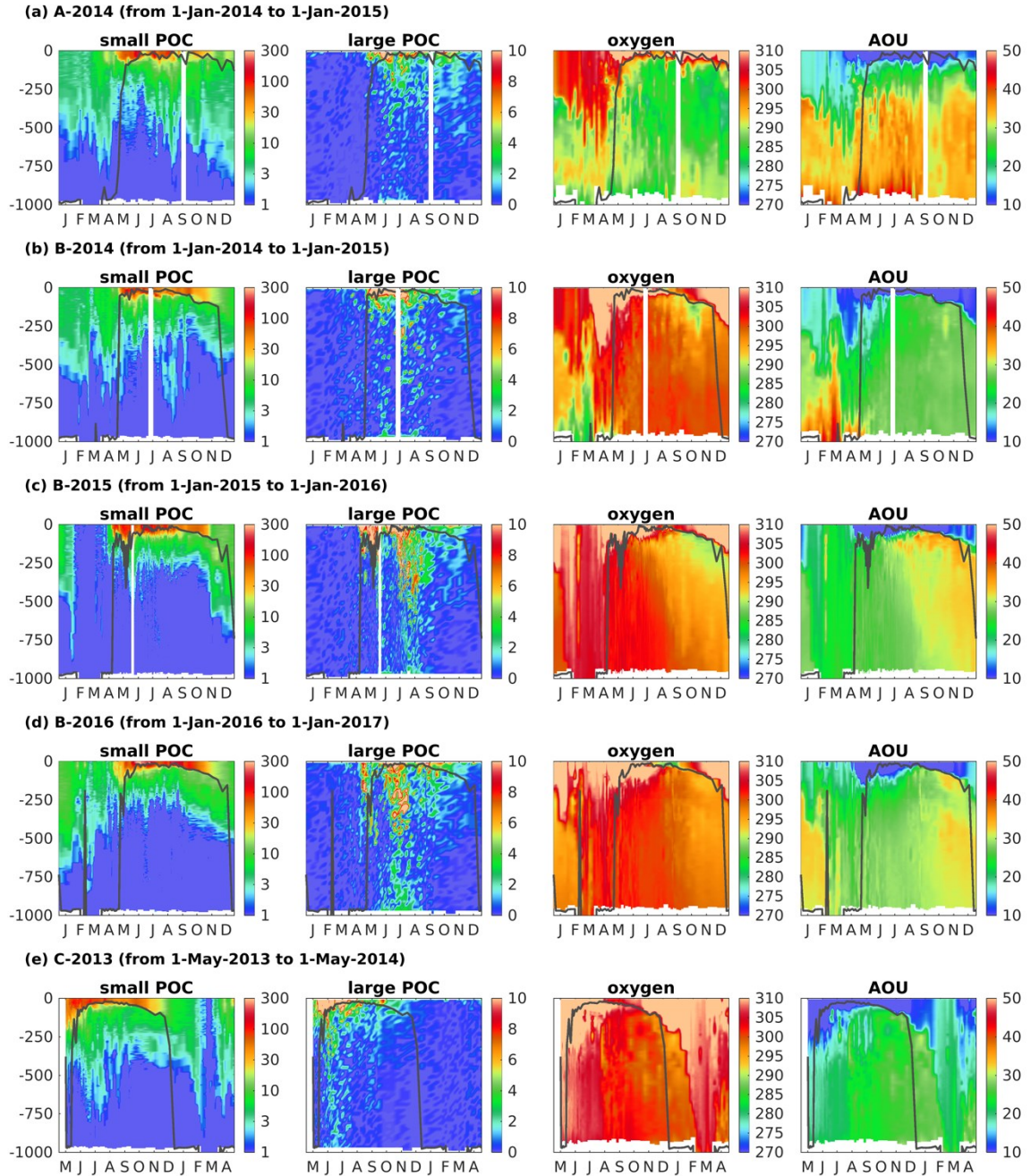
Figure 5.2. The vertical distributions of small slowing-sinking POC (mg C m⁻³), large fast-sinking POC (mg C m⁻³), dissolved oxygen (mmol O₂ m⁻³), and AOU (mmol O₂ m⁻³) from each float segment. The mixed layer depth is shown by the black solid lines.

5.2.2 POC flux due to different mechanisms

In this chapter, I extend the approach of Dall'Olmo and Mork (2014) to explicitly account for remineralization and fragmentation. As shown in Fig. 5.3, the small POC

within the mesopelagic zone can be supplied by the downward transport from the upper layers. At the same time, it will be remineralized to consume oxygen and be produced by the fragmentation of large POC. To estimate the vertical flux of small POC, it was integrated over progressively deeper parts of the mesopelagic zone ($iPOC_S^{900}(z,t)$, in units of mg C m^{-2}, with $100\,m \leq z \leq 900\,m$; please see Table E.1 for parameters and abbreviations used in this chapter) as follows:

$$iPOC_S^{900}(z,t) = \int_z^{900} POC_S(z,t)dz, \tag{5.1}$$

Assuming no small POC flux at the base of mesopelagic zone at 900 m and that the carbon-specific remineralization rate of small POC (r_s, day^{-1}) and the fragmentation rate of large POC (d_L, day^{-1}) are constant, the temporal evolution of $iPOC_S^{900}(z,t)$ is then given by:

$$\frac{\partial iPOC_S^{900}(z,t)}{\partial t} = S^{900}(z,t) - r_s \cdot iPOC_S^{900}(z,t), \tag{5.2}$$

where $S^{900}(z,t)$ (mg C m^{-2} day^{-1}) represents the supply of small POC including the total carbon flux at depth z due to different mechanisms ($totF_s(z,t)$, mg C m^{-2} day^{-1}) and the vertically integrated fragmentation flux below depth z ($iFrag^{900}(z,t)$, mg C m^{-2} day^{-1}), or:

$$S^{900}(z,t) = totF_s(z,t) + iFrag^{900}(z,t), \tag{5.3}$$

$$iFrag^{900}(z,t) = \int_z^{900} d_L \cdot POC_L(z,t)dz, \tag{5.4}$$

Following Briggs et al. (2020), the fragmentation was assumed to be proportional to large POC ($POC_L(z,t)$) and refers to a net effect of aggregation and fragmentation.

As stated above, the remineralization rate (r_s) was assumed to be constant. Although it is dependent on temperature and will be slowed by low oxygen, given the relatively constant temperature profiles and abundant oxygen within the mesopelagic zone in the study region (Fig. E.2), this is a reasonable assumption.
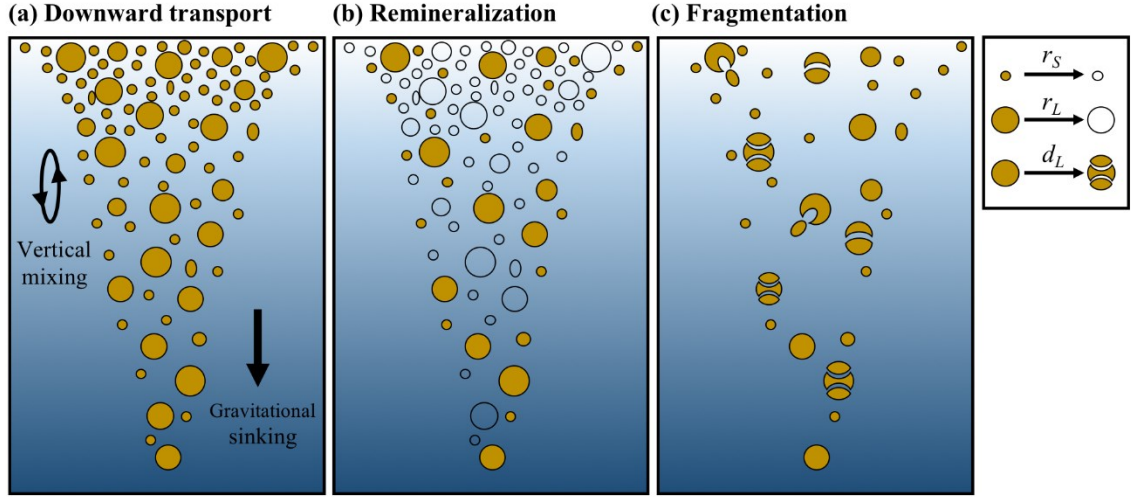
Figure 5.3. A schematic illustrating the processes considered, i.e., downward transport of small and large POC into the deep ocean (a), remineralization (b), and fragmentation of large POC into small POC (c). The open circles in panel (b) refer to small and large POC that was removed from the water column due to remineralization.

I further assumed that the supply $S^{900}(z,t)$ is constant in time between two consecutive sampling dates and therefore can be estimated as (see Appendix E for detailed derivation):

$$S^{900}(z) = \frac{r_s \cdot (iPOC_S^{900}(z, t_1) - iPOC_S^{900}(z, t_0)e^{-r_s \Delta t})}{1 - e^{-r_s \Delta t}}, \tag{5.5}$$

where t_0 and t_1 are two adjacent sampling times which can be between 1 and 11 days apart, and are typically within 50 km (Fig. E.3), Δt is the time interval between them. When remineralization and fragmentation are neglected (i.e., $r_s = 0$, $d_L = 0$), Eq. 5.5 simplifies to the equation used by Dall'Olmo and Mork (2014), meaning that the vertical flux of small POC is equivalent to the accumulation rate of $iPOC_S^{900}(z,t)$ (see Appendix E).

Small POC can be transported through various mechanisms including gravitational settling, vertical mixing, and downward circulation components (Resplandy et al. 2019). So far, no assumption was made about the nature of the vertical flux ($totF_s(z,t)$ includes all possible mechanisms). The gravitational sinking flux of small POC ($GravF_S(z,t)$, mg C m^{-2} day^{-1}) can be estimated by multiplying its concentration and sinking velocity as:

$$GravF_S(z,t) = w_s \cdot POC_S(z,t), \tag{5.6}$$

Then the gravitational sinking flux of large POC can be estimated similarly. Finally, the difference between $GravF_S(z,t)$ and $totF_S(z,t)$ can be attributed to other downward transport mechanisms as:

$$otherF_S(z,t) = totF_S(z,t) - GravF_S(z,t). \tag{5.7}$$

5.2.2.1 Remineralization rate

Remineralization rates of small and large POC were estimated using oxygen observations below the mixed layer. The rate of change of subsurface oxygen can be written as:

$$\frac{\partial O_2(z,t)}{\partial t} = -1.45 \cdot Resp(z,t) - \vec{u} \cdot \nabla O_2(z,t) + \nabla\big(\kappa \cdot \nabla O_2(z,t)\big), \tag{5.8}$$

where the respiration ($Resp(z,t)$) is scaled by 1.45 to convert between carbon and oxygen (Anderson and Sarmiento 1994). After neglecting physical advection ($\vec{u} \cdot \nabla O_2(z,t)$) and diffusion ($\nabla(\kappa \cdot \nabla O_2(z,t))$) similar to Hennon et al. (2016), the oxygen change rate was integrated over time and related to the small and large POC as:

$$\frac{\Delta O_2(z,t)}{1.45} = \int resp(z,t)dt = -r_s \cdot \int \frac{POC_S(z,t)}{12}dt - r_L \cdot \int \frac{POC_L(z,t)}{12}dt. \tag{5.9}$$

To remove the influence of temperature and salinity changes, the oxygen concentration was replaced by the Apparent Oxygen Utilization $AOU(z,t)$ (mmol O_2 m^{-3}) which is defined as the oxygen deficit relative to its saturation:

$$\frac{\Delta AOU(z,t)}{1.45} = r_s \cdot \int \frac{POC_S(z,t)}{12}dt + r_L \cdot \int \frac{POC_L(z,t)}{12}dt. \tag{5.10}$$

The factor 12 is to convert POC concentration from mg C m^{-3} into mmol C m^{-3}. To follow the movement of water masses, I divided the mesopelagic zone into 20 isopycnal levels. Sensitivity tests showed that the number of isopycnal levels has little influence on the results. I then tested a range of parameter values for r_s and r_L by calculating the root-mean-square-error (RMSE) between the observed and fitted $\Delta AOU(z,t)$ (Fig. 5.4). The optimal values can be estimated by minimizing the RMSE. To account for the uncertainty, all

values with an RMSE within 0.1 mmol O_2 m^{-3} of the minimal RMSE were considered as likely values (Table 5.1, Fig. 5.4).

Table 5.1. A list of modelled key parameter values and vertical carbon fluxes due to different mechanisms at 100 and 600 m. The standard deviations are given in parentheses.

	A-2014	B-2014	B-2015	B-2016	C-2013
r_S (day^{-1})	0.05 (0.01)	0.06 (0.02)	0.03 (0.01)	0.06 (0.01)	0.10 (0.02)
w_S (m day^{-1})	4.42 (1.37)	5.78 (1.66)	1.84 (0.40)	6.04 (1.10)	6.66 (1.42)
$l_{S,r}$ (m)	92.25	92.73	68.28	102.08	67.48
r_L (day^{-1})	0.12 (0.07)	0.10 (0.06)	0.11 (0.02)	0.08 (0.03)	0.11 (0.06)
d_L (day^{-1})	0.12 (0.04)	0.12 (0.03)	0.01 (0.00)	0.01 (0.00)	0.23 (0.05)
A_L (day^{-1})	0.25 (0.03)	0.22 (0.03)	0.12 (0.02)	0.08 (0.03)	0.34 (0.02)
w_L (m day^{-1})	87.18 (11.33)	78.62 (10.49)	28.58 (3.96)	32.92 (10.30)	59.54 (3.79)
l_L (m)	354.11	359.84	245.46	399.36	177.65
The vertical carbon fluxes at 100m (unit: g C m^{-2} yr^{-1})					
totF	58.12 (2.85)	63.35 (3.24)	35.75 (1.57)	59.18 (2.86)	74.05 (7.09)
GravF$_L$	36.73 (4.77)	40.10 (5.35)	23.00 (3.19)	22.13 (6.92)	38.75 (2.47)
GravF$_S$	13.21 (4.10)	17.04 (4.89)	5.84 (1.27)	21.47 (3.92)	23.18 (4.94)
OtherF$_S$	8.19 (2.21)	6.20 (1.77)	6.90 (1.17)	15.58 (2.94)	12.12 (3.30)
iFrag	16.27 (5.05)	16.09 (4.62)	1.99 (0.43)	1.60 (0.29)	29.77 (6.34)
The vertical carbon fluxes at 600m (unit: g C m^{-2} yr^{-1})					
totF	9.93 (0.84)	11.99 (1.62)	4.42 (0.35)	6.94 (1.27)	7.25 (0.42)
GravF$_L$	8.53 (1.11)	12.15 (1.62)	3.43 (0.48)	5.18 (1.62)	6.98 (0.44)
GravF$_S$	2.64 (0.82)	2.25 (0.65)	0.39 (0.09)	1.63 (0.30)	2.85 (0.61)
OtherF$_S$	-1.24 (0.51)	-2.41 (0.65)	0.60 (0.07)	0.14 (0.09)	-2.58 (0.57)
iFrag	2.90 (0.90)	3.73 (1.07)	0.31 (0.07)	0.29 (0.05)	6.35 (1.35)
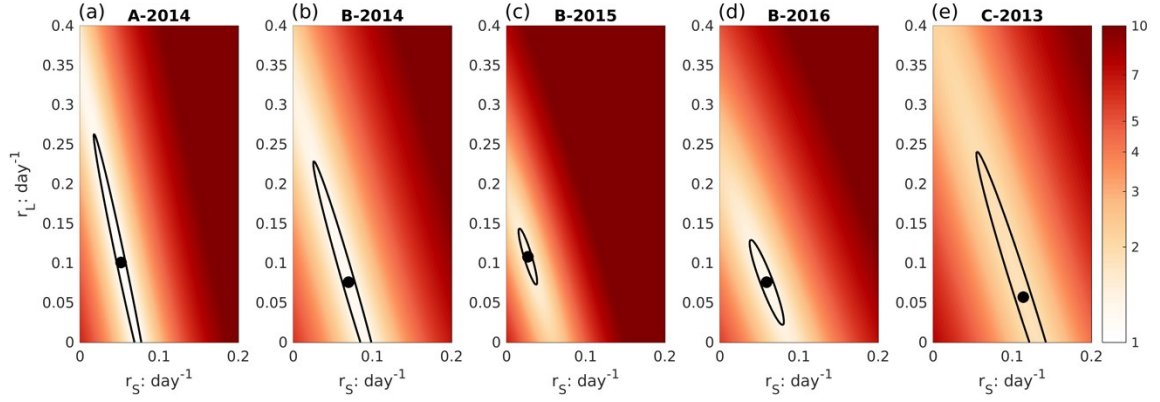
Figure 5.4. The RMSE of different remineralization rates for small (r_s) and large POC (r_L). The black dots represent the RMSE minima and the black contour lines include all values within 0.1 mmol O_2 m^{-3} of the minimum.

5.2.2.2 Remineralization length scale

Assuming a constant sinking velocity (w_L, m day^{-1}) and net attenuation rate (A_L, day^{-1}) of large POC, the temporally averaged vertical profile of large POC can be represented by:

$$\frac{\overline{POC_L(z)}}{\overline{POC_L(100)}} = exp\left(-A_L \frac{z-100}{w_L}\right),\tag{5.11}$$

where $\overline{POC_L(z)}$ is the temporally averaged large POC concentration at depth z (noting that $z = 100$ m defines the base of euphotic zone). The net attenuation rate of large POC is the sum of the remineralization rate (r_L, day^{-1}) and the fragmentation rate (d_L, day^{-1}), i.e.,

$$A_L = r_L + d_L.\tag{5.12}$$

Therefore, the remineralization length scale of large POC ($l_L = w_L/A_L$, m) can be estimated by fitting the temporally averaged vertical profile of large POC to Eq. 5.11 (Fig. 5.5, Table 5.1).
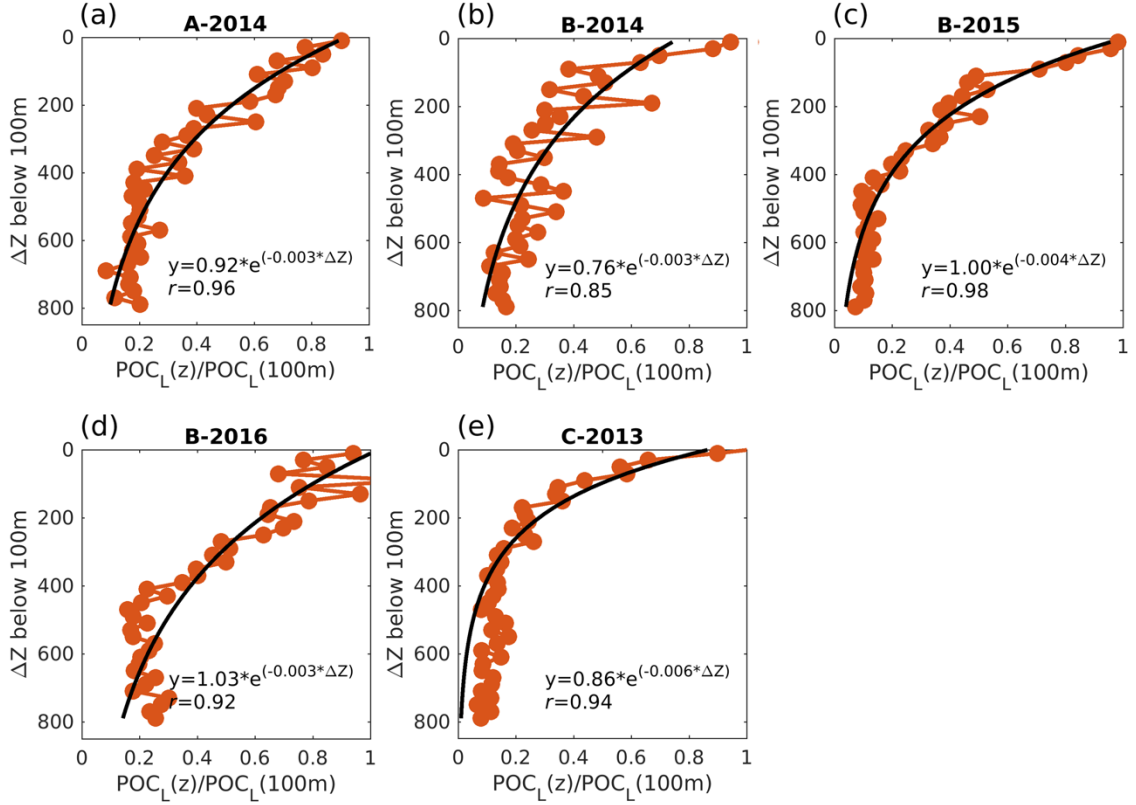
Figure 5.5. The vertical profiles of large POC and their fitting curves of each float segment.

Likewise, by assuming a constant sinking velocity (w_S, m day^{-1}) and remineralization rate (r_S, day^{-1}) for small particles, the remineralization length scale of small POC ($l_S(z) = w_S/A_S(z)$, m) is modulated by the fragmentation rate (d_L) and the ratio of large to small POC (Fig. 5.6) as follows (see Appendix E for detailed derivation)

$$\frac{1}{l_S(z)} = \frac{1}{l_{S,r}} - \frac{1}{l_{S,r}} \cdot \frac{d_L}{r_s} \cdot \frac{\overline{POC_L(z)}}{\overline{POC_S(z)}}. \tag{5.13}$$

To solve Eq. 5.13, the temporally averaged vertical profiles of small and large POC are divided into 100 m vertical bins. Within each vertical bin, the ratio between large and small POC ($\overline{POC_L(z)}/\overline{POC_S(z)}$) is estimated and the remineralization length scale ($l_S(z)$) is obtained by fitting the temporal averaged vertical profile of small POC to Eq. E.19. As a result, the remineralization length scale when fragmentation is not considered ($l_{S,r} = w_S/r_S$, m) can be derived from the inverse of regression intercept shown in Fig. 5.6. The

ratio between fragmentation and remineralization rate of small POC (d_L/r_s) can be obtained by dividing the regression slope by the intercept.
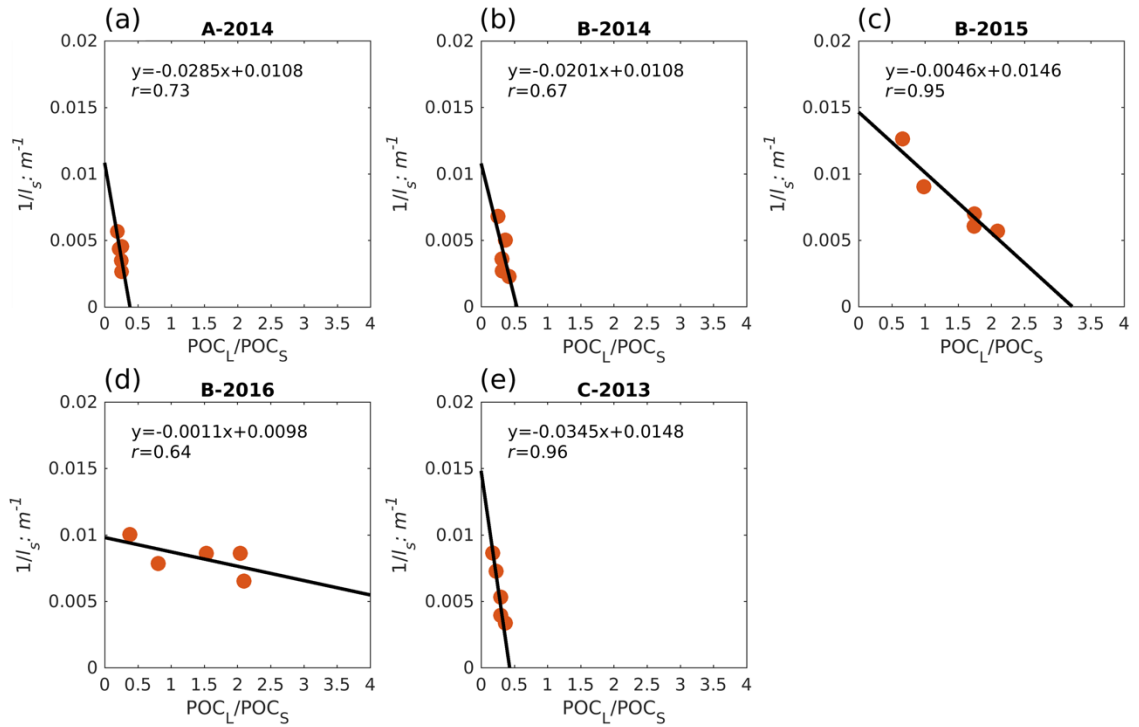
Figure 5.6. Relationships between the remineralization length scale of small POC and the ratio of large POC to small POC

Since Eq.s 5.11 and 5.13 do not apply during periods of deep winter mixing, only profiles from May to October were used. Also, observations from below 600 m were not used because the small POC concentrations are not distinguishable from zero and would introduce large uncertainties when calculating their remineralization length scale ($l_S(z)$).

5.2.3 Comparisons with in-situ and satellite-based vertical flux

In-situ [234]Th-based measurements of the vertical carbon flux at 100 m are obtained from the supplement of Henson et al. (2019) (locations shown in Fig. 5.1) and are averaged into the monthly climatology. Given that the [234]Th-based fluxes are typically interpreted as an integrated measurement over several days to weeks prior to the sampling (Buesseler et al. 2006) and the derived flux based on the BGC-Argo float data are average fluxes over two consecutive sampling times (1-11 days), the [234]Th-based fluxes will be compared with

my estimates of the total carbon flux at 100 m which have been smoothed using a 24-day filter because the half-live of ^{234}Th decay is 24 days.

In addition, a compilation of satellite-derived vertical flux estimates at 100 m including two net primary production (NPP) algorithms and four estimates of the flux-to-NPP ratio is used for comparison. The NPP estimates, namely the Vertically Generalized Production Model (VGPM, Behrenfeld & Falkowski, 1997) and the Carbon-based Production Model (CbPM, Westberry et al., 2008), are obtained from Oregon State University (http://sites.science.oregonstate.edu/ocean.productivity/index.php). The flux-to-NPP ratio is determined by four commonly used algorithms. Specifically, the algorithm from Dunne et al., (2005) is based on sea surface temperature (SST) and NPP (or surface chlorophyll), which hereafter is named as Dunne_NPP (or Dunne_CHLA). To maximize the data availability, they used all data of new production, the net community production, and the sinking flux from in-situ sediment traps and ^{234}Th-based method. The algorithm from Henson et al., (2011) relies on observations from Laws et al., (2000) to predict the f-ratio (the ratio of new production to total production) based on SST and hereafter is referred to as Laws. These three algorithms have been widely used to represent the net community production, which is equivalent to the flux of organic carbon under steady state. Finally, the SST-based algorithm is formulated from ^{234}Th-based measurements by Henson et al., (2011) (hereafter Henson). Therefore, all of these satellite algorithms will be compared to my estimates of total vertical carbon flux at 100 m.

To calculate the flux-to-NPP ratio, the daily-averaged SST is obtained from Advanced Very High Resolution Radiometer (AVHRR; Martin et al., 2012) and the monthly-averaged surface chlorophyll is provided by the Ocean-Colour Climate Change Initiative project (OC-CCI; Sathyendranath et al., 2018). All these satellite data are averaged into an annual climatology and grouped into 1×2 degrees bins (~100 km) before calculating the vertical carbon flux (Fig. E.4).

5.3 Results

The annually averaged vertical carbon fluxes at 100 and 600 m due to gravitational settling and other mechanisms, and the fragmentation flux are shown in Fig. 5.7 and Table

5.1 for each float segment. The estimates of key parameters, e.g., the remineralization rate, the fragmentation rate, and the sinking velocity, are also shown in Table 5.1. The total vertical flux (*totF*) is the sum of the different downward transport mechanisms; it does not include the fragmentation flux (Fig. 5.7a, f). The annually averaged *totF* varies from 35.75 ± 1.57 to 74.05 ± 7.09 g C m^{-2} yr^{-1} at 100 m (Fig. 5.7a, Table 5.1), which is in general higher than the Henson-algorithm (Fig. E.5g, h) possibly because this algorithm underpredicted the large uncertainties of carbon flux in high latitudes (Henson et al. 2011). After excluding the Henson-algorithm, my results are similar with CbPM-based estimates of 47.36 to 71.31 g C m^{-2} yr^{-1} (Fig. E.5a, c, e) but lower than the VGPM-based ones of 76.36-114.83 g C m^{-2} yr^{-1} (Fig. E.5b, d, f). In addition, comparisons with the in-situ ^{234}Th fluxes also suggest that my estimates are in a reasonable magnitude (Fig. E.6). At 600 m, *totF* decreases to between 4.42 ± 0.35 and 11.99 ± 1.62 g C m^{-2} yr^{-1} (Fig. 5.7f, Table 5.1). The transfer efficiency, defined here as the flux ratio between 600 and 100 m, ranges from $10\pm1\%$ to $19\pm3\%$.
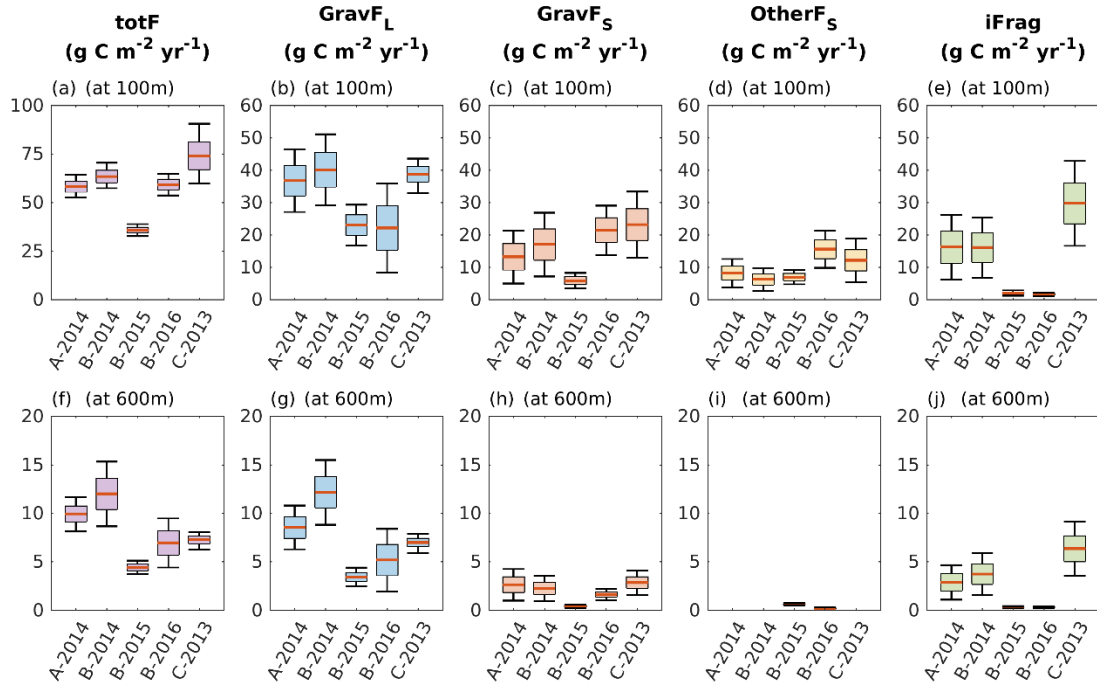

Figure 5.7. Annually averaged vertical carbon flux due to gravitational settling and other mechanisms, and fragmentation of large to small POC from each float segment at 100 and 600 m. The orange lines represent the mean values while the colored boxes represent +/- one standard deviation. The upper and lower error bars represent maximum and minimum values.

At 100 m, the gravitational sinking flux of large POC ($GravF_L$) is 22.13±6.92 to 40.10±5.35 g C m^{-2} yr^{-1}, which accounts for more than 60% of *totF* in three of the five float segments, 53±7% in C-2013, and 37±11% in B-2016 (Fig. 5.7b). At 600 m, the relative contribution of large POC increases to more than 70% due to its relatively higher transfer efficiency (15%-30%).

The gravitational settling of small POC ($GravF_S$) accounts for 16±4% to 36±7% of *totF* at 100 m and 9±3% to 40±10% at 600 m (Fig. 5.7c, h). The vertical flux of small POC due to other mechanisms ($OtherF_S$; Fig. 5.7d) including vertical mixing and downward transport contributes less (10±3% to 26±5%). This flux attenuates quickly to about 0 at 600 m. In addition to transport from above, fragmentation (*iFrag*) is also a source of small POC within the mesopelagic zone and supplies small POC at a rate comparable to the total vertical flux of small POC ($totF_S$) in some float segments, i.e. A-2014, B-2014, and C-2013 (Fig. 5.7e).

To account for the uncertainties of each mechanism, I defined the coefficient of variation as the ratio between standard deviation and mean. As shown in Fig. 5.7, the uncertainty of *totF* is usually lower than that of each component. Except for C-2013, the coefficient of variation at 100 m varies from 13% to 31% for the $GravF_L$ and from 18% to 31% for the $GravF_S$ but is only 5% for *totF*. The uncertainty of *totF* grows with increasing depth. At 600 m, the coefficient of variation for *totF* varies from 8% to 18% (Fig. 5.7f), a 1.6 to 3.6-fold increase from 100 m.

5.4 Discussion

5.4.1   Importance of remineralization and fragmentation

To the best of my knowledge, this is a first observation-based study to estimate the annual vertical carbon flux due to different mechanisms that explicitly accounts for remineralization and fragmentation. Previous studies which estimated the vertical flux of small POC assumed that its seasonal accumulation (i.e., during the winter-to-summer transition period) within the mesopelagic zone is due only to transport from upper layers (e.g., Dall'Olmo and Mork 2014; Bol et al. 2018; Kheireddine et al. 2020). Although there are differences in the details of these previous algorithms, this assumption was made in all

of them. Some studies suggested that this seasonal flux can contribute more than 20% of the total vertical flux at the base of euphotic zone in high latitudes (e.g., Bol et al., 2018; Dall'Olmo et al., 2016). However, this simple estimate is likely biased by neglecting the remineralization and fragmentation, and will confound our understanding of the relative contributions from small and large POC. For instance, if I estimated the annual vertical flux of small POC ($totF_S$) at 100 m in my data set while neglecting the fragmentation ($d_L = 0$), it would increase by over 70% in three of five float segments, i.e. A-2014, B-2014, C-2013 (Fig. 5.8), indicating that the fragmentation flux can be as important as the vertical flux of small POC. Although its importance has been acknowledged previously (e.g., Dall'Olmo and Mork 2014; Baker et al. 2017; Briggs et al. 2020), the fragmentation has not been subtracted when estimating the vertical flux of small POC and is indeed double accounted (Boyd et al. 2019). Neglecting fragmentation and remineralization ($d_L = r_S = 0$) will markedly decrease the estimate of annual vertical flux of small POC. As shown in Fig. 5.8, it would range from -3.34 to 1.52 g C m^{-2} yr^{-1} at 100 m and very different from my estimates that consider remineralization and fragmentation. This is because the majority of small POC flux is remineralized in the mesopelagic zone. Although the part that is being remineralized does not contribute to the accumulation of small POC, it provides substantial energy to the heterotrophic metabolism in the mesopelagic zone, and neglecting it underestimates the contributions of small POC to the mesopelagic metabolism. Therefore, quantifying remineralization and fragmentation is important when estimating the vertical flux of small POC. Given their key roles in flux attenuation, knowing these two rates also improves our understanding of the transfer efficiency of the biological carbon pump.
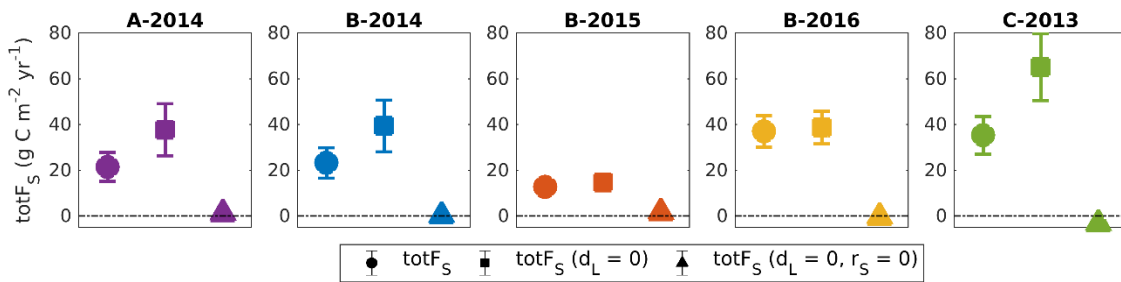

Figure 5.8. Annually averaged vertical flux of small POC ($totF_S$) at 100 m from each float segment when considering remineralization and fragmentation (circles), when neglecting

fragmentation (squares), and when neglecting both remineralization and fragmentation (triangles). The error bars represent the mean values and +/- one standard deviation.

In addition, by calculating the remineralization rate, the fragmentation rate, and other associated parameters (e.g., sinking velocity), I decoupled the vertical carbon flux due to different mechanisms and compared their relative contributions. In previous studies, the seasonal accumulation of small POC was attributed to variations of mixed layer depth and its derived flux was referred to as mixed layer pump (e.g., Dall'Olmo and Mork 2014; Bol et al. 2018; Kheireddine et al. 2020). However, this seasonal accumulation of small POC is a combination of multiple processes. Apart from remineralization and fragmentation, which have been addressed above, small POC can be transferred into the mesopelagic zone by different mechanisms, e.g., gravitational settling, vertical mixing, and downward circulation components (Stukel et al. 2017, 2018; Resplandy et al. 2019). Results show that the gravitational sinking flux of large POC is the dominant vertical carbon flux. At the same time, small POC supplements the total flux significantly at 100 m through gravitational settling and other mechanisms.

Small POC is not an efficient contributor to long-term carbon sequestration. Based on Eq. 5.13, if there is no fragmentation, the remineralization length scale of small POC ($l_{S,r}$) varies from about 70 to 100 m (Fig. 5.6, Table 5.1). This implies that after escaping the surface layer, a vast majority of small POC is remineralized leaving only a tiny fraction (<1%) that can reach the lower mesopelagic zone at 600 m. As a result, the $GravF_S$ will only account for less than 1% in four of five float segments and about 2±1% in B-2016 of the total flux at 600 m. However, the transfer efficiency (from 7% to 20%) and the relative contributions (from 9±3% to 40±10%) of $GravF_S$ are much higher. This is partly because fragmentation supplies small POC along its pathway of gravitational settling and prolongs its actual remineralization length scale, emphasizing again that fragmentation is an important source of small POC within the mesopelagic zone (Table 5.1). Small POC can also be directly injected to below 600 m but this contribution to the annual flux is small (Table 5.1).

5.4.2 Uncertainty assessment

The uncertainties of individual mechanisms shown in Fig. 5.7 are large because the two remineralization rates (r_S and r_L) are interdependent and thus difficult to constrain simultaneously. Both of them lead to a decrease in oxygen (Fig. 5.3b), therefore an increase in one remineralization rate can be compensated by the decrease in the other, while resulting in similar oxygen respiration. Once the remineralization length scale is determined, the estimates of $GravF_S$ and $GravF_L$ will change proportional to r_S and r_L, respectively. This issue is referred to as underdetermination and happens because this model is complicated in terms of what can be constrained by the observations, although it is simple when compared to nature. Therefore, more independent observations that contain new information and prior knowledge of controlling processes that can be used to fix some parameters, e.g., the sinking velocity and remineralization rate, would provide additional constraints and reduce the uncertainties of each mechanism. For instance, the sinking velocity of particles can be measured by imaging techniques (see review by Giering et al. 2020) and the emergence of imaging sensors which can be deployed on profiling floats (e.g., the miniaturized Underwater Vision Profiler; Picheral et al. 2022) are promising to provide a global monitoring of sinking velocity. Finally, since reverse changes in remineralization rates largely cancel each other out when estimating $totF$, its uncertainty is smaller than that of the individual mechanisms.

The uncertainty of $totF$ grows with increasing depth because the transfer efficiency varies across different mechanisms. $GravF_L$ is most efficient. Its dominance increases with depth while the relative contributions from other mechanisms decrease. Therefore, a better characterization of the relative contributions from each mechanism is key to better constrain the transfer efficiency of $totF$.

It has been suggested that uncertainty in the conversion from backscatter to POC could introduce significant uncertainties in derived estimates (Bol et al. 2018). I found that estimates in the remineralization rates are indeed affected by changes in the conversion while the vertical flux estimates themselves are not. For instance, the POC/bbp slope in the conversion from Stramski et al. (2008, 53607 mg C m^{-2} at the wavelength of 555nm) is over 50% higher than the slope from Cetinić et al., (2012) which I used below the mixed

layer (assuming a spectral dependence of 0.41 or bbp(λ) $\sim \lambda^{-0.41}$). In my calculations, increasing/decreasing the POC/bbp slope by 50% will lead to an inverse change in the two remineralization rates but leaves carbon fluxes due to each mechanism unchanged. This is because the slope of the POC/bbp conversion does not change the relative vertical profiles or the remineralization length scales of small and large POC (Figs. 5.5 and 5.6). For a given respiration rate, POC concentrations and remineralization rates change in reverse directions when the slope of the POC/bbp conversion is altered (Eq. 5.10). This will yield proportional changes in sinking velocities and fragmentation rate to remineralization rates but leave the resulting fluxes unchanged. Nevertheless, the parallel cruises are encouraged for calibrating proxy measurements from autonomous platforms such as the BGC-Argo floats and for estimating the parameter values, e.g., the remineralization rate, the fragmentation rate, and sinking velocity.

Finally, the respiration quotient which describes the molar ratio between oxygen and POC consumed during respiration will introduce additional uncertainties into the estimates of the vertical carbon flux. In this chapter, the respiration quotient of POC is fixed at 1.45 based on Anderson and Sarmiento (1994) who suggested little variability across different depth and basins. However, a distinct latitudinal gradient was reported in a recent study (Moreno et al. 2020), possibly driven by a shift in molecular compositions of the POC in different ecosystem communities.

5.4.3 Variability between float segments

As shown in Fig. 5.7, there is no significant discrepancy of *totF* at 100 m among three float segments, i.e. A-2014, B-2014, and B-2016. However, the similar *totF* at 100 m results from different contributions of each mechanism, which in turn leads to diverging transfer efficiencies of *totF*. For instance, *GravF$_L$* is much higher in A-2014 and B-2014 (Fig. 5.7). As shown in Fig. 5.6, the ratio of large to small POC (POC_L/POC_S) is almost constant with depth in A-2014 and B-2014 but increases significantly with depth in the B-2016. Given that remineralization will remove small POC preferentially while the fragmentation tends to redistribute mass from large to small POC, fragmentation is likely more important in A-2014 and B-2014. This increases the net attenuation rate (A_L, based on Eq. 5.12), the sinking velocity (w_L), and the *GravF$_L$* simultaneously (Table 5.1).

Nevertheless, the differences in POC_L/POC_S ratios could be also explained by other processes that are not considered in this simple model, e.g., depth-dependent remineralization, fragmentation, and sinking velocities.

5.4.4 Caveats and limitations

In this chapter, I assumed constant remineralization and fragmentation rates. However, previous studies suggested that these rates depend on temperature and oxygen to explain the latitudinal patterns of the transfer efficiency and the slow attenuation in the oxygen minimum zones (Weber et al. 2016; Laufkötter et al. 2017; Weber and Bianchi 2020). Therefore, my method is appropriate in regions with low temperature variations and replete in oxygen and can be extended to other regions by accounting for the temperature- and oxygen-dependence (see Appendix E). Other environmental factors that can change the remineralization rate, e.g., the ecosystem structures, are difficult to explicitly consider in such a simple model. However, this model is a start to decouple the vertical carbon flux due to different mechanisms based on BGC-Argo floats and the constant remineralization and fragmentation rates can be interpreted as the averaged rate.

In addition, I have assumed that lateral advection can be ignored. Whenever lateral advection introduces water masses with different age and AOU, this will introduce biases in the remineralization rate estimates. Therefore, I removed float segments with obvious intrusion of water masses.

Finally, my estimates of the remineralization rate, fragmentation rate, and sinking velocity are consistent with several estimates using other methods. Briggs et al. (2020) applied a different method to BGC-Argo float data from the north Atlantic and Southern Ocean and obtained the sinking velocity (58-100 m day^{-1}) and fragmentation rate of large particles (0.03-0.27 day^{-1}). My estimates are similar, except in B-2015 and B-2016 (Table 5.1), which are lower than theirs. Measurements from a suite of marine snow catchers deployed from 25-600 m depth in the subpolar and polar Atlantic yielded median concentrations of small and large POC of 5.5 mg C m^{-3} and 0.07 mg C m^{-3}, respectively, and fluxes of 99.0 mg C m^{-2} day^{-1} and 14.1 mg C m^{-2} day^{-1} (Baker et al. 2017). The weighted average sinking velocity of POC can then be estimated as about 20 m day^{-1}, which is close

to my estimates from 9 to 18 m day^{-1}. A recent study by Durkin et al. (2021) estimated the carbon flux of nine different sinking particle classes using imaging techniques and also suggested that small particles contributed less to the modelled total flux except that their contribution (5±3%) in samples with high fluxes (2-20 mmol C m^{-2} day^{-1}, which is equivalent to 8.76-87.6 g C m^{-2} yr^{-1}) is much lower than my estimates. However, comparisons between different methods are difficult because the definition of small/large particles varies and there is no consensus as to the particle size that is represented by the baseline and spike signals of backscattering. The baseline signals have been interpreted as representative of particles with a diameter of 0.2-20 μm (Dall'Olmo and Mork 2014; Lacour et al. 2019), <100 μm (Briggs et al. 2020), and even <150 μm (Giering et al. 2020).

5.5 Conclusions

In this chapter, I estimated vertical carbon flux, its transfer efficiency between 100 and 600 m, and the relative contributions of different mechanisms to the flux from BGC-Argo profiles of backscattering and dissolved oxygen by explicitly accounting for remineralization and fragmentation. Results show that on annual timescales in the subpolar North Atlantic, the gravitational sinking flux of large POC is the dominant mechanism and most efficient in surpassing flux attenuation within the mesopelagic zone. However, small POC are also transported out of the euphotic zone via different mechanisms and can make a large contribution to the flux at 600 m due to the fragmentation of large POC in the mesopelagic zone. Without the continuous supply from fragmentation, small POC would be fully remineralized before reaching the lower mesopelagic zone at 600 m. In addition, this chapter also shows the importance of remineralization and fragmentation to the estimates of the vertical flux of small POC.

In general, this method can well constrain the total vertical flux at 100 m but has larger uncertainties in each mechanism and therefore in estimating the transfer efficiency of the total flux. More independent observations and prior knowledge of the controlling processes, e.g., sinking velocity, remineralization rate, and fragmentation rate, can help reduce these uncertainties.

CHAPTER 6
CONCLUSIONS

The ocean's BCP is fundamentally important as it can sequester carbon in the deep ocean and control atmospheric CO_2 levels but remains poorly characterized. Conventional methods of observing the vertical flux of organic matter, by sediment traps and radioactive tracers, are limited in their spatiotemporal coverage because of the effort and cost involved and hence insufficient to constrain the BCP. In addition, some mechanisms driving the BCP, e.g., the mixed layer pump and the eddy subduction pump, are likely not well sampled by these techniques due to their localized and episodic nature. The deployment of BGC-Argo floats in recent years has provided numerous profile observations of key biogeochemical properties in the global ocean and opens opportunities for better understanding the marine ecosystem including the BCP. Therefore, the potential value and new applications of BGC-Argo observations for understanding the BCP warrant further exploration.

My thesis is motivated by these facts and aims to explore potential applications of BGC-Argo data for improving estimates and our mechanistic understanding of the BCP by exploring synergies between BGC-Argo float data and biogeochemical models, as well as comprehensive data analyses of the high frequency BGC-Argo observations. Specifically, a suite of optimization experiments was conducted using different combinations of satellite chlorophyll and profiling observations (i.e., chlorophyll, phytoplankton, and POC) from five BGC-Argo floats in the Gulf of Mexico, by which the additional benefits of BGC-Argo floats in reducing model errors due to the poorly known parameters were evaluated (Chapter 2). Then a multivariate physical-biological data assimilation scheme was applied to the coupled physical-biological model, of which the biological parameters have been optimized in Chapter 2, to reduce model uncertainties inherited from stochastic processes, e.g., the Loop Current and the Loop Current eddies. An alternative light parameterization scheme that has been calibrated *a priori* by the BGC-Argo observations was also applied

and the data assimilation experiments repeated. Results show that a well-calibrated model with accurate parameterization schemes is important to the success of data assimilation (Chapter 3). This finding motivated me to investigate to what extent the BGC-Argo float data could help in distinguishing different alternative parameterization schemes of POC flux, which have been reported to fit the sparse in situ observations of POC flux equivalently well but produce different atmospheric CO_2 levels (Chapter 4). Finally, a new method based on a mass balance of POC and dissolved oxygen was introduced to evaluate the relative contributions of small versus large particles to the BCP in the subpolar North Atlantic when taking effects of remineralization and fragmentation into consideration (Chapter 5).

6.1 Major findings

The major findings of my thesis and their significance are summarized below for each of the research questions posed in Chapter 1.

(1) What is the value of BGC-Argo profiles for parameter optimization (Chapter 2)?

As parameter optimization in 3D models is computationally expensive, the biological parameters are optimized in a 1D model version and then used to perform 3D simulations. The optimization experiments show that the use of optimal 1D parameters, with a few modifications, improves the skill of the 3D model. Parameters that are only optimized with respect to satellite surface chlorophyll cannot reproduce the subsurface distribution of biological properties. Adding profiles of chlorophyll in the parameter optimization yields significant improvements for surface and subsurface chlorophyll but does not well capture subsurface distributions of phytoplankton and POC because the parameter that controls the chlorophyll-to-phytoplankton-carbon ratio is not well constrained in that case. Using all available observations leads to significant improvements of both observed (chlorophyll, phytoplankton, and POC) and unobserved (e.g., primary production and carbon export flux at 200 m) variables. These results highlight the significant benefits of BGC-Argo observations for parameter optimization and model calibration, not only because of their abilities to provide subsurface measurements but also to observe multiple independent properties simultaneously.

(2) Can data assimilation of satellite observations in combination with a priori model calibration by BGC-Argo profiles improve 3D distributions of biological properties (Chapter 3)?

The data assimilation results show that assimilating satellite data improves model representation of major circulation features, i.e., the Loop Current and Loop Current eddies, which translate into an improved 3D distribution of temperature and salinity. The multivariate assimilation also improves the agreement of subsurface nitrate through its tight correlation with temperature, but the improvements in subsurface chlorophyll are modest initially due to suboptimal choice of the optical parameterization scheme. Repeating the assimilation run by using an alternative light parameterization that has been calibrated *a priori* by BGC-Argo observations greatly improves the subsurface distribution of chlorophyll. Given that, so far, the abundance of BGC-Argo profiles in the Gulf of Mexico and elsewhere is still insufficient for sequential assimilation, with only a few exceptions, even sparse BGC-Argo observations can provide substantial benefits for biological data assimilation. These sparse profiles enable *a priori* model tuning. Updating 3D biological properties in a model that has been well calibrated is an intermediate step toward full assimilation of BGC Argo data.

(3) Do BGC-Argo float data add information when assessing the predictive skill of alternative vertical carbon flux parameterizations (Chapter 4)?

By comparing different parameterization schemes for vertical carbon flux from 12 ESMs that are part of CMIP6, this chapter reveals the large model-to-model variability in simulated POC flux and transfer efficiency across the ESMs. These differences lead to substantially different atmospheric CO_2 levels. Comparison between the ballast and WLin schemes in the same 1D model framework shows distinctly different simulated POC concentrations below 2000 m and suggests that it is possible to distinguish between the two model schemes by expanding backscatter measurements to the full ocean depth. In addition, the sensitivity experiments show that the observations of POC concentration can derive a unique estimate of POC flux. In the contrast, observations of POC flux cannot determine the POC concentration.

(4) What are the relative contributions from small and large particles to deep carbon sequestration (Chapter 5)?

On annual timescales, the gravitational settling of large organic particles is dominating the vertical carbon flux through the mesopelagic zone in the subpolar North Atlantic. However, small particles contribute significantly to the vertical carbon flux at 100 m, via gravitational settling and other mechanisms, and at 600 m since they can be produced by the fragmentation within the mesopelagic zone. In addition, this chapter also shows the importance of remineralization and fragmentation to the estimate of vertical carbon flux of small particles. Finally, the large uncertainties in the estimates of carbon flux due to different mechanisms can be translated into uncertainties in carbon sequestration and be reduced by more independent observations of the controlling processes.

6.2 Future work

This thesis has explored the potential applications and shown the great benefits of BGC-Argo floats to improve estimates of the BCP. However, all these applications rely on the conversion from backscatter coefficient to POC concentration using empirical relationships, which are controlled by particle composition and thus vary by geographic location, the depth, and season. For instance, a depth dependent POC/bbp slope was applied in Briggs et al., (2011) and Bol et al., (2018) to account for the preferential remineralization of organic matters without proportional reduction in the backscatter coefficient. In this thesis, I applied a constant POC/bbp slope in chapters 2 and 3. Although in chapters 4 and 5, two distinct slopes were used above and below the mixed layer depth, this slope kept constant within each of these two layers. This introduces uncertainties into estimates of POC concentration and processes associated with the BCP that should be evaluated comprehensively. In addition, parallel cruises are encouraged for collecting concurrent measurements of POC concentration from different depth and seasons to better constrain the POC/bbp slopes.

Although the availability of BGC-Argo float data is increasing rapidly, profile observations of biogeochemical properties are still insufficient for 3D data assimilation except in a few specific regions with high float densities, e.g., the Mediterranean Sea (Cossarini et al. 2019) and the Southern Ocean (Verdy and Mazloff 2017). Chapter 3 has

shown that even sparse BGC-Argo float data can provide substantial benefits for biological data assimilation by *a priori* reducing model systematic errors such as inappropriate model parameterization and inaccurate parameters. This method can be an intermediate step toward full assimilation of BGC-Argo float data. In addition, the present BGC-Argo float data can be expanded by machine learning techniques. For instance, a neural network-based method has been developed to infer the vertical distributions of backscatter from the satellite estimates and T-S profiles (Sauzède et al. 2016). Motivated by the applications of assimilating synthetic salinity observations from temperature and T-S climatological relationships into the model before abundant salinity observations were available (Huang et al. 2008), machine learning can be used to provide synthetic profiles of biogeochemical properties from other observation types that are currently more abundant, e.g., the satellite estimates and T-S profiles collected by Argo floats. Impacts of assimilating these synthetic profiles deserve to be assessed.

Previous studies have shown a projected declining trend in the globally integrated carbon export flux out of the euphotic zone over the 21st century yet with a large disagreement on the magnitude across different ESMs (Laufkötter et al. 2016; Henson et al. 2022). In addition to the carbon exported out of the euphotic zone, carbon sequestration is also controlled by the transfer efficiency which represents the net effects of vertical transport and local respiration of organic carbon after escaping the surface layer. Chapter 4 has shown large model-to-model variability in the current vertical profiles of POC flux and transfer efficiency across ESMs that are used by the CMIP6 due to different parameterization schemes and other model discrepancies. This will introduce additional uncertainties to predict the ocean's response to climate changes. Therefore, future studies should be conducted to investigate the impact of these model discrepancies on the projection of the BCP.

APPENDIX A   COPYRIGHT PERMISSION

Author's certification ▸

By submitting a manuscript, the authors certify that they have read and agreed to the following terms:

- The authors are authorized by their co-authors to enter into these arrangements.
- The work is original and has not been formally published before (except in the form of an abstract, preprint, or as part of a published lecture, review, or thesis), that it is not under consideration for publication elsewhere, that its publication has been approved by all the author(s) and by the responsible authorities – tacitly or explicitly – of the institutes where the work has been carried out, and that the article does not infringe copyright or any other rights by third parties.
- The work does not contain content that is unlawful, abusive, or constitute a breach of contract or of confidence or of commitment given to secrecy.
- The authors warrant that they secure the right to reproduce any material that has already been published or copyrighted elsewhere and that they identified such objects with appropriate citations and copyright statements, if applicable, in captions or even within the objects themselves (e.g. copyrights of maps).
- They agree to the following licence and copyright agreement:

Copyright ▸

- Authors retain the copyright of their manuscript and its final journal article. Regarding copyright transfers please see below.
- Authors grant Copernicus Publications an irrevocable non-exclusive licence to publish the article or versions of the manuscript, if preprints are foreseen, electronically and in print format and to identify itself as the original publisher.
- Authors grant Copernicus Publications commercial rights to produce hardcopy volumes of the journal for sale to libraries and individuals.
- Authors grant any third party the right to use the article or versions of the manuscript, if preprints are foreseen, freely as long as its original authors and citation details are identified.
- The article and corresponding preprints are distributed under the Creative Commons Attribution 4.0 License. Unless otherwise stated, associated material is distributed under the same licence:

Creative Commons Attribution 4.0 License

You are free to:

Share — copy and redistribute the material in any medium or format

Adapt — remix, transform, and build upon the material for any purpose, even commercially.

Under the following conditions:

Attribution — You must give appropriate credit, provide a link to the licence, and indicate if changes were made. You may do so in any reasonable manner, but not in any way that suggests the licenser endorses you or your use.

No additional restrictions — You may not apply legal terms or technological measures that legally restrict others from doing anything the licence permits.

Notices

- The licenser cannot revoke these freedoms as long as you follow the licence terms.
- You do not have to comply with the licence for elements of the material in the public domain or where your use is permitted by an applicable exception or limitation.
- No warranties are given. The licence may not give you all of the permissions necessary for your intended use. For example, other rights such as publicity, privacy, or moral rights may limit how you use the material.
- The CC BY License, of which 4.0 is the recent version, was developed to facilitate open access – namely, free immediate access to, and unrestricted reuse of, original works of all types.
- Under this liberal licence, authors agree to make posted materials legally available for reuse, without permission or fees, for virtually any purpose. Anyone may copy, distribute, or reuse these works, as long as the author and original source are properly cited. Thus, CC BY facilitates the dissemination, transfer, and growth of scientific knowledge.
- Please read the full legal code of this licence.

Copyright transfers ›

Many authors have strict regulations in their contract of employment regarding their works. A transfer of copyright to the institution or company, as well as the reservation of specific usage rights, is typical. Please note that in the case of open-access publications in combination with a Creative Commons License, a transfer of the **copyright** to the institution is possible, as it belongs to the author anyway and is not subject to the publisher.

Any **usage rights** are regulated through the Creative Commons License. As Copernicus Publications uses the Creative Commons Attribution 4.0 License, anyone (the author, their institution/company, the publisher, as well as the public) is free to copy, distribute, transmit, and adapt the work as long as the original author is given credit (see above). Therefore, specific usage rights cannot be reserved by the author or their institution/company, and the publisher cannot include a statement "all rights reserved" in any published paper.

A copyright transfer from the author to their institution/company must be expressed in a special "copyright statement" according to our manuscript preparation guidelines. Authors are asked to include the following sentence: "The author's copyright for this publication is transferred to *institution/company*".
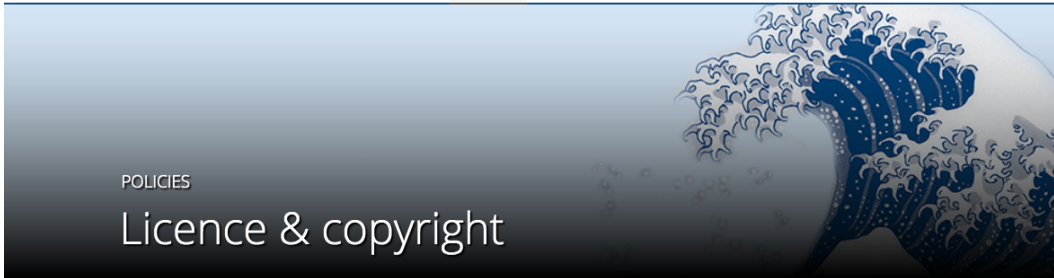
Crown copyright ›

The licence and copyright agreement of Copernicus Publications respects the Crown copyright. For works written by authors affiliated with the British Government and its institutions, a copyright statement must be included according to our manuscript preparation guidelines. Authors are asked to use the following statement, which has been approved by the Information Policy department of The National Archives:

The works published in this journal are distributed under the Creative Commons Attribution 4.0 License. This licence does not affect the Crown copyright work, which is re-usable under the Open Government Licence (OGL). The Creative Commons Attribution 4.0 License and the OGL are interoperable and do not conflict with, reduce or limit each other.

© Crown copyright YEAR

Reproduction request ›

All articles and preprints posted by Copernicus Publications have been licenced under the Creative Commons Attribution 4.0 License since 6 June 2017 or under its former version 3.0 since 10 December 2007. Under these licences the authors retain the copyright. There is no need from the publisher's side to allow/confirm a reproduction. We suggest contacting the authors to inform them about the further usage of the material. In any case, the authors must be given credit. If articles contain figures, maps, or other objects cited by the authors, the individual copyrights and distribution licences must be clarified individually.

Search ⌕

Author's certification ▸

By submitting a manuscript, the authors certify that they have read and agreed to the following terms:

- The authors are authorized by their co-authors to enter into these arrangements.
- The work is original and has not been formally published before (except in the form of an abstract, preprint, or as part of a published lecture, review, or thesis), that it is not under consideration for publication elsewhere, that its publication has been approved by all the author(s) and by the responsible authorities – tacitly or explicitly – of the institutes where the work has been carried out, and that the article does not infringe copyright or any other rights by third parties.
- The work does not contain content that is unlawful, abusive, or constitute a breach of contract or of confidence or of commitment given to secrecy.
- The authors warrant that they secure the right to reproduce any material that has already been published or copyrighted elsewhere and that they identified such objects with appropriate citations and copyright statements, if applicable, in captions or even within the objects themselves (e.g. copyrights of maps).
- They agree to the following licence and copyright agreement:

Copyright ▸

- Authors retain the copyright of their manuscript and its final journal article. Regarding copyright transfers please see below.
- Authors grant Copernicus Publications an irrevocable non-exclusive licence to publish the article or versions of the manuscript, if preprints are foreseen, electronically and in print format and to identify itself as the original publisher.
- Authors grant Copernicus Publications commercial rights to produce hardcopy volumes of the journal for sale to libraries and individuals.
- Authors grant any third party the right to use the article or versions of the manuscript, if preprints are foreseen, freely as long as its original authors and citation details are identified.
- The article and corresponding preprints are distributed under the Creative Commons Attribution 4.0 License. Unless otherwise stated, associated material is distributed under the same licence:

Creative Commons Attribution 4.0 License

You are free to:

Share — copy and redistribute the material in any medium or format

Adapt — remix, transform, and build upon the material for any purpose, even commercially.

Under the following conditions:

Attribution — You must give appropriate credit, provide a link to the licence, and indicate if changes were made. You may do so in any reasonable manner, but not in any way that suggests the licenser endorses you or your use.

No additional restrictions — You may not apply legal terms or technological measures that legally restrict others from doing anything the licence permits.

Notices

- The licenser cannot revoke these freedoms as long as you follow the licence terms.

- You do not have to comply with the licence for elements of the material in the public domain or where your use is permitted by an applicable exception or limitation.

- No warranties are given. The licence may not give you all of the permissions necessary for your intended use. For example, other rights such as publicity, privacy, or moral rights may limit how you use the material.

- The CC BY License, of which 4.0 is the recent version, was developed to facilitate open access – namely, free immediate access to, and unrestricted reuse of, original works of all types.

- Under this liberal licence, authors agree to make posted materials legally available for reuse, without permission or fees, for virtually any purpose. Anyone may copy, distribute, or reuse these works, as long as the author and original source are properly cited. Thus, CC BY facilitates the dissemination, transfer, and growth of scientific knowledge.

- Please read the full legal code of this licence.

Copyright transfers ›

Many authors have strict regulations in their contract of employment regarding their works. A transfer of copyright to the institution or company, as well as the reservation of specific usage rights, is typical. Please note that in the case of open-access publications in combination with a Creative Commons License, a transfer of the **copyright** to the institution is possible, as it belongs to the author anyway and is not subject to the publisher.

Any **usage rights** are regulated through the Creative Commons License. As Copernicus Publications uses the Creative Commons Attribution 4.0 License, anyone (the author, their institution/company, the publisher, as well as the public) is free to copy, distribute, transmit, and adapt the work as long as the original author is given credit (see above). Therefore, specific usage rights cannot be reserved by the author or their institution/company, and the publisher cannot include a statement "all rights reserved" in any published paper.

A copyright transfer from the author to their institution/company must be expressed in a special "copyright statement" according to our manuscript preparation guidelines. Authors are asked to include the following sentence: "The author's copyright for this publication is transferred to *institution/company*".

Crown copyright ›

The licence and copyright agreement of Copernicus Publications respects the Crown copyright. For works written by authors affiliated with the British Government and its institutions, a copyright statement must be included according to our manuscript preparation guidelines. Authors are asked to use the following statement, which has been approved by the Information Policy department of The National Archives:

The works published in this journal are distributed under the Creative Commons Attribution 4.0 License. This licence does not affect the Crown copyright work, which is re-usable under the Open Government Licence (OGL). The Creative Commons Attribution 4.0 License and the OGL are interoperable and do not conflict with, reduce or limit each other.

© Crown copyright YEAR

Reproduction request ›

All articles and preprints posted by Copernicus Publications have been licenced under the Creative Commons Attribution 4.0 License since 6 June 2017 or under its former version 3.0 since 10 December 2007. Under these licences the authors retain the copyright. There is no need from the publisher's side to allow/confirm a reproduction. We suggest contacting the authors to inform them about the further usage of the material. In any case, the authors must be given credit. If articles contain figures, maps, or other objects cited by the authors, the individual copyrights and distribution licences must be clarified individually.

Limnology and Oceanography

Published by Wiley on behalf of Association for the Sciences of Limnology and Oceanography (the "Owner")

LICENSE AGREEMENT FOR PUBLISHING CC-BY-NC-ND

Date: August 22, 2022

Contributor name: Bin Wang

Contributor address: Department of Oceanography, Dalhousie University, 1355 Oxford Street, Halifax, NS, B3H 4R2, Canada

Manuscript number: LO-22-0021.R2

Re: Manuscript entitled Biogeochemical Argo data suggest significant contributions of small particles to the vertical carbon flux in the subpolar North Atlantic (the "Contribution")

for publication in Limnology and Oceanography (the "Journal")

published by Wiley Periodicals LLC ("Wiley")

Dear Contributor(s):

Thank you for submitting your Contribution for publication. In order to expedite the editing and publishing process and enable Wiley to disseminate your Contribution to the fullest extent, we need to have this Agreement executed. If the Contribution is not accepted for publication, or if the Contribution is subsequently rejected, this Agreement will be null and void.
Publication cannot proceed without a signed copy of this Agreement and payment of the appropriate article publication charge in full (without deduction of any taxes or fees).

A. TERMS OF USE

1. The Contribution will be made Open Access under the terms of the Creative Commons Attribution-NonCommercial-NoDerivatives License which permits use, distribution and reproduction in any medium, provided that the Contribution is properly cited, the use is non-commercial and no modifications or adaptations are made.
2. For an understanding of what is meant by the terms of the Creative Commons License, please refer to Wiley's Open Access Terms and Conditions (http://www.wileyauthors.com/OAA).
3. Notwithstanding acceptance, the Owner or Wiley may (but is not obliged to) require changes to the Contribution, including changes to the length of the Contribution, and/or elect not to publish the Contribution if for any reason, in the Owner's or Wiley's reasonable judgment, such publication would be inconsistent with the Core Practices and associated guidelines set forth by the Committee on Publication Ethics (a not-for-profit organization based in the UK: https://publicationethics.org/core-practices) or would result in legal liability, violation of Wiley's ethical guidelines, or violation of journal ethical practices. If the Owner (or Wiley, where Wiley is not the Owner) decides not to publish the Contribution, no Article Processing Charge or any other fee shall be charged. The Contributor is free to submit the Contribution to any other journal from any other publisher.

B. RETAINED RIGHTS

The Contributor or, if applicable, the Contributor's Employer, retains all proprietary rights in addition to copyright, such as patent rights in any process, procedure or article of manufacture described in the Contribution.

C. LICENSE

In addition to the non-exclusive rights to the Contribution the Owner has under the CC-BY-NC-ND license, the Contributor grants to the Owner, during the full term of the Contributor's copyright and any extensions or renewals, an exclusive license of all rights of copyright in and to the Contribution that the Contributor does not grant under the CC-BY-NC-ND license, and all rights therein, including but not limited to the right to publish, republish, transmit, sell, distribute and otherwise use the Contribution in whole or in part in electronic and print editions of the Journal and in derivative works throughout the world, in all languages and in all media of expression now known or later developed, for commercial purposes, and to license or permit others to do so. Such exclusive rights do not conflict with the rights granted to users under the terms of the Creative Commons Attribution-Non-Commercial-NoDerivs License. "Contribution" means the article submitted by the Contributor for publication in the Journal (including any embedded rich media) and all subsequent versions. The definition of Contribution does not extend to any supporting information submitted with or referred to in the Contribution ("Supporting Information"). To the extent that any Supporting Information is submitted to the Journal, the Owner is granted a perpetual, non-exclusive license to publish, republish, transmit, sell, distribute and otherwise use this Supporting Information in whole or in part in electronic and print editions of the Journal and in derivative works throughout the world, in all languages and in all media of expression now known or later developed, and to license or permit others to

do so. If the Contribution was shared as a preprint, the Contributor grants to the Owner exclusivity as to any rights retained by the Contributor in the preprint.

D. CONTRIBUTIONS OWNED BY EMPLOYER

If the Contribution was written by the Contributor in the course of the Contributor's employment as a "work-made-for-hire" and the employer owns the copyright in the Contribution, the employer company/institution agrees to the terms of use set forth in paragraph A above and must execute this Agreement (in addition to the Contributor) in the space provided below. In such case, the company/institution hereby grants to the Owner, during the full term of copyright, an exclusive license of all rights of copyright in and to the Contribution throughout the world for commercial purposes and/or to create derivative works as specified in paragraph C above.

E. GOVERNMENT CONTRACTS

In the case of a Contribution prepared under U.S. Government contract or grant, the U.S. Government may reproduce, without charge, all or portions of the Contribution and may authorize others to do so, for official U.S. Government purposes only, if the U.S. Government contract or grant so requires. (U.S. Government, U.K. Government, and other government employees: see notes at end.)

F. COPYRIGHT NOTICE

Owner (and Wiley, where Wiley is not the Owner), the Contributor, and the company/institution agree that any and all copies of the Contribution or any part thereof distributed or posted by them in print or electronic format as permitted will include the notice of copyright as stipulated in the Journal and a full citation to the final published version of the Contribution in the Journal as published by Wiley.

G. CONTRIBUTOR'S REPRESENTATIONS

The Contributor represents that: (i) the Contributor and all co-Contributors have the full power, authority and capability to enter into this Agreement, to grant the rights and license granted herein and to perform all obligations hereunder; (ii) neither the Contributor nor any co-Contributor has granted exclusive rights to, or transferred their copyright in, any version of the Contribution to any third party; (iii) the Contribution is the Contributor's original work, all individuals identified as Contributors actually contributed to the Contribution, and all individuals who contributed are included; (iv) if the Contribution was prepared jointly, the Contributor has informed the co-Contributors of the terms of this Agreement and has obtained their signed written permission to execute this Agreement on their behalf as their agent; (v) the Contribution is submitted only to this Journal and has not been published before, has not been included in another manuscript, and is not currently under consideration or accepted for publication elsewhere; (vi) if excerpts from copyrighted works owned by third parties are included, the Contributor shall obtain written permission from the copyright owners for all uses as set forth in the standard permissions form and the Journal's Author Guidelines, and show credit to the

125

sources in the Contribution; (vii) the Contribution and any submitted Supporting Information contain no libelous or unlawful statements, do not infringe upon the rights (including without limitation the copyright, patent or trademark rights) or the privacy of others, do not breach any confidentiality obligation, do not violate a contract or any law, or do not contain material or instructions that might cause harm or injury, and only utilize data that has been obtained in accordance with applicable legal requirements and Journal policies; (viii) there are no conflicts of interest relating to the Contribution, except as disclosed. Accordingly, the Contributor represents that the following information shall be clearly identified on the title page of the Contribution: (1) all financial and material support for the research and work; (2) any financial interests the Contributor or any co-Contributors may have in companies or other entities that have an interest in the information in the Contribution or any submitted Supporting Information (e.g., grants, advisory boards, employment, consultancies, contracts, honoraria, royalties, expert testimony, partnerships, or stock ownership); and (3) indication of no such financial interests if appropriate.

H. USE OF INFORMATION

The Contributor acknowledges that, during the term of this Agreement and thereafter (for as long as necessary), the Owner (and Wiley, where Wiley is not the Owner) may process the Contributor's personal data, including storing or transferring data outside of the country of the Contributor's residence, in order to process transactions related to this Agreement and to communicate with the Contributor, and that the Publisher has a legitimate interest in processing the Contributor's personal data. By entering into this Agreement, the Contributor agrees to the processing of the Contributor's personal data (and, where applicable, confirms that the Contributor has obtained the permission from all other contributors to process their personal data). Wiley shall comply with all applicable laws, statutes and regulations relating to data protection and privacy and shall process such personal data in accordance with Wiley's Privacy Policy located at: https://www.wiley.com/en-us/privacy.

[X] I agree to the OPEN ACCESS AGREEMENT as shown above, consent to execution and delivery of the Open Access Agreement electronically and agree that an electronic signature shall be given the same legal force as a handwritten signature, and have obtained written permission from all other contributors to execute this Agreement on their behalf.

Contributor's signature (type name here):   Bin Wang

Date: August 22, 2022

APPENDIX B

B.1. References for observations of carbon export fluxes in Fig. 2.10

Hung, C.-C., Guo, L., Roberts, K. A. and Santschi, P. H.: Upper ocean carbon flux determined by the 234Th approach and sediment traps using size-fractionated POC and 234Th data from the Gulf of Mexico, GEOCHEMICAL JOURNAL, 38(6), 601–611, doi:10.2343/geochemj.38.601, 2004.

Hung, C.-C., Xu, C., Santschi, P. H., Zhang, S.-J., Schwehr, K. A., Quigg, A., Guo, L., Gong, G.-C., Pinckney, J. L., Long, R. A. and Wei, C.-L.: Comparative evaluation of sediment trap and 234Th-derived POC fluxes from the upper oligotrophic waters of the Gulf of Mexico and the subtropical northwestern Pacific Ocean, Marine Chemistry, 121(1), 132–144, doi:https://doi.org/10.1016/j.marchem.2010.03.011, 2010.

Passow, U.: Sediment trap (Kiel 21- trap, KUM) particle flux measurements, Gulf of Mexico, August 2010 to October 2011., Distributed by: Gulf of Mexico Research Initiative Information and Data Cooperative (GRIIDC), Harte Research Institute, Texas A&M University-Corpus Christi. doi:10.7266/N7MK69V2., 2016.

Passow, U.: Sediment Trap (raw data) - Green Canyon, Gulf of Mexico, 1260m, April 16, 2012 - September 4, 2012., Distributed by: Gulf of Mexico Research Initiative Information and Data Cooperative (GRIIDC), Harte Research Institute, Texas A&M University-Corpus Christi. doi:10.7266/N7PN93PS., 2017a.

Passow, U.: Sediment Trap (raw data) - Green Canyon, Gulf of Mexico, 1260m, September 10, 2012 - April 30, 2013., Distributed by: Gulf of Mexico Research Initiative Information and Data Cooperative (GRIIDC), Harte Research Institute, Texas A&M University-Corpus Christi. doi:10.7266/N7JW8BXM., 2017b.

Passow, U.: Sediment Trap (raw data) - Mississippi Canyon, Gulf of Mexico, 1040m, June 28, 2012 - September 8, 2012., Distributed by: Gulf of Mexico Research Initiative Information and Data Cooperative (GRIIDC), Harte Research Institute, Texas A&M University-Corpus Christi. doi:10.7266/N7F47M6M., 2017c.

Passow, U.: Sediment Trap (raw data) - Mississippi Canyon, Gulf of Mexico, 1540m, September 18, 2015 - September 12, 2016., Distributed by: Gulf of Mexico Research Initiative Information and Data Cooperative (GRIIDC), Harte Research Institute, Texas A&M University-Corpus Christi. doi:10.7266/N71C1V8T., 2017d.

Passow, U. and Giering, S.: Sediment Trap (raw data) - Atwater Valley, Gulf of Mexico, 1040m, April 16, 2012 - April 11, 2013., Distributed by: Gulf of Mexico Research Initiative Information and Data Cooperative (GRIIDC), Harte Research Institute, Texas A&M University-Corpus Christi. DOI: 10.7266/N7H993KF., 2017a.

Passow, U. and Giering, S.: Sediment Trap (raw data) - Atwater Valley, Gulf of Mexico, 1040m, June 5, 2013 - April 15, 2014., Distributed by: Gulf of Mexico Research Initiative Information and Data Cooperative (GRIIDC), Harte Research Institute, Texas A&M University-Corpus Christi. doi:10.7266/N7CJ8BVQ., 2017b.

Passow, U. and Giering, S.: Sediment Trap (raw data) - Atwater Valley, Gulf of Mexico, 1040m, May 6, 2014 - April 20, 2015., Distributed by: Gulf of Mexico Research Initiative Information and Data Cooperative (GRIIDC), Harte Research Institute, Texas A&M University-Corpus Christi. doi:10.7266/N7416VD0., 2017c.

Passow, U. and Giering, S.: Sediment Trap (raw data) - Green Canyon, Gulf of Mexico, 1260m, April 23, 2015 - April 15, 2016., Distributed by: Gulf of Mexico Research Initiative Information and Data Cooperative (GRIIDC), Harte Research Institute, Texas A&M University-Corpus Christi. doi:10.7266/N7BR8QKF., 2017d.

Passow, U. and Giering, S.: Sediment Trap (raw data) - Green Canyon, Gulf of Mexico, 1260m, June 8, 2013 - April 15, 2014., Distributed by: Gulf of Mexico Research Initiative Information and Data Cooperative (GRIIDC), Harte Research Institute, Texas A&M University-Corpus Christi. doi:10.7266/N7CR5RQT., 2017e.

Passow, U. and Giering, S.: Sediment Trap (raw data) - Green Canyon, Gulf of Mexico, 1260m, May 4, 2014 - April 20, 2015., Distributed by: Gulf of Mexico Research Initiative Information and Data Cooperative (GRIIDC), Harte Research Institute, Texas A&M University-Corpus Christi. doi:10.7266/N7VT1QGS., 2017f.

Passow, U. and Giering, S.: Sediment Trap (raw data) - Mississippi Canyon, Gulf of Mexico, 1040m, October 9, 2013 - September 15, 2014., Distributed by: Gulf of Mexico Research Initiative Information and Data Cooperative (GRIIDC), Harte Research Institute, Texas A&M University-Corpus Christi. doi:10.7266/N7XK8CZS., 2017g.

Passow, U. and Giering, S.: Sediment Trap (raw data) - Mississippi Canyon, Gulf of Mexico, 1040m, September 12, 2012 - September 12, 2013., Distributed by: Gulf of Mexico Research Initiative Information and Data Cooperative (GRIIDC), Harte Research Institute, Texas A&M University-Corpus Christi. doi:10.7266/N79C6VHB., 2017h.

Passow, U. and Giering, S.: Sediment Trap (raw data) - Mississippi Canyon, Gulf of Mexico, 1040m, September 22, 2014 - September 15, 2015., Distributed by: Gulf of Mexico Research Initiative Information and Data Cooperative (GRIIDC), Harte Research Institute, Texas A&M University-Corpus Christi. doi:10.7266/N78W3BQJ., 2017i.

Passow, U. and Sweet, J.: Sediment Trap (raw data) - Mississippi Canyon, Gulf of Mexico, 1630m, September 12, 2012 - September 12, 2013., Distributed by: Gulf of Mexico Research Initiative Information and Data Cooperative (GRIIDC), Harte Research Institute, Texas A&M University-Corpus Christi. doi:10.7266/N7W66J7K., 2017.
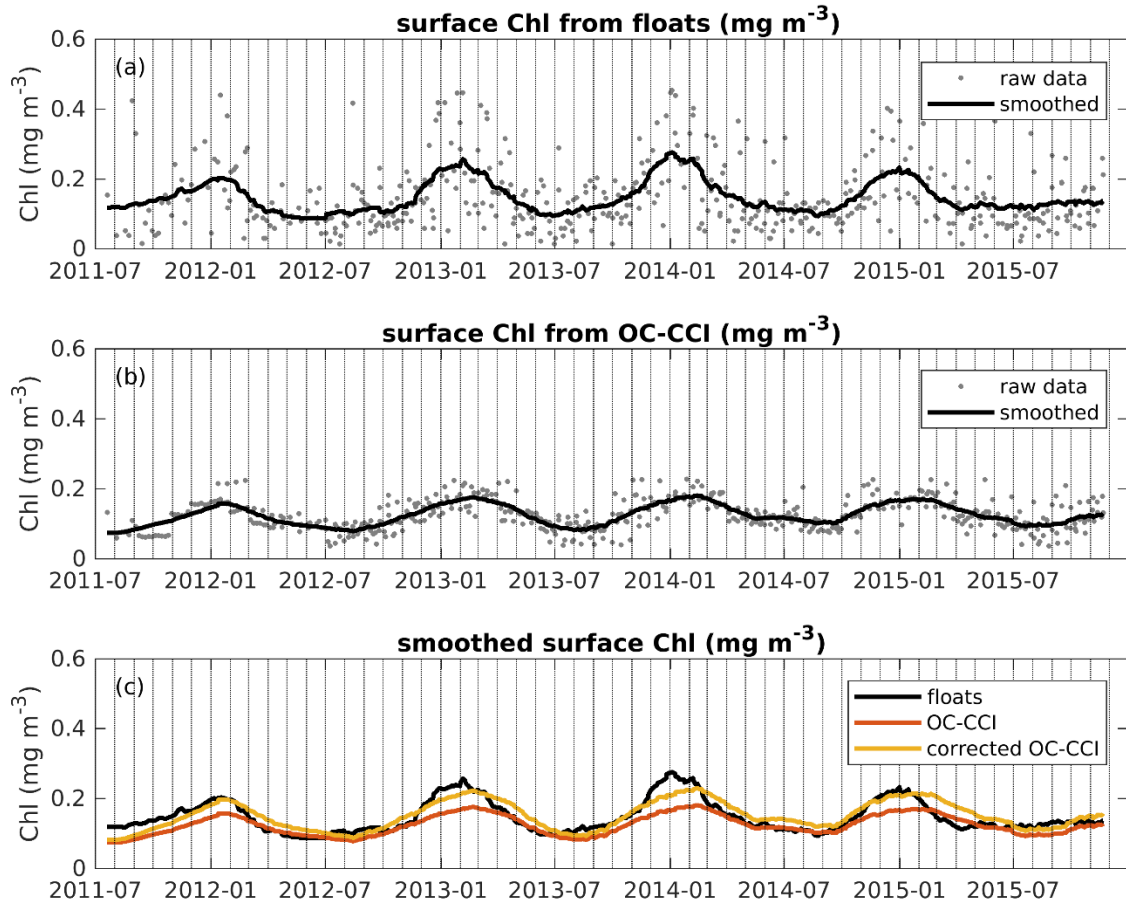
Figure B.1. Time series of surface chlorophyll measurements from floats (a) and corresponding satellite matchups from OC-CCI (b). (c) Comparisons of 30-points smoothed surface chlorophyll between floats, OC-CCI, and corrected satellite estimates from OC-CCI.
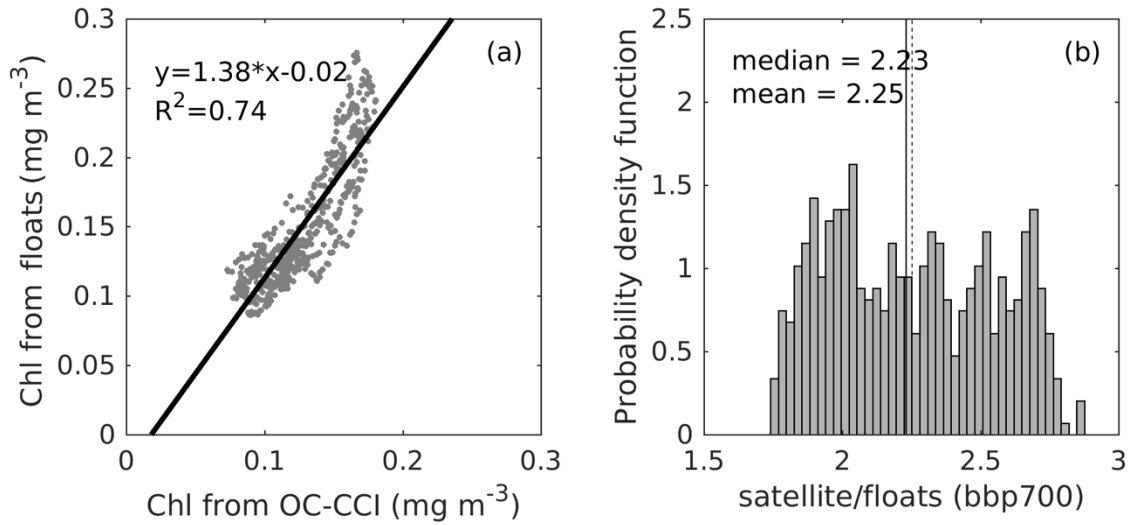
Figure B.2. (a) Regression analysis of 30-point smoothed surface chlorophyll between OC-CCI and floats; (b) histogram of ratio of 30-point smoothed surface bbp700 between OC-CCI and floats.
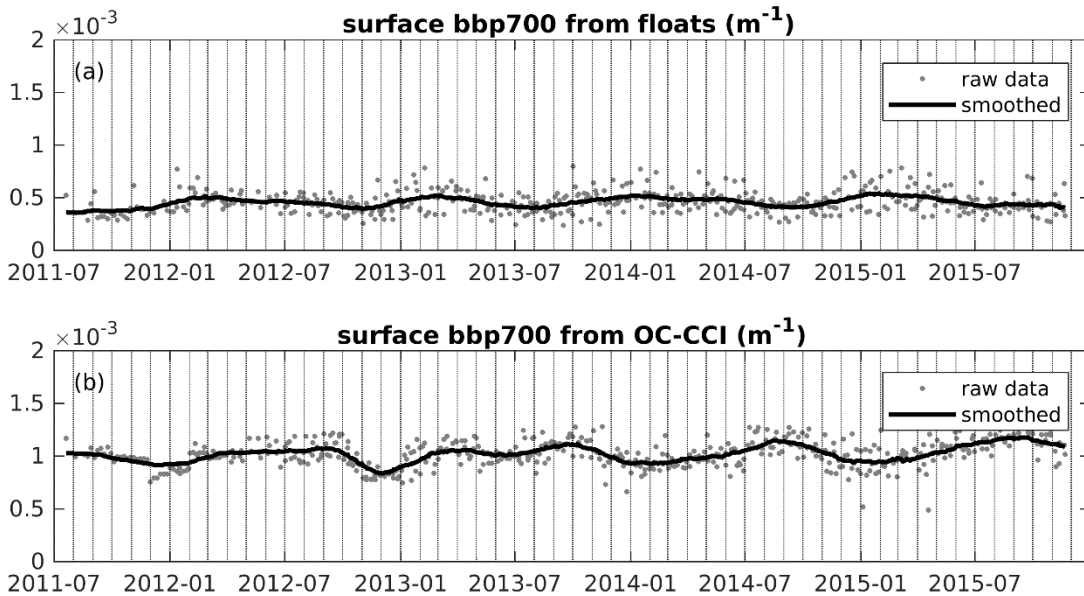

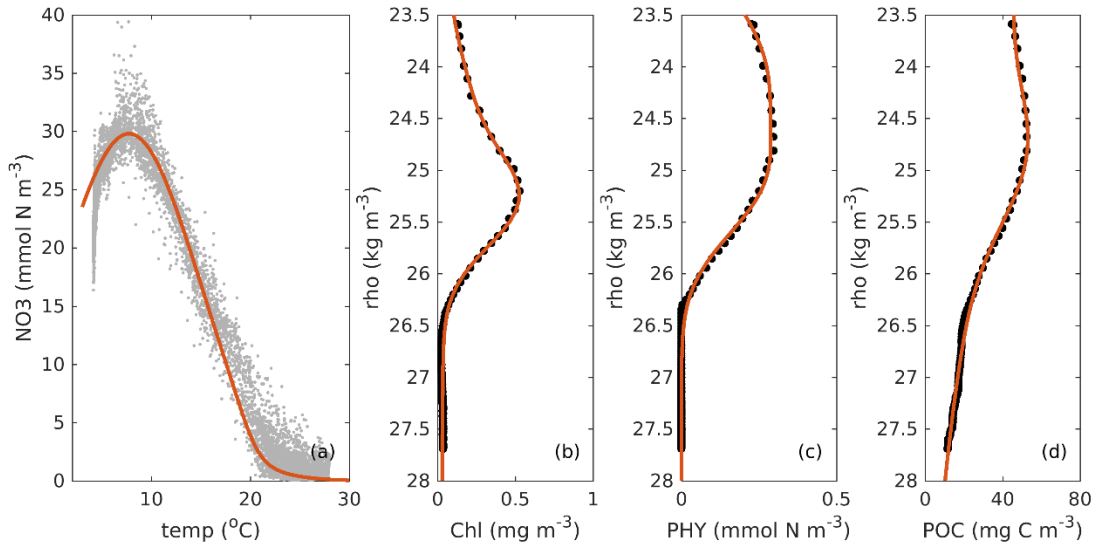**Figure B.3.** Time series of matching-up surface bbp700 from floats (a) and OC-CCI (b).

Figure B.4. Empirical relations of temperature-NO_3 (a) derived from World Ocean Atlas, density-chlorophyll (b), density-phytoplankton (c), and density-POC (d) derived from the median vertical profile of floats
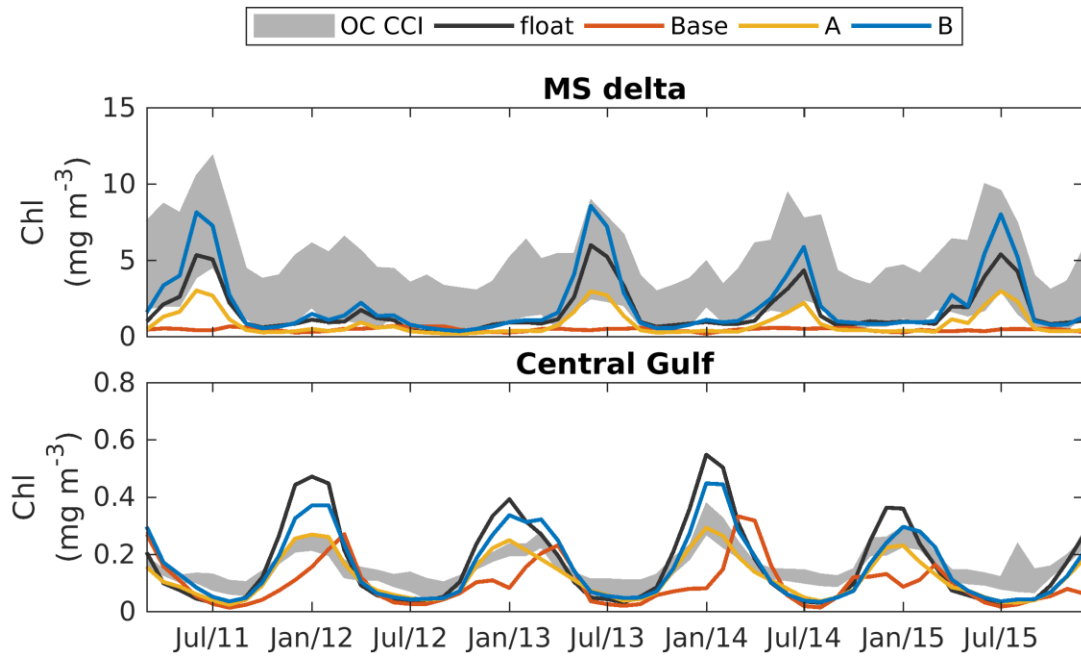

Figure B.5. Observed and simulated seasonal cycles of surface chlorophyll from the Mississippi delta and the central gulf. Gray shades represent the interquartile ranges of satellite estimates. Positions of the Mississippi Delta and the central gulf are shown in Fig. 2.1.
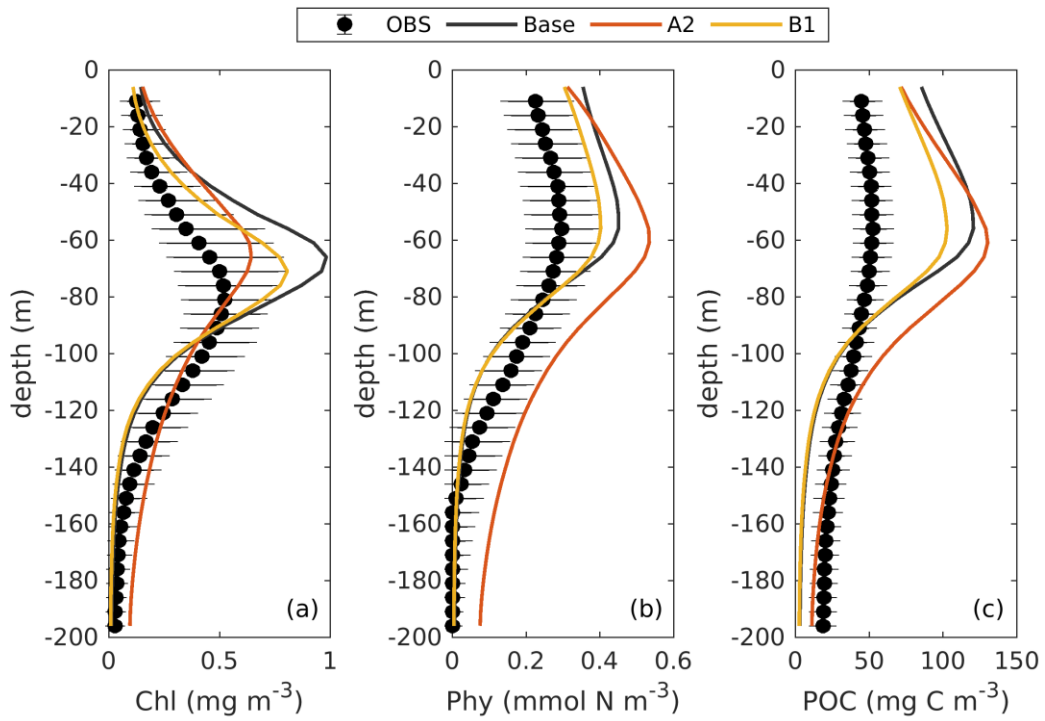
Figure B.6. Observed (black error bars) and simulated (colored lines) vertical profiles of chlorophyll (a), phytoplankton (b), and POC (c).
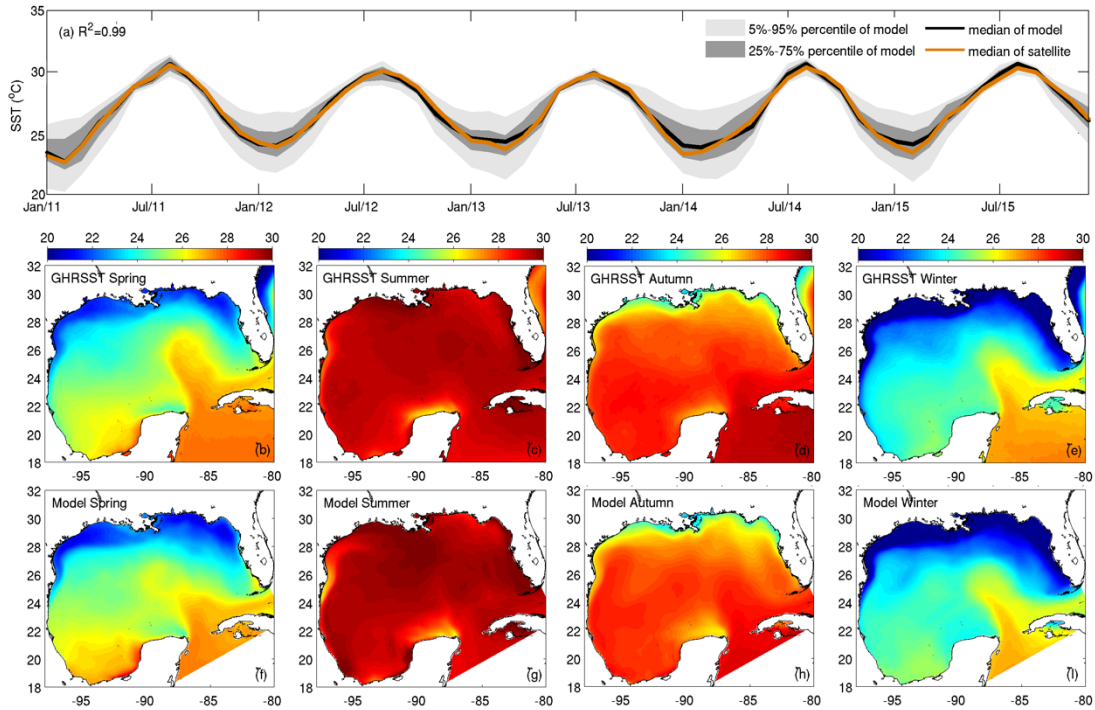
Figure B.7. (a) Monthly time series of SST from model outputs and GHRSST for the deep ocean of GOM. (b-i) SST climatology derived from the GHRSST and model outputs during 2011-2015.
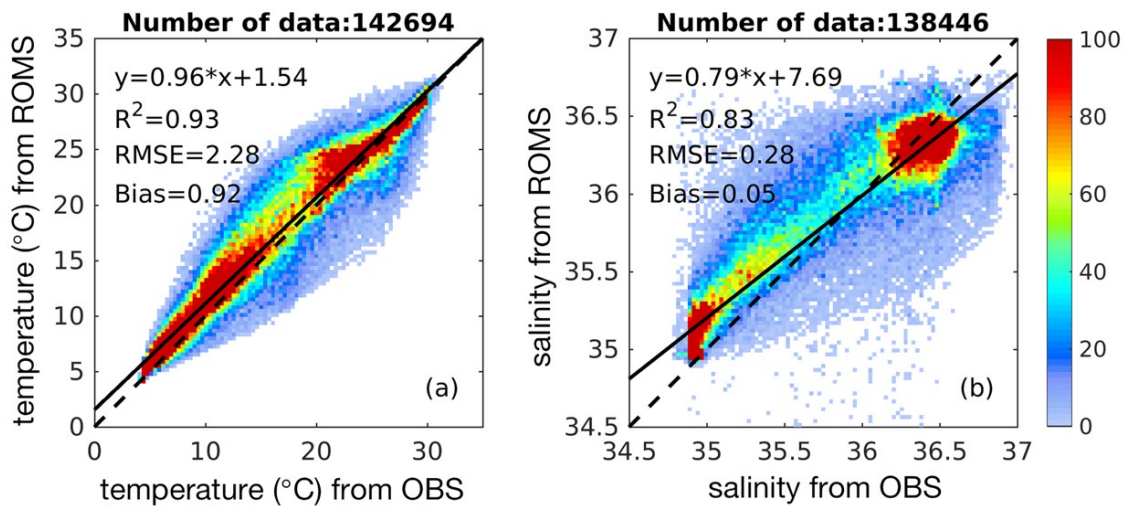

Figure B.8. Point-by-point comparisons between measured and simulated temperature (a) and salinity (b) in the Gulf of Mexico during 2011-2015. In-situ observations are from the USGODAE Argo GDAC profiles (available at https://www.usgodae.org//cgi-bin/argo_select.pl) and the BGC floats in Chapter 2.
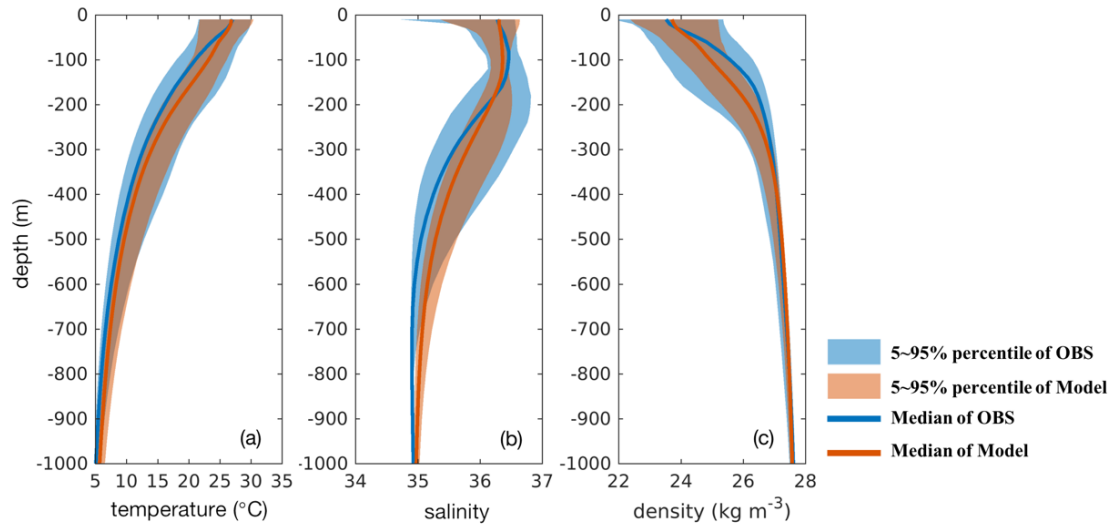
Figure B.9. Point-by-point comparisons between the measured and simulated vertical profiles of temperature (a), salinity (b), and density (c) during 2011-2015. In-situ observations are from the USGODAE Argo GDAC profiles (available at https://www.usgodae.org//cgi-bin/argo_select.pl) and the BGC floats from Chapter 2.
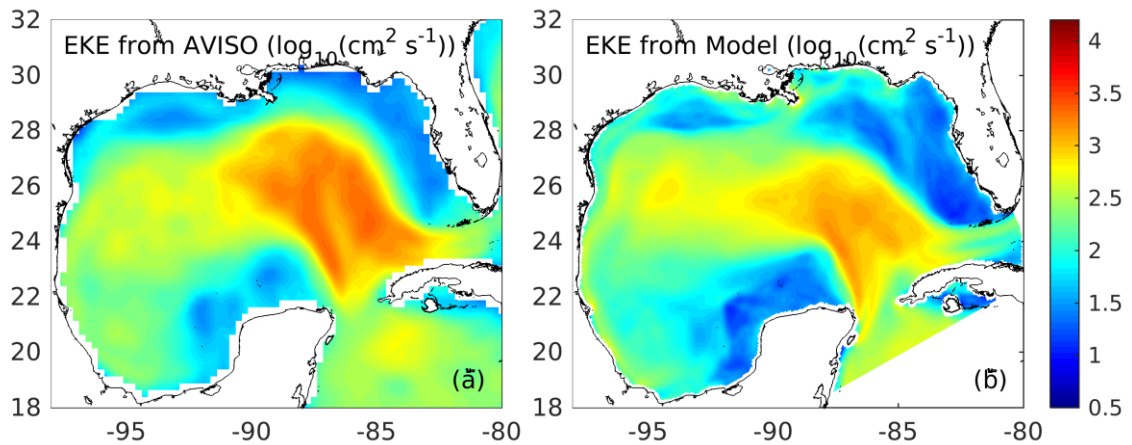

Figure B.10. Comparisons of 5-year (2010-2015) mean eddy kinetic energy (EKE) based on AVISO sea level anomalies (available at http://marine.copernicus.eu) and model results.
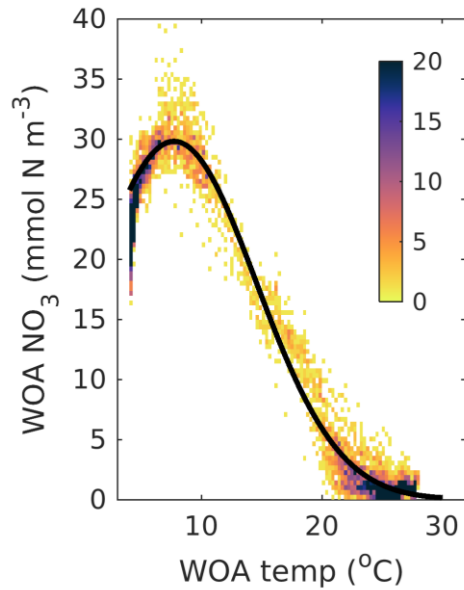
APPENDIX C

Figure C.1. Empirical relations of temperature-NO_3 derived from World Ocean Atlas in the Gulf of Mexico. Colors indicate the number of observations within each bin.
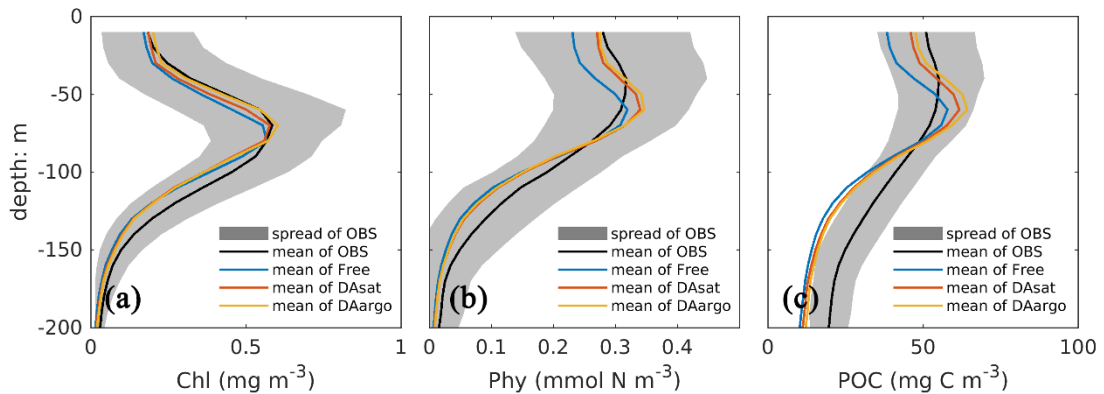
Figure C.2. Vertical profiles of chlorophyll (a), phytoplankton (b), and POC (c) from BOEM floats and model experiments.
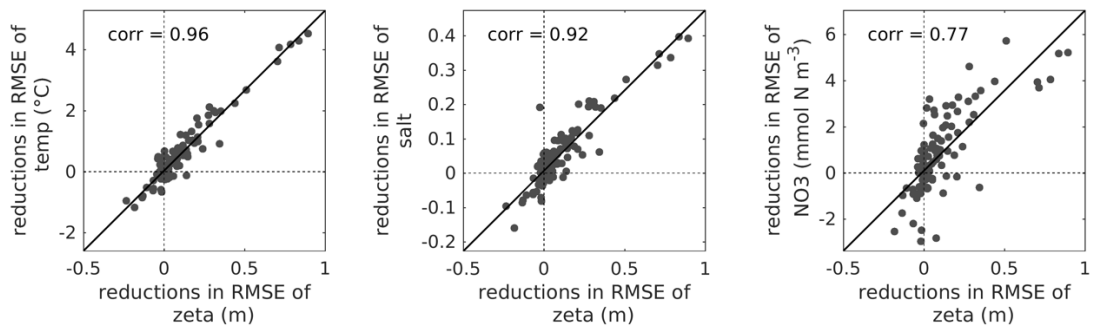
Figure C.3. Correlations of improvement between zeta and temperature, salinity, and NO₃

Figure C.4. The root mean square difference (RMSD) of temperature from each BOEM profile between two data assimilative runs, DAsat and DAargo (indicated by the color). The x-axis represents days of each BOEM profile after each data assimilation cycle and the y-axis represents distance to the nearest Argo profile

APPENDIX D

D.1. The machine-learning model to estimate NO₃

A machine-learning model is developed to construct the three-dimensional distributions of NO_3 in the North Atlantic (Fig. D.1), w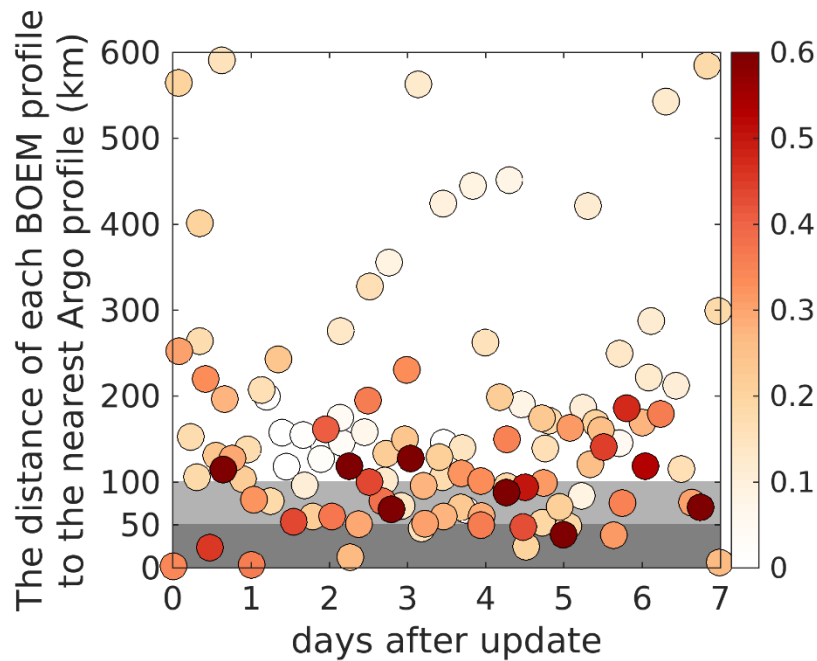hich aims to support the setup of the 1D model in chapter 4 and the future development of a regional 3D model, e.g., by providing the initial and open boundary conditions. Although there have been previous studies to estimate nutrients based on machine-learning models (e.g., Bittig et al., 2018; Sauzède et al., 2017), in those dissolved oxygen is required as a model input in addition to the sampling information (i.e., location, depth, and time) and physical observations (i.e., temperature and salinity). One common practice for providing initial and dynamic, open-boundary conditions for a physical model is to nest it into a data-assimilative global circulation model (e.g., Feucher et al., 2019; Ridenour et al., 2019; Xue et al., 2013; Yu et al., 2019). Motivated by this, dissolved oxygen was removed from the predictors in my machine-learning model so that it can be applied to data-assimilative circulation models to provide dynamically consistent initial and open boundary conditions of biogeochemical properties.

A regression learner toolbox, provided by MATLAB, is used to estimate the NO_3 based on longitude, latitude, depth of measurements, the day of year (doy), as well as temperature and salinity. This toolbox contains a wide range of regression models including different versions of linear regression models, regression trees, support vector machines, and Gaussian process regression models. I tested all these regression models and selected the bootstrap-aggregated ensemble of regression trees (Bagged Trees), which is often accurate but computationally expensive and memory intensive.

Since the first day of a year is similar to the last day from a seasonal perspective, the doy was transformed using a sine function following Sauzède et al., (2015, 2017) to account for its periodic features:

$$\text{doy} = \sin\left(\frac{doy \times \pi}{182.625}\right), \tag{D.1}$$

where the constant of 182.625 days is the half of 365.25 days every year. Observations used to build the machine-learning model are provided by concurrent measurements of temperature, salinity, and NO_3 from the World Ocean Database 2013 (WOD13; Boyer et al., 2013) in the North Atlantic (Fig. D.1). Only those data where all the measured variables have the 'WODflag' of 0 (equivalent to accepted data) will be used. In coastal regions, the relationship between NO_3 and environmental factors is usually different due to the river input and other factors. Therefore, I limited observations to the open ocean (depth > 1000 m). In addition, the observations in semi-enclosed and enclosed marginal seas, e.g., the Gulf of Mexico and the Mediterranean Sea, were removed. As a result, more than 12000 profiles were available, of which the majority (80%) are used as the training data and the remaining profiles (20%) as the testing data (Fig. D.1). To evaluate the performance of the machine-learning model, the predicted NO_3 concentrations are compared with observations from both the training data and testing data. As shown in Fig. D.2, the overall performance of this machine-learning model to predict the observed NO_3 is robust with only a few data points diverging from the 1:1 line.

I also used the BGC-Argo float data of NO_3 which are collected across a wide range of ecosystems in the North Atlantic to conduct independent validation (Fig. D.1). In addition, particular attention is paid to the study region in Chapter 4 (60° W, 42° N ~ 10° W, 66° N) which is represented by the black box in Fig. D.1. In general, the agreement between the predicted NO_3 and the BGC-Argo float data is satisfactory since most of the data points are concentrated along the 1:1 line and the R^2 values (> 0.94) are high (Fig. D.2). Comparisons of the observed NO_3 and its predicted counterpart from this machine-learning model and the CANYON-B in Bittig et al., (2018) are shown for three BGC-Argo floats that were deployed in my study domain and one float that moves across the subtropical North Atlantic (Fig. D.1). As shown in Figs. D.3-D.6, this machine-learning model can well reproduce the vertical distributions of NO_3. With respect to the float 6901485 and the float 6901515 in the Labrador Sea and Irminger Sea, the CANYON-B in Bittig et al., (2018) performs better because the dissolved oxygen used provides additional information.

Table D.1. The POC fluxes (mg C m^{-2} day^{-1}) and transfer efficiency (TE, in unit of %) at different depth from the 12 ESMs

Model name	POC flux (100m)	POC flux (1000m)	TE (1000m)	POC flux (3000m)	TE (3000m)
CESM2	87.96	10.67	12.14	0.49	0.56
CESM2-FV2	93.14	11.63	12.49	0.56	0.60
CESM2-WACCM	91.52	11.20	12.23	0.53	0.58
CESM2-WACCM-FV2	88.79	10.98	12.37	0.55	0.62
GFDL-CM4	190.39	21.12	11.09	4.19	2.20
GFDL-ESM4	78.53	8.51	10.84	3.52	4.48
IPSL-CM5A2-INCA	62.20	21.40	34.40	8.10	13.02
IPSL-CM6A-LR	54.55	14.22	26.08	6.07	11.14
IPSL-CM6A-LR-INCA	58.77	16.54	28.14	6.87	11.69
MPI-ESM-1-2-HAM	34.78	4.33	12.46	0.88	2.52
MPI-ESM1-2-HR	35.37	3.83	10.83	0.72	2.05
MPI-ESM1-2-LR	31.84	3.43	10.79	0.64	2.00

Table D.2. The fitted Martin curve equation of simulated transfer efficiency from each ESM, as well as the RMSE and correlation coefficient (Corr) between the fitted and simulated transfer efficiency.

ESMs	Martin curve equation	RMSE	Corr
CESM2	$y=1.07\times(depth/100)^{-0.96}$	1.51	0.98
CESM2-FV2	$y=1.07\times(depth/100)^{-0.96}$	1.49	0.98
CESM2-WACCM	$y=1.07\times(depth/100)^{-0.96}$	1.49	0.98
CESM2-WACCM-FV2	$y=1.07\times(depth/100)^{-0.96}$	1.44	0.98
GFDL-CM4	$y=1.12\times(depth/100)^{-0.92}$	0.59	0.97
GFDL-ESM4	$y=1.07\times(depth/100)^{-0.90}$	0.27	0.99
IPSL-CM5A2-INCA	$y=1.10\times(depth/100)^{-0.57}$	0.20	0.98
IPSL-CM6A-LR	$y=1.03\times(depth/100)^{-0.64}$	0.29	0.99
IPSL-CM6A-LR-INCA	$y=1.06\times(depth/100)^{-0.62}$	0.28	0.99
MPI-ESM-1-2-HAM	$y=1.06\times(depth/100)^{-0.92}$	0.56	0.99
MPI-ESM1-2-HR	$y=1.06\times(depth/100)^{-0.97}$	0.60	0.99
MPI-ESM1-2-LR	$y=1.06\times(depth/100)^{-0.97}$	0.59	0.99

Table D.3. Parameters for the 1D biogeochemical model used in Chapter 4

Descriptions	symbol	Values	Unit
Nutrient			
Radiation threshold for nitrification inhibition	E_0	0.0095	W m^{-2}
Light intensity for half-saturated nitrification inhibition	k_E	0.1	W m^{-2}
Maximum nitrification rate	n_{max}	0.2	d^{-1}
Phytoplankton			
Half saturation concentration of NO$_3$ for P$_S$	$k_{NO_3 P_S}$	0.5	mmol N m^{-3}
Half saturation concentration of NH$_4$ for P$_S$	$k_{NH_4 P_S}$	0.5	mmol N m^{-3}
Half saturation concentration of NO$_3$ for P$_L$	$k_{NO_3 P_L}$	2.0	mmol N m^{-3}
Half saturation concentration of NH$_4$ for P$_L$	$k_{NH_4 P_L}$	2.0	mmol N m^{-3}
Maximum growth rate at 0°C for P$_S$	$\mu_{P_S}^0$	0.69	d^{-1}
Maximum growth rate at 0°C for P$_L$	$\mu_{P_L}^0$	4.0	d^{-1}
Initial slope of the instantaneous growth rate for P$_S$	α_{P_S}	0.065	(W m^{-2})$^{-1}$ d^{-1}
Initial slope of the instantaneous growth rate for P$_L$	α_{P_L}	0.04	(W m^{-2})$^{-1}$ d^{-1}
Mortality rate at 0°C for P$_S$	$m_{P_S}^0$	0.06	d^{-1}
Mortality rate at 0°C for P$_L$	$m_{P_L}^0$	0.15	d^{-1}
Maximum chlorophyll to carbon ratio for P$_S$	$\theta_{P_S}^{max}$	0.04	mg Chl (mg C)$^{-1}$
Maximum chlorophyll to carbon ratio for P$_L$	$\theta_{P_L}^{max}$	0.04	mg Chl (mg C)$^{-1}$
Sinking velocity for phytoplankton	w_P	0.1	m d^{-1}
Small Detritus			
Remineralization rate at 0°C for small detritus	r_S^0	0.06	d^{-1}
Sinking velocity for small detritus	w_S	2.0	m d^{-1}
Aggregation rate	τ	0.1	d^{-1}

(To be continued)

| Descriptions	symbol	Values	Unit
Zooplankton			
Maximum grazing rate at 0°C of Z_S on P_S	$g^0_{Z_S P_S}$	7.0	d^{-1}
Maximum grazing rate at 0°C of Z_S on P_L	$g^0_{Z_S P_L}$	3.8	d^{-1}
Maximum grazing rate at 0°C of Z_L on P_S	$g^0_{Z_L P_S}$	2.8	d^{-1}
Maximum grazing rate at 0°C of Z_L on P_L	$g^0_{Z_L P_L}$	2.0	d^{-1}
Maximum grazing rate at 0°C of Z_L on Z_S	$g^0_{Z_L Z_S}$	4.0	d^{-1}
Maximum grazing rate at 0°C of Z_L on D_S	$g^0_{Z_L D_S}$	7.0	d^{-1}
Inhibition coefficient for Z_S grazing on P_L	$\psi_{Z_S P_L}$	3.010	$(mmol\ N\ m^{-3})^{-1}$
Inhibition coefficient for Z_L grazing on P_S	$\psi_{Z_L P_S}$	3.010	$(mmol\ N\ m^{-3})^{-1}$
Inhibition coefficient for Z_L grazing on D_S	$\psi_{Z_L D_S}$	3.010	$(mmol\ N\ m^{-3})^{-1}$
Zooplankton grazing half saturation of Z_S on P_S	$k_{Z_S P_S}$	1.2	$(mmol\ N\ m^{-3})^2$
Zooplankton grazing half saturation of Z_L on P_S	$k_{Z_L P_S}$	1.2	$(mmol\ N\ m^{-3})^2$
Zooplankton grazing half saturation of Z_S on P_L	$k_{Z_S P_L}$	0.5	$(mmol\ N\ m^{-3})^2$
Zooplankton grazing half saturation of Z_L on P_L	$k_{Z_S P_S}$	0.5	$(mmol\ N\ m^{-3})^2$
Zooplankton grazing half saturation of Z_L on Z_S	$k_{Z_L Z_S}$	1.2	$(mmol\ N\ m^{-3})^2$
Zooplankton grazing half saturation of Z_L on D_S	$k_{Z_L D_S}$	0.5	$(mmol\ N\ m^{-3})^2$
Assimilation efficiency for Z_S	β_{Z_S}	0.75	unitless
Assimilation efficiency for Z_L	β_{Z_L}	0.75	unitless
Excretion rate due to basal metabolism at 0°C for Z_S	$l^0_{Z_S}$	0.1	d^{-1}
Excretion rate due to basal metabolism at 0°C for Z_L	$l^0_{Z_L}$	0.2	d^{-1}
Maximum rate of assimilation related excretion at 0°C for Z_S	$E^0_{Z_S}$	0.1	d^{-1}
Maximum rate of assimilation related excretion at 0°C for Z_L	$E^0_{Z_L}$	0.2	d^{-1}
Mortality rate at 0°C for Z_S	$m^0_{Z_S}$	0.05	d^{-1}
Mortality rate at 0°C for Z_L	$m^0_{Z_L}$	0.08	d^{-1}
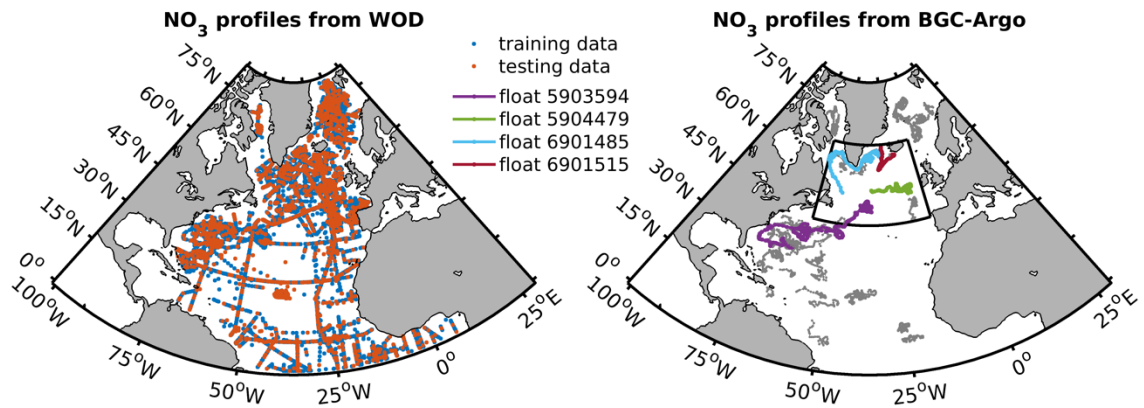
Figure D.1. The geographic distributions of profiles from the WOD13 that are used to build the machine-learning model and the BGC-Argo floats that are used for independent validations. Colored lines represent the four BGC-Argo floats in Figs. D.3-D.6. The black box represents the study region in Chapter 4 (60º W, 42º N ~ 10º W, 66º N).
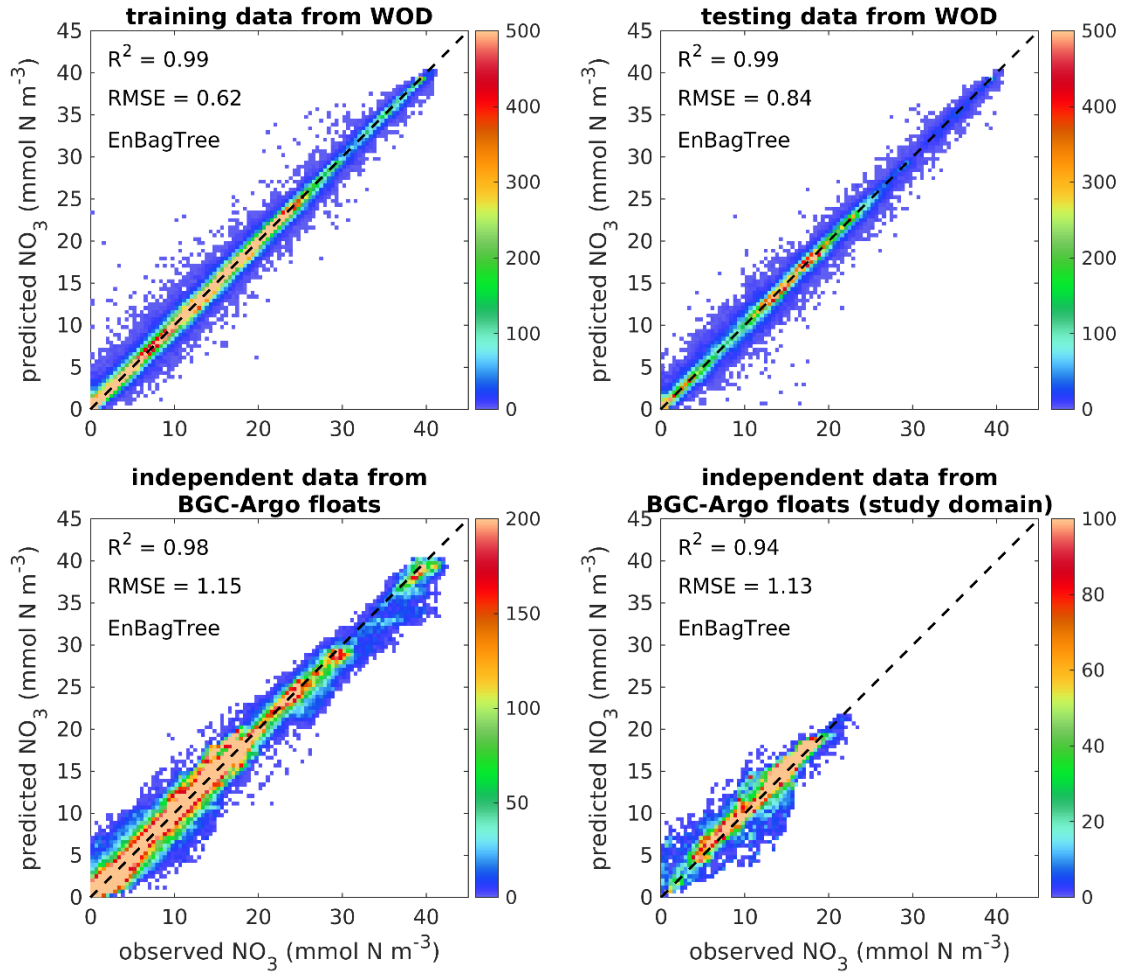
Figure D.2. Comparisons of the predicted NO₃ with observations from the training dataset, the testing dataset, and the BGC-Argo float data in the North Atlantic and the study domain in Chapter 4 (60° W, 42° N ~ 10° W, 66° N).
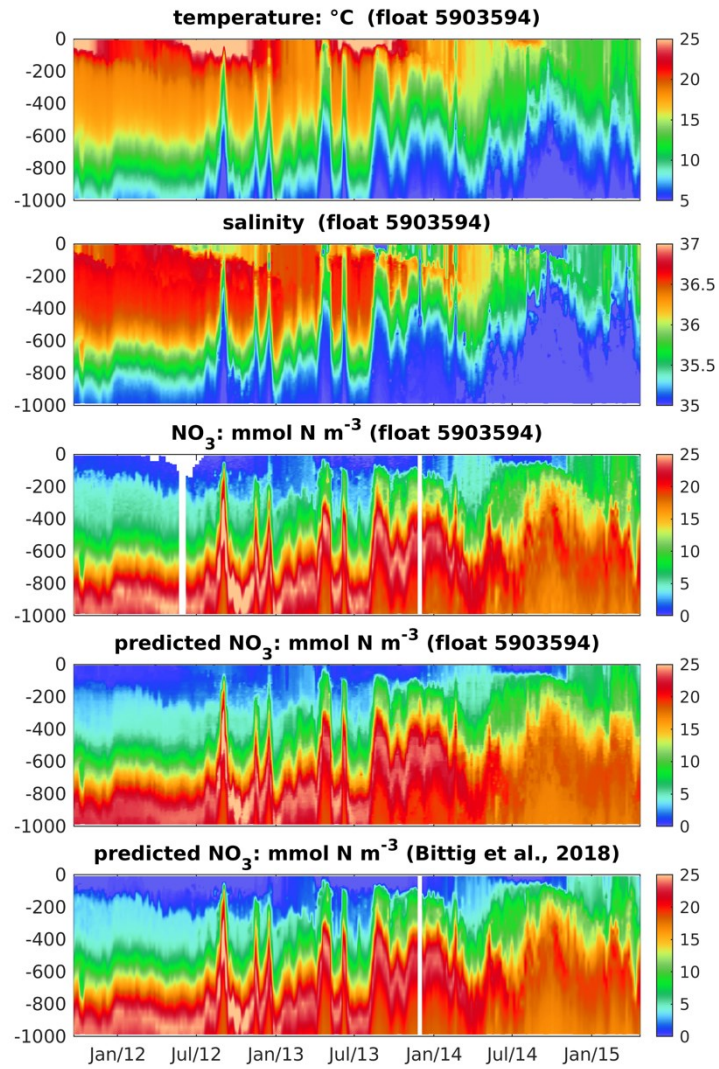
Figure D.3. The vertical distributions of observed temperature, salinity, and NO$_3$ as well as the predicted NO$_3$ by my machine-learning model and the CANYON-B in Bittig et al., (2018) following the float 5903594.
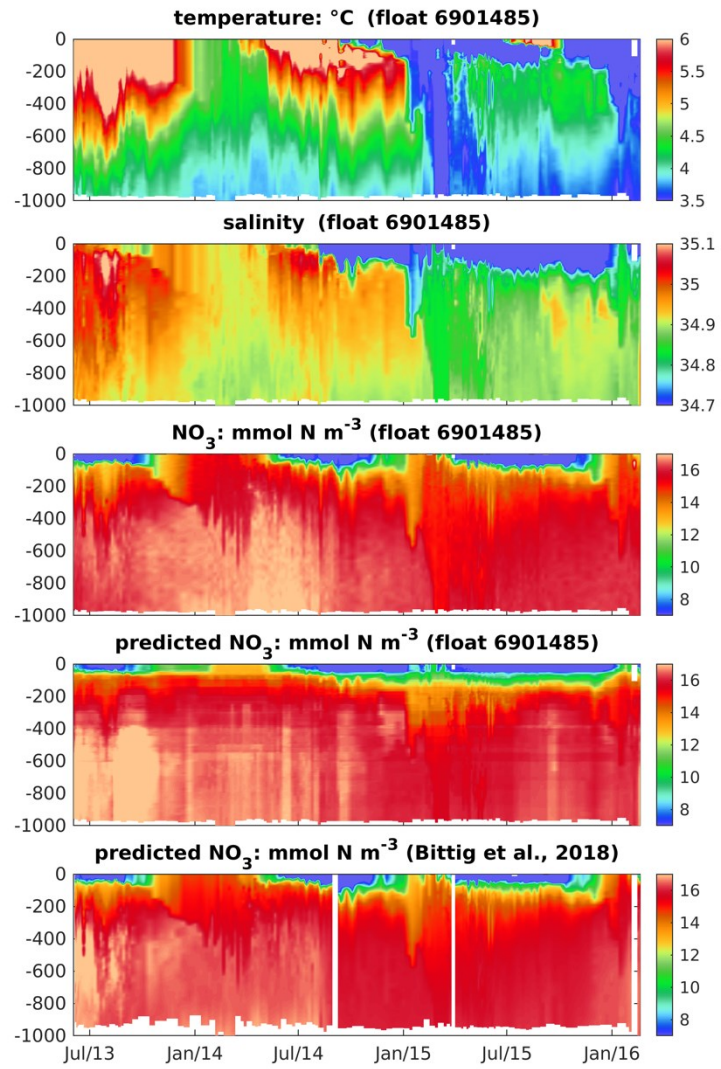
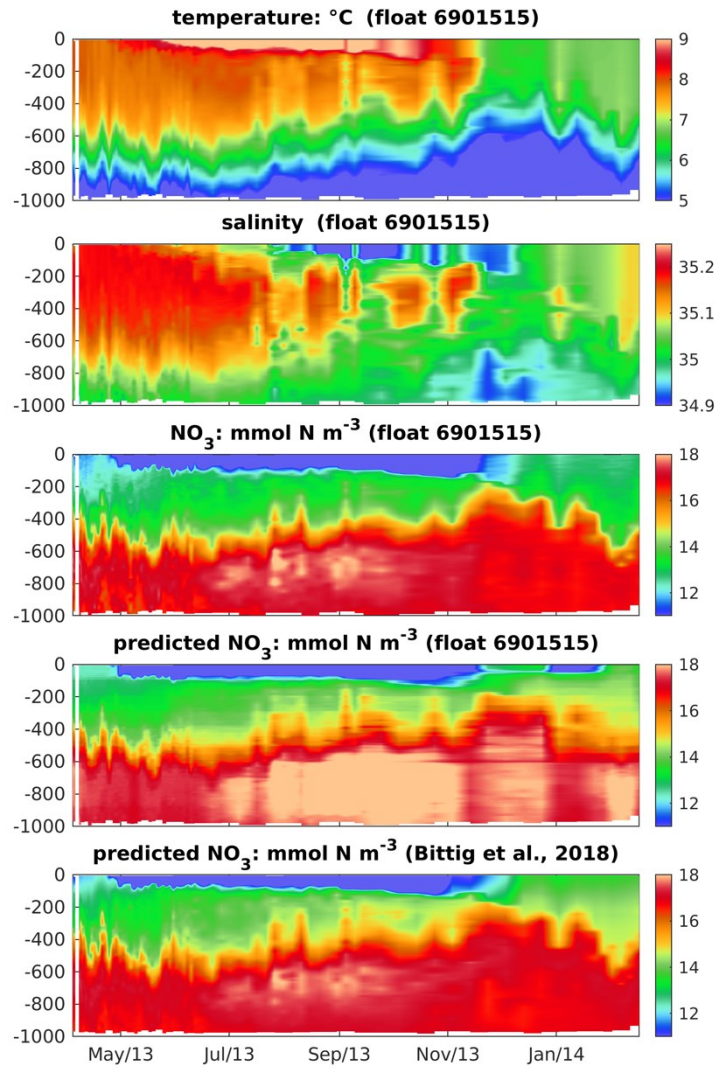**Figure D.4.** The same as Fig. D.3 except for float 6901485.

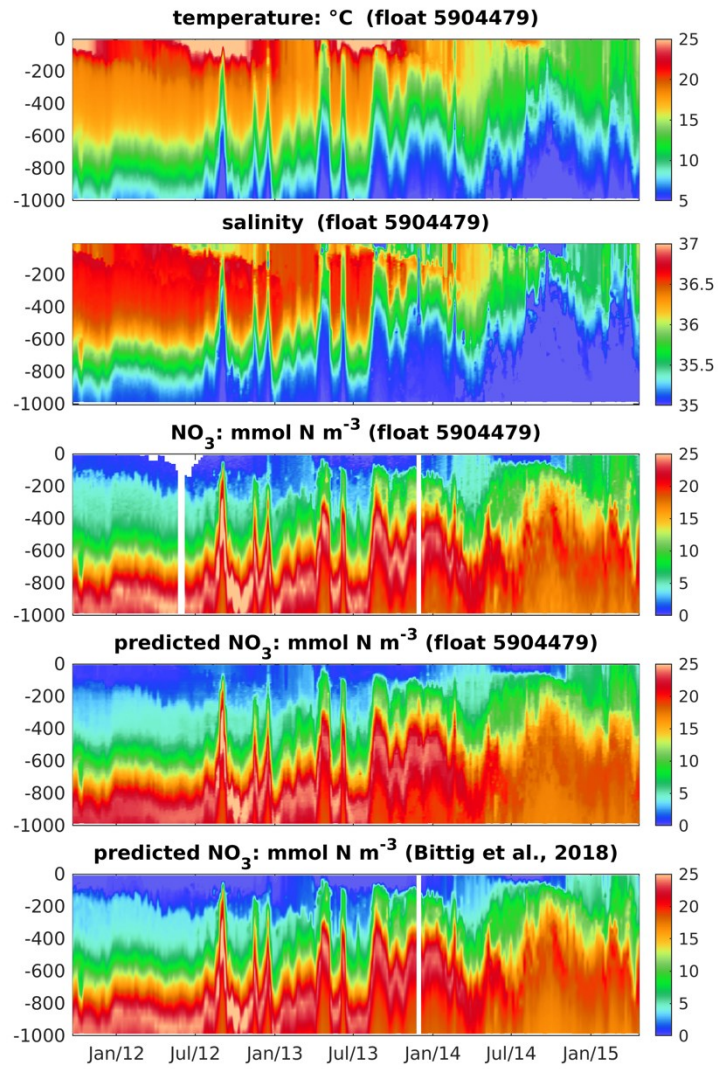**Figure D.5.** The same as Fig. D.3 except for float 6901515.

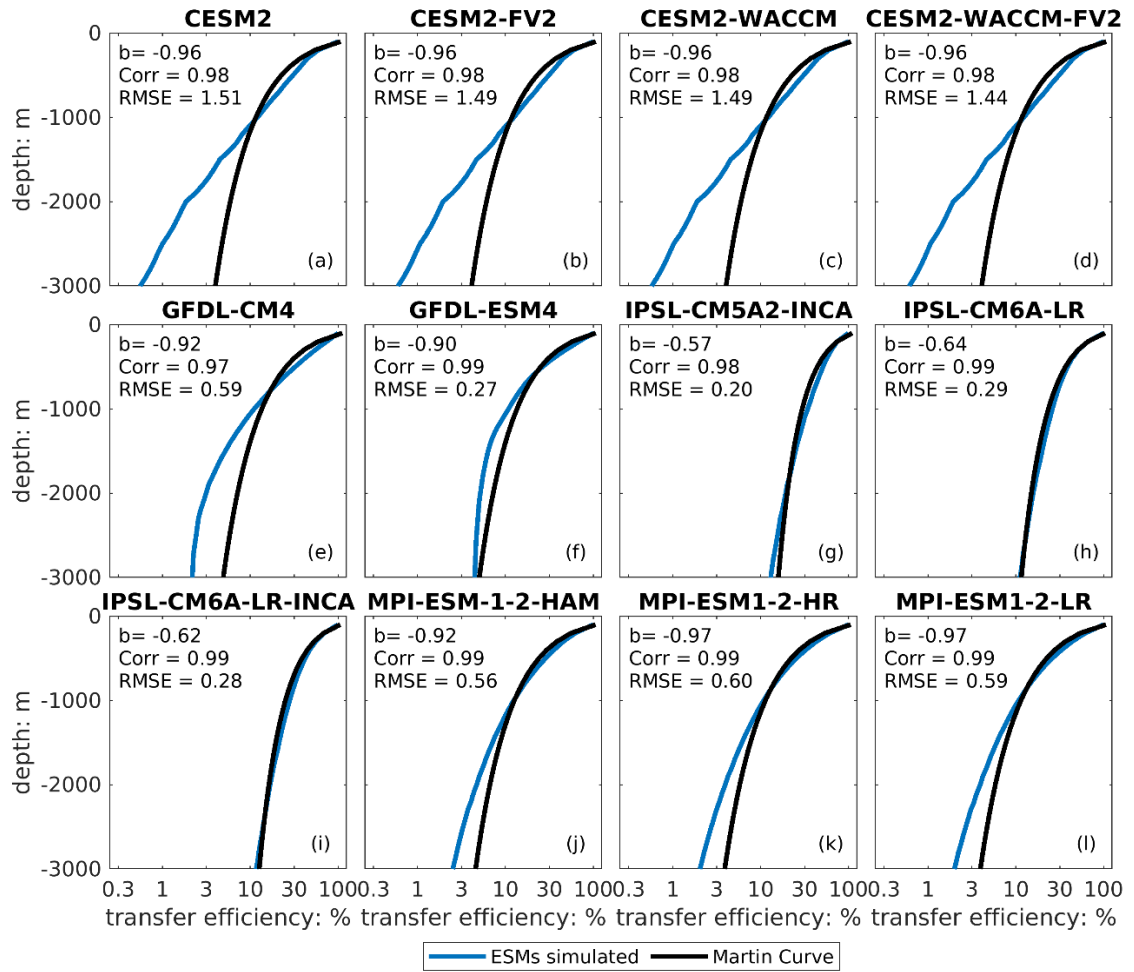**Figure D.6.** The same as Fig. D.3 except for float 5904479.

Figure D.7. The simulated (blue) and fitted (black) transfer efficiency from each ESM.

APPENDIX E

E.1. Derivation of small POC flux

The temporal evolution of $iPOC_S^{900}(z,t)$ is represented by:

$$\frac{\partial iPOC_S^{900}(z,t)}{\partial t} = S^{900}(z,t) - r_s \cdot iPOC_S^{900}(z,t). \qquad (E.1)$$

The general solution to this first order non-homogeneous linear differential equation is

$$iPOC_S^{900}(z,t) = e^{-r_s t} \cdot \left(\int e^{r_s t} \cdot S^{900}(z,t)dt + C_1 \right), \qquad (E.2)$$

where C_1 is an integration constant. Since this equation will be applied to only short time intervals between consecutive sampling dates, I now assume that $S^{900}(z,t)$ is constant in time. Then

$$iPOC_S^{900}(z,t) = e^{-r_s t} \cdot \left(\int e^{r_s t} \cdot S^{900}(z)dt + C_1 \right)$$

$$= e^{-r_s t} \cdot \left(\frac{S^{900}(z)}{r_s} \cdot \int e^{r_s t} \cdot dr_s t + C_1 \right)$$

$$= e^{-r_s t} \cdot \left(\frac{S^{900}(z)}{r_s} \cdot (e^{r_s t} + C_2) + C_1 \right)$$

$$= e^{-r_s t} \cdot \left(\frac{S^{900}(z)}{r_s} \cdot e^{r_s t} + \frac{S^{900}(z)}{r_s} \cdot C_2 + C_1 \right)$$

$$= e^{-r_s t} \cdot \left(\frac{S^{900}(z)}{r_s} \cdot e^{r_s t} + C(z) \right)$$

$$= \frac{S^{900}(z)}{r_s} + C(z) \cdot e^{-r_s t}, \qquad (E.3)$$

where C_2 is an integration constant and $C(z) = \frac{S^{900}(z)}{r_S} \cdot C_2 + C_1$ is a coefficient which is independent of time. To determine the coefficient $C(z)$, I substitute $t_0 = 0$ and $t_1 = \Delta t$ into Eq. E.3 as follows:

$$iPOC_S^{900}(z, t_0) = \frac{S^{900}(z)}{r_S} + C(z), \tag{E. 4}$$

$$iPOC_S^{900}(z, t_1) = \frac{S^{900}(z)}{r_S} + C(z) \cdot e^{-r_S \Delta t}, \tag{E. 5}$$

and then subtract Eq. E.5 from Eq. E.4 and isolate $C(z)$ which yields

$$C(z) = \frac{iPOC_S^{900}(z, t_0) - iPOC_S^{900}(z, t_1)}{1 - e^{-r_S \Delta t}}. \tag{E. 6}$$

Hence, the solution between two sampling steps $(t_0 \leq t \leq t_1)$ is

$$iPOC_S^{900}(z, t) = \frac{S^{900}(z)}{r_S} + e^{-r_S t} \cdot \frac{iPOC_S^{900}(z, t_0) - iPOC_S^{900}(z, t_1)}{1 - e^{-r_S \Delta t}} \tag{E. 7}$$

Finally, I substitute $t_1 = \Delta t$ into Eq. E.7 to find $S^{900}(z)$ according to

$$iPOC_S^{900}(z, t_1) = \frac{S^{900}(z)}{r_S} + e^{-r_S t} \cdot \frac{iPOC_S^{900}(z, t_0) - iPOC_S^{900}(z, t_1)}{1 - e^{-r_S \Delta t}} \tag{E. 8}$$

and the source of small POC is

$$S^{900}(z) = \frac{r_S \cdot (iPOC_S^{900}(z, t_1) - iPOC_S^{900}(z, t_0) e^{-r_S \Delta t})}{1 - e^{-r_S \Delta t}}. \tag{E. 9}$$

When the remineralization and fragmentation can be ignored ($r_S = 0$ day^{-1}, $d_L = 0$ day^{-1}), the source of small POC becomes

$$\lim_{r_S \to 0} S^{900}(z) = \lim_{r_S \to 0} \frac{r_S \cdot (iPOC_S^{900}(z, t_1) - iPOC_S^{900}(z, t_0) e^{-r_S \Delta t})}{1 - e^{-r_S \Delta t}}$$

$$= \lim_{r_S \to 0} \frac{r_S \cdot e^{r_S \Delta t} \cdot (iPOC_S^{900}(z, t_1) - iPOC_S^{900}(z, t_0) e^{-r_S \Delta t})}{e^{r_S \Delta t} - 1}$$

$$= \lim_{r_s \to 0} \frac{r_s}{e^{r_s \Delta t} - 1} \cdot \lim_{r_s \to 0} e^{r_s \Delta t} \cdot \lim_{r_s \to 0} (iPOC_S^{900}(z, t_1) - iPOC_S^{900}(z, t_0)e^{-r_s \Delta t})$$

$$= \lim_{r_s \to 0} \frac{r_s}{r_s \Delta t} \cdot \left(iPOC_S^{900}(z, t_1) - iPOC_S^{900}(z, t_0) \right)$$

$$= \frac{iPOC_S^{900}(z, t_1) - iPOC_S^{900}(z, t_0)}{\Delta t}, \tag{E.10}$$

and the vertical flux becomes

$$\lim_{\substack{r_s \to 0 \\ d_L \to 0}} totF_s(z) = \lim_{r_s \to 0} S^{900}(z) - \lim_{d_L \to 0} \int_z^{900} d_L \cdot POC_L(z, t) dz$$

$$= \frac{iPOC_S^{900}(z, t_1) - iPOC_S^{900}(z, t_0)}{\Delta t}. \tag{E.11}$$

E.2. Remineralization length scale of small POC

The budgets of small and large POC are:

$$\frac{\partial POC_S(z, t)}{\partial t} = -r_s \cdot POC_S(z, t) + d_L \cdot POC_L(z, t) + w_s \cdot \frac{\partial POC_S(z, t)}{\partial z}$$

$$= -\left(r_s - d_L \cdot \frac{POC_L(z, t)}{POC_S(z, t)} \right) \cdot POC_S(z, t) + w_s \cdot \frac{\partial POC_S(z, t)}{\partial z}, \tag{E.12}$$

and

$$\frac{\partial POC_L(z, t)}{\partial t} = -r_L \cdot POC_L(z, t) - d_L \cdot POC_L(z, t) + w_L \cdot \frac{\partial POC_L(z, t)}{\partial z}$$

$$= -(r_L + d_L) \cdot POC_L(z, t) + w_L \cdot \frac{\partial POC_L(z, t)}{\partial z}, \tag{E.13}$$

where r_S and w_S represent the remineralization rate and sinking velocity of small POC; r_L, d_L, and w_L represent the remineralization rate, the fragmentation rate, and the sinking velocity of large POC. Therefore, the net attenuation rate of small (A_S) and large POC (A_L) can be estimated as:

$$A_S(z,t) = r_S - d_L \cdot \frac{POC_L(z,t)}{POC_S(z,t)}, \tag{E.14}$$

$$A_L = r_L + d_L. \tag{E.15}$$

Assuming that the net attenuation rate of small POC is constant in time, it can be represented by:

$$A_S(z) = r_S - d_L \cdot \frac{\overline{POC_L(z)}}{\overline{POC_S(z)}}. \tag{E.16}$$

Dividing the Eq. E.16 by sinking velocity of small POC (w_S), yields

$$\frac{A_S(z)}{w_S} = \frac{r_S}{w_S} - \frac{r_S}{w_S} \cdot \frac{d_L}{r_S} \cdot \frac{\overline{POC_L(z)}}{\overline{POC_S(z)}}, \tag{E.17}$$

$$\frac{1}{l_S(z)} = \frac{1}{l_{S,r}} - \frac{1}{l_{S,r}} \cdot \frac{d_L}{r_S} \cdot \frac{\overline{POC_L(z)}}{\overline{POC_S(z)}}, \tag{E.18}$$

where l_S is the actual remineralization length scale of small POC ($l_S = w_S/A_S$, m) and can be estimated by fitting the vertical profiles of small POC within each 100m bin as

$$\frac{POC_S(z+100)}{POC_S(z)} = exp\left(-\frac{100}{l_S(z)}\right). \tag{E.19}$$

The parameter $l_{S,r}$ is the remineralization length scale when fragmentation is not considered ($l_{S,r} = w_S/r_S$, m).

E.3. To account for temperature- and oxygen-dependence

When accounting for the temperature- and oxygen-dependence on remineralization rate, the equation of POC respiration becomes:

$$\frac{\Delta O_2(z,t)}{1.45} = \int resp(z,t)dt$$

$$= -\int \frac{r_s \cdot f_T(z,t) \cdot f_{O_2}(z,t) \cdot POC_S(z,t)}{12} dt$$

$$- \int \frac{r_L \cdot f_T(z,t) \cdot f_{O_2}(z,t) \cdot POC_L(z,t)}{12} \, dt, \tag{E.20}$$

where $f_T(z,t)$ and $f_{O_2}(z,t)$ are temperature- and oxygen-dependence functions.

In addition, the temporal evolution of small POC inventory will be:

$$\frac{\partial iPOC_S^{900}(z,t)}{\partial t} = S^{900}(z,t) - \int_z^{900} r_s \cdot f_T(z,t) \cdot f_{O_2}(z,t) \cdot POC_S(z,t) dz. \tag{E.21}$$

However, this equation cannot be resolved analytically. Therefore, I will divide the water column into a couple of vertical layers (Fig. E.1). Within each vertical layer (e.g., the kth layer), the small POC can be supplied by the vertical carbon flux from the upper layer (e.g., $totF_S(k,t)$) and will be also transported into the lower layer (e.g., $totF_S(k+1,t)$). In addition, the small POC concentrations can be changed by remineralization and fragmentation. Therefore, the temporal evolution of small POC inventory within the kth vertical layer is:

$$\frac{\partial POC_S(k,t) \cdot \Delta z(k)}{\partial t} = NS(k,t) - R_s \cdot POC_S(k,t) \cdot \Delta z(k), \tag{E.22}$$

where $POC_S(k,t)$ is the small POC concentrations within the kth vertical layer, $\Delta z(k)$ is the thickness, $NS(k,t)$ is the net source of small POC within the kth vertical layer, which includes the vertical carbon flux of small POC into ($totF_S(k,t)$) and out of ($totF_S(k+1,t)$) the kth vertical layer and the fragmentation flux of large POC ($d_L \cdot POC_L(k,t) \cdot \Delta z(k)$):

$$NS(k,t) = totF_S(k,t) - totF_S(k+1,t) + d_L \cdot POC_L(k,t) \cdot \Delta z(k), \tag{E.23}$$

where R_s is the net remineralization rate:

$$R_s = r_s \cdot f_T(z,t) \cdot f_{O_2}(z,t). \tag{E.24}$$

Assuming that the vertical carbon flux of small POC and the environmental factors (e.g., temperature, oxygen, and large POC concentrations) are constant between two consecutive

sampling times, the net source of small POC will be also constant and can be resolved similarly as Eq.s E.1-E.9:

$$NS(z) = \frac{R_s \cdot (POC_S(z, t_1) - POC_S(z, t_0)e^{-R_s\Delta t})\Delta z(k)}{1 - e^{-R_s\Delta t}} .$$

(E. 25)

By assuming the boundary conditions that there is no vertical carbon flux of small POC out of the mesopelagic zone, the vertical carbon flux of small POC is:

$$totF_S(n) = NS(n) - d_L \cdot POC_L(n) \cdot \Delta z(n)$$

(E. 26)

into the bottom layer (nth grid) and is:

$$totF_S(k) = NS(k) + totF_S(k + 1) - d_L \cdot POC_L(k) \cdot \Delta z(k)$$

(E. 27)

in other vertical layers.

Table E.1. Summary of parameters and abbreviations used in Chapter 5

| Symbol	Description	Units
	Variables	
POC_S	Small POC concentration	mg C m^{-3}
POC_L	Large POC concentration	mg C m^{-3}
$iPOC_S^{900}$	The vertical integration of small POC from 900m	mg C m^{-2}
$iPOC_L^{900}$	The vertical integration of large POC from 900m	mg C m^{-2}
O_2	Dissolved oxygen concentration	mmol O$_2$ m^{-3}
AOU	The Apparent Oxygen Utilization	mmol O$_2$ m^{-3}
	Parameters	
r_S	Carbon specific remineralization rate of small POC	day^{-1}
r_L	Carbon specific remineralization rate of large POC	day^{-1}
d_L	Carbon specific fragmentation rate of large POC	day^{-1}
A_S	Carbon specific net attenuation rate of small POC	day^{-1}
A_L	Carbon specific net attenuation rate of large POC	day^{-1}
w_S	Sinking velocity of small POC	m day^{-1}
w_L	Sinking velocity of large POC	m day^{-1}
l_S	Remineralization length scale of small POC	m
$l_{S,r}$	Remineralization length scale of small POC when fragmentation is not considered	m
l_L	Remineralization length scale of large POC	m
	Fluxes	
$totF$	The total vertical carbon flux	mg C m^{-2} day^{-1}
S^{900}	The supply of small POC	mg C m^{-2} day^{-1}
$totF_s$	The total vertical carbon flux of small POC	mg C m^{-2} day^{-1}
$OtherF_S$	The carbon flux of small POC due to other mechanisms	mg C m^{-2} day^{-1}
$GravF_S$	The gravitational sinking flux of small POC	mg C m^{-2} day^{-1}
$GravF_L$	The gravitational sinking flux of large POC	mg C m^{-2} day^{-1}
$iFrag$	The integrated fragmentation flux	mg C m^{-2} day^{-1}
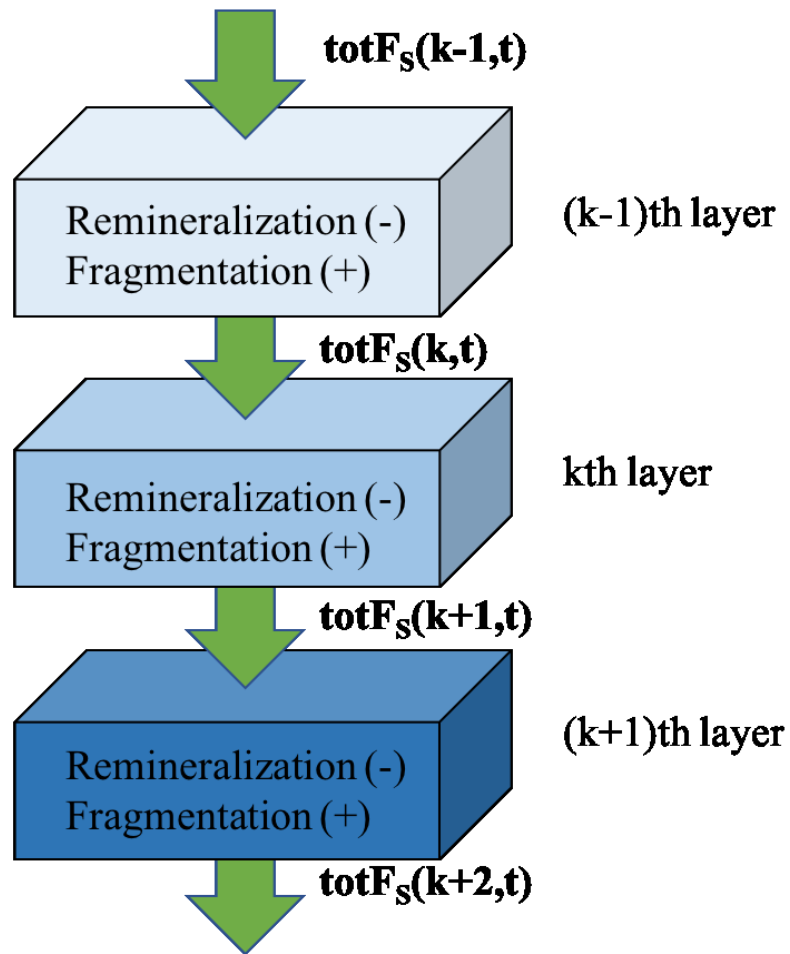
Figure E.1. A schematic to show the processes controlling the small POC concentrations within each vertical layer
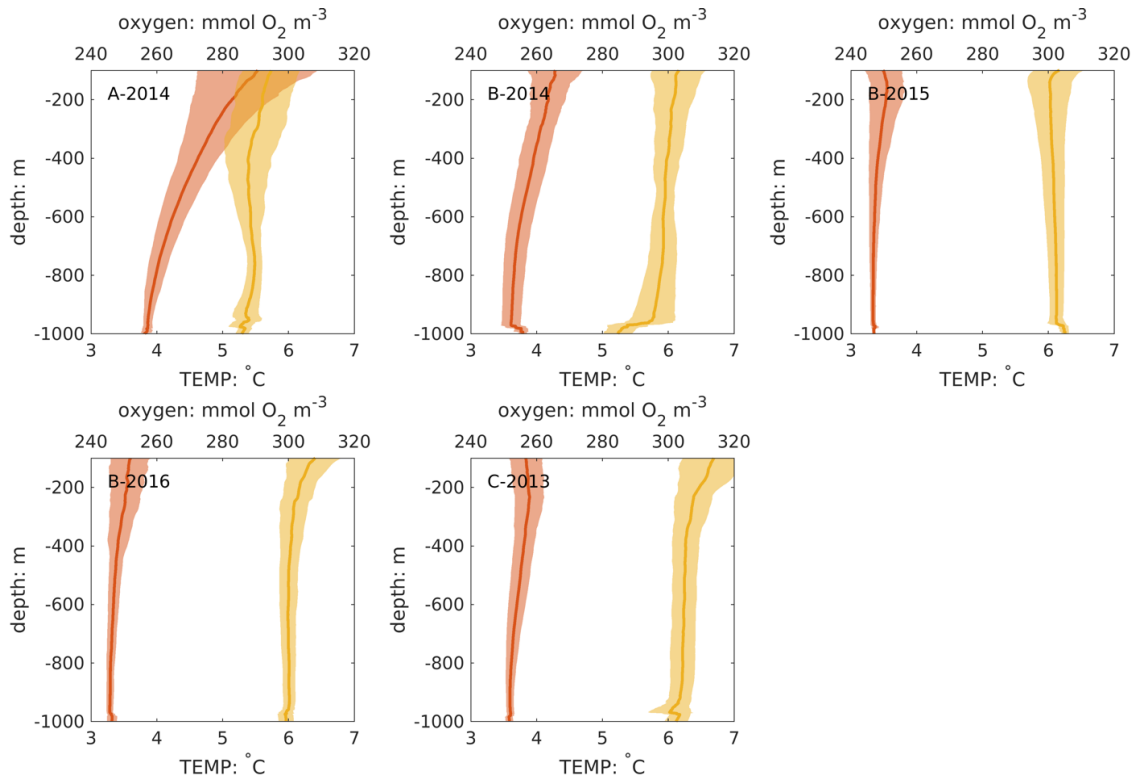
Figure E.2. The vertical profiles of temperature (orange) and oxygen (yellow) from each float segment. The shadow areas represent the standard deviation.
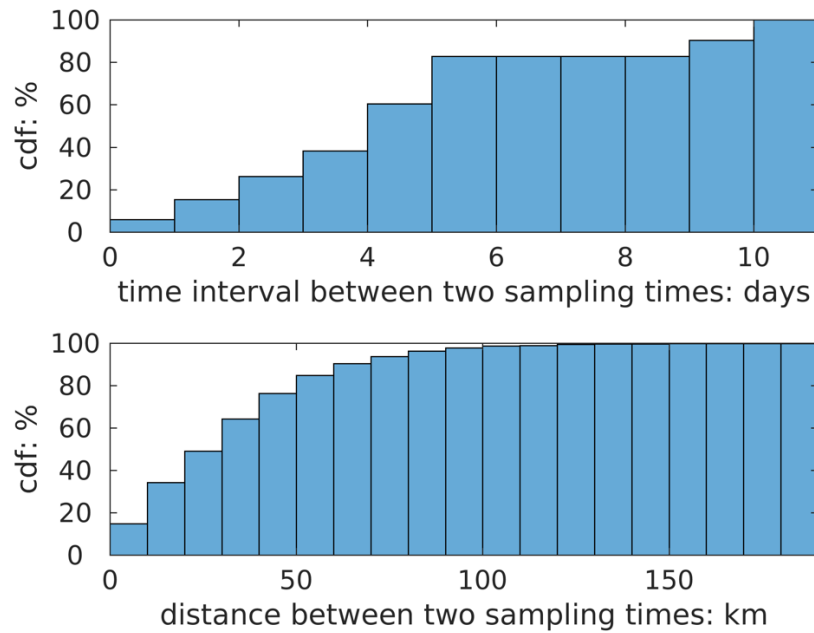

Figure E.3. The cumulative probabilities of the time interval (days) and distance (km) between two consecutive sampling times of BGC-Argo floats that I used
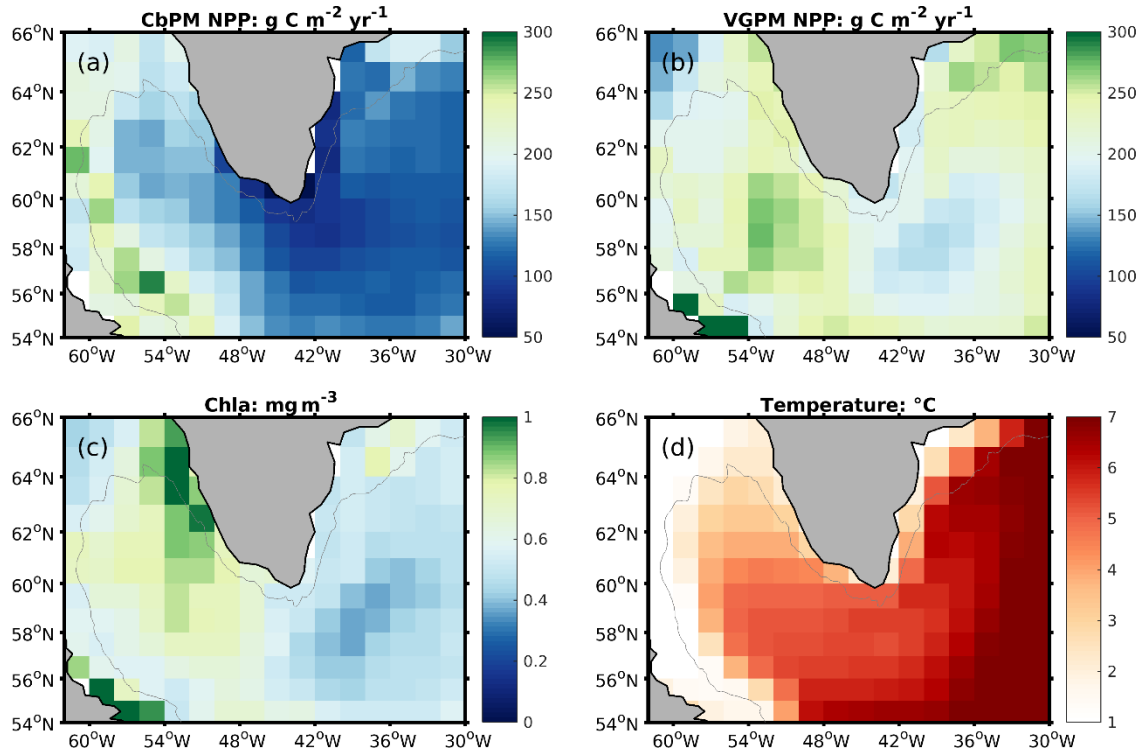
Figure E.4. The spatial distributions of net primary production (NPP), surface chlorophyll, and sea surface temperature from satellite data. The 1,000 m isobath is represented by the gray line.

Figure E.5. The spatial distributions of satellite derived carbon flux at 100m (g C m^{-2} yr^{-1}). The 1,000 m isobath is represented by the gray line. The spatial mean (standard deviation) of the carbon flux over the deep ocean (depth>1,000m) are shown in each panel.

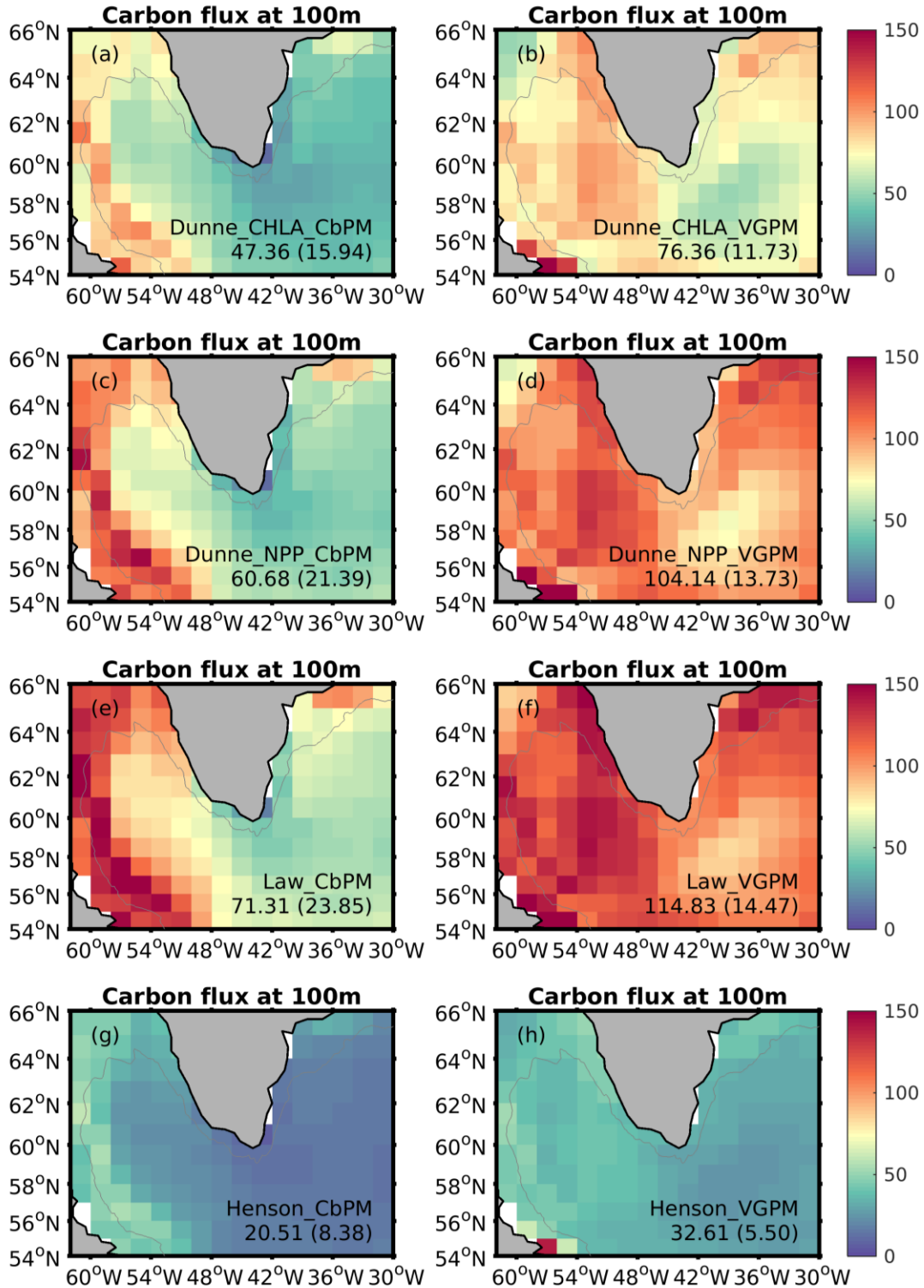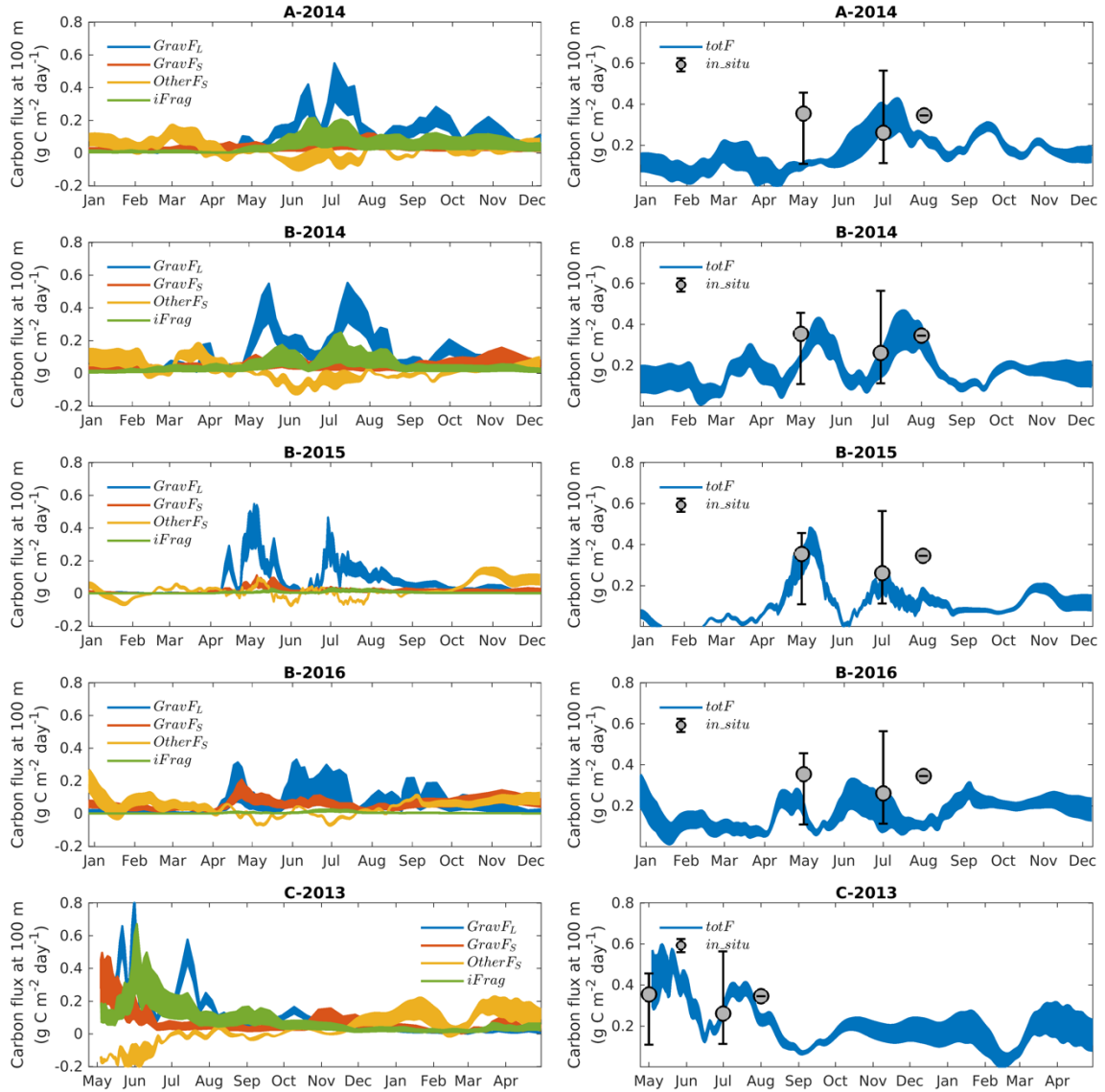**Figure E.6.** Time series of the vertical carbon flux due to different mechanisms (left column) and comparisons between the estimated total carbon flux at 100 m and the monthly climatology of ^{234}Th-derived carbon fluxes (right column). The time series of *otherF$_S$* and *totF* are smoothed by a 24-day running mean because of the episodic features in the mixed layer pump and eddy subduction pump and to make them more directly comparable to the ^{234}Th-based fluxes.

BIBLIOGRAPHY

Anderson, J. L., and S. L. Anderson. 1999. A Monte Carlo Implementation of the Nonlinear Filtering Problem to Produce Ensemble Assimilations and Forecasts. Mon. Weather Rev. **127**: 2741–2758.

Anderson, L. A., A. R. Robinson, and C. J. Lozano. 2000. Physical and biological modeling in the Gulf Stream region:: I. Data assimilation methodology. Deep Sea Res. Part I Oceanogr. Res. Pap. **47**: 1787–1827. doi:https://doi.org/10.1016/S0967-0637(00)00019-4

Anderson, L. A., and J. L. Sarmiento. 1994. Redfield ratios of remineralization determined by nutrient data analysis. Global Biogeochem. Cycles **8**: 65–80. doi:https://doi.org/10.1029/93GB03318

Armstrong, R. A., C. Lee, J. I. Hedges, S. Honjo, and S. G. Wakeham. 2001. A new, mechanistic model for organic carbon fluxes in the ocean based on the quantitative association of POC with ballast minerals. Deep Sea Res. Part II Top. Stud. Oceanogr. **49**: 219–236. doi:https://doi.org/10.1016/S0967-0645(01)00101-1

Aumont, O., C. Ethé, A. Tagliabue, L. Bopp, and M. Gehlen. 2015. PISCES-v2: an ocean biogeochemical model for carbon and ecosystem studies. Geosci. Model Dev. **8**: 2465–2513. doi:10.5194/gmd-8-2465-2015

Aumont, O., M. van Hulten, M. Roy-Barman, J.-C. Dutay, C. Éthé, and M. Gehlen. 2017. Variable reactivity of particulate organic matter in a global ocean biogeochemical model. Biogeosciences **14**: 2321–2341. doi:10.5194/bg-14-2321-2017

Bagniewski, W., K. Fennel, M. J. Perry, and E. A. D'Asaro. 2011. Optimizing models of the North Atlantic spring bloom using physical, chemical and bio-optical observations from a Lagrangian float. Biogeosciences **8**: 1291–1307. doi:10.5194/bg-8-1291-2011

Baker, C. A., S. A. Henson, E. L. Cavan, and others. 2017. Slow-sinking particulate organic carbon in the Atlantic Ocean: Magnitude, flux, and potential controls. Global Biogeochem. Cycles **31**: 1051–1065. doi:https://doi.org/10.1002/2017GB005638

Behrenfeld, M. J., E. Boss, D. A. Siegel, and D. M. Shea. 2005. Carbon-based ocean productivity and phytoplankton physiology from space. Global Biogeochem. Cycles **19**: 1–14. doi:10.1029/2004GB002299

Behrenfeld, M. J., and P. G. Falkowski. 1997. Photosynthetic rates derived from satellite-based chlorophyll concentration. Limnol. Oceanogr. **42**: 1–20.

Biogeochemical-Argo Planning Group. 2016. The scientific rationale, design and implementation plan for a Biogeochemical-Argo float array.

Bisson, K., D. A. Siegel, and T. DeVries. 2020. Diagnosing Mechanisms of Ocean Carbon Export in a Satellite-Based Food Web Model. Front. Mar. Sci. **7**: 505. doi:10.3389/fmars.2020.00505

Bittig, H. C., T. Steinhoff, H. Claustre, B. Fiedler, N. L. Williams, R. Sauzède, A. Körtzinger, and J.-P. Gattuso. 2018. An Alternative to Static Climatologies: Robust Estimation of Open Ocean CO2 Variables and Nutrient Concentrations From T, S, and O2 Data Using Bayesian Neural Networks. Front. Mar. Sci. **5**. doi:10.3389/fmars.2018.00328

Bol, R., S. A. Henson, A. Rumyantseva, and N. Briggs. 2018. High-Frequency Variability of Small-Particle Carbon Export Flux in the Northeast Atlantic. Global Biogeochem. Cycles **32**: 1803–1814. doi:10.1029/2018GB005963

Boss, E. B., and N. Haëntjens. 2016. Primer regarding measurements of chlorophyll fluorescence and the backscattering coefficient with WETLabs FLBB on profiling floats.

Boyd, P. W., H. Claustre, M. Levy, D. A. Siegel, and T. Weber. 2019. Multi-faceted particle pumps drive carbon sequestration in the ocean. Nature **568**: 327–335. doi:10.1038/s41586-019-1098-2

Boyer, T. P., J. I. Antonov, O. K. Baranova, and others. 2013. World ocean database 2013 O.C.L. National Oceanographic Data Center (U.S.) [ed.].doi:http://doi.org/10.7289/V5NZ85MT

Briggs, N., G. Dall'Olmo, and H. Claustre. 2020. Major role of particle fragmentation in regulating biological sequestration of CO2 by the oceans. Science (80-.). **367**: 791–793. doi:10.1126/science.aay1790

Briggs, N., M. J. Perry, I. Cetinic´, C. Lee, E. D'Asaro, A. M. Gray, and E. Rehm. 2011. High-resolution observations of aggregate flux during a sub-polar North Atlantic spring bloom. Deep. Res. I **58**: 1031–1039. doi:10.1016/j.dsr.2011.07.007

Bruggeman, J., and K. Bolding. 2014. A general framework for aquatic biogeochemical models. Environ. Model. Softw. **61**: 249–265. doi:https://doi.org/10.1016/j.envsoft.2014.04.002

Buesseler, K. O., C. R. Benitez-Nelson, S. B. Moran, and others. 2006. An assessment of particulate organic carbon to thorium-234 ratios in the ocean and their impact on the application of 234Th as a POC flux proxy. Mar. Chem. **100**: 213–233. doi:https://doi.org/10.1016/j.marchem.2005.10.013

Burd, A. B., D. A. Hansell, D. K. Steinberg, and others. 2010. Assessing the apparent imbalance between geochemical and biochemical indicators of meso- and bathypelagic biological activity: What the @$♯! is wrong with present calculations of carbon budgets? Deep Sea Res. Part II Top. Stud. Oceanogr. **57**: 1557–1571. doi:https://doi.org/10.1016/j.dsr2.2010.02.022

Cael, B. B., and K. Bisson. 2018. Particle Flux Parameterizations: Quantitative and Mechanistic Similarities and Differences. Front. Mar. Sci. **5**. doi:10.3389/fmars.2018.00395

Cetinić, I., M. J. Perry, N. T. Briggs, E. Kallin, E. A. D'Asaro, and C. M. Lee. 2012. Particulate organic carbon and inherent optical properties during 2008 North Atlantic Bloom Experiment. J. Geophys. Res. Ocean. **117**. doi:10.1029/2011JC007771

Chai, F., K. S. Johnson, H. Claustre, and others. 2020. Monitoring ocean biogeochemistry with autonomous platforms. Nat. Rev. Earth Environ. **1**: 315–326. doi:10.1038/s43017-020-0053-y

Chassignet, E. P., H. E. Hurlburt, O. M. Smedstad, and others. 2005. Assessment of Data Assimilative Ocean Models in the Gulf of Mexico Using Ocean Color, p. 87–100. *In* Circulation in the Gulf of Mexico: Observations and Models. American Geophysical Union (AGU).

Ciavatta, S., R. J. W. Brewin, J. Skakala, L. Polimene, L. de Mora, Y. Artioli, and J. I. Allen. 2018. Assimilation of Ocean-Color Plankton Functional Types to Improve Marine Ecosystem Simulations. J. Geophys. Res. Ocean. **123**: 834–854. doi:10.1002/2017JC013490

Ciavatta, S., S. Kay, R. J. W. Brewin, and others. 2019. Ecoregions in the Mediterranean Sea Through the Reanalysis of Phytoplankton Functional Types and Carbon Fluxes. J. Geophys. Res. Ocean. **124**: 6737–6759. doi:https://doi.org/10.1029/2019JC015128

Ciavatta, S., R. Torres, V. Martinez-vicente, T. Smyth, G. D. Olmo, L. Polimene, and J. I. Allen. 2014. Progress in Oceanography Assimilation of remotely-sensed optical properties to improve marine biogeochemistry modelling. Prog. Oceanogr. **127**: 74–95. doi:10.1016/j.pocean.2014.06.002

Cossarini, G., L. Mariotti, L. Feudale, A. Mignot, S. Salon, V. Taillandier, A. Teruzzi, and F. D'Ortenzio. 2019. Towards operational 3D-Var assimilation of chlorophyll Biogeochemical-Argo float data into a biogeochemical model of the Mediterranean Sea. Ocean Model. **133**: 112–128. doi:https://doi.org/10.1016/j.ocemod.2018.11.005

Cullen, J. J. 2015. Subsurface Chlorophyll Maximum Layers : Enduring Enigma or Mystery Solved ? Ann. Rev. Mar. Sci. **7**: 207–239. doi:10.1146/annurev-marine-010213-135111

Dall'Olmo, G., J. Dingle, L. Polimene, R. J. W. Brewin, and H. Claustre. 2016. Substantial energy input to the mesopelagic ecosystem from the seasonal mixed-layer pump. Nat. Geosci. **9**: 820–823. doi:10.1038/ngeo2818

Dall'Olmo, G., and K. A. Mork. 2014. Carbon export by small particles in the Norwegian Sea. Geophys. Res. Lett. **41**: 2921–2927. doi:https://doi.org/10.1002/2014GL059244

Dee, D. P., S. M. Uppala, A. J. Simmons, and others. 2011. The ERA-Interim reanalysis: configuration and performance of the data assimilation system. Q. J. R. Meteorol. Soc. **137**: 553–597. doi:https://doi.org/10.1002/qj.828

DeVries, T., and T. Weber. 2017. The export and fate of organic matter in the ocean: New constraints from combining satellite and oceanographic tracer observations. Global Biogeochem. Cycles **31**: 535–555. doi:10.1002/2016GB005551

Doney, S. C. 1999. Major challenges confronting marine biogeochemical modeling. Global Biogeochem. Cycles **13**: 705–714. doi:10.1029/1999GB900039

Doney, S. C., I. Lima, J. K. Moore, and others. 2009. Skill metrics for confronting global upper ocean ecosystem-biogeochemistry models against field and remote sensing data. J. Mar. Syst. **76**: 95–112. doi:10.1016/j.jmarsys.2008.05.015

Doney, S. C., K. Lindsay, K. Caldeira, and others. 2004. Evaluating global ocean carbon models: The importance of realistic physics. Global Biogeochem. Cycles **18**. doi:10.1029/2003GB002150

Dunne, J. P., R. A. Armstrong, A. Gnanadesikan, and J. L. Sarmiento. 2005. Empirical and mechanistic models for the particle export ratio. Global Biogeochem. Cycles **19**. doi:10.1029/2004GB002390

Dunne, J. P., I. Bociu, B. Bronselaer, and others. 2020. Simple Global Ocean Biogeochemistry With Light, Iron, Nutrients and Gas Version 2 (BLINGv2): Model Description and Simulation Characteristics in GFDL's CM4.0. J. Adv. Model. Earth Syst. **12**: e2019MS002008. doi:https://doi.org/10.1029/2019MS002008

Durkin, C. A., K. O. Buesseler, I. Cetinić, M. L. Estapa, R. P. Kelly, and M. Omand. 2021. A Visual Tour of Carbon Export by Sinking Particles. Global Biogeochem. Cycles **35**: e2021GB006985. doi:https://doi.org/10.1029/2021GB006985

Edwards, C. A., A. M. Moore, I. Hoteit, and B. D. Cornuelle. 2015. Regional Ocean Data Assimilation. Ann. Rev. Mar. Sci. **7**: 21–42. doi:10.1146/annurev-marine-010814-015821

Evensen, G. 2003. The Ensemble Kalman Filter: theoretical formulation and practical implementation. Ocean Dyn. **53**: 343–367. doi:10.1007/s10236-003-0036-9

Falkowski, P. G., R. T. Barber, and V. V Smetacek. 1998. Biogeochemical Controls and Feedbacks on Ocean Primary Production. Science (80-.). **281**: 200–207.

Fennel, K., and E. Boss. 2003. Subsurface maxima of phytoplankton and chlorophyll : Steady-state solutions from a simple model. Limnol. Oceanogr. **48**: 1521–1534.

Fennel, K., M. Gehlen, P. Brasseur, and others. 2019. Advancing Marine Biogeochemical and Ecosystem Reanalyses and Forecasts as Tools for Monitoring and Managing Ecosystem Health. Front. Mar. Sci. **6**: 89. doi:10.3389/fmars.2019.00089

Fennel, K., R. Hetland, Y. Feng, and S. Dimarco. 2011. A coupled physical-biological model of the Northern Gulf of Mexico shelf: Model description, validation and analysis of phytoplankton variability. Biogeosciences **8**: 1881–1899. doi:10.5194/bg-8-1881-2011

Fennel, K., M. Losch, J. Schroter, and M. Wenzel. 2001. Testing a marine ecosystem model : sensitivity analysis and parameter optimization. J. Mar. Syst. **28**: 45–63.

Fennel, K., J. P. Mattern, S. C. Doney, L. Bopp, A. M. Moore, B. Wang, and L. Yu. 2022. Ocean biogeochemical modelling. Nat. Rev. Methods Prim. doi:10.1038/s43586-022-00154-2

Fennel, K., J. Wilkin, J. Levin, J. Moisan, J. O. Reilly, and D. Haidvogel. 2006. Nitrogen cycling in the Middle Atlantic Bight : Results from a three-dimensional model and implications for the North Atlantic nitrogen budget. Global Biogeochem. Cycles **20**: 1–14. doi:10.1029/2005GB002456

Feucher, C., Y. Garcia-Quintana, I. Yashayaev, X. Hu, and P. G. Myers. 2019. Labrador Sea Water Formation Rate and Its Impact on the Local Meridional Overturning Circulation. J. Geophys. Res. Ocean. **124**: 5654–5670. doi:https://doi.org/10.1029/2019JC015065

Fiechter, J., G. Broquet, A. M. Moore, and H. G. Arango. 2011. A data assimilative, coupled physical–biological model for the Coastal Gulf of Alaska. Dyn. Atmos. Ocean. **52**: 95–118. doi:https://doi.org/10.1016/j.dynatmoce.2011.01.002

Fontana, C., P. Brasseur, and J. M. Brankart. 2013. Toward a multivariate reanalysis of the North Atlantic Ocean biogeochemistry during 1998 – 2006 based on the assimilation of SeaWiFS chlorophyll data Toward a multivariate reanalysis of the North Atlantic Ocean biogeochemistry during 1998 – 2006 based on. Ocean Sci. **9**: 37–56. doi:10.5194/os-9-37-2013

Ford, D. 2020. Assimilating synthetic Biogeochemical-Argo and ocean colour observations into a global ocean model to inform observing system design. Biogeosciences Discuss. **2020**: 1–34. doi:10.5194/bg-2020-152

Ford, D. 2021. Assimilating synthetic Biogeochemical-Argo and ocean colour observations into a global ocean model to inform observing system design. Biogeosciences **18**: 509–534. doi:10.5194/bg-18-509-2021

Ford, D., and R. Barciela. 2017. Global marine biogeochemical reanalyses assimilating two different sets of merged ocean colour products. Remote Sens. Environ. **203**: 40–54. doi:https://doi.org/10.1016/j.rse.2017.03.040

Francois, R., S. Honjo, R. Krishfield, and S. Manganini. 2002. Factors controlling the flux of organic carbon to the bathypelagic zone of the ocean. Global Biogeochem. Cycles **16**: 20–34. doi:10.1029/2001GB001722

Friedrichs, M. A. M., J. A. Dusenberry, L. A. Anderson, and others. 2007. Assessment of skill and portability in regional marine biogeochemical models: Role of multiple planktonic groups. J. Geophys. Res. **112**: 1–22. doi:10.1029/2006JC003852

Friedrichs, M. A. M., R. R. Hood, and J. D. Wiggert. 2006. Ecosystem model complexity versus physical forcing: Quantification of their relative impact with assimilated Arabian Sea data. Deep. Res. Part II **53**: 576–600. doi:10.1016/j.dsr2.2006.01.026

Galí, M., M. Falls, H. Claustre, O. Aumont, and R. Bernardello. 2022. Bridging the gaps between particulate backscattering measurements and modeled particulate organic carbon in the ocean. Biogeosciences **19**: 1245–1275. doi:10.5194/bg-19-1245-2022

Gehlen, M., L. Bopp, N. Emprin, O. Aumont, C. Heinze, and O. Ragueneau. 2006. Reconciling surface ocean productivity, export fluxes and sediment composition in a global biogeochemical ocean model. Biogeosciences **3**: 521–537. doi:10.5194/bg-3-521-2006

Geider, R. J. 1987. Light and temperature dependence of the carbon to chlorophyll a ratio in microalgae and cyanobacteria: implications for physiology and growth of phytoplankton. New Phytol. **106**: 1–34.

Geider, R. J., H. L. MacIntyre, and T. M. Kana. 1997. Dynamic model of phytoplankton growth and acclimation : responses of the balanced growth rate and the chlorophyll a : carbon ratio to light , nutrient-limitation and temperature. Mar. Ecol. Prog. Ser. **148**: 187–200.

Giering, S. L. C., E. L. Cavan, S. L. Basedow, and others. 2020. Sinking Organic Particles in the Ocean—Flux Estimates From in situ Optical Devices. Front. Mar. Sci. **6**. doi:10.3389/fmars.2019.00834

Giering, S. L. C., R. Sanders, R. S. Lampitt, and others. 2014. Reconciliation of the carbon budget in the ocean's twilight zone. Nature **507**: 480–483. doi:10.1038/nature13123

Giering, S. L. C., R. Sanders, A. P. Martin, C. Lindemann, K. O. Möller, C. J. Daniels, D. J. Mayor, and M. A. St. John. 2016. High export via small particles before the onset of the North Atlantic spring bloom. J. Geophys. Res. Ocean. **121**: 6929–6945. doi:https://doi.org/10.1002/2016JC012048

Giering, S. L. C., B. Yan, J. Sweet, V. Asper, A. Diercks, J. P. Chanton, M. Pitiranggon, and U. Passow. 2018. The ecosystem baseline for particle flux in the Northern Gulf of Mexico. Elementa **6**: 1–22. doi:10.1525/elementa.264

Gloege, L., G. A. McKinley, C. B. Mouw, and A. B. Ciochetto. 2017. Global evaluation of particulate organic carbon flux parameterizations and implications for atmospheric pCO2. Global Biogeochem. Cycles **31**: 1192–1215. doi:https://doi.org/10.1002/2016GB005535

Gomez, F. A., S. Lee, Y. Liu, F. J. H. Jr, F. E. Muller-karger, and J. T. Lanmkin. 2018. Seasonal patterns in phytoplankton biomass across the northern and deep Gulf of Mexico : a numerical model study. Biogeosciencesg **15**: 3561–3576. doi:10.5194/bg-15-3561-2018

Goodliff, M., T. Bruening, F. Schwichtenberg, X. Li, A. Lindenthal, I. Lorkowski, and L. Nerger. 2019. Temperature assimilation into a coastal ocean-biogeochemical model: assessment of weakly and strongly coupled data assimilation. Ocean Dyn. **69**: 1217–1237. doi:10.1007/s10236-019-01299-7

Greatbatch, R. J., J. Sheng, C. Eden, L. Tang, X. Zhai, and J. Zhao. 2004. The semi-prognostic method. Cont. Shelf Res. **24**: 2149–2165. doi:10.1016/j.csr.2004.07.009

Green, R. E., A. S. Bower, and A. Lugo-Fernandez. 2014. First Autonomous Bio-Optical Profiling Float in the Gulf of Mexico Reveals Dynamic Biogeochemistry in Deep Waters. PLoS One **9**: 1–9. doi:10.1371/journal.pone.0101658

Gregg, W. W. 2008. Assimilation of SeaWiFS ocean chlorophyll data into a three-dimensional global ocean model. J. Mar. Syst. **69**: 205–225. doi:10.1016/j.jmarsys.2006.02.015

Gregg, W. W., and C. S. Rousseaux. 2017. Simulating PACE Global Ocean Radiances. Front. Mar. Sci. **4**: 60. doi:10.3389/fmars.2017.00060

Guidi, L., L. Legendre, G. Reygondeau, J. Uitz, L. Stemmann, and S. A. Henson. 2015. A new look at ocean carbon remineralization for estimating deepwater sequestration. Global Biogeochem. Cycles **29**: 1044–1059. doi:https://doi.org/10.1002/2014GB005063

Haidvogel, D. B., H. Arango, W. P. Budgell, and others. 2008. Ocean forecasting in terrain-following coordinates : Formulation and skill assessment of the Regional Ocean Modeling System. J. Comput. Phys. **227**: 3595–3624. doi:10.1016/j.jcp.2007.06.016

Haines, K., J. Johannessen, P. Knudsen, D. Lea, M.-H. Rio, L. Bertino, F. Davidson, and F. Hernandez. 2011. An ocean modelling and assimilation guide to using GOCE geoid products. Ocean Sci. **7**: 151–164. doi:10.5194/os-7-151-2011

Hennon, T. D., S. C. Riser, and S. Mecking. 2016. Profiling float-based observations of net respiration beneath the mixed layer. Global Biogeochem. Cycles **30**: 920–932. doi:https://doi.org/10.1002/2016GB005380

Henson, S. A., C. Laufkötter, S. Leung, S. L. C. Giering, H. I. Palevsky, and E. L. Cavan. 2022. Uncertain response of ocean biological carbon export in a changing world. Nat. Geosci. **15**: 248–254. doi:10.1038/s41561-022-00927-0

Henson, S. A., F. Le Moigne, and S. Giering. 2019. Drivers of Carbon Export Efficiency in the Global Ocean. Global Biogeochem. Cycles **33**: 891–903. doi:https://doi.org/10.1029/2018GB006158

Henson, S. A., R. Sanders, and E. Madsen. 2012. Global patterns in efficiency of particulate organic carbon export and transfer to the deep ocean. Global Biogeochem. Cycles **26**: 1–14. doi:10.1029/2011GB004099

Henson, S. A., R. Sanders, E. Madsen, P. J. Morris, F. Le Moigne, and G. D. Quartly. 2011. A reduced estimate of the strength of the ocean's biological carbon pump. Geophys. Res. Lett. **38**. doi:10.1029/2011GL046735

Henson, S. A., A. Yool, and R. Sanders. 2015. Variability in efficiency of particulate organic carbon export: A model study. Global Biogeochem. Cycles **29**: 33–45. doi:10.1002/2014GB004965

Honjo, S., S. J. Manganini, R. A. Krishfield, and R. Francois. 2008. Particulate organic carbon fluxes to the ocean interior and factors controlling the biological pump: A synthesis of global sediment trap programs since 1983. Prog. Oceanogr. **76**: 217–285. doi:https://doi.org/10.1016/j.pocean.2007.11.003

Hoshiba, Y., T. Hirata, M. Shigemitsu, H. Nakano, T. Hashioka, Y. Masuda, and Y. Yamanaka. 2018. Biological data assimilation for parameter estimation of a phytoplankton functional type model for the western North Pacific. Ocean Sci. **14**: 371–386. doi:10.5194/os-14-371-2018

Howard, M. T., A. M. E. Winguth, C. Klaas, and E. Maier-Reimer. 2006. Sensitivity of ocean carbon tracer distributions to particulate organic flux parameterizations. Global Biogeochem. Cycles **20**. doi:https://doi.org/10.1029/2005GB002499

Hu, J., K. Fennel, J. P. Mattern, and J. Wilkin. 2012. Data assimilation with a local Ensemble Kalman Filter applied to a three-dimensional biological model of the Middle Atlantic Bight. J. Mar. Syst. **94**: 145–156. doi:10.1016/j.jmarsys.2011.11.016

Huang, B., Y. Xue, and D. W. Behringer. 2008. Impacts of Argo salinity in NCEP Global Ocean Data Assimilation System: The tropical Indian Ocean. J. Geophys. Res. Ocean. **113**. doi:10.1029/2007JC004388

Hung, C.-C., C. Xu, P. H. Santschi, and others. 2010. Comparative evaluation of sediment trap and 234Th-derived POC fluxes from the upper oligotrophic waters of the Gulf of Mexico and the subtropical northwestern Pacific Ocean. Mar. Chem. **121**: 132–144. doi:https://doi.org/10.1016/j.marchem.2010.03.011

Jones, E. M., M. E. Baird, M. Mongin, and others. 2016. Use of remote-sensing reflectance to constrain a data assimilating marine biogeochemical model of the Great Barrier Reef. Biogeosciences **13**: 6441–6469. doi:10.5194/bg-13-6441-2016

Kane, A., C. Moulin, S. Thiria, and others. 2011. Improving the parameters of a global ocean biogeochemical model via variational assimilation of in situ data at five time series stations. J. Geophys. Res. Ocean. **116**: 1–14. doi:10.1029/2009JC006005

Kerry, C., B. Powell, M. Roughan, and P. Oke. 2016. Development and evaluation of a high-resolution reanalysis of the East Australian Current region using the Regional Ocean Modelling System (ROMS~3.4) and Incremental Strong-Constraint 4-Dimensional Variational (IS4D-Var) data assimilation. Geosci. Model Dev. **9**: 3779–3801. doi:10.5194/gmd-9-3779-2016

Kheireddine, M., G. Dall'Olmo, M. Ouhssain, and others. 2020. Organic Carbon Export and Loss Rates in the Red Sea. Global Biogeochem. Cycles **34**: e2020GB006650. doi:https://doi.org/10.1029/2020GB006650

Kidston, M., R. Matear, and M. E. Baird. 2011. Parameter optimisation of a marine ecosystem model at two contrasting stations in the Sub-Antarctic Zone. Deep. Res. II **58**: 2301–2315. doi:10.1016/j.dsr2.2011.05.018

Kuhn, A. M., and K. Fennel. 2019. Evaluating ecosystem model complexity for the northwest North Atlantic through surrogate-based optimization. Ocean Model. **142**: 101437. doi:https://doi.org/10.1016/j.ocemod.2019.101437

Kuhn, A. M., K. Fennel, and I. Berman-frank. 2018. Modelling the biogeochemical effects of heterotrophic and autotrophic N2 fixation in the Gulf of Aqaba (Israel), Red Sea. Biogeosciences **15**: 7379–7401. doi:10.5194/bg-15-7379-2018

Kuhn, A. M., K. Fennel, and J. P. Mattern. 2015. Progress in Oceanography Model investigations of the North Atlantic spring bloom initiation. Prog. Oceanogr. **138**: 176–193. doi:10.1016/j.pocean.2015.07.004

Kwon, E. Y., F. Primeau, and J. L. Sarmiento. 2009. The impact of remineralization depth on the air–sea carbon balance. Nat. Geosci. **2**: 630–635. doi:10.1038/ngeo612

Lacour, L., N. Briggs, H. Claustre, M. Ardyna, and G. Dall'Olmo. 2019. The Intraseasonal Dynamics of the Mixed Layer Pump in the Subpolar North Atlantic Ocean: A Biogeochemical-Argo Float Approach. Global Biogeochem. Cycles **33**: 266–281. doi:10.1029/2018GB005997

Lagman, K. B., K. Fennel, K. R. Thompson, and L. Bianucci. 2014. Assessing the utility of frequency dependent nudging for reducing biases in biogeochemical models. Ocean Model. **81**: 25–35. doi:https://doi.org/10.1016/j.ocemod.2014.06.006

Lauderdale, J. M., and B. B. Cael. 2021. Impact of Remineralization Profile Shape on the Air-Sea Carbon Balance. Geophys. Res. Lett. **48**: e2020GL091746. doi:https://doi.org/10.1029/2020GL091746

Laufkötter, C., J. G. John, C. A. Stock, and J. P. Dunne. 2017. Temperature and oxygen dependence of the remineralization of organic matter. Global Biogeochem. Cycles **31**: 1038–1050. doi:https://doi.org/10.1002/2017GB005643

Laufkötter, C., M. Vogt, N. Gruber, and others. 2016. Projected decreases in future marine export production: the role of the carbon flux through the upper ocean ecosystem. Biogeosciences **13**: 4023–4047. doi:10.5194/bg-13-4023-2016

Laurent, A., K. Fennel, W. J. Cai, W. J. Huang, L. Barbero, and R. Wanninkhof. 2017. Eutrophication-induced acidification of coastal waters in the northern Gulf of Mexico: Insights into origin and processes from a coupled physical-biogeochemical model. Geophys. Res. Lett. **44**: 946–956. doi:10.1002/2016GL071881

Laurent, A., K. Fennel, and A. Kuhn. 2021. An observation-based evaluation and ranking of historical Earth system model simulations in the northwest North Atlantic Ocean. Biogeosciences **18**: 1803–1822. doi:10.5194/bg-18-1803-2021

Laws, E. A., P. G. Falkowski, W. O. Smith Jr., H. Ducklow, and J. J. McCarthy. 2000. Temperature effects on export production in the open ocean. Global Biogeochem. Cycles **14**: 1231–1246. doi:10.1029/1999GB001229

Lehmann, M. K., K. Fennel, and R. He. 2009. Statistical validation of a 3-D bio-physical model of the western North Atlantic. Biogeosciences **6**: 1961–1974. doi:10.5194/bg-6-1961-2009

Li, G., M. Iskandarani, M. Le Hénaff, J. Winokur, O. P. Le Maître, and O. M. Knio. 2016. Quantifying initial and wind forcing uncertainties in the Gulf of Mexico. Comput. Geosci. **20**: 1133–1153. doi:10.1007/s10596-016-9581-4

Lima, I. D., P. J. Lam, and S. C. Doney. 2014. Dynamics of particulate organic carbon flux in a global ocean model. Biogeosciences **11**: 1177–1198. doi:10.5194/bg-11-1177-2014

Llort, J., C. Langlais, R. Matear, S. Moreau, A. Lenton, and P. G. Strutton. 2018. Evaluating Southern Ocean Carbon Eddy-Pump From Biogeochemical-Argo Floats. J. Geophys. Res. Ocean. **123**: 971–984. doi:10.1002/2017JC012861

Long, M. C., J. K. Moore, K. Lindsay, and others. 2021. Simulations With the Marine Biogeochemistry Library (MARBL). J. Adv. Model. Earth Syst. **13**: e2021MS002647. doi:https://doi.org/10.1029/2021MS002647

Marsay, C. M., R. J. Sanders, S. A. Henson, K. Pabortsava, E. P. Achterberg, and R. S. Lampitt. 2015. Attenuation of sinking particulate organic carbon flux through the mesopelagic ocean. Proc. Natl. Acad. Sci. **112**: 1089–1094. doi:10.1073/pnas.1415311112

Martin, J. H., G. A. Knauer, D. M. Karl, and W. W. Broenkow. 1987. VERTEX: carbon cycling in the northeast Pacific. Deep Sea Res. Part A. Oceanogr. Res. Pap. **34**: 267–285. doi:https://doi.org/10.1016/0198-0149(87)90086-0

Martin, M., P. Dash, A. Ignatov, and others. 2012. Group for High Resolution Sea Surface temperature (GHRSST) analysis fields inter-comparisons. Part 1: A GHRSST multi-product ensemble (GMPE). Deep Sea Res. Part II Top. Stud. Oceanogr. **77**–**80**: 21–30. doi:https://doi.org/10.1016/j.dsr2.2012.04.013

Martínez-López, B., and J. Zavala-Hidalgo. 2009. Seasonal and interannual variability of cross-shelf transports of chlorophyll in the Gulf of Mexico. J. Mar. Syst. **77**: 1–20. doi:10.1016/j.jmarsys.2008.10.002

Martinez-Vicente, V., G. Dall'Olmo, G. Tarran, E. Boss, and S. Sathyendranath. 2013. Optical backscattering is correlated with phytoplankton carbon across the Atlantic Ocean. Geophys. Res. Lett. **40**: 1154–1158. doi:10.1002/grl.50252

Matear, R. J. 1995. Parameter optimization and analysis of ecosystem models using simulated annealing : A case study at Station P. J. Mar. Res. **53**: 571–607.

Mattern, J. P., M. Dowd, and K. Fennel. 2013. Particle filter-based data assimilation for a three-dimensional biological ocean model and satellite observations. J. Geophys. Res. Ocean. **118**: 2746–2760. doi:10.1002/jgrc.20213

Mattern, J. P., and C. A. Edwards. 2017. Simple parameter estimation for complex models — Testing evolutionary techniques on 3-dimensional biogeochemical ocean models. J. Mar. Syst. **165**: 139–152. doi:10.1016/j.jmarsys.2016.10.012

Mattern, J. P., K. Fennel, and M. Dowd. 2012. Estimating time-dependent parameters for a biological ocean model using an emulator approach. J. Mar. Syst. **96**–**97**: 32–47. doi:https://doi.org/10.1016/j.jmarsys.2012.01.015

Mattern, J. P., H. Song, C. A. Edwards, A. M. Moore, and J. Fiechter. 2017. Data assimilation of physical and chlorophyll a observations in the California Current System using two biogeochemical models. Ocean Model. **109**: 55–71. doi:https://doi.org/10.1016/j.ocemod.2016.12.002

Mauritsen, T., J. Bader, T. Becker, and others. 2019. Developments in the MPI-M Earth System Model version 1.2 (MPI-ESM1.2) and Its Response to Increasing CO2. J. Adv. Model. Earth Syst. **11**: 998–1038. doi:https://doi.org/10.1029/2018MS001400

McDonnell, A. M. P., P. W. Boyd, and K. O. Buesseler. 2015. Effects of sinking velocities and microbial respiration rates on the attenuation of particulate carbon fluxes through the mesopelagic zone. Global Biogeochem. Cycles **29**: 175–193. doi:https://doi.org/10.1002/2014GB004935

Mellor, G. L., and T. Yamada. 1982. Development of a turbulence closure model for geophysical fluid problems. Rev. Geophys. Sp. Phys. **20**: 851–875. doi:10.1029/RG020i004p00851

Mignot, A., H. Claustre, J. Uitz, A. Poteau, F. D'Ortenzio, and X. Xing. 2014. Understanding the seasonal dynamics of phytoplankton biomass and the deep chlorophyll maximum in oligotrophic environments: A Bio-Argo float investigation. Global Biogeochem. Cycles **28**: 1–21. doi:10.1002/2013GB004781

Le Moigne, F. A. C., M. Villa-Alfageme, R. J. Sanders, C. Marsay, S. Henson, and R. García-Tenorio. 2013. Export of organic carbon and biominerals derived from 234Th and 210Po at the Porcupine Abyssal Plain. Deep Sea Res. Part I Oceanogr. Res. Pap. **72**: 88–101. doi:https://doi.org/10.1016/j.dsr.2012.10.010

Morel, A. 1991. Light and marine photosynthesis: a spectral model with geochemical and climatological implications. Prog. Oceanogr. **26**: 263–306. doi:https://doi.org/10.1016/0079-6611(91)90004-6

Moreno, A. R., C. A. Garcia, A. A. Larkin, J. A. Lee, W.-L. Wang, J. K. Moore, F. W. Primeau, and A. C. Martiny. 2020. Latitudinal gradient in the respiration quotient and the implications for ocean oxygen availability. Proc. Natl. Acad. Sci. **117**: 22866–22872. doi:10.1073/pnas.2004986117

Mouw, C. B., A. Barnett, G. A. McKinley, L. Gloege, and D. Pilcher. 2016. Global ocean particulate organic carbon flux merged with satellite parameters. Earth Syst. Sci. Data **8**: 531–541. doi:10.5194/essd-8-531-2016

Muller-Karger, F. E., J. P. Smith, S. Werner, and others. 2015. Natural variability of surface oceanographic conditions in the offshore Gulf of Mexico. Prog. Oceanogr. **134**: 54–76. doi:10.1016/j.pocean.2014.12.007

Muller-Karger, F. E., J. J. Walsh, R. H. Evans, and M. B. Meyers. 1991. On the Seasonal Phytoplankton Concentration and Sea Surface Temperature Cycles of the Gulf of Mexico as Determined by Satellites. J. Geophys. Res. **96**: 12645–12665.

Niemeyer, D., I. Kriest, and A. Oschlies. 2019. The effect of marine aggregate parameterisations on nutrients and oxygen minimum zones in a global biogeochemical model. Biogeosciences **16**: 3095–3111. doi:10.5194/bg-16-3095-2019

Nowicki, M., T. DeVries, and D. A. Siegel. 2022. Quantifying the Carbon Export and Sequestration Pathways of the Ocean's Biological Carbon Pump. Global Biogeochem. Cycles **36**: e2021GB007083. doi:https://doi.org/10.1029/2021GB007083

Oke, P. R., D. A. Griffin, A. Schiller, and others. 2013. Evaluation of a near-global eddy-resolving ocean model. Geosci. Model Dev. **6**: 591–615. doi:10.5194/gmd-6-591-2013

Omand, M. M., E. A. D\textquoterightAsaro, C. M. Lee, M. J. Perry, N. Briggs, I. Cetinić, and A. Mahadevan. 2015. Eddy-driven subduction exports particulate organic carbon from the spring bloom. Science (80-.). **348**: 222–225. doi:10.1126/science.1260062

Oschlies, A., and V. Garçon. 1999. An eddy-permitting coupled physical-biological model of the North Atlantic: 1. Sensitivity to advection numerics and mixed layer physics. Global Biogeochem. Cycles **13**: 135–160. doi:10.1029/98GB02811

Oschlies, A., and M. Schartau. 2005. Basin-scale performance of a locally optimized marine ecosystem model. J. Mar. Res. **63**: 335–358.

Ourmières, Y., P. Brasseur, M. Lévy, J.-M. Brankart, and J. Verron. 2009. On the key role of nutrient data to constrain a coupled physical–biogeochemical assimilative model of the North Atlantic Ocean. J. Mar. Syst. **75**: 100–115. doi:https://doi.org/10.1016/j.jmarsys.2008.08.003

Palevsky, H. I., and S. C. Doney. 2021. Sensitivity of 21st Century Ocean Carbon Export Flux Projections to the Choice of Export Depth Horizon. Global Biogeochem. Cycles **35**: e2020GB006790. doi:https://doi.org/10.1029/2020GB006790

Pasqueron de Fommervault, O., P. Perez-brunius, P. Damien, V. F. Camacho-ibar, and J. Sheinbaum. 2017. Temporal variability of chlorophyll distribution in the Gulf of Mexico: bio-optical data from profiling floats. Biogeosciences **14**: 5647–5662. doi:10.5194/bg-14-5647-2017

Picheral, M., C. Catalano, D. Brousseau, and others. 2022. The Underwater Vision Profiler 6: an imaging sensor of particle size spectra and plankton, for autonomous and cabled platforms. Limnol. Oceanogr. Methods **20**: 115–129. doi:https://doi.org/10.1002/lom3.10475

Pradhan, H. K., C. Völker, S. N. Losa, A. Bracher, and L. Nerger. 2019. Assimilation of Global Total Chlorophyll OC-CCI Data and Its Impact on Individual Phytoplankton Fields. J. Geophys. Res. Ocean. **124**: 470–490. doi:10.1029/2018JC014329

Pradhan, H. K., C. Völker, S. N. Losa, A. Bracher, and L. Nerger. 2020. Global Assimilation of Ocean-Color Data of Phytoplankton Functional Types: Impact of Different Data Sets. J. Geophys. Res. Ocean. **125**: e2019JC015586. doi:https://doi.org/10.1029/2019JC015586

Prunet, P., J. Minster, V. Echevin, and I. Dadou. 1996a. Assimilation of surface data in a one-dimensional physical-biogeochemical model of the surface ocean 2. Ajusting a simple trophic model to chlorophyll, temperature, nitrate, and pCO2 data. Global Biogeochem. Cycles **10**: 139–158.

Prunet, P., J. Minster, D. Ruiz-Pino, and I. Dadou. 1996b. Assimilation of surface data in a one-dimensional physical-biogeochemical model of the surface ocean 1 . Method and preliminary results. Global Biogeochem. Cycles **10**: 111–138.

Quay, P., S. Emerson, and H. Palevsky. 2020. Regional Pattern of the Ocean's Biological Pump Based on Geochemical Observations. Geophys. Res. Lett. **47**: e2020GL088098. doi:https://doi.org/10.1029/2020GL088098

Raghukumar, K., C. A. Edwards, N. L. Goebel, G. Broquet, M. Veneziani, A. M. Moore, and J. P. Zehr. 2015. Impact of assimilating physical oceanographic data on modeled ecosystem dynamics in the California Current System. Prog. Oceanogr. **138**: 546–558. doi:https://doi.org/10.1016/j.pocean.2015.01.004

Rasse, R., G. Dall'Olmo, J. Graff, T. K. Westberry, V. van Dongen-Vogels, and M. J. Behrenfeld. 2017. Evaluating Optical Proxies of Particulate Organic Carbon across the Surface Atlantic Ocean. Front. Mar. Sci. **4**: 1–18. doi:10.3389/fmars.2017.00367

Resplandy, L., M. Lévy, and D. J. McGillicuddy Jr. 2019. Effects of Eddy-Driven Subduction on Ocean Biological Carbon Pump. Global Biogeochem. Cycles **33**: 1071–1084. doi:10.1029/2018GB006125

Ridenour, N. A., X. Hu, K. Sydor, P. G. Myers, and D. G. Barber. 2019. Revisiting the Circulation of Hudson Bay: Evidence for a Seasonal Pattern. Geophys. Res. Lett. **46**: 3891–3899. doi:https://doi.org/10.1029/2019GL082344

Rio, M.-H., S. Mulet, and N. Picot. 2013. New global mean dynamic topography from a goce geoid model, altimeter measurements and oceanographic in-situ data. ESA Living Planet Symp. Proc. Conf. held 9-13 Sept. 2013 Edinburgh United Kingdom. ESA SP-722. 2-13, p.27 **2013**: 2–13.

Roemmich, D., M. H. Alford, H. Claustre, and others. 2019. On the Future of Argo: A Global, Full-Depth, Multi-Disciplinary Array. Front. Mar. Sci. **6**: 439.

Roesler, C., J. Uitz, H. Claustre, and others. 2017. Recommendations for obtaining unbiased chlorophyll estimates from in situ chlorophyll fluorometers: A global analysis of WET Labs ECO sensors. Limnol. Oceanogr. Methods **15**: 572–585. doi:10.1002/lom3.10185

Sakov, P., G. Evensen, and L. Bertino. 2010. Asynchronous data assimilation with the EnKF. Tellus A Dyn. Meteorol. Oceanogr. **62**: 24–29. doi:10.1111/j.1600-0870.2009.00417.x

Sakov, P., and P. R. Oke. 2008. A deterministic formulation of the ensemble Kalman filter: an alternative to ensemble square root filters. Tellus A Dyn. Meteorol. Oceanogr. **60**: 361–371. doi:10.1111/j.1600-0870.2007.00299.x

Salon, S., G. Cossarini, G. Bolzon, L. Feudale, P. Lazzari, A. Teruzzi, C. Solidoro, and A. Crise. 2019. Novel metrics based on Biogeochemical Argo data to improve the model uncertainty evaluation of the CMEMS Mediterranean marine ecosystem forecasts. Ocean Sci. **15**: 997–1022. doi:10.5194/os-15-997-2019

Santana-Falcón, Y., P. Brasseur, J. M. Brankart, and F. Garnier. 2020. Assimilation of chlorophyll data into a stochastic ensemble simulation for the North Atlantic Ocean. Ocean Sci. **16**: 1297–1315. doi:10.5194/os-16-1297-2020

Sathyendranath, S., M. Grant, R. J. W. Brewin, and others. 2018. ESA Ocean Colour Climate Change Initiative (Ocean_Colour_cci): Version 3.1 Data. Centre for Environmental Data Analysis, 04 July 2018.

Sauzède, R., H. C. Bittig, H. Claustre, O. de Fommervault, J.-P. Gattuso, L. Legendre, and K. S. Johnson. 2017. Estimates of Water-Column Nutrient Concentrations and Carbonate System Parameters in the Global Ocean: A Novel Approach Based on Neural Networks. Front. Mar. Sci. **4**. doi:10.3389/fmars.2017.00128

Sauzède, R., H. Claustre, C. Jamet, J. Uitz, J. Ras, A. Mignot, and F. D'Ortenzio. 2015. Retrieving the vertical distribution of chlorophyll a concentration and phytoplankton community composition from in situ fluorescence profiles: A method based on a neural network with potential for global-scale applications. J. Geophys. Res. Ocean. **120**: 451–470. doi:https://doi.org/10.1002/2014JC010355

Sauzède, R., H. Claustre, J. Uitz, and others. 2016. A neural network-based method for merging ocean color and Argo data to extend surface bio-optical properties to depth: Retrieval of the particulate backscattering coefficient. J. Geophys. Res. Ocean. **121**: 2552–2571. doi:https://doi.org/10.1002/2015JC011408

Schartau, M., and A. Oschlies. 2003. Simultaneous data-based optimization of a 1D-ecosystem model at three locations in the North Atlantic : Part I — Method and parameter estimates. J. Mar. Res. **61**: 765–793.

Shchepetkin, A. F., and J. C. Mcwilliams. 2005. The regional oceanic modeling system (ROMS): a split-explicit, free-surface, topography-following-coordinate oceanic model. Ocean Model. **9**: 347–404. doi:10.1016/j.ocemod.2004.08.002

Sheng, J., R. J. Greatbatch, and D. G. Wright. 2001. Improving the utility of ocean circulation models through adjustment of the momentum balance. J. Geophys. Res. Ocean. **106**: 16711–16728. doi:10.1029/2000JC000680

Shulman, I., S. Frolov, S. Anderson, B. Penta, R. Gould, P. Sakalaukus, and S. Ladner. 2013. Impact of bio-optical data assimilation on short-term coupled physical , bio-optical model predictions. J. Geophys. Res. Ocean. **118**: 2215–2230. doi:10.1002/jgrc.20177

Siegel, D. A., K. O. Buesseler, S. C. Doney, S. F. Sailley, M. J. Behrenfeld, and P. W. Boyd. 2014. Global assessment of ocean carbon export by combining satellite observations and food-web models. Global Biogeochem. Cycles **28**: 181–196. doi:10.1002/2013GB004743

Skákala, J., J. Bruggeman, R. J. W. Brewin, D. A. Ford, and S. Ciavatta. 2020. Improved Representation of Underwater Light Field and Its Impact on Ecosystem Dynamics: A Study in the North Sea. J. Geophys. Res. Ocean. **125**: e2020JC016122. doi:https://doi.org/10.1029/2020JC016122

Skákala, J., D. Ford, R. J. W. Brewin, R. McEwan, S. Kay, B. Taylor, L. de Mora, and S. Ciavatta. 2018. The Assimilation of Phytoplankton Functional Types for Operational Forecasting in the Northwest European Shelf. J. Geophys. Res. Ocean. **123**: 5230–5247. doi:10.1029/2018JC014153

Skákala, J., D. Ford, J. Bruggeman, and others. 2021. Towards a Multi-Platform Assimilative System for North Sea Biogeochemistry. J. Geophys. Res. Ocean. **126**: e2020JC016649. doi:https://doi.org/10.1029/2020JC016649

Smagorinsky, J. 1963. General circulation experiments with the primitive equations: I. the basic experiment. Mon. Weather Rev. **91**: 99–164.

Smolarkiewicz, P. K., and L. G. Margolin. 1998. MPDATA : A Finite-Difference Solver for Geophysical Flows. J. Comput. Phys. **140**: 459–480.

Song, H., C. A. Edwards, A. M. Moore, and J. Fiechter. 2016a. Data assimilation in a coupled physical-biogeochemical model of the California current system using an incremental lognormal 4-dimensional variational approach: Part 3—Assimilation in a realistic context using satellite and in situ observations. Ocean Model. **106**: 159–172. doi:https://doi.org/10.1016/j.ocemod.2016.06.005

Song, H., C. A. Edwards, A. M. Moore, and J. Fiechter. 2016b. Data assimilation in a coupled physical-biogeochemical model of the California Current System using an incremental lognormal 4-dimensional variational approach: Part 2—Joint physical and biological data assimilation twin experiments. Ocean Model. **106**: 146–158. doi:https://doi.org/10.1016/j.ocemod.2016.09.003

Stock, C. A., J. P. Dunne, S. Fan, and others. 2020. Ocean Biogeochemistry in GFDL's Earth System Model 4.1 and Its Response to Increasing Atmospheric CO2. J. Adv. Model. Earth Syst. **12**: e2019MS002043. doi:https://doi.org/10.1029/2019MS002043

Stukel, M. R., L. I. Aluwihare, K. A. Barbeau, and others. 2017. Mesoscale ocean fronts enhance carbon export due to gravitational sinking and subduction. Proc. Natl. Acad. Sci. **114**: 1252–1257. doi:10.1073/pnas.1609435114

Stukel, M. R., H. Song, R. Goericke, and A. J. Miller. 2018. The role of subduction and gravitational sinking in particle export, carbon sequestration, and the remineralization length scale in the California Current Ecosystem. Limnol. Oceanogr. **63**: 363–383. doi:10.1002/lno.10636

Teruzzi, A., G. Bolzon, S. Salon, P. Lazzari, and C. Solidoro. 2018. Assimilation of coastal and open sea biogeochemical data to improve phytoplankton simulation in the Mediterranean Sea. Ocean Model. **132**: 46–60. doi:10.1016/j.ocemod.2018.09.007

Teruzzi, A., S. Dobricic, C. Solidoro, and G. Cossarini. 2014. A 3-D variational assimilation scheme in coupled transport-biogeochemical models: Forecast of Mediterranean biogeochemical properties. J. Geophys. Res. Ocean. **119**: 200–217. doi:10.1002/2013JC009277

Terzić, E., P. Lazzari, E. Organelli, C. Solidoro, S. Salon, F. D'Ortenzio, and P. Conan. 2019. Merging bio-optical data from Biogeochemical-Argo floats and models in marine biogeochemistry. Biogeosciences **16**: 2527–2542. doi:10.5194/bg-16-2527-2019

Thacker, W. C., A. Srinivasan, M. Iskandarani, O. M. Knio, and M. Le Hénaff. 2012. Propagating boundary uncertainties using polynomial expansions. Ocean Model. **43**–**44**: 52–63. doi:https://doi.org/10.1016/j.ocemod.2011.11.011

Tjiputra, J. F., D. Polzin, and A. M. E. Winguth. 2007. Assimilation of seasonal chlorophyll and nutrient data into an adjoint three-dimensional ocean carbon cycle model : Sensitivity analysis and ecosystem parameter optimization. Global Biogeochem. Cycles **21**: 1–13. doi:10.1029/2006GB002745

Tjiputra, J. F., J. Schwinger, M. Bentsen, and others. 2020. Ocean biogeochemistry in the Norwegian Earth System Model version 2 (NorESM2). Geosci. Model Dev. **13**: 2393–2431. doi:10.5194/gmd-13-2393-2020

Verdy, A., and M. R. Mazloff. 2017. A data assimilating model for estimating Southern Ocean biogeochemistry. J. Geophys. Res. Ocean. **122**: 6968–6988. doi:https://doi.org/10.1002/2016JC012650

Villa-Alfageme, M., F. C. de Soto, E. Ceballos, S. L. C. Giering, F. A. C. Le Moigne, S. Henson, J. L. Mas, and R. J. Sanders. 2016. Geographical, seasonal, and depth variation in sinking particle speeds in the North Atlantic. Geophys. Res. Lett. **43**: 8609–8616. doi:https://doi.org/10.1002/2016GL069233

Villa-Alfageme, M., F. de Soto, F. A. C. Le Moigne, S. L. C. Giering, R. Sanders, and R. García-Tenorio. 2014. Observations and modeling of slow-sinking particles in the twilight zone. Global Biogeochem. Cycles **28**: 1327–1342. doi:https://doi.org/10.1002/2014GB004981

Wang, B., and K. Fennel. 2022. Biogeochemical-Argo data suggest significant contributions of small particles to the vertical carbon flux in the subpolar North Atlantic. Limnol. Oceanogr. **n/a**. doi:https://doi.org/10.1002/lno.12209

Wang, B., K. Fennel, and L. Yu. 2021. Can assimilation of satellite observations improve subsurface biological properties in a numerical model? A case study for the Gulf of Mexico. Ocean Sci. **17**: 1141–1156. doi:10.5194/os-17-1141-2021

Wang, B., K. Fennel, L. Yu, and C. Gordon. 2020. Assessing the value of biogeochemical Argo profiles versus ocean color observations for biogeochemical model optimization in the Gulf of Mexico. Biogeosciences **17**: 4059–4074. doi:10.5194/bg-17-4059-2020

Ward, B. A., M. A. M. Friedrichs, T. R. Anderson, and A. Oschlies. 2010. Parameter optimisation techniques and the problem of underdetermination in marine biogeochemical models. J. Mar. Syst. **81**: 34–43. doi:10.1016/j.jmarsys.2009.12.005

Ward, B. A., M. Schartau, A. Oschlies, A. P. Martin, M. J. Follows, and T. R. Anderson. 2013. When is a biogeochemical model too complex? Objective model reduction and selection for North Atlantic time-series sites. Prog. Oceanogr. **116**: 49–65. doi:https://doi.org/10.1016/j.pocean.2013.06.002

Weber, T., and D. Bianchi. 2020. Efficient Particle Transfer to Depth in Oxygen Minimum Zones of the Pacific and Indian Oceans. Front. Earth Sci. **8**: 376. doi:10.3389/feart.2020.00376

Weber, T., J. A. Cram, S. W. Leung, T. DeVries, and C. Deutsch. 2016. Deep ocean nutrients imply large latitudinal variation in particle transfer efficiency. Proc. Natl. Acad. Sci. **113**: 8606–8611. doi:10.1073/pnas.1604414113

Westberry, T., M. J. Behrenfeld, D. A. Siegel, and E. Boss. 2008. Carbon-based primary productivity modeling with vertically resolved photoacclimation. Global Biogeochem. Cycles **22**: 1–18. doi:10.1029/2007GB003078

Wilson, J. D., A. Ridgwell, and S. Barker. 2015. Can organic matter flux profiles be diagnosed using remineralisation rates derived from observed tracers and modelled ocean transport rates? Biogeosciences **12**: 5547–5562. doi:10.5194/bg-12-5547-2015

Xiao, Y., and M. A. M. Friedrichs. 2014a. The assimilation of satellite-derived data into a one-dimensional lower trophic level marine ecosystem model. J. Geophys. Res. Ocean. **119**: 2691–2712. doi:10.1002/2013JC009433

Xiao, Y., and M. A. M. Friedrichs. 2014b. Using biogeochemical data assimilation to assess the relative skill of multiple ecosystem models in the Mid-Atlantic Bight : effects of increasing the complexity of the planktonic food web. Biogeosciences **11**: 3015–3030. doi:10.5194/bg-11-3015-2014

Xu, D., J. Zhu, Y. Qi, X. Li, and Y. Yan. 2012. The impact of mean dynamic topography on a sea-level anomaly assimilation in the South China Sea based on an eddy-resolving model. Acta Oceanol. Sin. **31**: 11–25. doi:10.1007/s13131-012-0232-x

Xue, Z., R. He, K. Fennel, W. Cai, S. Lohrenz, and C. Hopkinson. 2013. Modeling ocean circulation and biogeochemical variability in the Gulf of Mexico. Biogeosciences **10**: 7219–7234. doi:10.5194/bg-10-7219-2013

Yool, A., E. Popova, and T. R. Anderson. 2011. MEDUSA-1.0: A new intermediate complexity plankton ecosystem model for the global domain. Geosci. Model Dev. **4**. doi:10.5194/gmd-4-381-2011

Yu, L., K. Fennel, L. Bertino, M. El Gharamti, and K. R. Thompson. 2018. Insights on multivariate updates of physical and biogeochemical ocean variables using an Ensemble Kalman Filter and an idealized model of upwelling. Ocean Model. **126**: 13–28. doi:https://doi.org/10.1016/j.ocemod.2018.04.005

Yu, L., K. Fennel, and A. Laurent. 2015. A modeling study of physical controls on hypoxia generation in the northern Gulf of Mexico. J. Geophys. Res. Ocean. **120**: 5019–5039. doi:10.1002/2014JC010634

Yu, L., K. Fennel, B. Wang, A. Laurent, K. R. Thompson, and L. K. Shay. 2019. Evaluation of nonidentical versus identical twin approaches for observation impact assessments: an ensemble-Kalman-filter-based ocean assimilation application for the Gulf of Mexico. Ocean Sci. **15**: 1801–1814. doi:10.5194/os-15-1801-2019

Zahariev, K., J. R. Christian, and K. L. Denman. 2008. Preindustrial, historical, and fertilization simulations using a global ocean carbon model with new parameterizations of iron limitation, calcification, and N2 fixation. Prog. Oceanogr. **77**: 56–82. doi:https://doi.org/10.1016/j.pocean.2008.01.007